National Science Foundation #ATM-9118963

JET-INDUCED INERTIAL INSTABILITIES AND THE GROWTH OF MESOSCALE CONVECTIVE SYSTEMS

by David O. Blanchard

William R. Cotton, P.I.

Colorado State University

DEPARTMENT OF ATMOSPHERIC SCIENCE

PAPER NO. 571

JET-INDUCED INERTIAL INSTABILITIES AND THE GROWTH OF MESOSCALE CONVECTIVE SYSTEMS

by
David O. Blanchard
Department of Atmospheric Science
Colorado State University
Fort Collins, CO 80523

Research Supported in part by

National Science Foundation
under grant #ATM-9118963

January 5, 1995

Atmospheric Science Paper No. 571

ABSTRACT

JET-INDUCED INERTIAL INSTABILITIES AND THE GROWTH OF MESOSCALE CONVECTIVE SYTEMS.

Many mesoscale convective systems (MCSs) have been observed to form in environments where the isentropic absolute vorticity may have values that approach zero, resulting in regions with weak inertial stability. It has been demonstrated that for a given amount of convective available potential energy (CAPE), deep convective circulations can be modified and enhanced as the inertial stability is reduced. Consequently, there has been speculation that the evolution and organization of convection into MCSs may be related to the presence of an environment in which the inertial stability is weak or unstable.

In some mesoscale environments, particularly in the springtime when CAPE is large and a strong jet stream is still present, the atmosphere is unstable to both upright and slantwise convection. Because the time scales of these two modes are considerably different, upright convection will typically dominate. It is hypothesized that this upright convection can, over longer time scales, exploit the weak restoring force present in the mesoscale inertial stability.

To explore the hypothesis that inertial instability plays a role in the development of mesoscale growth and organization, both observational and model data were examined. Environments that supported the growth of MCSs in the PRE-STORM network were sampled with high quality special soundings. Secondary circulations that occurred in the presence of inertial instabilies were analyzed and documented using the high spatial and temporal resolution rawinsonde data from the PRE-STORM field program.

Additional examples of MCS environments were examined using data from the MAPS analysis system. The high resolution of the model, coupled with the ingest of multiple data types, result in the improved analysis of small-scale and short-lived features such as mesoscale inertial instabilities.

To increase the understanding of the basic processes that enhance MCS growth in inertially unstable environments, the RAMS mesoscale model was used. Model results indicate that the strength of the divergent outflow was strongly linked to the degree of inertial stability in the local environment. The results also showed a strong dependence on the magnitude of the Coriolis parameter. Finally, simulations using varying degrees of vertical stability indicated that there was also significant sensitivity to this parameter.

David Owen Blanchard
Atmospheric Science Department
Colorado State University
Fort Collins, Colorado 80523
Fall, 1994

ACKNOWLEDGMENTS

The completion of this study was made possible with the guidance, encouragement, and assistance of many people. Thanks and sincere appreciation are given to the members of my Ph.D. committee (Professors. William Cotton, Paul Mielke, Steven Rutledge, Wayne Schubert, and Dr. John Brown) for their efforts in the development of the original research proposal. Special thanks are extended to my advisor, Professor Cotton, and committee member Dr. Brown (NOAA/FSL), for the immense amount of time they have given to examining model results during the early stages, and for their particularly thorough reviews of an early draft. Their efforts have resulted in a much improved study.

A significant portion of the data used in this study was made available by the invaluable contributions of many scientists during the PRE-STORM field program. In particular, I would like to thank Mr. John Cunning (NOAA/USWRP) for allowing me to participate in PRE-STORM, and for some of the original suggestions for research topics using this data. I would also like to thank Dr. Stanley Benjamin (NOAA/FSL) for providing the MAPS mesoscale analysis products, and Ms. Tracy Lorraine Smith (NOAA/FSL) for providing the code to read and translate the MAPS data.

A heartfelt thanks is extended to Mr. Rolf Hertenstein (CSU) for guiding me on my way in the use of the RAMS model, and for providing the original code for the heating functions used in the model study. Thanks are also given to Mr. Peter Olsson (CSU) for convincing me that Unix is the only way to go, and for some enlightening discussions on balanced flow.

Mr. John Augustine (NOAA/NSSL) graciously provided the results of his compositing study of MCCs and allowed me to report on his work here. Dr. David Jorgensen (NOAA/NSSL) wrote much of the software used to analyze the radar data and Mr. Irv Watson (NOAA/NSSL) provided much of the instruction in the use of these programs.

Finally, I want to thank the director of the National Severe Storms Laboratory, Dr. Robert Maddox, for allowing me to take time off from my job responsibilities to attend classes, and for permitting me to work on this topic as part of my job requirements.

This research was supported in part under National Science Foundation grant ATM-9118963.

TABLE OF CONTENTS

1. INTRODUCTION 1

2. CONCEPTUAL MODEL 4

3. CASE STUDIES 19
   3.1. Data sources 20
      3.1.1. Surface data 21
      3.1.2. Rawinsonde 21
      3.1.3. Radar 22
   3.2. PRE-STORM cases 23
      3.2.1. 12–13 May 1985 24
      3.2.2. 6–7 May 1985 30
      3.2.3. 16–17 June 1985 33
   3.3. MAPS cases 36
      3.3.1. 13–14 May 1992 36
      3.3.2. 7–8 July 1992 39
   3.4. Augustine composites 41
   3.5. Discussion of case studies 42

4. RAMS NUMERICAL MODEL 87
   4.1. Model description 87
      4.1.1. Theoretical development of model equations 87
      4.1.2. Finite differences 92
      4.1.3. Model domain 93
      4.1.4. Boundary conditions 93
      4.1.5. Initialization 94
   4.2. Discussion of model configuration 96
   4.3. Discussion of heating rates 96
   4.4. Discussion of 2-D vs. 3-D 98
   4.5. Preliminary experiments 100
   4.6. Modeling experiments 102
   4.7. Simulation 1 104
      4.7.1. Simulation 1a–c 104
      4.7.2. Simulation 1d-f 106
      4.7.3. Discussion 107
   4.8. Simulation 4 108

4.8.1. Simulation 4a 109
4.8.2. Simulation 4b 110
4.8.3. Simulation 4e 111
4.8.4. Discussion 112
4.9. Discussion of other simulations 113
4.10. Sensitivity tests 116
4.10.1. Vertical stability 116
4.10.2. Vertical shear 119
4.10.3. Model resolution 120
4.10.4. Discussion 121

5. SUMMARY AND CONCLUSIONS 168
5.1. Summary of case studies 169
5.2. Summary of model studies 172
5.3. Discussion of conceptual model 177
5.4. Future Research 178

6. REFERENCES 180

7. APPENDIX 189
7.1. Description of Eliassen's basic model 189
7.2. Determination of initial state 190
7.3. Description of angular momentum changes 190

LIST OF FIGURES

Figure 1. Typical regions in which mesoscale convective systems (MCS) occur. 15

Figure 2. Equilibrium level outflow in regions of inertial instability (top) and inertial stability (bottom). 16

Figure 3. Cross section in the *y*-*z* plane showing differences in inertially stable and unstable regions. 17

Figure 4. Cross section in the *y*-*z* plane showing representative trajectories of air parcels.. 18

Figure 5. Location of the PRE-STORM field program and placement of the observational network. 44

Figure 6. Base scan image from the Norman, Oklahoma, Doppler radar at a) 0015, b) 0138, and c) 0258 UTC on 13 May 1985. 45

Figure 7. Evolution of precipitation and rain volume 48

Figure 8. Composite chart at 0000 UTC on 13 May 1985 depicting conditions at 500 mb with surface fronts and pressure centers superimposed. 49

Figure 9. PAM and SAM mesonet data and surface boundaries at 0000 UTC on 13 May 1985. 50

Figure 10. Plan view (x–y plane) of the inertial stability parameter, defined as $\alpha = (\zeta_\theta + f)/f$, over the PRE-STORM network on the 330 K isentrope at 0000 UTC on 13 May 1985. 51

Figure 11. Vertical cross section of the inertial instability parameter at 0000 UTC on 13 May 1985 52

Figure 12. Vertical cross section of symmetric stability, $S = (\eta_\theta / f) R_i$ at 0000 UTC on 13 May 1985. 53

Figure 13. Plan view on the a) 308 K and b) 330 K isentropic surfaces showing the 3-hour changes in temperature, pressure and winds. 54

Figure 14. Vertical profile of 3-hour changes in the height (solid), temperature (dotted) and dewpoint (dashed) for Enid, Oklahoma. 56

Figure 15. Vertical cross section showing pseudo-momentum surfaces (thin lines), θ_e (thick lines), and relative humidity in excess of 80% (shading)....................57

Figure 16. As in Fig. 15, except the cross section is through the PRE-STORM network and uses the special PRE-STORM sounding data. 58

Figure 17. Vertical cross section of the divergence of the Q-vector. 59

Figure 18. Composite chart at 0000 UTC on 7 May 1985 depicting conditions at 500 mb with surface fronts and pressure centers superimposed. 60

Figure 19. Satellite imagery at 0630 UTC on 7 May 1985....................61

Figure 20. Vertical cross section of the divergence of Q-vectors at 0000 UTC on 7 May 1985. 62

Figure 21. Sounding for IAB (Wichita, Kansas) at 0000 UTC on 7 May 1985. Dotted lines are representative θ, θ_e, and mixing ratios. 63

Figure 22. Plan view of the inertial stability parameter ($\alpha = \eta/f$) at a) 0000 and b) 0600 UTC on 7 May 1985 on the 330 K isentrope. 64

Figure 23. Vertical cross section through the PRE-STORM network depicting the inertial instability....................66

Figure 24. Radar imagery at a) 0700 and b) 1000 UTC on 7 May 1985. 67

Figure 25. Vertical profile of 3-hour changes in the height (solid), temperature (dotted) and dewpoint (dashed) for Chanute, Kansas (CNU) for the period 0000–0300 UTC on 7 May 1985. 69

Figure 26. As in Fig. 25, except for Ft. Riley, Kansas (FRI)....................70

Figure 27. As in Fig. 25, except for Wichita, Kansas (IAB). 71

Figure 28. Composite chart for 0000 UTC on 17 June 1985 depicting conditions at 500 mb with surface fronts and pressure centers superimposed. 500-mb height contours every 30 m. 72

Figure 29. Plan view of the inertial instability parameter on the 326 K isentrope at 0000 UTC on 17 June 1985. Positive values are solid..................73

Figure 30. Vertical profile of 3-hour changes in the height (solid), temperature (dotted) and dewpoint (dashed) for Fort Riley, Kansas (FRI) for the period 0000–0300 UTC on 17 June 1985. 74

Figure 31. Satellite infrared image at 0000 UTC on 14 May 1992. 75

Figure 32. Composite chart for 0000 UTC on 14 May 1992 depicting conditions at 500 mb with surface fronts and pressure centers superimposed. 76

Figure 33. Plan view at 0000 UTC on 14 May 1992 showing the inertial stability parameter on the 330 K isentropic surface. 77

Figure 34. Vertical cross section showing the inertial stability......................78

Figure 35. Vertical cross section showing momentum surfaces (contour interval 5 m s-1) and equivalent potential temperature, θ_e (contour interval is 2 K). 79

Figure 36. Satellite imagery for 7–8 July, 1992, at a) 0001 UTC and b) 0601 UTC. 80

Figure 37. Composite chart for 0000 UTC on 8 July 1992 depicting conditions at 500 mb with surface fronts and pressure centers superimposed. 500-mb height contours every 30 m. 82

Figure 38. Plot of temperature, dewpoint, heights, and winds on the 300-mb pressure surface at 0000 UTC on 8 July 1992. 83

Figure 39. Inertial stability parameter on the 342 K isentropic surface at 0000 UTC on 8 July 1992. 84

Figure 40. Cross section of the inertial stability parameter from northern Nebraska to southern Kansas...85

Figure 41. Composite of 38 events depicting the large scale environment associated with the development of large MCSs at 200 mb. Contours represent inertial stability. 86

Figure 42. Skew T–ln P diagram of the two soundings used in the model simulations. 123

Figure 43. Vertical cross section of the heating function profile. 124

Figure 44. Vertical cross section of the potential temperature field, θ, at t=0 h for experiment 1. 125

Figure 45. Vertical cross section of the vertical velocity field, w, at t=2 h for experiment 1b. 126

Figure 46. Vertical cross section of the u-component of the wind at t=3 h for experiment 1b 127

Figure 47. As in Fig. 46, except for t=6 h. 128

Figure 48. Vertical cross section of the v -component of the wind at t=6 h for experiment 1b 129

Figure 49. Vertical cross section of the absolute vorticity, $(\zeta + f)$, at t=6 h for experiment 1b 130

Figure 51. As in Fig. 49, except for t=6 h and for simulation 1f 132

Figure 52. As in Fig. 46, except for t=0 h and for experiment 4. 133

Figure 53. As in Fig. 48, except for t=0 h and for experiment 4. 134

Figure 54. As in Fig. 44, except for t=0 h and for experiment 4. 135

Figure 55. As in Fig. 49, except for t=0 h and for experiment 4. 136

Figure 56. As in Fig. 46, except for t=2 h and for experiment 4a. 137

Figure 57. As in Fig. 46, except for t=3 h and for experiment 4a. 138

Figure 58. As in Fig. 46, except for t=4 h and for experiment 4a. 139

Figure 59. As in Fig. 49, except for t=4 h and for experiment 4a. 140

Figure 60. As in Fig. 46, except for t=6 h and for experiment 4a. 141

Figure 61. As in Fig. 46, except for t=6 h and for experiment 4b. 142

Figure 62. As in Fig. 48, except for t=6 h and for experiment 4b. 143

Figure 63. As in Fig. 49, except for t=6 h and for experiment 4b. 144

Figure 64. As in Fig. 46, except for t=1 h and for experiment 4e. 145

Figure 65. As in Fig. 46, except for t=3 h and for experiment 4e. 146

Figure 66. As in Fig. 46, except for t=6 h and for experiment 4e. 147

Figure 67. Time profile showing the rate of change of the *u*-component of the wind for the four wind strengths (0, 10, 20, and 30 m s^{-1}) for a heating rate of a) 1°C h^{-1}, b) 3°C h^{-1}, and c) 5°C h^{-1}. 148

Figure 68. As in Fig. 67a, except for a latitude of 25° and heating rate of 3°C h^{-1}. 151

Figure 69. As in Fig. 67a, except for 3°C h^{-1} and only the winds with a westerly component are shown. 152

Figure 70. Time profiles showing the rate of change of the vertical velocities associated with different strengths of the jet (0, 10, 20, and 30 m s^{-1}) at latitude 40°. 153

Figure 71. Time profiles showing the rate of change of the vertical velocities associated with different strengths of the jet (0, 10, 20, and 30 m s^{-1}) at latitude 25°. 154

Figure 72a. As in Fig. 44, except for t=0 h and for experiment 5. 155

Figure 72b. As in Fig. 44, except for t=0 h and for experiment 4b. 156

Figure 73a. As in Fig 46, except for t=3 h and for experiment 5. 157

Figure 73b. As in Fig. 46, except for t=3 h and for experiment 4b. 158

Figure 74a. As in Fig. 44, except for t=3 h and for experiment 5. 159

Figure 74b. As in Fig. 44, except for t=3 h and for experiment 4b. 160

Figure 75a. As in Fig. 46, except for t=6 h and for experiment 5. 161

Figure 75b. As in Fig. 46, except for t=6 h and for experiment 4b. 162

Figure 76. As in Fig. 67, except comparing the results of the OKC sounding and the WK sounding. 163

Figure 77. As in Fig. 48, except for t=0 h and for experiment 6. 164

Figure 78. As in Fig. 46, except for t=6 h and for experiment 6. 165

Figure 79. As in Fig. 48, except for t=6 h and for experiment 6. 166

Figure 80. As in Fig. 49, except for t=6 h and for experiment 6. 167

LIST OF TABLES

TABLE PAGE

1. Values for fixed parameters used in RAMS. 103

2. Characteristic values for the jet and heating profiles and variable3latitudes used in the model simulations....101

1. INTRODUCTION

The mesoscale convective complex (MCC), described by Maddox (1980), and the more general mesoscale convective system (MCS) encompass a broad distribution of convective organizations, with squall lines, meso-α-scale and meso-β-scale convective clusters, and other non-squall linear or banded structures (McAnelly and Cotton 1986; Blanchard 1990; Houze et al. 1990). MCCs, in particular, are large thunderstorm conglomerates that produce significant convective season rainfall in the Midwest (Maddox 1983; Fritsch et al. 1986; Kane et al. 1987). They generally reach sizes of 10^5 km^2, last six to eighteen hours, and travel hundreds of kilometers during their lifetimes (Fritsch and Maddox 1981; McAnelly and Cotton 1989).

The development of nocturnal MCSs has been shown to be a function of large-scale synoptic patterns, terrain-induced features, such as elevated heat sources, and localized mesoscale forcing (Maddox 1980; Cotton et al. 1983; Wetzel et al. 1983; Doswell 1987; Tripoli and Cotton 1989a). Using objective analysis and compositing techniques for ten MCCs, Maddox (1983) identified several distinctive features at the surface and in the lower, middle, and upper troposphere during the formation, maturation, and dissipation stages of MCCs. Classification as an MCC was based on characteristics observable in satellite imagery because of the wide range of atmospheric scales that could be monitored, but did not address internal structural characteristics. More recently, Cotton et al. (1989), using compositing techniques that permit greater temporal resolution, examined 134 MCC events. Their results are similar to those of Maddox, but are more detailed regarding the temporal evolution of the system. Like Maddox, however, Cotton et al. (1989) did not directly address the question of variable structures within the MCCs. They concluded that an MCC is an inertially stable form of an MCS and proposed that a more dynamic definition of an MCC is "an MCS that is nearly geostrophically balanced and whose horizontal scale is comparable to or greater than the (modified) Rossby radius of deformation, λ_R." Blanchard (1990) has shown there are three basic, recurring mesoscale patterns of convection associated with MCSs, while Houze et al. (1990) have introduced a complex classification system for mesoscale convection associated with springtime rainstorms (i.e., at least 25 mm of rain in 24 h over an area exceeding 12,500 km^2). None of these studies, however, have addressed the dynamic and kinematic evolution associated with the upscale development of individual cloud elements into the mesoscale system; instead they focus on the organization of the convection after it has already developed into a mesoscale system and only provide a "snapshot" of the system structure.

Tripoli and Cotton (1989a), using the RAMS mesoscale model, investigated the genesis of an MCS that had its origins in the Colorado mountains. They were able to simulate both the mountain-generated solenoidal circulation and the solenoidal circulation that resides over the High Plains. Their results indicated that both features are important in the genesis of the MCC. The simulation, however, was restricted to two dimensions and could not accurately model the low-level jet, a feature of importance for MCC intensification. Nonetheless, they were able to simulate the upscale growth of convection from the meso-γ-scale to the larger meso-β-scale because of the growth of a deep meso-α-scale circulation. This result suggests the importance of the secondary circulations generated by the mesoscale convection and supports the findings of previous work (e.g., Zhang and Cho 1992; Zhang and Fritsch 1988).

Nachamkin et al. (1994) examined PRE-STORM (Cunning 1986) data to describe the upscale evolution of an MCC. They noted that mesoscale organization occurred shortly after the upper-level cloud shield reached MCC proportions and the organization manifested itself as a rapid, almost discreet transition. Nachamkin et al. noted that their result agrees with the assertion made in McAnelly and Cotton (1992) that the upscale transition from separate convective clusters to a coherent MCC may occur early in the MCC life cycle, and more abruptly than inferred from previous MCC life cycle research (i.e., Maddox 1983; Cotton et al. 1989; McAnelly and Cotton 1989). Because the earlier studies used composite data, smoothing of both spatial and temporal events was unavoidable and rapid changes were hidden in the composite, or not sampled at all.

Substantial effort has been made over many years to address the issues of convective evolution from the meso-γ-scale to the meso-β- and meso-α-scales associated with MCCs and MCSs. Some of these studies have dealt with kinematic structures observable with satellite, radar, rain gage, rawinsonde, and other data sets and have documented the evolution and structure of these systems. Others have used model simulations to address the evolution of the convective and the dynamic characteristics associated with the convection itself. Still others have attempted to deal with the problem of scale interaction in which the convective scale processes modify the mesoscale environment, resulting in changes that are resolvable with conventional data. Here, we will address issues of synergistic responses between both the convective scale processes and the mesoscale environment.

2. CONCEPTUAL MODEL

Much of the work on MCC/MCS development and evolution has concentrated on systems exhibiting a strong degree of linearity (e.g., Smull and Houze 1985, 1987; Rutledge et al. 1988; Johnson and Hamilton 1988). These linear systems (which include squall lines) can attribute a significant portion of the mesoscale organizing mechanisms to the presence of surface boundaries driven and maintained, in part, by baroclinic synoptic waves traversing the region. The frontogenetical nature of these waves can produce linear patterns of upward motion on the synoptic scale, resulting in similarly shaped regions of strong conditional or convective instability that is released by lifting associated with the passage of the surface boundary. As the convection matures, a large cold pool may develop that plays a significant role in the generation of horizontal vorticity, tilted updrafts and rear-inflow jets (Smull and Houze 1987; Rotunno et al. 1988; Rasmussen and Rutledge 1993; Skamarock et al. 1994). This development contributes to the generation of regions of trailing stratiform precipitation in which mesoscale updrafts and downdrafts (Brown 1979) play an important role in the generation and maintenance of the MCS.

An alternative conceptual model, proposed by Schmidt and Cotton (1990), is that particular shear profiles can excite gravity waves that are spatially asymmetric and experience a Doppler shift in phase speed and magnitude. The result is a consolidation of the upshear rear-to-front and front-to-rear flows (Smull and Houze 1985) and the reemergence of the deep convective-scale updraft. These gravity waves can be linearly organized and produce squall line systems that move at speeds corresponding to internal gravity wave speeds (Cram et al. 1992).

Similarly, Seman (1990) observed in his numerical study that the spatial scale of the new cell initiation appeared to be related to the spatial scale of outflow boundaries and to a superposition of convectively-generated gravity waves. He hypothesized that when the waves propagated over the outflow boundaries, vertical accelerations were enhanced in regions where the pressure field was more non-hydrostatic. Additionally, he noted that the response was stronger where the upper-level dynamic [inertial] stability was weaker; e.g., gravity waves amplified as they entered the unstable region, while those moving through the stable region merely propagated away from the system.

The gravity wave model is not new, having often been discussed in the literature. Raymond (1987) used a 2D, hydrostatic, nonrotating model to analyze self-organizing convective systems; i.e., systems that intensify, propagate, and maintain themselves without the help of external forcing such as might be produced by orographic effects, frontal circulations, or other sources of localized lifting. He introduced the term "forced gravity wave mechanism" as a replacement for wave-CISK and suggested that there was a cooperative instability between convective cells and gravity waves in the surrounding environment. This conceptual model depended on contributions of energy from updraft heating.

In contrast to the linear systems that often develop in an environment with strong embedded short waves and cyclonic vorticity, many MCCs and MCSs have been observed to form in environments where the isentropic absolute vorticity may have values that approach zero, resulting in regions with weak inertial stability. Further, if certain vertical stability criteria are also met, then symmetric instability may also be present. Symmetric instability, a fundamental instability in a rotating fluid, is a combined buoyant-inertial instability that can be viewed as inertial instability on a buoyancy surface or buoyant instability on a surface of constant angular momentum (Xu 1986). It has been demonstrated that, for a given amount of convective available potential energy (CAPE), deep convective circulations can be modified and enhanced as the symmetric stability is reduced (Eliassen 1951; Emanuel 1980, 1982, 1983; Xu 1986)

Consequently, there has been speculation that the mesoscale evolution and organization of these MCCs and MCSs may be related to the existence of an environment in which the inertial stability is weak (Emanuel 1979, 1980, 1982, 1983; Jascourt et al., 1988; Seman, 1990). Two typical regions in which inertial stability is weak or is unstable are 1) just equatorward of a wind maximum where the anticyclonic shear is large, and 2) in subsynoptic-scale ridges where the anticyclonic curvature is large. Figure 1 is a schematic representation of both types of environments. Observations (Maddox 1983; Kane et al. 1987; Cotton et al. 1989; Blanchard 1990) indicate that these are preferred regions for the upscale development of convection into MCSs.

It has been shown (Eliassen 1951; Bennetts and Hoskins 1979; Emanuel 1979) that in an environment where the atmosphere is stable to vertical (buoyancy) and horizontal (inertial) displacements, parcels may still be displaced along slantwise paths if both rotation and static stability are considered together. If the mean zonal flow increases with height and is in geostrophic and thermal wind balance, then the absolute angular momentum, M, is conserved approximately in the absence of frictional and diabatic effects. If a parcel of air is lifted in an environment that is at or near saturation along a surface of constant M and becomes warmer than its environment because of the release of latent heat, then the atmosphere is in a state of conditional symmetric instability (CSI). A conditionally or convectively stable atmosphere may still be conditionally symmetrically unstable allowing "slantwise" convection to take place. Additionally, if the environment is symmetrically unstable, then saturation is no longer a conditional requirement.

In certain mesoscale environments, particularly in the springtime when CAPE is large and a strong jet stream is still present, the atmosphere may be both convectively and symmetrically unstable. In this situation it is hypothesized that the secondary circulations generated by the upright convection can exploit the weak restoring force present in the mesoscale inertial stability. Air parcels move vertically through upright convection and on reaching the equilibrium level expand preferentially in the region that is inertially least stable.

Recent modeling work by Seman (1994) suggests that parcel descent in these conditions occurs on slant trajectories taking the path of least resistance, is directed back towards the generating convection, and occurs preferentially in the inertially unstable region. This coupling of the vertical updraft and slanted downdraft is called both "Convective-Symmetric Instability" (Conv-SI; Emanuel 1980, Seman 1991) and "nonlinear, nonhydrostatic Conditional Symmetric Instability" (Seman 1994). Further, Emanuel (1992) has noted in his analysis of Doppler radar data of winter storms that the development of slant downdrafts may be sensitive to the phase transition of ice at the melting level. Since there is a pronounced melting level in MCSs, this effect probably should be taken into account in moist simulations. On the other hand, the aforementioned simulations did not include ice phase microphysics in the development of the slant downdraft, yet were successful in demonstrating the existence of the downdraft.

In a paper discussing inertial stability and meridional motion in a circular vortex, Eliassen (1951) made some key points that are relevant to the current study. He notes the following:

> (a) In the gradient-balance, quasi-static theory, determining the meridional motion is not an initial value problem; the meridional motion depends only on the instantaneous sources of heat and angular momentum.
>
> (b) For a given heat or angular momentum source, stronger meridional motions develop the weaker the [inertial] stability of the vortex.
>
> (c) The meridional currents are assumed to be very slow compared to the vortex motion, so that the direct effect of the meridional circulation on the field of motion is slight. The importance of such weak meridional currents, however, does not lie in their direct effect on the wind field, but in their ability to change profoundly the structure of the vortex by transporting the fields of the quasi-conservative properties of angular momentum and entropy.
>
> (d) The meridional streamlines are ellipses. The vertical extent of the ellipses is very small compared to their horizontal extent, and the major axis will in all cases be oriented approximately along the isentropic lines.

His results allow us to set up a model simulation and provide a simple [instantaneous] source of heating, and suggest that decreasing inertial stability (produced by stronger jets) should provide a stronger response in the model. Additional discussion of these points is made in the Appendix.

In recent papers (Raymond and Jiang 1990; Raymond 1992; Seman 1994), *in situ* generation of potential vorticity anomalies was invoked to explain the upscale growth of convection into mature mesoscale systems. In these studies, there were no regions of inertial instability (i.e., negative potential vorticity) before the onset of convection; local convection was responsible for the development of the inertial instability. It was shown by Raymond and Jiang (1990) how the potential vorticity anomalies generated by an MCS itself can provide a mesoscale lifting mechanism to help maintain a convective system on mesoscale time scales. They argued that the net upward mass transport associated with the (relatively large-scale) convective heating within the system results in a negative (positive) potential vorticity anomaly at upper (lower) levels. With evaporation and melting of precipitation and thermal radiation, the low-level positive anomaly is strengthened, lifting the low-level isentropic surfaces further. Under favorable ambient vertical wind shear, low-level parcels approaching the MCS are forced to rise up the isentropic surfaces; if enough lifting occurs, conditional instability is realized. The convection, in turn, would act to reinforce the potential vorticity anomaly structure that caused it. It thus helps explain the longevity of an MCS after it has reached a relatively large size.

Although this model is very appealing because it can generate mesoscale jets (i.e., front-to-rear and rear-to-front flow) and both upper- and lower-level vortices within the MCS, it fails to address the question of why only some, instead of all, convective systems achieve this condition and grow upscale. A likely explanation lies in the work to be investigated here.

Hypothesis: If the environment is predisposed to a state of weak inertial stability, as suggested by the typical environments in which MCSs occur, then the divergent outflow at the equilibrium level can exploit the weak restoring force in the weakly inertially stable region and therefore be stronger and more persistent than otherwise. The result would be continued stronger updrafts, lower-level perturbation pressure falls and, eventually, the slant downdrafts suggested by CSI and Conv-SI theory. Further, the reduction of inertial stability results in less resistance to the growth of the convectively-generated secondary circulations and the realization of an upper-level (low-level) negative (positive) potential vorticity anomaly.

In accord with this conceptual model, Jascourt et al. (1988) completed a careful analysis of upright convection that acquired mesoscale organization in the presence of symmetric instability. They hypothesized that the difference between disorganized thundershowers and organized convection is that on a typical day, the organizing mesoscale circulation does not grow strong enough before the [diurnal] convection has ended, while on other days the symmetric stability is weak enough to permit rapid growth of the organizing mesoscale circulations.

Figure 2 illustrates how this occurs. Air parcels move vertically through the upright convection until the equilibrium level is reached. At this level, the ejection of mass from the updraft is constrained to a narrow channel downstream from the convection in an inertially stable environment (bottom), but is not constrained in an inertially unstable environment (top). In the latter environment, parcels can accelerate laterally through the inertially unstable or weakly stable region. The inertially unstable environment is able to diverge mass more efficiently than the stable environment.

Figure 3 illustrates the conceptual model in the y-z plane. In the inertially stable region, subsidence takes place in the near environment, resulting in drying and warming. This tends to stabilize the atmosphere and suppress new convection. In the inertially unstable region, parcels are accelerated away from the local environment before subsidence occurs, allowing the vertical instability to be maintained (Tripoli and Cotton 1989b). This meridional acceleration can advect the momentum field, as suggested by Eliassen (1951), so that inertially stable regions become less stable, leading to a positive feedback process. This enhancement of the divergence is partly a result of the change in Rossby radius when local angular momentum is taken into account (Schubert et al. 1980). Anticyclonic regions will expand the Rossby radius and, consequently, the time scale of the geostrophic adjustment process.

Figure 4, also in the *y*-*z* plane, indicates how meridional accelerations through the inertial instability at the equilibrium level begin to drive a solenoidal circulation. It is this circulation that is partially responsible for the continued generation of new convection through enhanced divergence aloft and convergence in the lower and middle troposphere. Tripoli (personal communication) suggests that although it is likely that convection can generate localized regions of inertial instability, this instability becomes a self-limiting process unless it can be maintained by mesoscale features in the form of sharply curved ridges or jet streaks where the inertial stability is weak. This may help explain why many convective systems do not grow upscale into mesoscale systems and why a special environment is favorable for development.

It is appropriate at this point to discuss the relationship between inertial instability and symmetric instability. Both terms have been used here and it is important to clarify their meanings. Holton (1992) discusses these two forms of instability and his comments are appropriate to the current problem. He notes that the comparative strength of the vertical and horizontal restoring forces in the mid-latitude troposphere are given by the ratio $N^2/(f\partial M/\partial y) \sim 10^4$, where N is the Brunt-Väisällä frequency, and the momentum $M = v_g + fx$. Thus, parcel motion in the plane orthogonal to the mean flow will remain much closer to θ surfaces than to M surfaces, so it is natural to use isentropic coordinates to analyze parcel displacements.

Holton (1992) notes that ordinarily the M surfaces will slope more than the θ surfaces and parcel displacements are stable, but when the θ surfaces slope more than the M surfaces so that

$$f(\partial M/\partial y)_\theta < 0, \tag{1}$$

the flow is unstable with respect to displacements along the θ surfaces. The condition is similar to the criterion for inertial instability (in z-coordinates), except that here the derivative of M is taken along a sloping θ surface; i.e., symmetric instability may be regarded as isentropic inertial instability (see also Xu 1986). Thus, it is appropriate to use the terms interchangeably.

Holton further notes that if (1) is multiplied by $-g(\partial\theta/\partial p)$ the criterion for symmetric instability can be expressed in terms of the distribution of Ertel potential vorticity in the simple form

$$f\overline{P} < 0 \tag{2}$$

where $\overline{P}$ is the potential vorticity of the basic state geostrophic flow. Thus, if the initial state potential vorticity is everywhere positive, then symmetric instability cannot develop through *adiabatic* motions, since potential vorticity is conserved following the motion and will always remain positive. Similarly, Hoskins (1974) notes that frictional and heating effects are needed to generate instability to symmetric motions in a previously stable atmosphere.

Finally, following Holton's (1992) derivation, and noting that symmetric instability requires that the slopes of the θ surfaces exceed those of the M surfaces, the necessary condition for instability of geostrophic flow parallel to the x-axis becomes

$$\frac{(\delta z/\delta y)_M}{(\delta z/\delta y)_\theta} = \frac{f\left(f - \partial u_g/\partial y\right)R_i}{f^2} < 1 \tag{3}$$

where the mean flow Richardson number R_i is defined as

$$R_i \equiv \frac{(g/\theta_0)\partial\theta/\partial z}{\left(\partial u_g/\partial z\right)^2}. \tag{4}$$

The condition for symmetric instability is infrequently satisfied; if the atmosphere is saturated, however, the relevant static stability condition involves the lapse rate of equivalent potential temperature (θ_e), and neutral conditions with respect to symmetric instability may easily occur.

Rewriting (3) for the x-y domain, we formally define the symmetric stability as

$$S = (\eta/f)R_i \tag{5}$$

A sufficient condition for symmetric instability is $S < 1$ (McIntyre, 1970).

Finally, it should be mentioned that the concept of inertial stability has played a role in the observational and modeling work of tropical cyclone systems. Work by Schubert and Hack (1982), and by Ooyama (1964, 1969), Charney and Eliassen (1964), and others have investigated the role of inertial stability within the vortex. They noted that during the rapid deepening phase, the increased inertial stability provides added resistance to the movement of air parcels in the (r,z) plane. This increase in inertial stability leads to a decrease in the forced secondary circulation and a change in the radial distribution of the warming. Tropical cyclone observations (Shea and Gray 1973; Holliday and Thompson 1979) show that as a cyclone develops, the size of the region of high inertial stability decreases while the magnitude of the inertial stability increases. Mid-latitude observational studies by Menard and Fritsch (1989) and Bartels and Maddox (1991) have suggested that a similar process can occur in long-lived (i.e. lifetime greater than an inertial period up to a few days) mesoscale convective complexes. This process of increased inertial stability plays an important role in the evolution and maintenance of long-lived systems. On the other hand, we are concerned here with the initial stages of convection before the development of a mid-tropospheric vortex or warm core, and reduced inertial stability at upper levels is more important to upscale growth than increased stability in the vortex column.

To explore the hypothesis that inertial instability plays a role in the development and evolution of mesoscale convection, MCSs that occurred in (1) the data-rich PRE-STORM network, and (2) environments sampled with new technology, were examined. The analysis of these data do not provide incontrovertible evidence that the inertial instability plays a role because of the large temporal and spatial gaps between observations. One way to overcome these shortcomings is to use a numerical model and analyze the simulation results. To this end the Regional Atmospheric Modeling System (RAMS), developed at Colorado State University, was used to simulate the conditions associated with weak inertial stability and inertial instability. The model simulations were used to develop a comprehensive understanding of the dynamics of this type of atmospheric motion, and for comparison with the observational data.

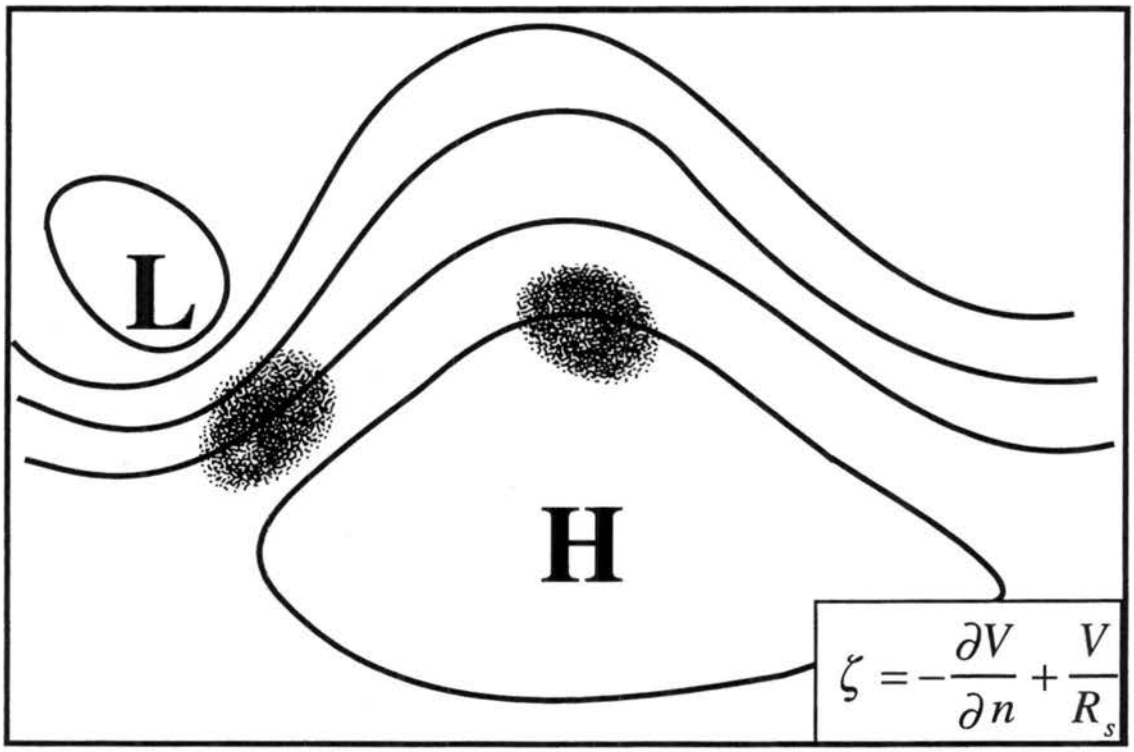

Figure 1. Typical regions in which mesoscale convective systems (MCS) occur. Contours are representative of heights (Montgomery stream function) on pressure (isentropic) surfaces. Lows and highs marked by "L" and "H", respectively. MCS is shown as a darkened region. MCSs tend to form in regions of strong baroclinity with jet streaks present as shown by the system on the left and in subsynoptic-scale ridges as shown by the system in the upper center. The definition of vorticity in lower right is given in natural coordinates. The first term on the right-hand side is the shear term and is large and negative in regions where jet streaks are present; the second term on the right is the curvature term and is large and negative in ridges. Large, negative values of vorticity can generate mesoscale regions of inertial instability.

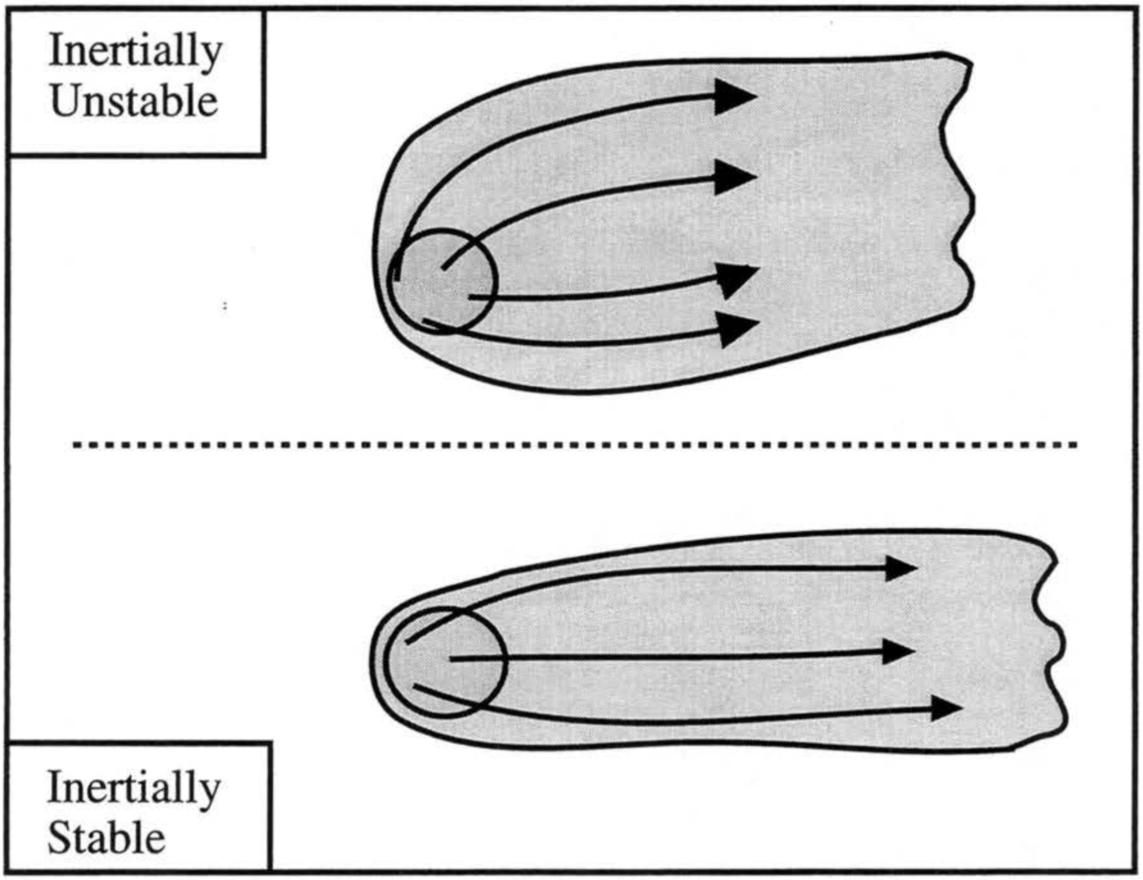

Figure 2. Equilibrium level outflow in regions of inertial instability (top) and inertial stability (bottom). Light shading is representative of anvil material. Circular region represents warm updraft core. Convective updraft material reaches the equilibrium level and is constrained to flow downstream in a channeled flow in the inertially stable environment. In the inertially unstable environment, updraft material is not constrained, resulting in an outflow that is more divergent than the stable case.

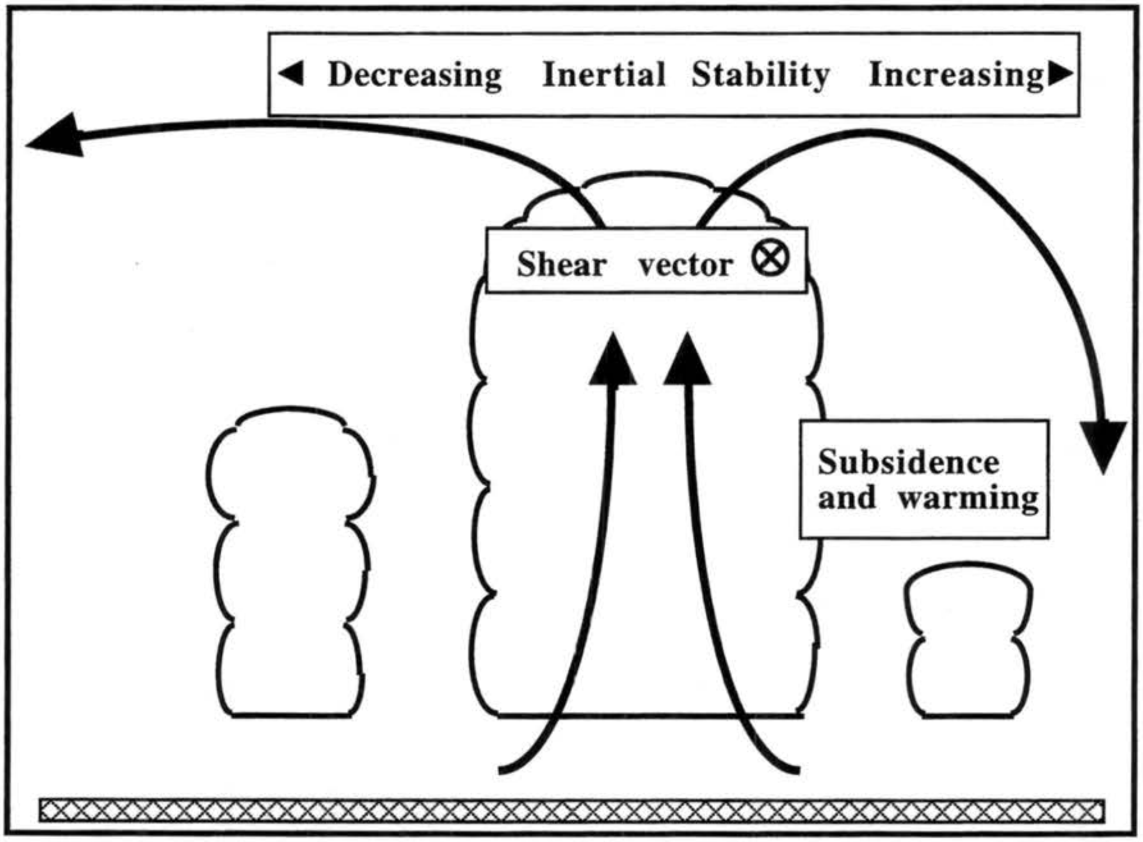

Figure 3. Cross section in the y-z plane showing differences in inertially stable and unstable regions. In the inertially stable region (right side), outflow material descends in the near environment, resulting in drying and warming. This will tend to reduce the buoyant instability and produce smaller and weaker convective clouds. The region of inertial instability (left side) permits meridional accelerations of outflow material. Descent of parcels does not occur locally. The buoyant instability is unaffected, allowing the convection to be more robust than in the stable region.

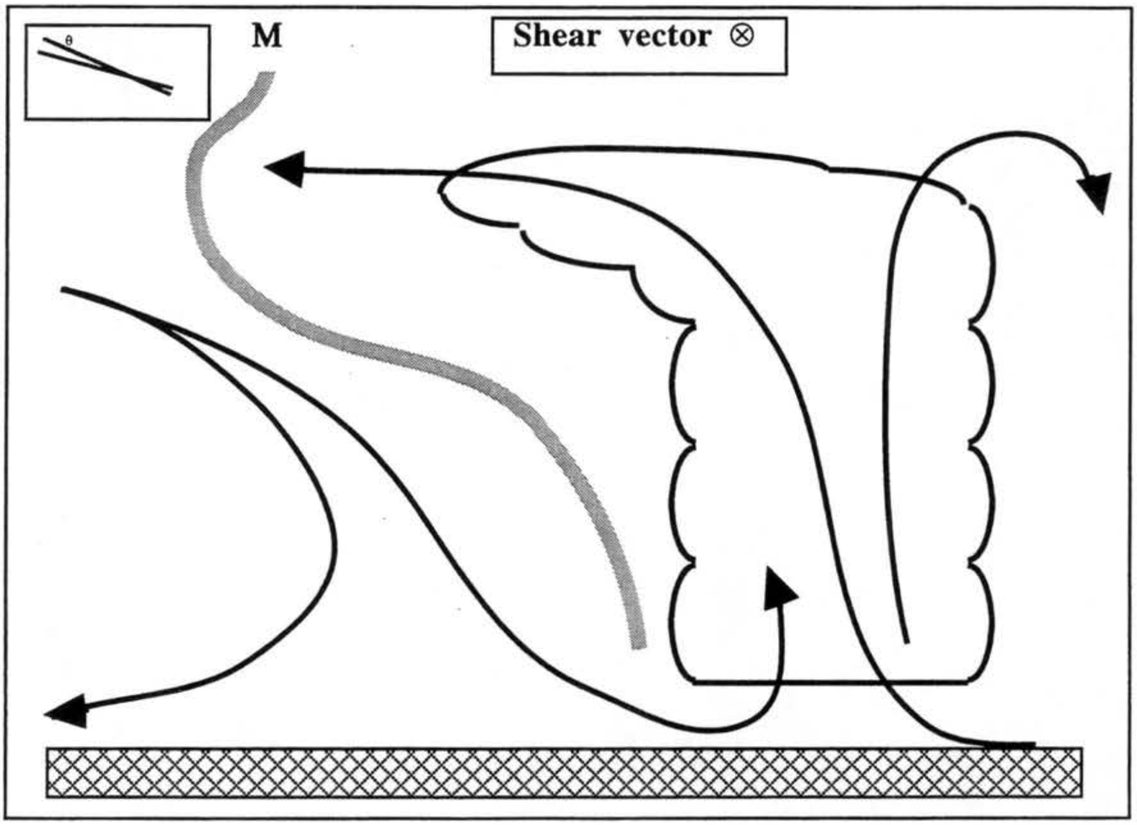

Figure 4. Cross section in the *y-z* plane showing representative trajectories of air parcels. Outflow material is meridionally accelerated through the region of inertial instability and returns on a slant downdraft trajectory. This return flow can lead to enhanced low-level convergence, which, coupled with the enhanced upper-level divergence, generates new convection. The thick, shaded line is a momentum surface and is distorted owing to advective processes in the upper region. The distortion can lead to regions that support conditional symmetric instability (CSI). Typical configuration of momentum and theta surfaces required for CSI is shown in the inset in the upper left corner.

3. CASE STUDIES

This study was motivated by the observations taken with high resolution PRE-STORM data. Some of the mesoscale convective events were observed to occur in regions that showed evidence of inertial instability prior to convection. Based on the analyses of those original observations, it was decided to do a modeling study (discussed later) and to analyze additional observational examples using newer data sets. It is useful now to examine the findings from the analysis of the observational data.

Special high temporal and spatial density rawinsonde data from the PRE-STORM field program (Cunning 1986) were objectively analyzed on isentropic surfaces, and the ratio $\alpha = \eta / f$ (where η is the isentropic absolute vorticity and f is the Coriolis parameter) was computed. A necessary condition for inertial instability is an environment in which $\alpha < 0$; days that satisfied this condition were selected for further investigation[1].

Twenty-one MCCs/MCSs occurred in the network during PRE-STORM and 17 were during IOPs (intensive operations periods) with special data sets. Of these, nearly 24% (4 of 17) of the MCC/MCS environments showed evidence of inertial instability; many others exhibited weak inertial stability. Analysis of the high-quality data from the MCC that occurred on 12-13 May 1985 strongly suggests that the responses expected owing to an inertial instability were present. These include enhanced divergence in the inertially

---

[1]Note that $\alpha < 0$ is also a sufficient condition to diagnose negative potential vorticity.

unstable region and enhanced low-level convergence in the region of slant downdraft return flow. Computations of the horizontal accelerations in the unstable regions agree with the velocities seen by Seman (1992) in his simulations of MCS development and the *in situ* generation of inertial instability. Data from three other PRE-STORM cases (6–7 May 1985, 16–17 June 1985, and 23–24 June 1985) are also suggestive but they are not as complete as those of 12–13 May 1985, and the special rawinsonde data collection did not start before the onset of convection. Owing to the late start of data collection, it cannot be stated with absolute certainty what is cause and what is effect in the latter three cases.

3.1. Data sources

Many of the cases selected for this study have data that vastly exceeds the quality and quantity of the standard data sets. Data collected during mesoscale meteorological field programs typically are comprised of both standard and experimental types. Often, both are collected at more frequent intervals and more locations than is typical during routine collection periods. These high spatial and temporal resolution data allowed an unprecedented examination of the small spatial variations and rapid temporal changes in the environment.

A second source of high quality data is available from the Mesoscale Analysis and Prediction System (MAPS; Benjamin et al. 1991, 1993)[2]. This analysis process incorporates surface reports, upper air soundings, profilers, and aircraft (ACARS) reports together with 3-hourly forecast cycles to produce 3-hourly analyses on a 60-km grid with data on isentropic surfaces at 4–8K

---

[2]Now available through the National Meteorological Center (NMC) as the Rapid Update Cycle (RUC).

intervals. Isentropic output is also interpolated to mandatory pressure levels; some smoothing is done during this step.

3.1.1. Surface data

The surface data typically includes the standard NWS surface aviation observation (SAO) data collected hourly and more frequently during periods of adverse or changing weather. During the PRE-STORM mesoscale meteorological field program, the SAO data were supplemented with the National Center for Atmospheric Research (NCAR) Portable Atmospheric Measurement systems (PAM II) that were designed to collect data every five minutes. The quality of the PAM II data was very good and was thoroughly examined and documented by Johnson and Toth (1986). Additional high resolution data were collected by the Stationary Atmospheric Measurement (SAM) systems operated by the National Severe Storms Laboratory (NSSL). These two sets of surface data were deployed to cover most of Oklahoma and Kansas with 50 km spacing. Both PAM and SAM sites recorded station pressure, temperature, dewpoint, wind speed and direction (including wind gusts) and precipitation. SAO data included all the above, plus cloud cover, present weather, and remarks.

3.1.2. Rawinsonde

To address the environmental conditions responsible for creating mesoscale regions of inertial instability (or weak stability), special high-density PRE-STORM and NWS soundings were examined. PRE-STORM soundings were taken every 3 h during IOPs, and occasionally as often as every 1.5 h. Locations of the sounding sites are shown in Fig. 5; station spacing averaged approximately 200 km. Data checks were performed on all soundings and included plotting thermodynamic diagrams and time-height cross-sections of potential temperature and winds, and the objective and subjective analyses of numerous parameters on constant pressure levels. With these analyses, bad data were detected and corrected, or deleted when not correctable.

The rawinsonde data were objectively analyzed using a modified Barnes analysis scheme (Koch et al. 1983; Barnes 1964). A two-stage objective analysis was executed to maximize the detail in the PRE-STORM network and to avoid boundary problems. This was done by first combining the PRE-STORM mesoscale rawinsonde data with the NWS synoptic-scale data. An objective analysis was done on the PRE-STORM analysis grid and the search radius in the Barnes scheme was set to a very large value so that boundary grid points could use data located far outside the domain of the grid. This resulted in a smooth analysis over the PRE-STORM gridded domain. The objective analysis was run a second time with a small search radius so that only the PRE-STORM data would be used in the analysis. This stage of the objective analysis used the previously objectively-analyzed grid as a first guess field. This two-step process allowed a maximization of detail both in the interior of the grid and along the boundaries.

3.1.3. Radar

Radar data were available from both the NWS WSR-57 sites and from four research Doppler radars. Examination of the mesoscale convection was accomplished by compositing digital reflectivity data from multiple radar sites. The composite radar data provided a large-scale overview of the mesoscale convection that could not be obtained from a single radar. NWS RADAP II (Greene et al. 1983) data were available from several NWS WSR57 radar sites within and adjacent to the PRE-STORM experimental network and consisted of digitized radar reflectivity from volume scans taken every 10–20 min. These digitized data have a spatial resolution of 2° azimuthally and 1.85 km (1.0 n mi) radially. Digitized radar data were also recorded by the NOAA/Hurricane Research Division (HRD) at the Wichita, Kansas, (ICT) radar site; these data had a resolution of 2° azimuthally and ~0.9 km (0.5 n mi) radially. The NWS operated another radar digitizer at Kansas City, Missouri, (MCI) with resolution similar to the HRD digitizer. The data from both digitizers had more quantization intervals and finer resolution than the RADAP II data.

The Doppler radars were sited so that there would be two pairs of dual-Doppler analysis, one in central Oklahoma and the other in south-central Kansas. The Oklahoma Doppler radar network consisted of the NSSL 10-cm radars located at Norman and Cimarron. NCAR operated two 5-cm radars located near Wichita, Kansas and Nickerson, Kansas. The radar pairs typically operated independently depending on the meteorological situation. Convective systems that passed through northern Oklahoma were within range of all four radars.

3.2. PRE-STORM cases

Following are three cases of MCSs that occurred in the presence of inertial instability during the PRE-STORM field program in 1985. Primary attention is given to the 12–13 May 1985 event because data collection started before the onset of convection and because the convection originated and matured within the confines of the mesonetwork. The remaining cases began data collection shortly after convection started; in some cases, the convection started outside the mesonetwork and moved into the network during its evolution into a mature system.

3.2.1. 12–13 May 1985

The mesoscale convective event that occurred on 12–13 May 1985 is one of only three during PRE-STORM in which upper-air soundings were released *before* the onset of convection, allowing an examination of the preconvective environment for conditions that were important to the subsequent development of the MCC. This MCC had its origins as a broken line of convective cells oriented NE–SW (Fig. 6a) along a quasi-stationary "secondary" dryline (Schaeffer 1986). Later, a mesoscale band of convection developed that was oriented NW–SE and moved to the northeast. During the transition from one orientation to the other (Fig. 6b–c), there were short, weak lines of convection having this northwest–southeast orientation superimposed on the original line of convection. The original NE–SW line of convection weakened while the NW–SE line continued to evolve and produce copious amounts of stratiform precipitation; stratiform precipitation was not an important feature of the original dry-line convection. The development of strong convection quickly followed by stratiform precipitation was similar to that described by McAnelly and Cotton (1992). The total rain volume[3] (Fig. 7) has an early peak associated with the original strong convection, followed by a short term reduction, then a long period of time in which the total rainfall increases owing to the significant

[3]The reduction in rain volume around 0400 UTC is a consequence of the MCC moving out of range of the radars. After 0500 UTC. the radar at Monett, Missouri (UMN), began to record data, resulting in the apparent sudden increase in volume.

contributions of the stratiform precipitation (Churchill and Houze 1984; Leary 1984; McAnelly and Cotton 1986; Rutledge et al. 1988; and Watson et al. 1988).

The duration of this MCC was the third longest of the season (of a total of 59 events), lasting over 21 hours. In terms of areal coverage, it was a small system and was ranked 51st for the season (Augustine and Howard 1988).

Figure 8 is a composite chart depicting conditions at 500 mb with surface fronts and pressure centers superimposed. The synoptic-scale trough over the west was moving eastward towards the plains. A surface front was oriented east–west near the Oklahoma-Kansas border and a dryline was in western Oklahoma; a secondary dryline was located in central Oklahoma (Fig. 9). Weak cyclonic vorticity was present to the southwest of the PRE-STORM network in response to the approaching short wave. Convection began during the afternoon in southwest Oklahoma and produced numerous severe thunderstorms; subsequent storms formed in central and northeast Oklahoma. These storms were not as severe and eventually evolved into the MCC. A mesoscale jet streak with winds in excess of 60 m s^{-1} was observed over PTT in west-central Kansas at 0000 UTC resulting in a region of strong anticyclonic shear. Figure 10 shows values of $\alpha = \eta / f$ on the 330 K isentrope; negative values indicate regions of inertial instability. The vertical depth of this unstable layer is shown in the vertical cross-section in Fig. 11. It should be clear from Figs. 10 and 11 that there is a large region, both horizontally and vertically, that is inertially unstable.

We now examine the symmetric instability for this event. In Fig. 12, we see that there is a deep layer that is symmetrically unstable (using the $S < 1$ criterion in (5)). It is not necessary to invoke moist parcel arguments to show that this environment is unstable to symmetric overturning—it is unstable to both moist and dry parcel motions. The horizontal scale and depth of this region are similar to that described by Emanuel (1983) and by Jascourt et al. (1988). The latter determined that upright convection exploited a pre-existing mesoscale instability that quickly led to highly organized bands of convection.

So far, we have examined fields at a specific time and level and discussed their implications on the subsequent evolution of the convective system. It is also useful to look at the temporal changes in these scaler and vector fields and determine how the changes are related to the instability.

By computing the difference in the winds between 0000 UTC and 0300 UTC, we can determine the local rate of change of the wind, $\delta\mathbf{V}/\delta t$. The vector change of the wind is plotted in Fig. 13a–b for two different levels. On the 308 K isentrope (ranging from approximately 825 mb in the south to 600 mb in the north), there is an increase in the southwesterly flow south and east of the convective system, and northerly flow north of the convective system. It is possible that the northerly current may be the return branch of the solenoidal circulation and this acceleration serves to increase the low-level convergence. At the upper level (330 K; approximately 300 to 230 mb), there are two distinct flow regimes present. Over Oklahoma the accelerations are generally upshear towards the west; over Kansas the accelerations are divergent and directed towards the northwest through the northeast. The winds over Oklahoma may represent a deceleration of the wind in the presence of convective "obstacles." The strength of the flow over Kansas, and the asymmetry and orientation of the winds suggest that a significant part of it is a result of accelerations through the region of the inertial instability. Inspection of animated satellite imagery clearly shows that portions of the spreading anvil moves across the mean flow; i.e., the anvil spreads to the north and northwest in a region where the large-scale flow is from the southwest at speeds of ~20–30 m s^{-1}.

To gain insight into where the air parcels are descending, we need to examine Fig. 14, which shows the change in height, temperature, dewpoint, and wind at Enid, Oklahoma (END). END is located on the southern edge of the region of symmetric instability and is where the NW–SE oriented convective bands developed. Above about 400 mb, the local rate of change of the wind is from the east-southeast, whereas below that level it is from the northeast. There is a positive height change that peaks at 200 mb; from 275–800 mb there is a negative height change. The geopotential height is computed from the virtual temperature and reflects the combined changes in the temperature and moisture. There is slight warming in a deep layer below the anvil level; the moisture shows a drying trend in the same layer. What is probably happening here is outflow from the strong, upright convection is being inertially accelerated to the north and northwest. If the solenoidal circulation exists, we would expect some of this air to be returned to lower levels along a slant trajectory. Parcels doing so would have a northerly component, much like the layer from 500 mb to near the surface. Additionally, these air parcels would undergo adiabatic warming and drying as they descended. The traces for temperature and moisture show that drying and warming occur in the layer from 300 to 800 mb. The combined effect is to lower the heights through a deep layer. These results offer evidence that a solenoidal circulation has developed north of the convection and in the region of symmetric instability.

Another way to view this type of instability is with cross sections of M, θ_e, and relative humidity. Regions where the slope of the M surfaces are less than the slope of the θ_e surfaces, and the relative humidity (RH) exceeds ~80%, are susceptible to CSI (Emanuel 1979, 1983). Figure 15 is a cross section from the northwest to the southeast and cuts through the PRE-STORM network. The region of RH > 80% is shaded; M surfaces are thin lines; θ_e lines are heavier. The PRE-STORM network is located in the center third of the plot. This region is characterized by rapid vertical changes in θ_e , signifying convective instability, but does not indicate that symmetric instability is present. Note, however, that this analysis is from the NWS rawinsonde network and cannot resolve the small-scale features that we are interested in diagnosing. (As a side note, the region of RH > 80% in the leftmost third is located near the eastern boundary of the Rocky Mountains and strongly suggests that CSI may be present. At this time, a storm system was producing bands of rain and snow along the Front Range.) Figure 16 is similar to Fig. 15, except it is a cross section through the PRE-STORM network and uses the high resolution data. Here we can see that CSI criteria may be satisfied at upper levels where the momentum surfaces are quasi-horizontal, but only if the relative humidity increases such that it exceeds ~80%. This is not difficult given that saturated material from the convective updrafts will satisfy this condition.[4]

It should be noted that these diagnoses required data of a resolution and quality not normally available for forecasting or real-time observations. The best that can be done at this time is the use of the Wind Profiler Demonstration Network (WPDN) and the use of these data in the MAPS and RUC mesoscale models. We shall examine other cases using these data later.

Finally, we examine some basic quasi-geostrophic analyses as part of our effort to diagnose the cause of the evolution of the convection into a

---

[4]It is not clear that an analysis of momentum surfaces and CSI is appropriate because of the requirement of symmetry along the normal component of the cross section. In regions of strong curvature, this requirement is not satisfied. On the other hand, cross sections of inertial stability do not suffer from this restriction and may be better suited (cf. Figs. 11 and 12) to this type of analysis.

mesoscale system. In Fig. 17 the diagnosed vertical structure of the divergence of the Q-vector (Hoskins et al. 1978; Hoskins and Pedder 1980; Barnes 1985), given as

$$\mathbf{Q} = \left[\frac{\partial \mathbf{V}_g}{\partial x} \cdot \nabla\left(\frac{\partial \Phi}{\partial p}\right), \frac{\partial \mathbf{V}_g}{\partial y} \cdot \nabla\left(\frac{\partial \Phi}{\partial p}\right) \right] \tag{6}$$

is shown. The cross section is the same as used in the earlier diagnosis of momentum surfaces, except that it extends farther to the northwest. The shaded areas correspond to areas with convergence and represent regions of upward forcing. The PRE-STORM network is located about 1/4 of the way from the right hand edge and is favored by strong upward forcing. It can be argued that the ensuing convection and upscale growth into an MCS is related entirely to quasi-geostrophic adjustments and not to inertial instability. However, if this was true, then the convection that developed farther south, but still in the region of upward forcing, should have also been favored to grow upscale. In fact, satellite imagery (not shown) indicates that it dissipated shortly after sunset while the convection in the PRE-STORM network continued to grow. Although the ageostrophic circulations required for quasi-geostrophy likely played a significant role in preparing the environment for convection by thermodynamically destabilizing the atmosphere, it is suggested that it was the presence of the inertial instability that allowed one region of convection to grow upscale into a mesoscale system while others dissipated.

3.2.2. 6–7 May 1985

One of the better examples of a convective system that developed into a mesoscale occlusion (i.e., occluded mesoscale fronts and outflow boundaries; Blanchard 1990) was observed on this date in the PRE-STORM network. Because of the focus on this MCS (Brandes 1990; Fortune et al. 1992), a second MCS that occurred to the east at about the same time has been overlooked. This MCS is more difficult to analyze than the previous case because convection was already underway before supplemental rawinsonde data collection began. Despite the late start, the convection was still weak and covered only a limited region, and the soundings do not appear to be convectively contaminated. There is a strong signal in the vorticity field much like the previous case; the strength of the instability as well as its location suggest that it probably was a precursor to the convection and not a consequence of it.

Figure 18 is a composite chart depicting the 500-mb height field, surface fronts, and pressure centers at 0000 UTC on 7 May 1985. A large ridge was located over the northern Rockies; farther south the ridge was flatter and zonal flow prevailed over the PRE-STORM region. A surface front extended from the eastern Great Lakes region southwestward and bisected the PRE-STORM mesonetwork. A weak surface low was located in the Great Basin; a stronger low was located in the eastern Great Lakes region. A surface high dominated the Midwest and was advecting cooler and drier air into the northern half of the mesonetwork. A dryline was oriented north-south and was located in the western portion of the Texas panhandle and west Texas. Satellite imagery (Fig. 19) at 0630 UTC shows the two convective systems. The MCS of interest here is located in southeastern Kansas. The upper level cloud shield from this system and the larger system to the west have merged, but a distinct break can be seen between the two areas of colder cloud tops.

A vertical cross section of quasi-geostrophic forcing is shown in Figure 20; divergence of Q-vectors is depicted with areas of upward forcing shaded. The convection in Kansas is located near and to the right of the midpoint of the cross section. The strongest forcing is located to the northwest (left edge). There is weak upward forcing over a very large region, while a shallow region of downward forcing is located near the surface and may be associated with the cool air on the north side of the front. The upward forcing provides a favorable environment for destabilizing the environment and supporting convection. Warm, moist air is moving northward and ascending along the isentropes as they lift up and over the frontal boundary, providing the forcing for convective initiation. The sounding from IAB (Fig. 21) clearly shows the low-level frontal inversion and the warm, moist air riding on top of the cooler air.

During the 6 h period from 0000 to 0600 UTC, convection was occurring in two separate locations. To the west, near the Texas panhandle, severe thunderstorms had been occurring for a few hours, but had shown little movement or organization. Farther east, along the Oklahoma-Kansas border, weaker convection was forming near and to the north of a quasi-stationary warm front. It is in this location that the upper-tropospheric mesoscale instability was located. The convection in the west eventually organized and accelerated eastward.

Figures 22a–b show the inertial stability on the 330 K isentrope at 0000 and 0600 UTC, respectively, on 7 May 1985; there was little change in location or strength of the instability during this period. A north-south vertical cross section bisecting the region of inertial instability is shown in Fig. 23. The vertical and horizontal extent of the instability is similar to that of the previous case.

There is one difference between this event and the previous one. In this case, the convection formed within and to the northwest of the region of inertial instability. In the previous case, the convection was initially located to the south and moved into the southern end of the region of instability resulting in an enhancement of outflow to the left (north) of the shear vector. In the present case, the location of the instability produced an enhancement of outflow directed along and to the right (south) of the shear vector.

The convection located in southeastern Kansas is shown in Figs. 24a–b. The two radar images indicate that there was little motion associated with this convective system, while the second system located in the west was progressively moving eastward.

As before, it is instructive to examine the 3-h changes in temperature, moisture, and winds at individual sounding sites. Figure 25 shows the changes in the local environment at Chanute, Kansas (CNU) from 0300 to 0600 UTC. CNU is located to the southeast of most of the convection. In the upper troposphere, the wind change, $\delta\mathbf{V}/\delta t$, is directed from the north, across the mean flow. Below about 300 mb, the local wind changes are from the southeast. Recall that the inertial instability is located to the east and southeast of the convection. Any accelerations associated with the upper-tropospheric instability should be directed towards the southeast, and any return circulations should be from that direction. The wind change vectors show that this is what is happening. The soundings at Ft. Riley, Kansas (FRI), unfortunately, terminate at a fairly low level and do not permit a complete look at the local changes. Nonetheless, the changes below 500 mb from 0300 to 0600 UTC (Fig. 26) show an increase in the winds from the northwest. This is the response that would be expected to occur in the presence of slant downdrafts.

Wichita, Kansas (IAB) is also located in the region of inertial instability, but it is also located upstream of the convection. The signal here is less clear, but there appears to be flow directed primarily upshear in the layer from 700 to 300 mb, and downshear below that level (Fig. 27). It is difficult to say whether this is a response to the presence of the inertial instability, or just a normal response to blocking flow aloft and increased inflow at lower levels.

3.2.3. 16–17 June 1985

The convection on the evening of 16–17 June 1985 is noteworthy because it was the largest MCC during the PRE-STORM field program and was also the largest system for the entire year (Augustine and Howard 1988). A series of short waves were embedded in a northwesterly flow (Fig. 28); a short-wave ridge was located over the PRE-STORM network. A strong surface low was located in south-central Canada and a front extended south and southwest to the southwest portion of Nebraska; from there it continued west into northern Utah. A wind shift boundary extended from southeastern Nebraska across central Kansas into the Oklahoma panhandle. Temperatures on both sides of the wind shift were similar, but dewpoints were notably lower behind the line. These boundaries served as the focus for convective initiation. A Pacific anticyclone was pushing eastward behind the front and was located just to the north of the PRE-STORM network. A second strong high pressure center was located over the Atlantic Ocean and was responsible for a moist, southerly flow over the southern part of the mesonetwork.

The large-scale environment favored convection moving from the northwest toward the southeast during the evening. Most of the convection did move in this direction; the exceptions were the small cluster of thunderstorms that veered to a more easterly direction early in the evening and grew upscale into the MCC. It is not clear if the presence of the inertial instability played a role in the directional change of the convection. It is possible that the environment was more favorable for the development of convection is this region and there was a tendency for the new cells to develop eastward into the region of inertial instability.

Verlinde and Cotton (1990) have investigated this MCC using dual-Doppler radar data and found the presence of a highly transient mesovortex having ~50-km horizontal dimension. They hypothesized that the development of the vortex couplet was a consequence of convective updrafts lifting strong southerly momentum associated with the low level jet to middle levels. Horizontal shear between the elevated low-level momentum and the ambient momentum assisted in the development of a dynamic pressure field favorable for the spinup of the circulations. They also noted that there were asymmetries between the cyclonic and anticyclonic vortices (i.e., the anticyclonic vortex was smaller and had less vertical extent). Although not mentioned in their discussion, it is plausible that the anticyclonic vortex was weaker because the lifting of high momentum air from lower levels resulted in smaller horizontal shear on the anticyclonic side than the cyclonic side because of the preexisting horizontal shear associated with the inertial instability. Stated differently, if the inertial instability had not been present, there would have been a more homogeneous wind field aloft and the vorticity pairs would have been more symmetric than what was actually observed.[5]

---

[5]On the other hand, recent modeling work (Skamarock et al. 1994) suggests that when vortex pairs are generated in mesoscale systems that the anticyclonic member will be weaker

Figure 29 shows the inertial stability parameter on the 326 K isentropic surface at 0600 UTC. As with the previous case, data collection started after the initial convection was underway making it difficult to determine precisely what the preconvective environment looked like. As before, the strength and location of the instability strongly suggests that it played a role in the upscale growth of the mesoscale convection. Note, also, that the convection for this event did not occur in the region of maximum instability (located in southeast Kansas), but just to its north in a region of weak stability.

The local changes in wind, temperature, and moisture are shown in Fig. 30 for Ft. Riley, Kansas (FRI). Because one of the two soundings was truncated, the differences are also truncated. We see the same type of signatures that have appeared in the other cases. For example, the winds in the middle troposphere exhibit an acceleration from the southwest. This is directed almost normal to the large-scale flow at this level and represents the cross-stream acceleration associated with inertial instability. At lower levels, the changes are directed from the northeast. Accompanying these vector changes, we note that there is moistening in the 500–600 mb layer, and drying below. The temperature changes indicate cooling in the layer that is moistening, and warming in the layer that is drying. This information suggests that there is a cross flow acceleration taking place in the middle troposphere with moistening and cooling occurring as convectively saturated air is accelerated away from the main convection; simultaneously, there is warming and drying concentrated in the layer with the increased northeast flow associated with the solenoidal return flow.

---

because it is opposite to the planetary vorticity. On the short time scales in the present case, planetary vorticity may play only a minor role.

The mesoscale convective complex moved to the southeast and east and out of range of the PRE-STORM data collection during its mature and decaying stage; little additional information is available on this convective system using the PRE-STORM data.

3.3. MAPS cases

To increase the number of cases exhibiting either weak inertial stability or inertial instability, a number of convective events that occurred during the warm season of 1992 were collected. The analysis of these events was accomplished with model data from MAPS, the Mesoscale Analysis and Prediction System (Benjamin et al. 1991, 1993), developed by the NOAA/Forecast System Laboratory. MAPS is a model used primarily for short-term forecasts (0–6 h) on small spatial scales. MAPS uses a hybrid isentropic vertical coordinate system that is ideal for the analysis required in this study. Horizontal resolution for the domain is 60 km. MAPS takes advantage of all available data types, including other model data, rawinsondes, surface data, wind profiler data, and aviation data from commercial airlines (ACARS). Consequently, MAPS is often able to analyze features that are too small in scale to be handled properly by other models. It is for these reasons that data from MAPS analyses (not forecasts) were used to investigate features associated with mesoscale convective systems occurring in regions of weak inertial stability.

3.3.1. 13–14 May 1992

The mesoscale convective events that occurred during the night of 13–14 May are especially interesting because two large mesoscale convective systems formed during the evening hours: one developed along the

Nebraska–Kansas border; the other formed in central Texas. Both systems occurred in regions of weak inertial instability. The northern system was one of the largest mesoscale convective complexes during 1992. Figure 31 is an infrared satellite image at 0000 UTC 14 May 1992. The southern system in Texas is weakening at this time and covers only a small fraction of the area covered during its largest size, approximately 3 hours earlier. The northern system is just beginning to take on mesoscale characteristics. The original convection consisted of individual thunderstorms in an arc from the South Dakota/Nebraska border south and southwest to the Kansas/Colorado border. Figure 32 is a composite chart showing 500 mb height contours and the location of surface fronts, highs and lows. A flattened high pressure ridge is present over much of the south-central plains and a broad flat trough covers the northern plains, resulting in an enhanced geopotential gradient over the central plains region. Low-latitude troughs are present over both the west and east coasts and a weak closed low is located in northern Mexico. A cold front from the northeast to the west separates the cooler air associated with the broad trough from the hotter, moister air to the south. The surface front was backed up against the eastern slope of the Rocky Mountains and was quasi-stationary. The surface high pressure was over the Great Lakes and was producing a southeasterly return flow over the western plains and was responsible for advecting low-level moisture back into the region.

The MAPS model was run every 3 h and data from the 1800 and 2100 UTC runs on 13 May 1992 and the 0000, 0300, and 0600 UTC runs on 14 May 1992 were saved for this case. The analysis at 0000 UTC is revealing. The inertial stability parameter, $\alpha = \eta / f$, shows a region of weak inertial instability over Nebraska and extending both to the southwest and east (Fig. 33).[6]

A crosssection of the MAPS analysis grid provides further insight into the environment. The cross section was taken from Bismark, North Dakota (BIS) to Stephenville, Texas (SEP). Along this cross section, (Fig. 34), the initial convection occurred in the shaded region. This region is dominated by weak inertial stability aloft and bounded on the south by a region of high inertial stability. Figure 35 is a crosssection of M and θ_e. There is a shallow pool of high θ_e air near the surface on the southern (right) portion of the cross section. This represents the low level source of moist air that fueled the mesoscale convective system during both the generation and mature phase. Above this moist pool is a dry region. The vertical gradient of θ_e provides a necessary condition for conditional instability of saturated parcels, i.e.,

$$\frac{\partial \theta_e}{\partial z} = \begin{cases} < 0 & \text{conditionally unstable} \\ = 0 & \text{saturated neutral} \\ > 0 & \text{absolutely stable} \end{cases}, \tag{7}$$

thus convection is favored in this region if sufficient low-level forcing is present to initiate it. Poleward of this region, the vertical gradient of θ_e changes so that the environment is convectively stable through a great depth. Figure 35 also shows a vertical cross section of pseudo momentum, given by

$$M = fx + v_g \tag{8}$$

---

[6]Another region of inertial instability was located along the Texas/Oklahoma border and was also associated with long-lived convection. Inspection of the data suggests that this region of instability may be the result of the earlier convection over Texas.

where M is momentum, f is the Coriolis force, x is the displacement from an (arbitrary) origin, and v_g is the component of the geostrophic wind normal to the crosssection. Typically, the intersection of M and θ_e lines occurs with quasi-horizontal θ_e surfaces and quasi-vertical M surfaces. Under certain conditions, the slopes can rearrange so that M is more horizontal and θ_e more vertical. It is under these conditions that CSI occurs. Parcels of air may glide up or down the momentum surfaces and eventually become convectively unstable, leading to upright convection in some cases. In this situation, upright convection is already present and the function of the slant trajectory along the solenoid is to return air parcels to lower levels.

3.3.2. 7–8 July 1992

During the afternoon of 7 July 1992, a few small thunderstorms began to develop in northwestern Kansas and southwestern Nebraska. Satellite imagery (Fig. 36a) shows the storms developing just to the south of a streak of clouds oriented southwest–northeast that are associated with a strong jet streak. The MCS continued to grow with time and reached its maximum size at 0600 UTC (Fig. 36b). The mesoscale system moved very little during this time, although individual thunderstorm cells undoubtedly moved to the east. During the time that the MCS existed, it remained very close to the banded clouds that marked the jet streak and a potential region of inertial instability.

A composite chart depicting the 500-mb heights and surface fronts and pressure centers is shown in Fig. 37. A large anticyclone is centered over the southern states and a ridge extends northward over the upper midwest, although the amplitude is slight. The height field shows a tightening of the gradient in this general region, suggesting a possibility of strong winds. At the surface, a front is located in northern Georgia, extending to the northwest into Iowa, thence back to the southwest into Colorado and the Great Basin. The 850-mb data (not shown) shows strong low-level winds impinging on the front near the thunderstorms. The presence of a low-level jet (LLJ) is well documented by many, including Maddox (1983), Cotton et al. (1989), and Augustine and Caracena (1994), as an important ingredient for the development of long-lived mesoscale convective systems. At 300 mb (Fig. 38), the winds at North Platte, Nebraska (LBF) and Omaha, Nebraska (3NO) are greater than 25 m s^{-1}, while the winds just to the south at Dodge City, Kansas (DDC) and Topeka (TOP), Kansas are considerably weaker. This strong north–south gradient, coupled with the anticyclonic curvature of the wind field, suggests the presence of inertial instabilities. If we turn our attention to Fig. 39, we see the inertial stability parameter on the 342 K isentropic surface. At this level, there is a sharp gradient with relatively large values of inertial stability through the northern states and in the southeast. The interior section shows a tendency towards a proliferation of local maxima and minima, but the basic pattern is one with weak stability present in the midsections of the region and local minima near the MCS. This is a clear case of a mesoscale convective system developing upscale in a region with weak inertial stability.

Figure 40 is a cross section of the inertial stability parameter from north-central South Dakota to south-central Kansas. There is a weakness in the stability in the upper center of the figure, corresponding to the region where the MCS developed. As with most of the other cases, there is a strong gradient of stability in the vertical, with large values of inertial stability (corresponding to strong cyclonic vorticity) in the lowest layers, and weak stability (corresponding to anticyclonic vorticity) in the upper regions. This pattern occurs often enough that it may be considered representative of this class of mesoscale systems.

3.4. Augustine composites

Recently, Augustine (personal communication) has composited rawinsonde data from many MCSs during the period 1990–1993. His composite technique is similar to that used by Maddox (1983), Cotton et al. (1989), and Augustine and Caracena (1994). MCS cases were divided into "large", "small", and "non-developing" events. Large MCSs were those that qualified as MCCs (Maddox 1980) or those that attained at least 100,000 km^2 at maximum areal extent (defined by the cloud-top area ≤ –52°C). Small MCSs were defined as those that did not satisfy large MCS or MCC criteria but were large enough at maximum areal extent to be considered multicell thunderstorm complexes. The non-developing class comprised the remainder of the cases where convection did not grow upscale to meet the small or large classification. This procedure is the same as that employed in Augustine and Caracena (1994). After compositing the rawinsonde data, the results were analyzed using the analytic approximation technique of Caracena (1987), where scaler fields are represented by weighted sums of all observations (i.e., no radius of influence is applied). The analytic weighting function also allows derivatives to be defined as weighted sums, and thus, errors associated with finite differencing are avoided.

At 200 mb, Augustine's composites show that there is a strong north-south gradient in the wind speed, similar to that shown by Maddox (1983) and Cotton et al. (1989). Because of the Caracena (1987) analysis scheme, however, the strength of the gradient is preserved better than is typical in other analysis schemes. Augustine computed the ratio of absolute vorticity to the Coriolis parameter, i.e., $(\zeta + f)/f$ and obtained values as small as 0.7 for "large" MCSs (Figs. 41). Although this is quite large (and stable) compared to the values we have seen here, it must be remembered that Augustine's results are for composites of many (38) events, and the results presented here are for individual cases. In that light, his results are very revealing about the nature of the upper-level flow associated with the vast majority of MCSs and MCCs. Although the composite results do not reveal inertial instability, they do show that there is a broad region of weak inertial stability associated with the pre-convective genesis region of both MCSs and MCCs. The compositing technique assures that there is little or no convection occurring that would contaminate the data with a convective signature. Thus, his results confirm the early results of both Maddox (1983) and Cotton et al. (1989) that identified a weak jet stream located poleward of the genesis region, and clearly show that the genesis region is located in an environment of weak inertial stability.

3.5. Discussion of case studies

We have seen that MCCs and MCSs often form in environments that exhibit weak inertial [in]stability owing to the presence of anticyclonic shear in the presence of a jet streak or anticyclonic curvature in strongly curved flow. Examination of these events using standard NWS rawinsonde data often fails to reveal the presence of these dynamic mesoscale features. Use of special rawinsonde data from field experiments or from 4-D data assimilation models (4DDA) such as MAPS are more successful in revealing the structure of these instabilities. The availability of rawinsonde data at frequent intervals (e.g., 1.5–3 h) allows for detailed examination of the short-term local changes in temperature, moisture, and winds. The results of these analyses indicate that the solenoidal circulations associated with the presence of convective-symmetric instability can be readily detected.

To examine the processes that are responsible for the solenoidal circulations and the enhancement that the circulations have on the developing convection, numerical simulations were performed using a nonhydrostatic mesoscale model. The results of the modeling study are discussed in the next chapter.

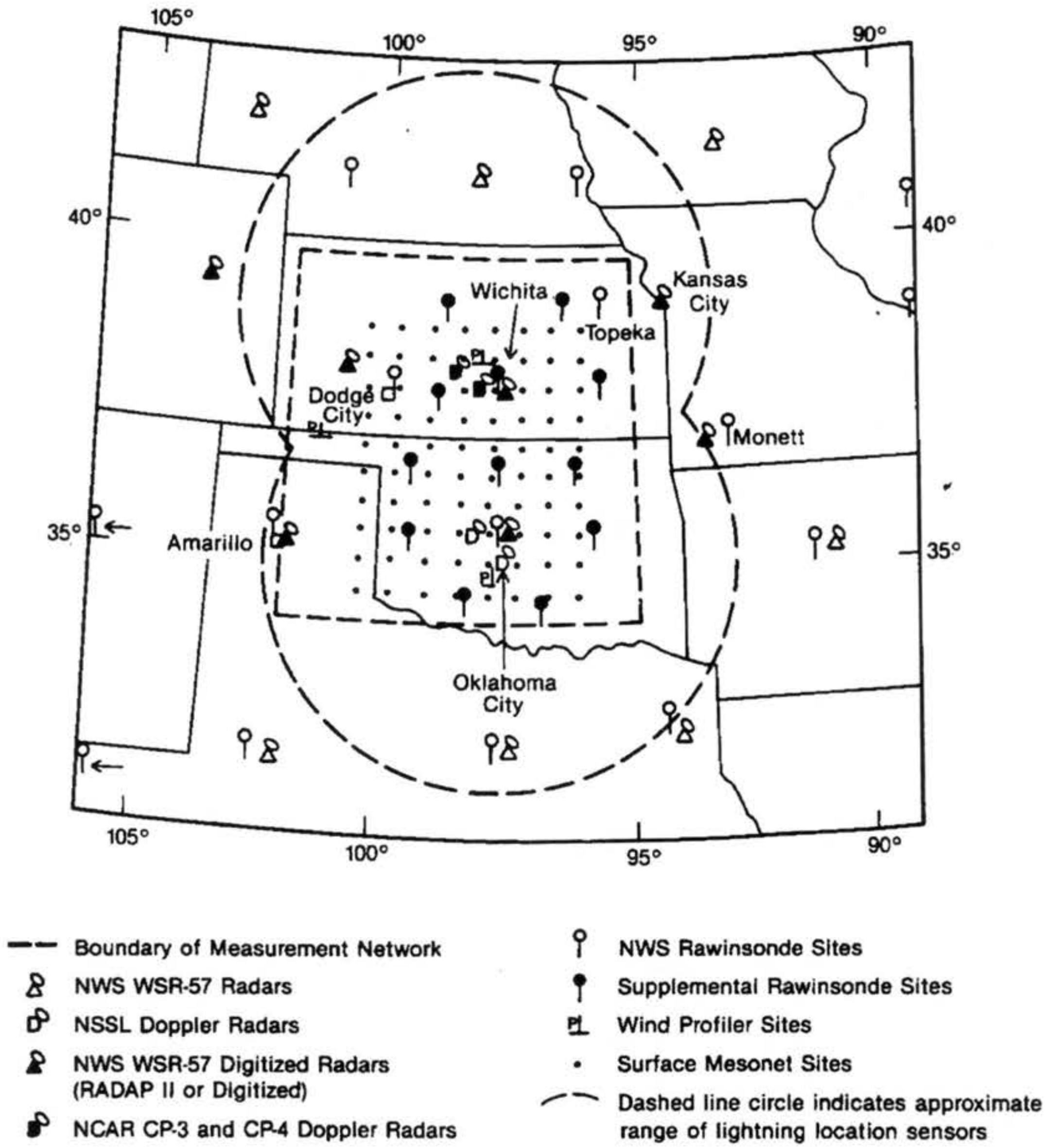

Figure 5. Location of the PRE-STORM field program and placement of the observational network.

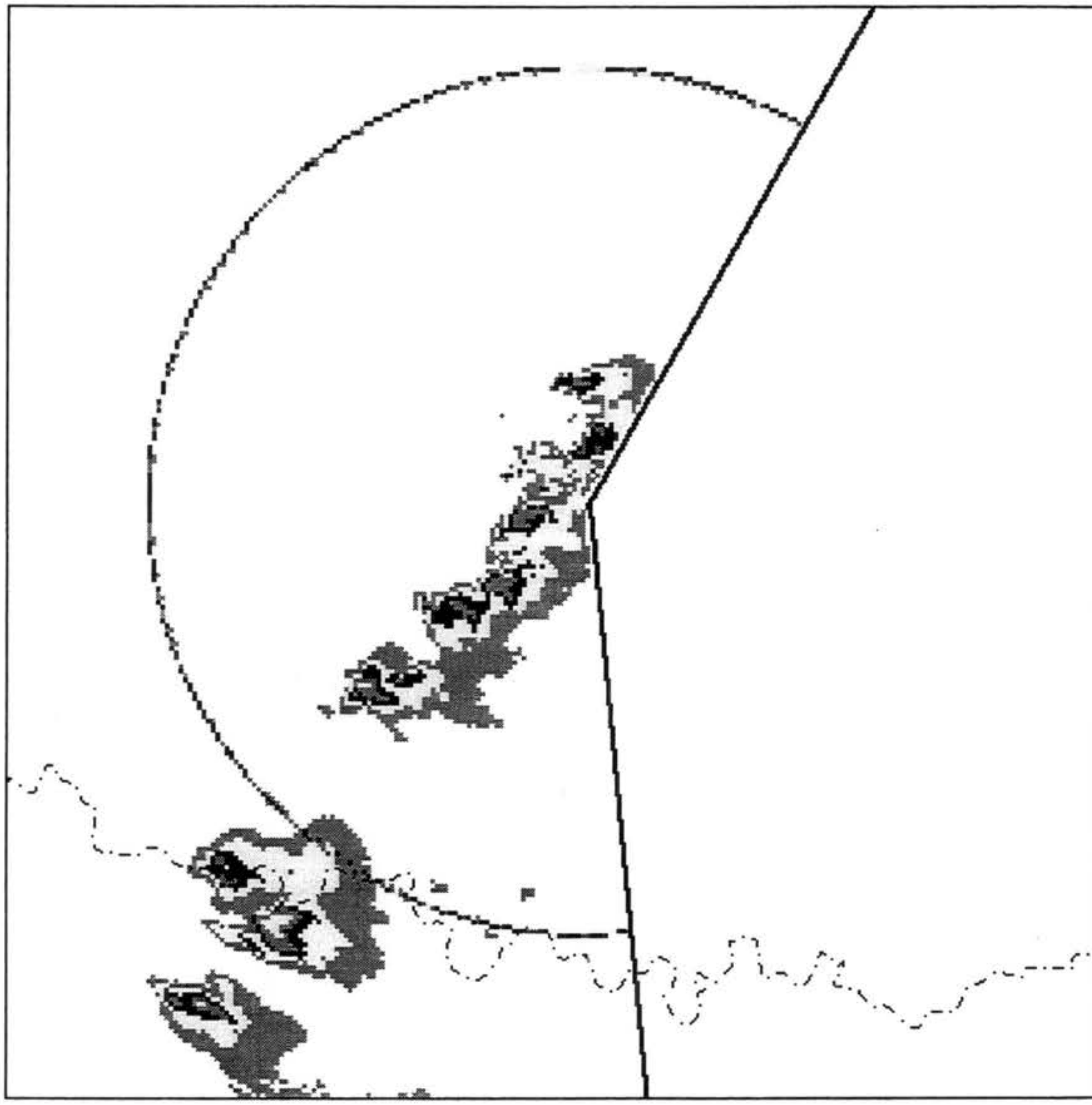

(a)

Figure 6. Base scan image from the Norman, Oklahoma, Doppler radar at a) 0015, b) 0138, and c) 0258 UTC on 13 May 1985. Reflectivities are depicted by repeating medium gray, light gray, and black shading, representing intensities of 15, 31, 40, 46, 53, and 59 dBz.

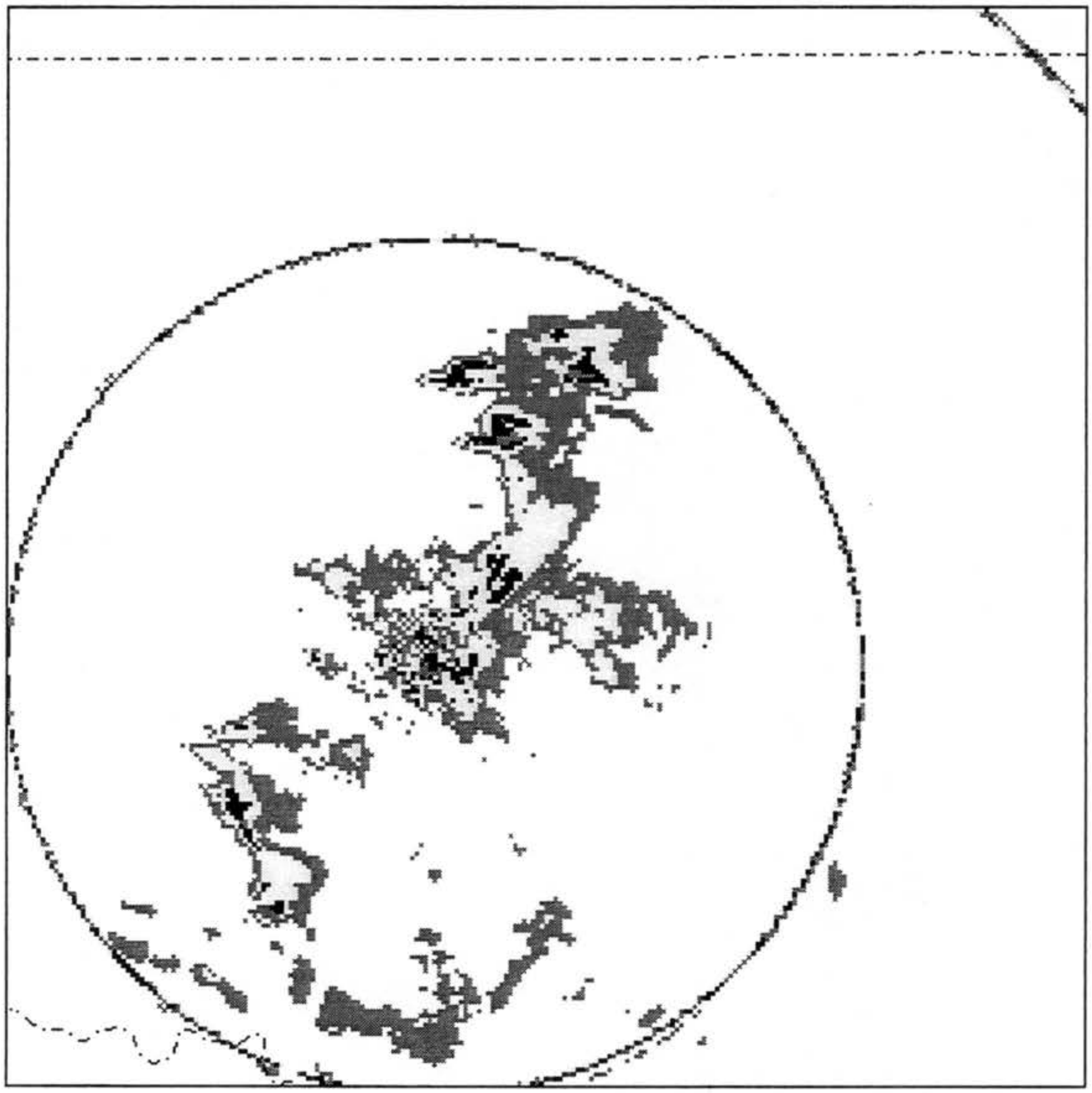

(b)

Figure 6. (Continued)

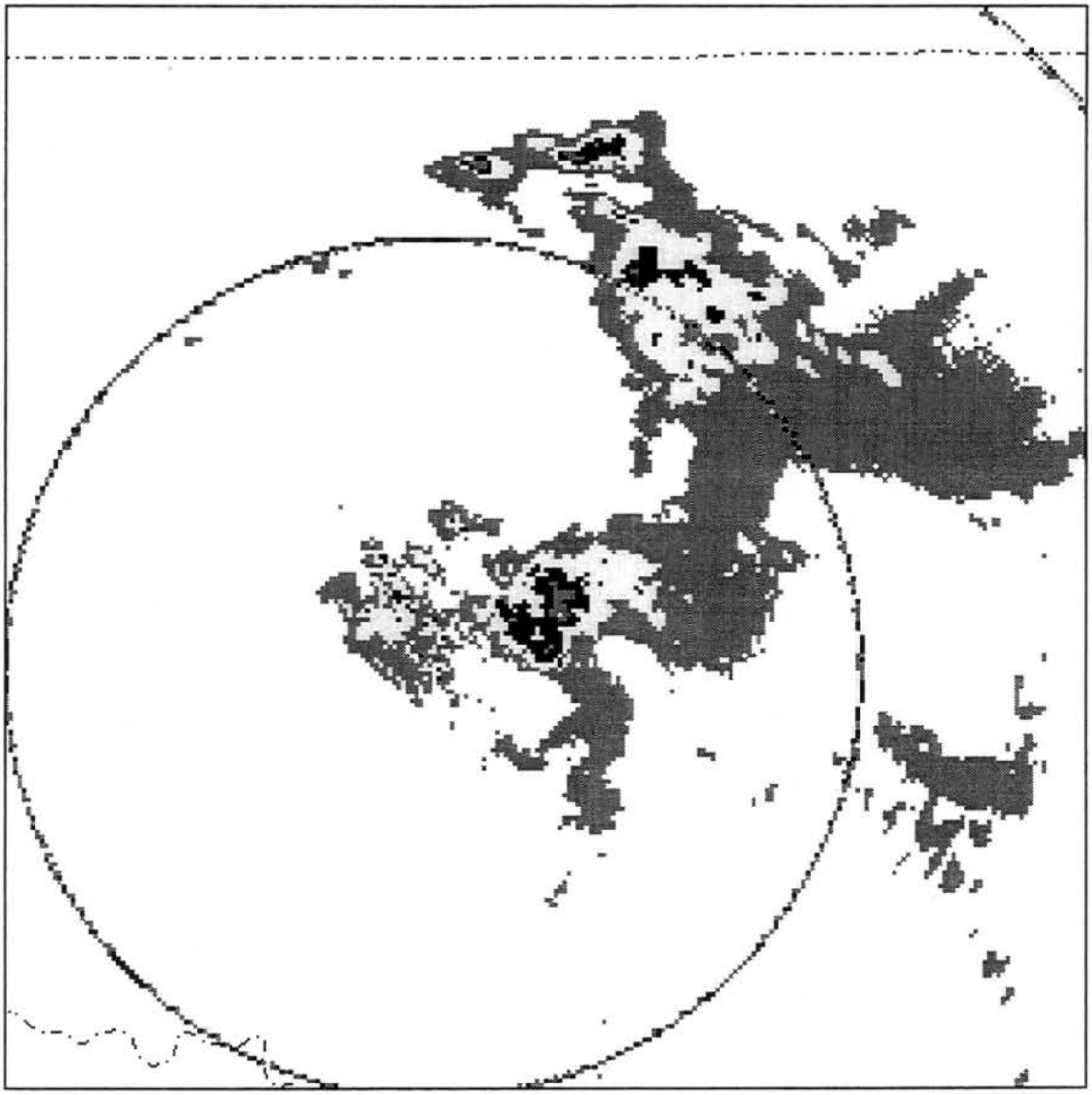

(c)

Figure 6. (Continued)

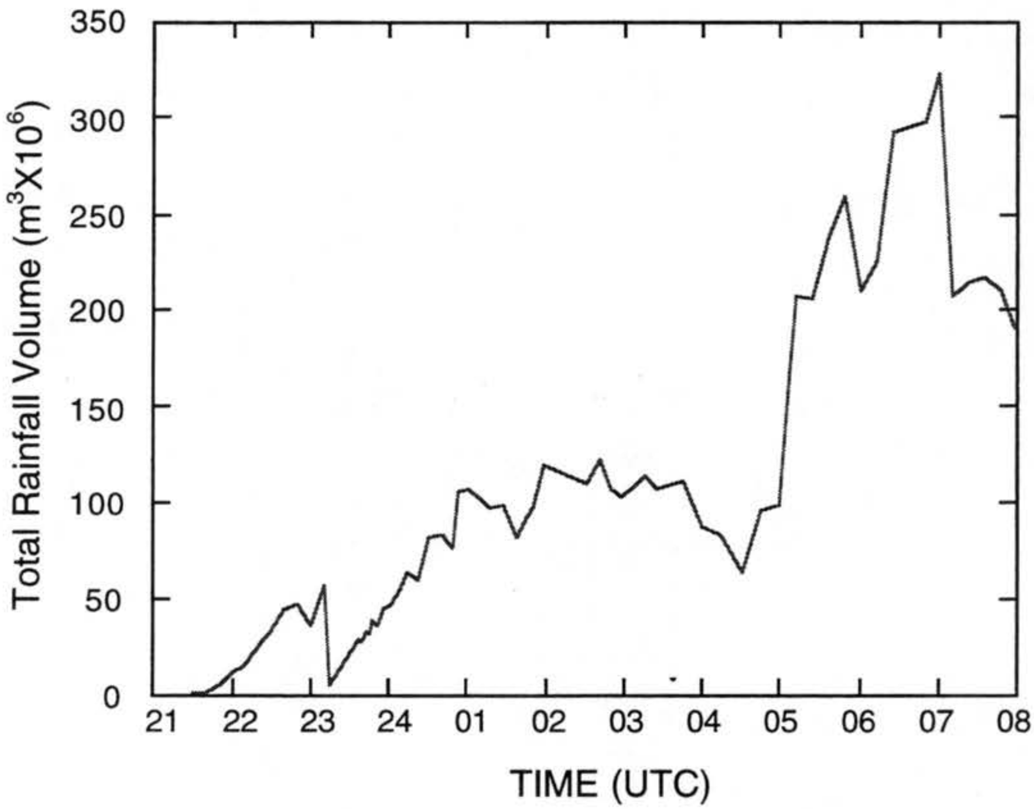

Figure 7. Evolution of precipitation and rain volume. Time is along the x-axis starting at 2100 UTC on 12 May 1985 and ending at 0800 UTC on 13 May 1985.

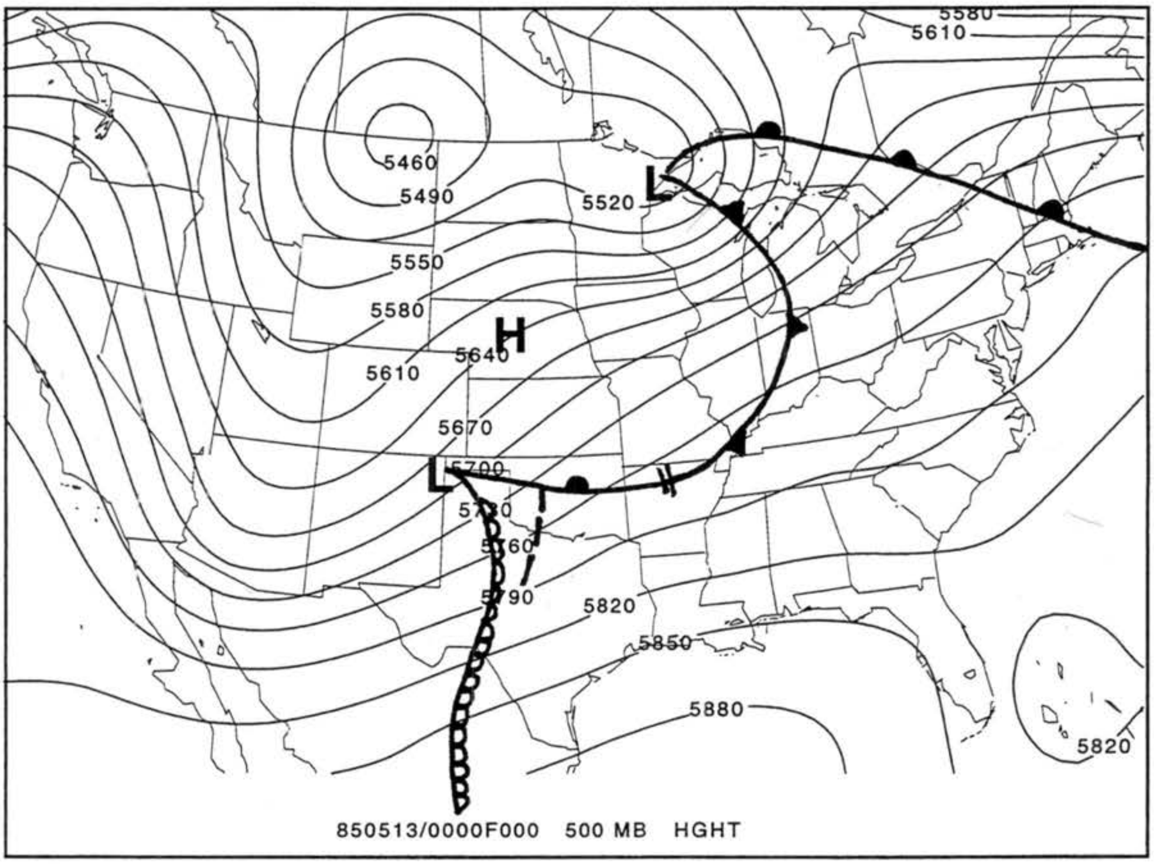

Figure 8. Composite chart at 0000 UTC on 13 May 1985 depicting conditions at 500 mb with surface fronts and pressure centers superimposed. 500-mb height contours every 30 m. High and low pressure centers marked with "H" and "L," respectively. Surface boundaries use standard convention for cold, warm and occluded fronts, and the dry line.

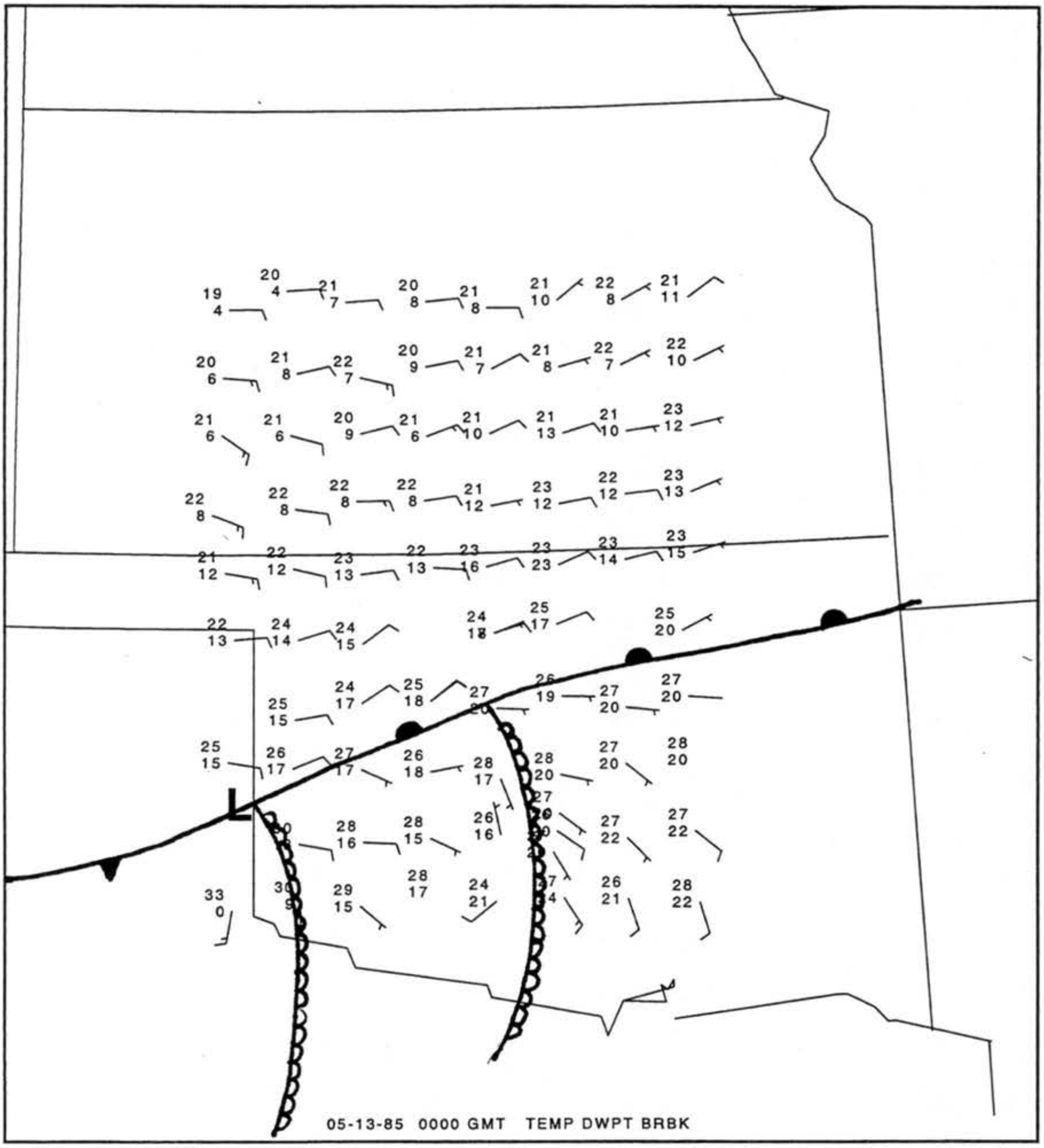

Figure 9. PAM and SAM mesonet data and surface boundaries at 0000 UTC on 13 May 1985. Station plot is shown with temperature and dewpoint (°C) on the upper and lower left. Wind barbs are shown with half barb equal to 2.5 m s^{-1} and full barb 5.0 m s^{-1}. Surface frontal boundaries and dry lines are shown as solid lines.

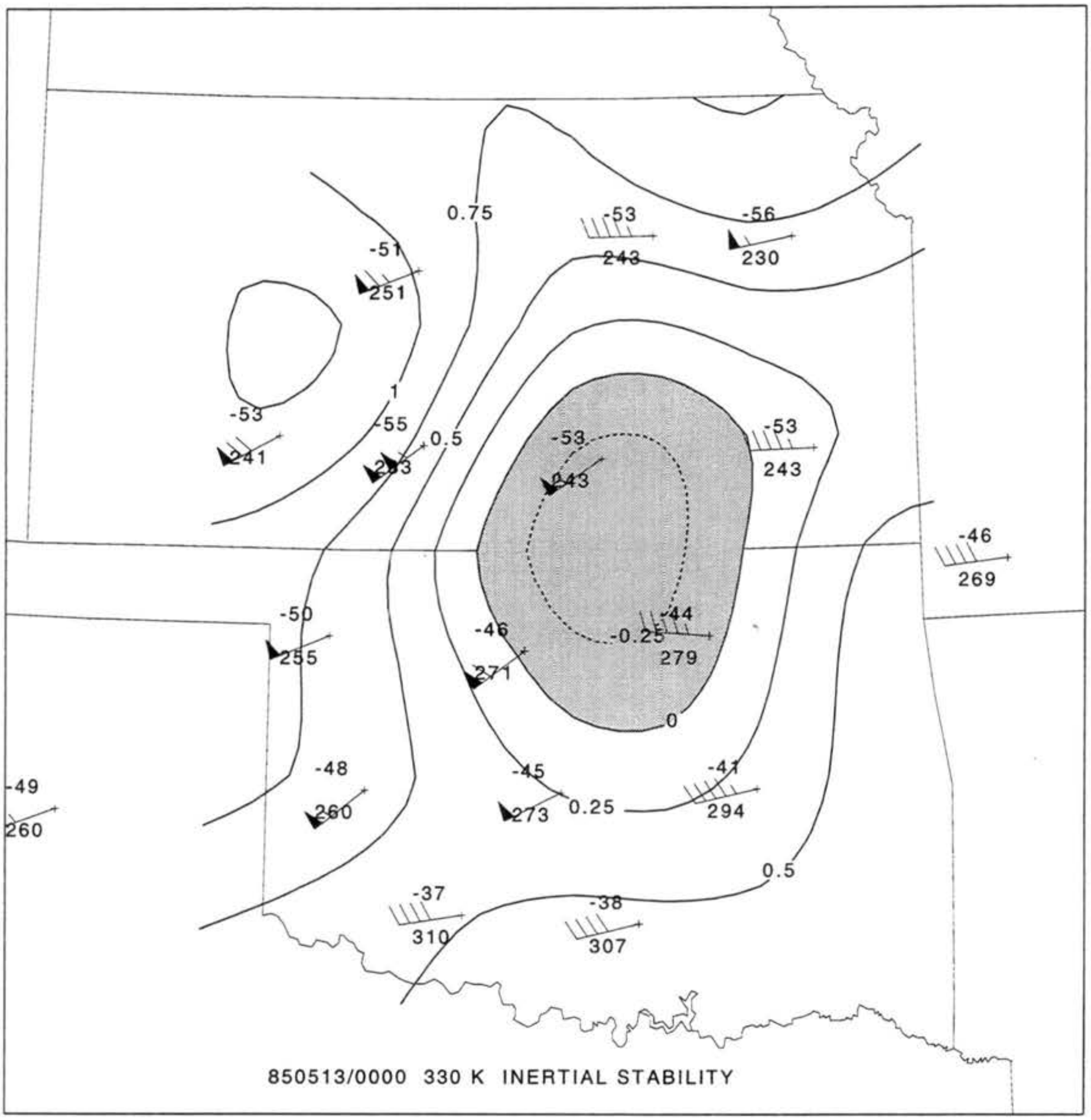

Figure 10. Plan view (x–y plane) of the inertial stability parameter, defined as $\alpha = (\zeta_\theta + f)/f$, over the PRE-STORM network on the 330 K isentrope at 0000 UTC on 13 May 1985. Contour interval every 0.25. Positive values shown with solid lines; negative values are dashed and shaded. Station plot shows temperature and pressure in the upper and lower left corners, respectively. Wind barbs are shown with half barb equal to 2.5 m s^{-1}, full barb is 5.0 m s^{-1}, and pennant is 25 m s^{-1}.

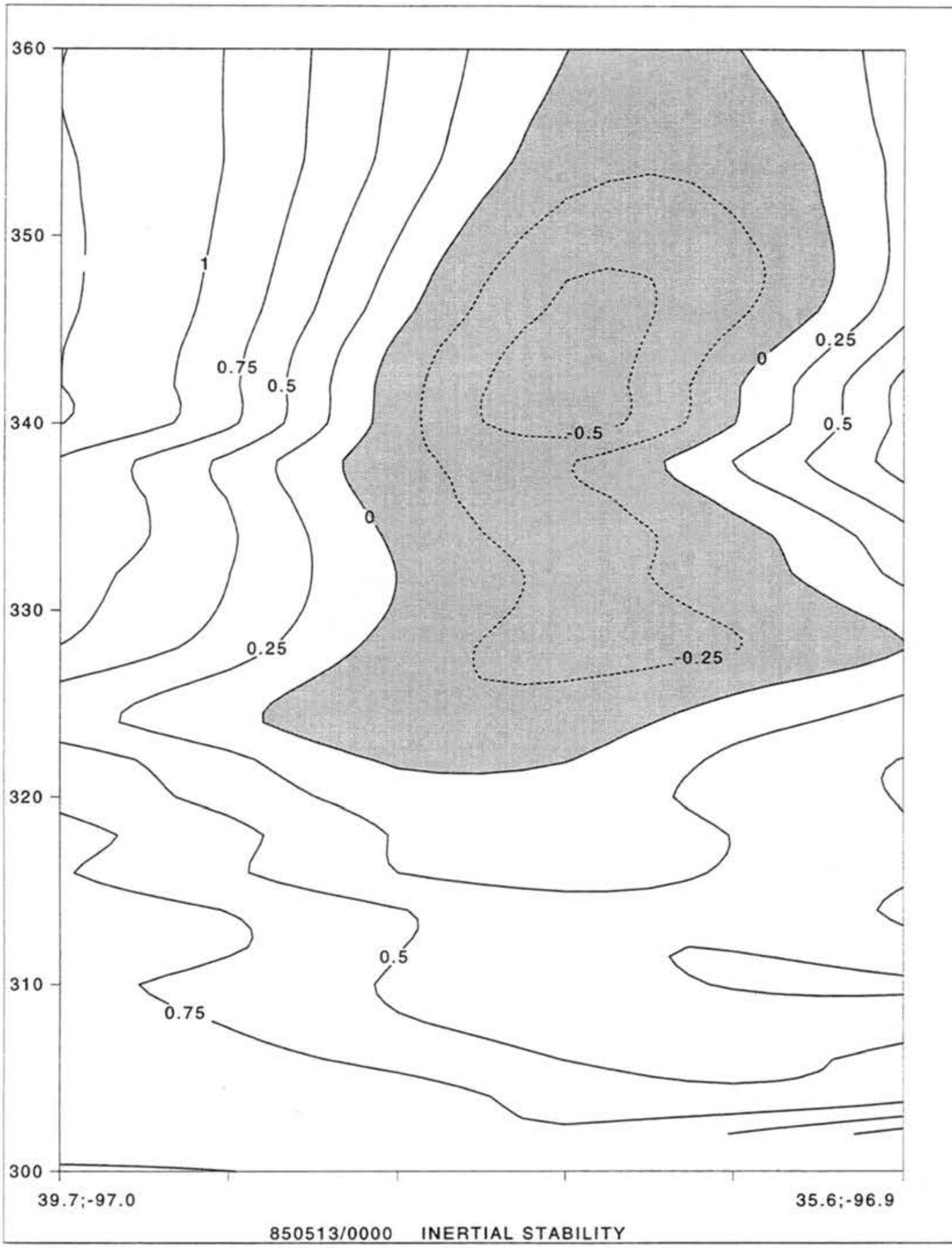

Figure 11. Vertical cross section of the inertial instability parameter at 0000 UTC on 13 May 1985. Cross section extends from the north-central to the south-central portion of the mesonetwork. Contours every 0.25; negative values are dashed and shaded.

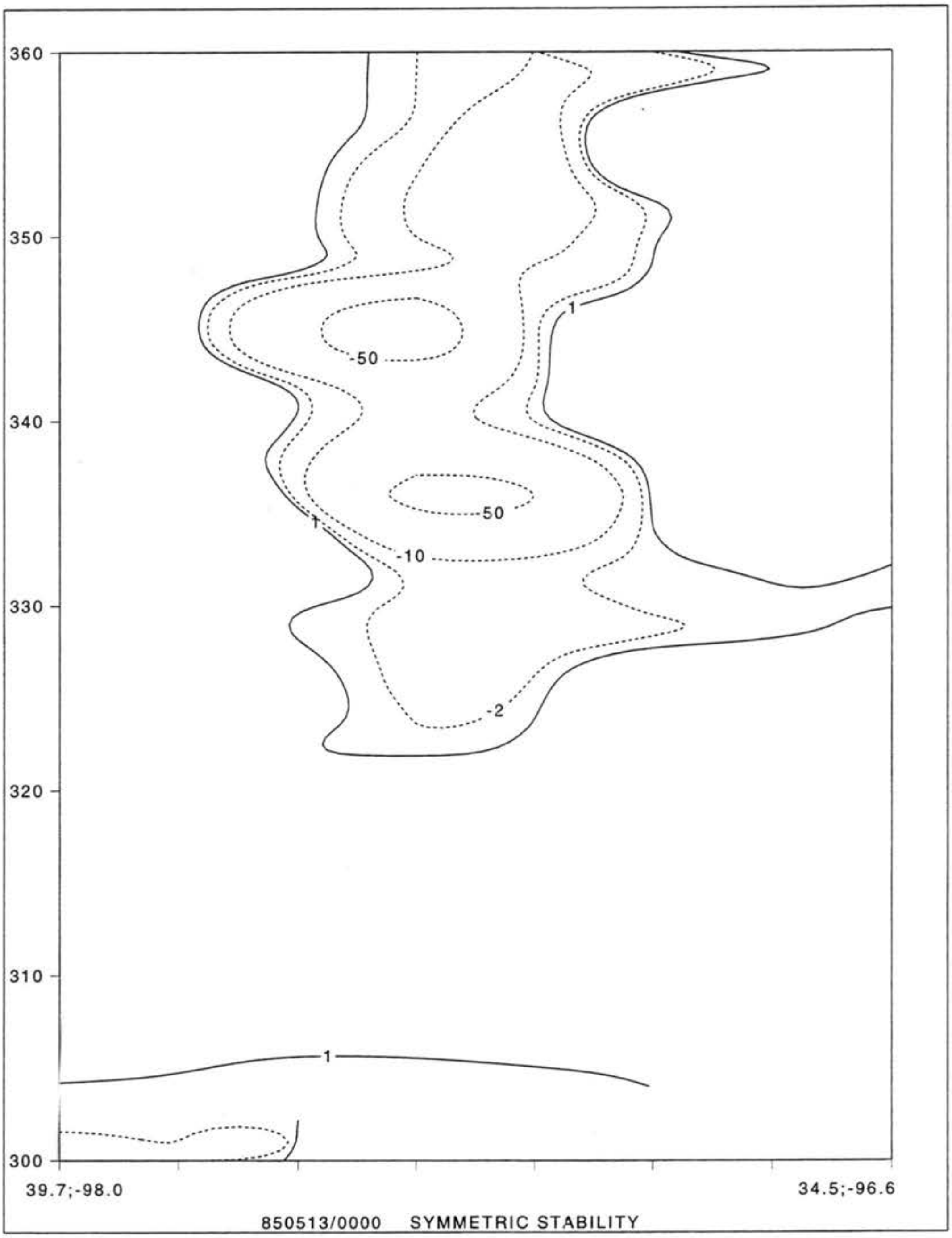

Figure 12. Vertical cross section of symmetric stability, $S=(\eta_\theta/f)R_i$ at 0000 UTC on 13 May 1985. Cross section extends from the north-central to the south-central portion of the mesonetwork. Contours are unevenly spaced and are shown for S = +1, −2, −10, and −50.

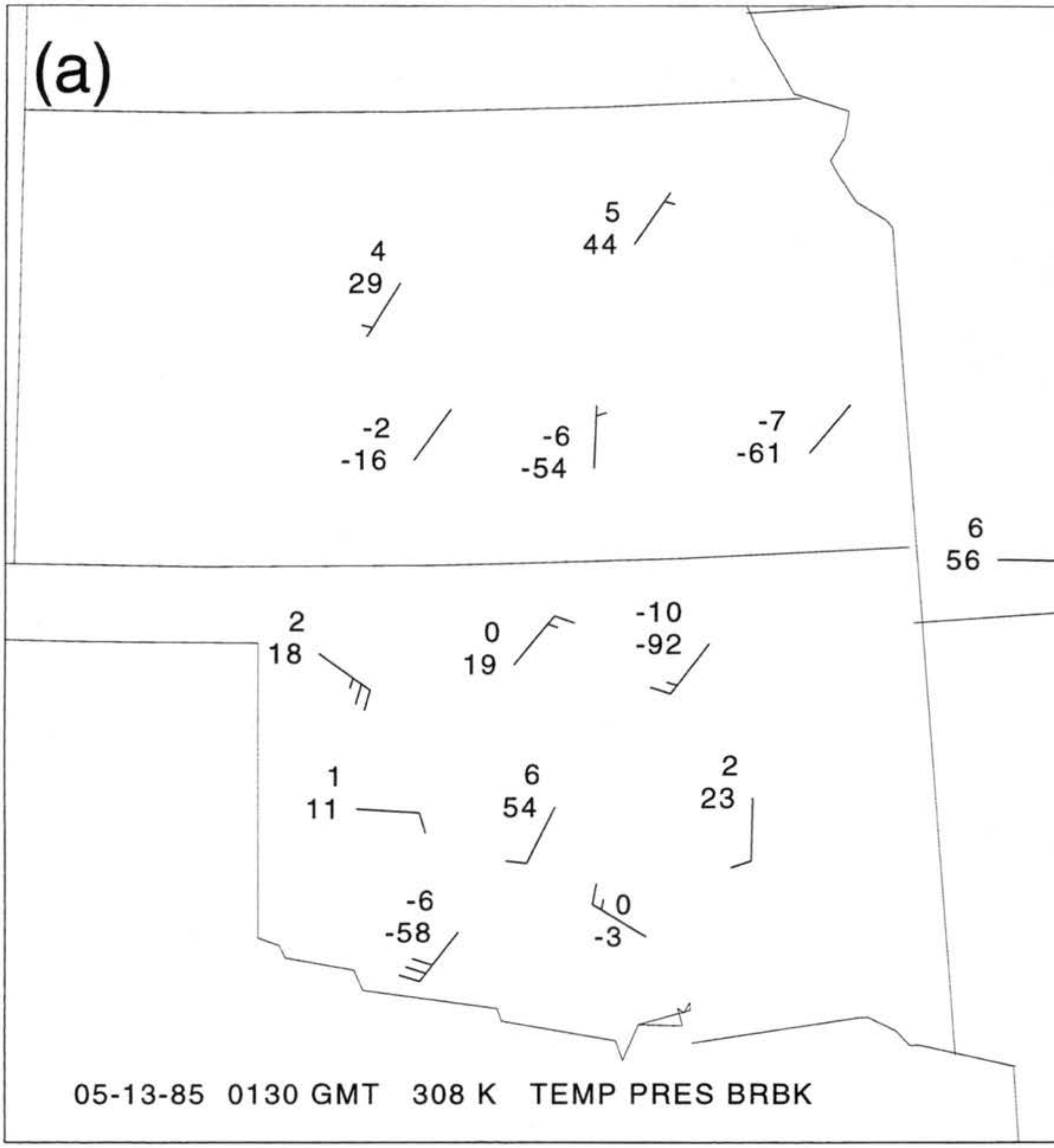

Figure 13. Plan view on the a) 308 K and b) 330 K isentropic surfaces showing the 3-hour changes in temperature, pressure and winds. Temperature and pressure changes are plotted on the left side of the station model and are in whole degrees and millibars. The vector change in the wind is plotted using the usual convention for wind speed.

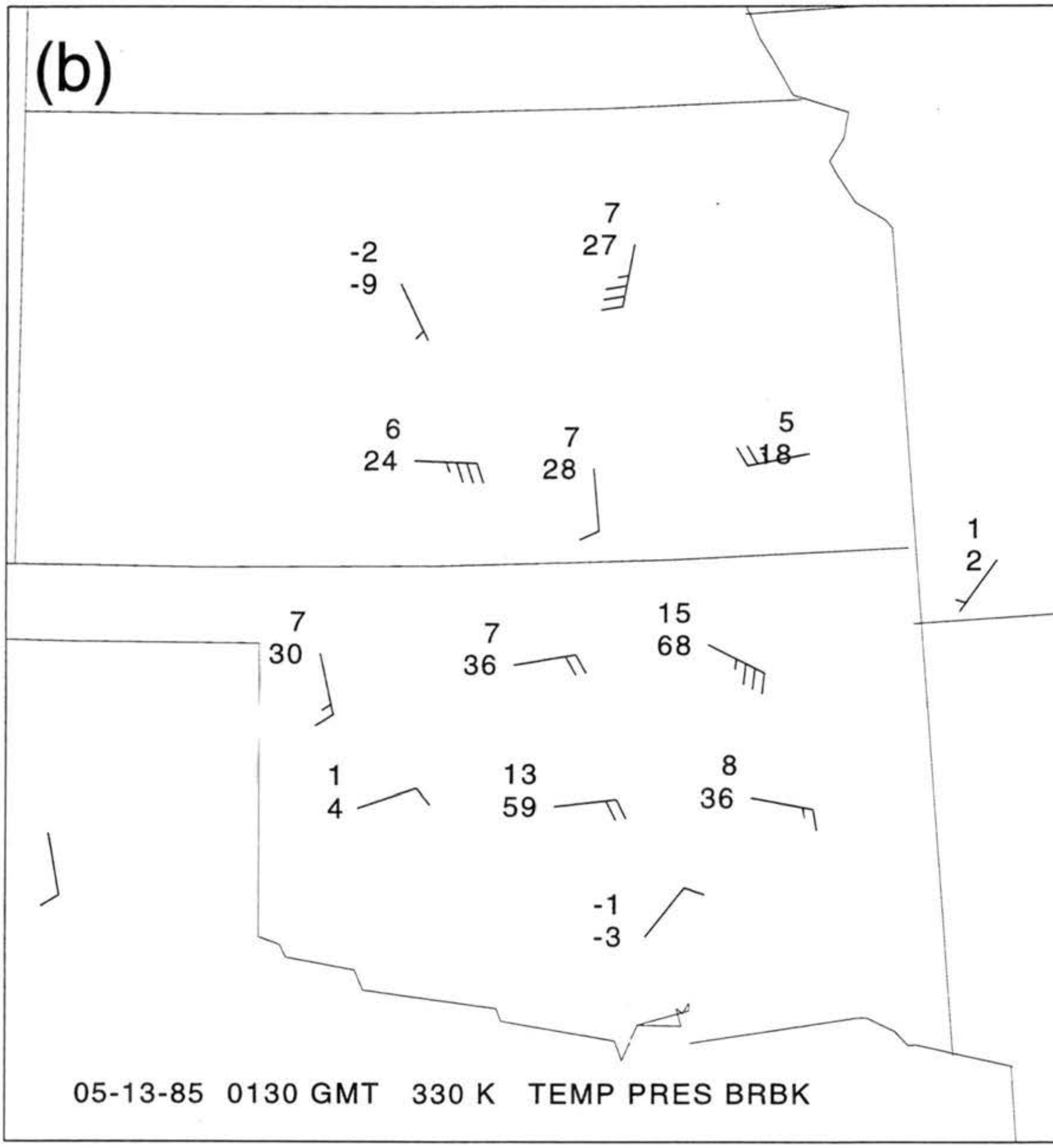

Figure 13. (Continued)

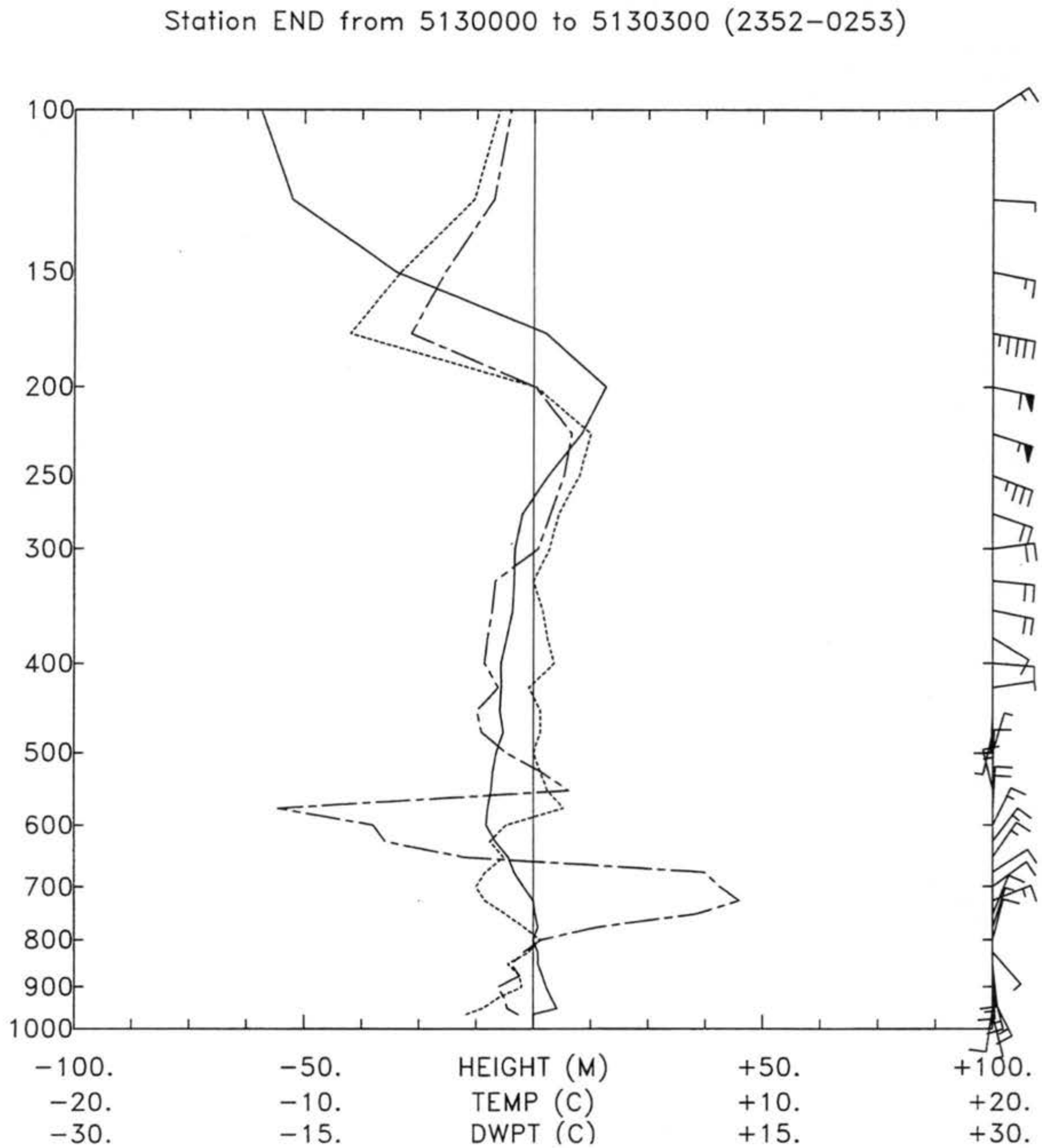

Figure 14. Vertical profile of 3-hour changes in the height (solid), temperature (dotted) and dewpoint (dashed) for Enid, Oklahoma (END). Scale for each parameter is at the bottom. The vector change in the wind is plotted using the usual convention for wind speed.

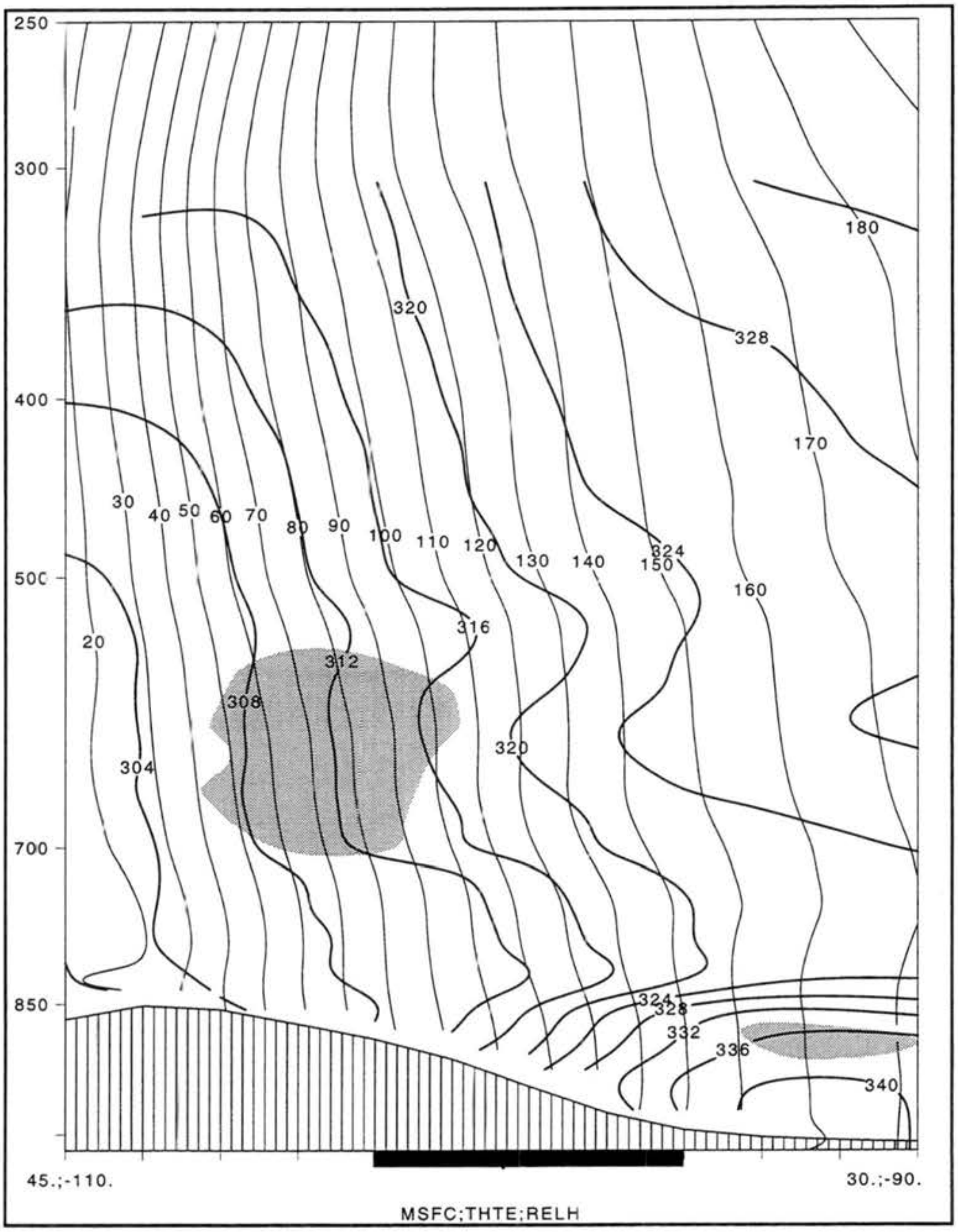

Figure 15. Vertical cross section showing pseudo-momentum surfaces (thin lines), θ_e (thick lines), and relative humidity in excess of 80% (shading). Cross section extends from the northwest to the southeast and cuts through the PRE-STORM network. Location of the cross section endpoints is plotted on the lower left and right corners. The PRE-STORM network is marked by the heavy bar at the bottom. Contour interval for momentum is 10 m s^{-1}; contour interval for θ_e is 4 K.

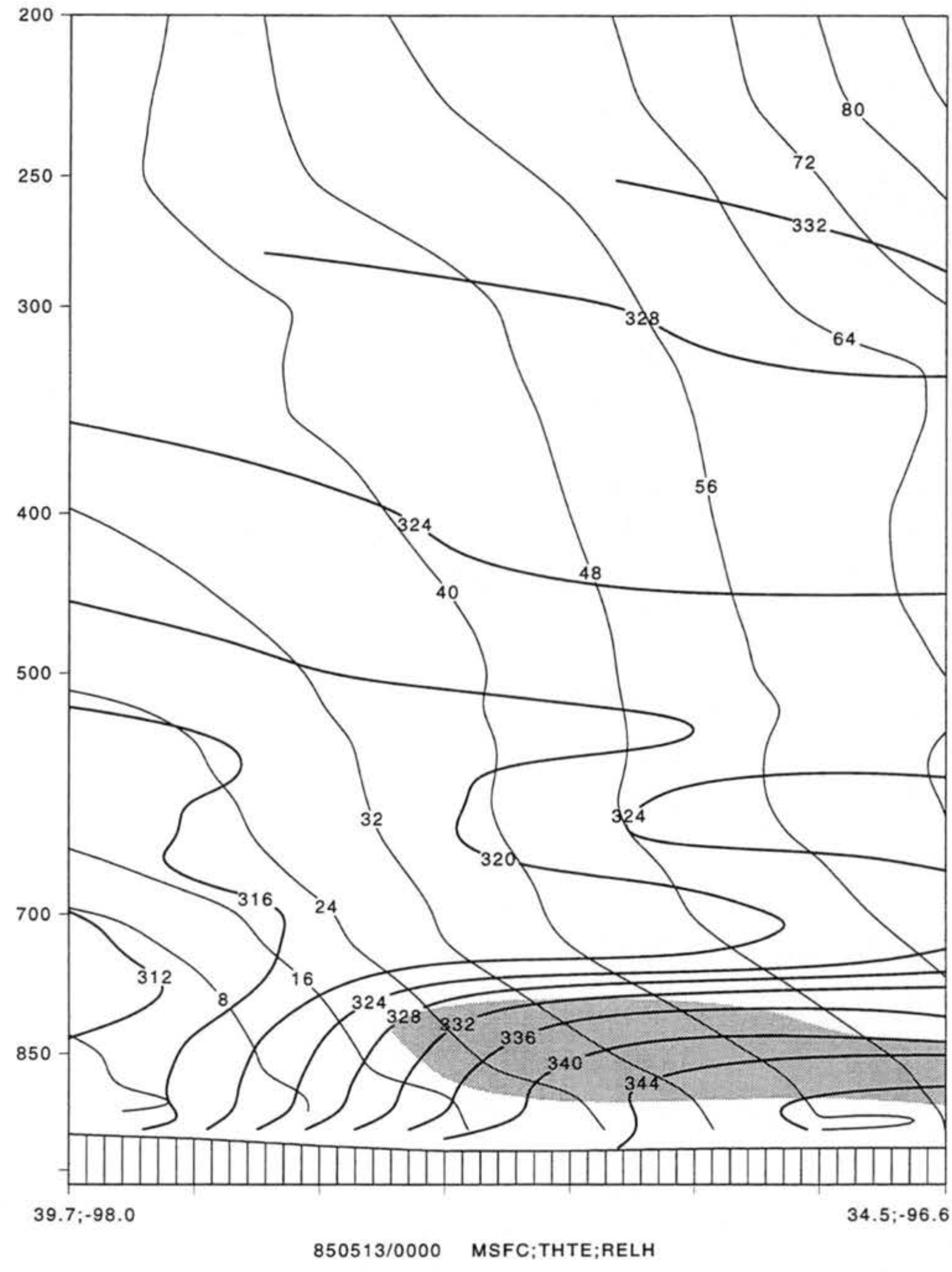

Figure 16. As in Fig. 15, except the cross section is through the PRE-STORM network and uses the special PRE-STORM sounding data. Contour interval for momentum surfaces is 8 m s^{-1}.

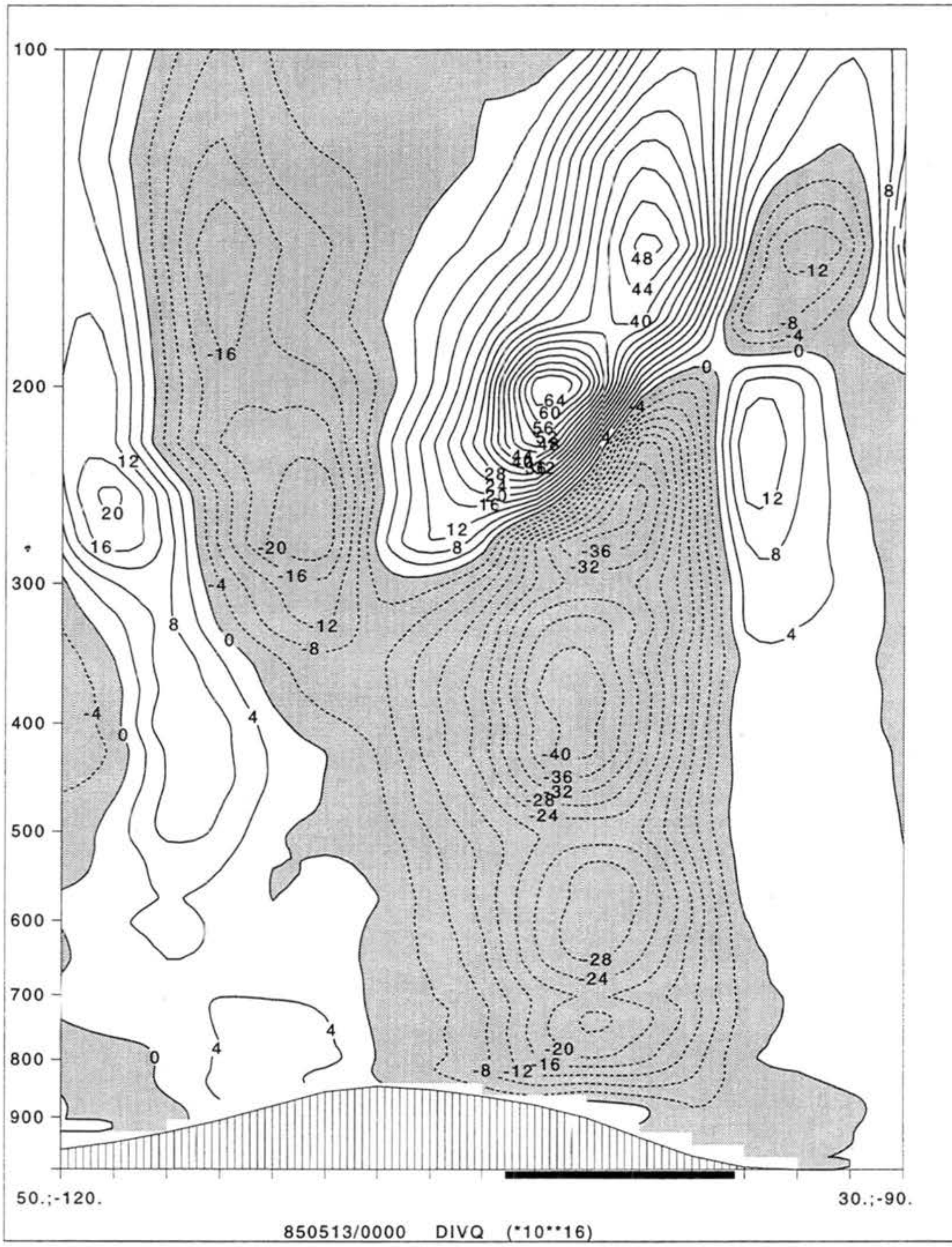

Figure 17. Vertical cross section of the divergence of the Q-vector. Solid lines positive; negative lines dashed. Region of Q-vector convergence, implying upward forcing, is shaded. The PRE-STORM network is marked by the heavy bar at the bottom. Contour interval $4x10^{-16}$ m^2 kg^{-1} s^{-1}.

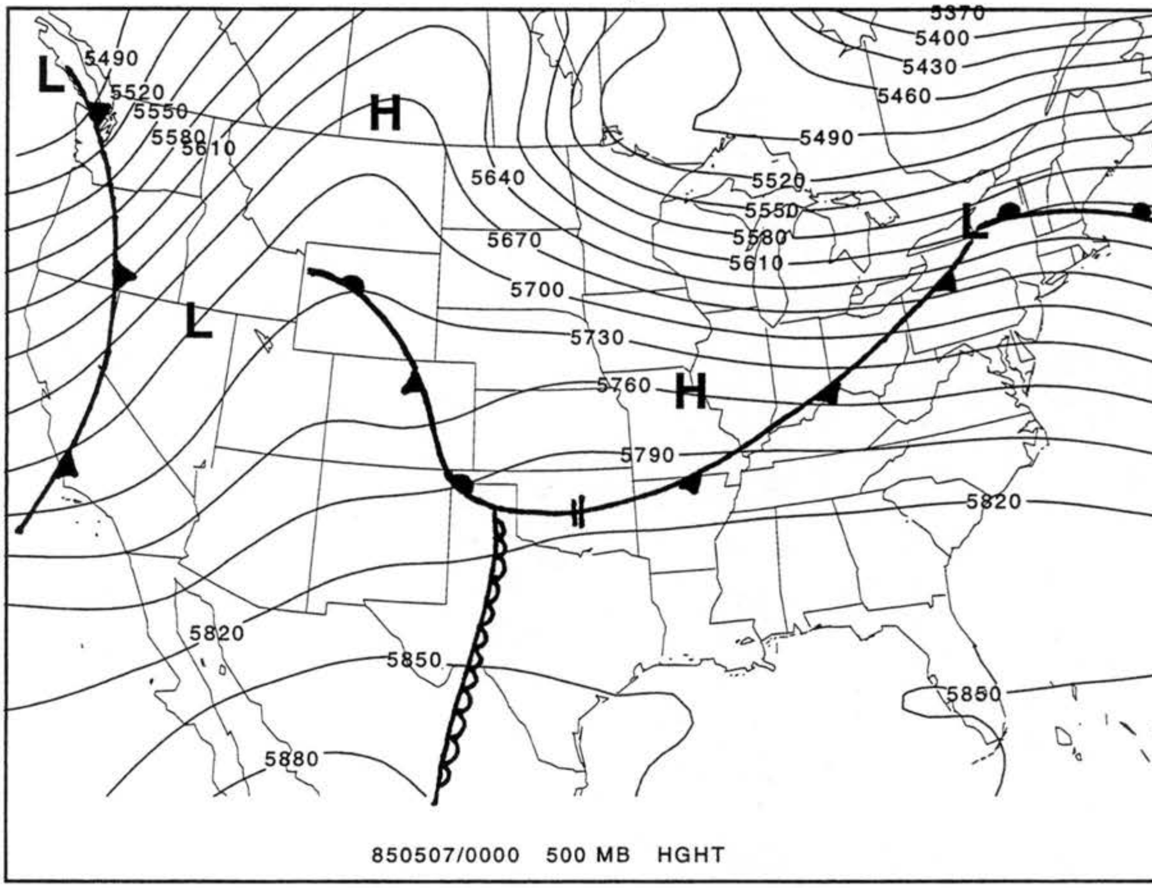

Figure 18. Composite chart at 0000 UTC on 7 May 1985 depicting conditions at 500 mb with surface fronts and pressure centers superimposed. 500-mb height contours every 30 m. High and low pressure centers marked with "H" and "L," respectively. Surface boundaries use standard convention for cold, warm and occluded fronts, and the dry line.

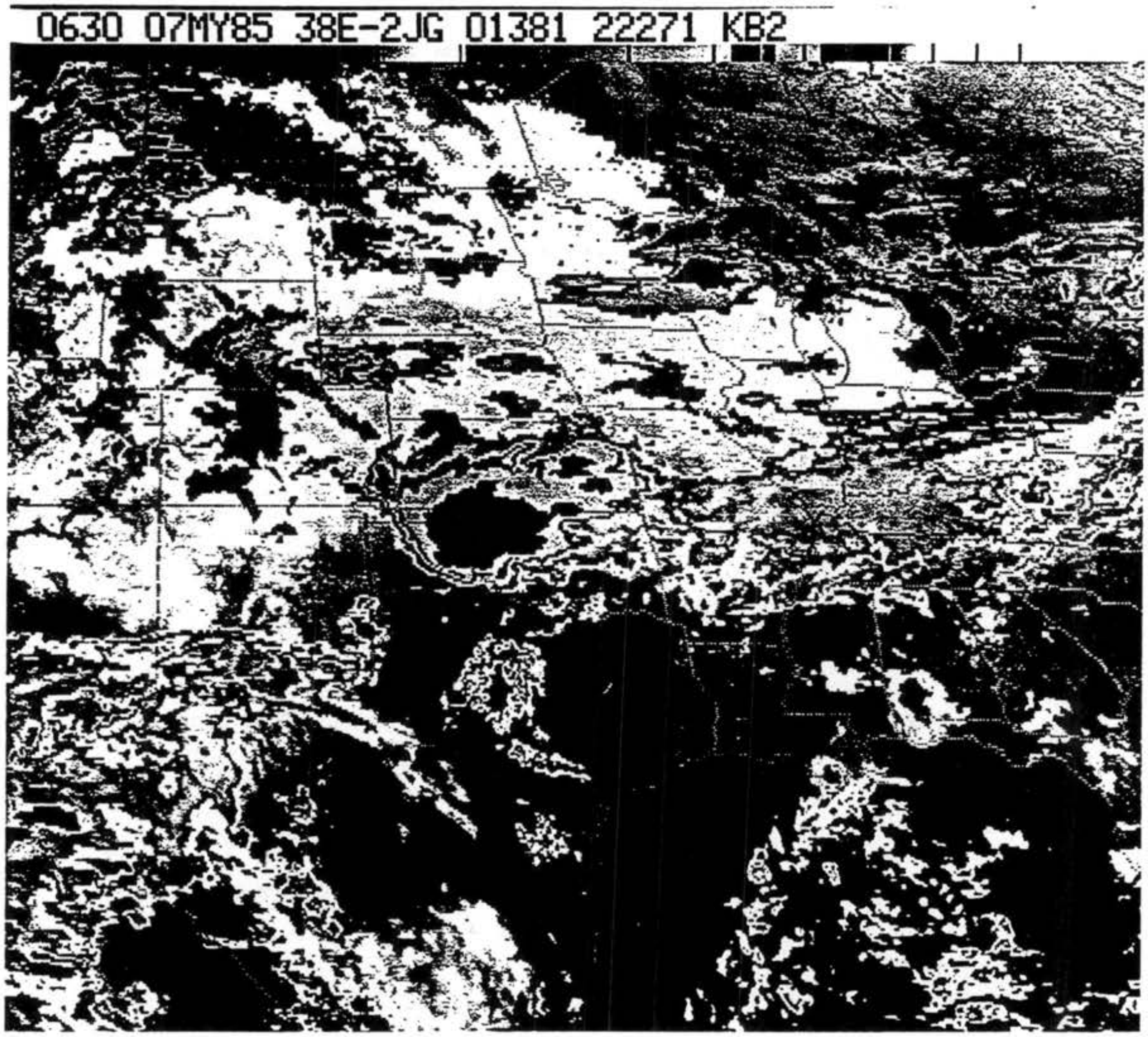

Figure 19. Satellite imagery at 0630 UTC on 7 May 1985.

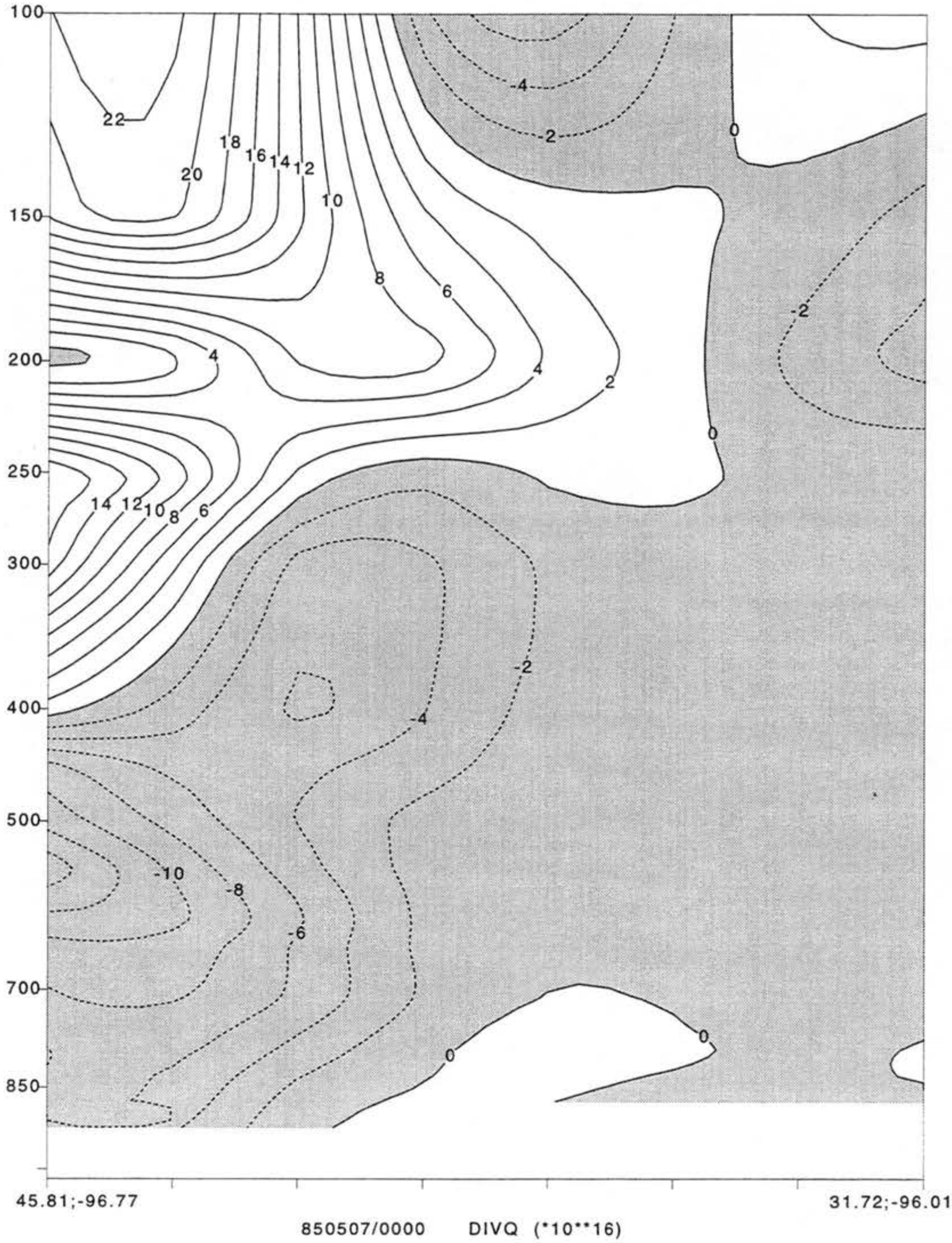

Figure 20. Vertical cross section of the divergence of Q-vectors at 0000 UTC on 7 May 1985. Shaded areas are convergent and represent regions of upward quasi-geostrophic forcing. Cross section extends from north to south across the U.S.; the PRESTORM region is marked by the heavy bar at the bottom.

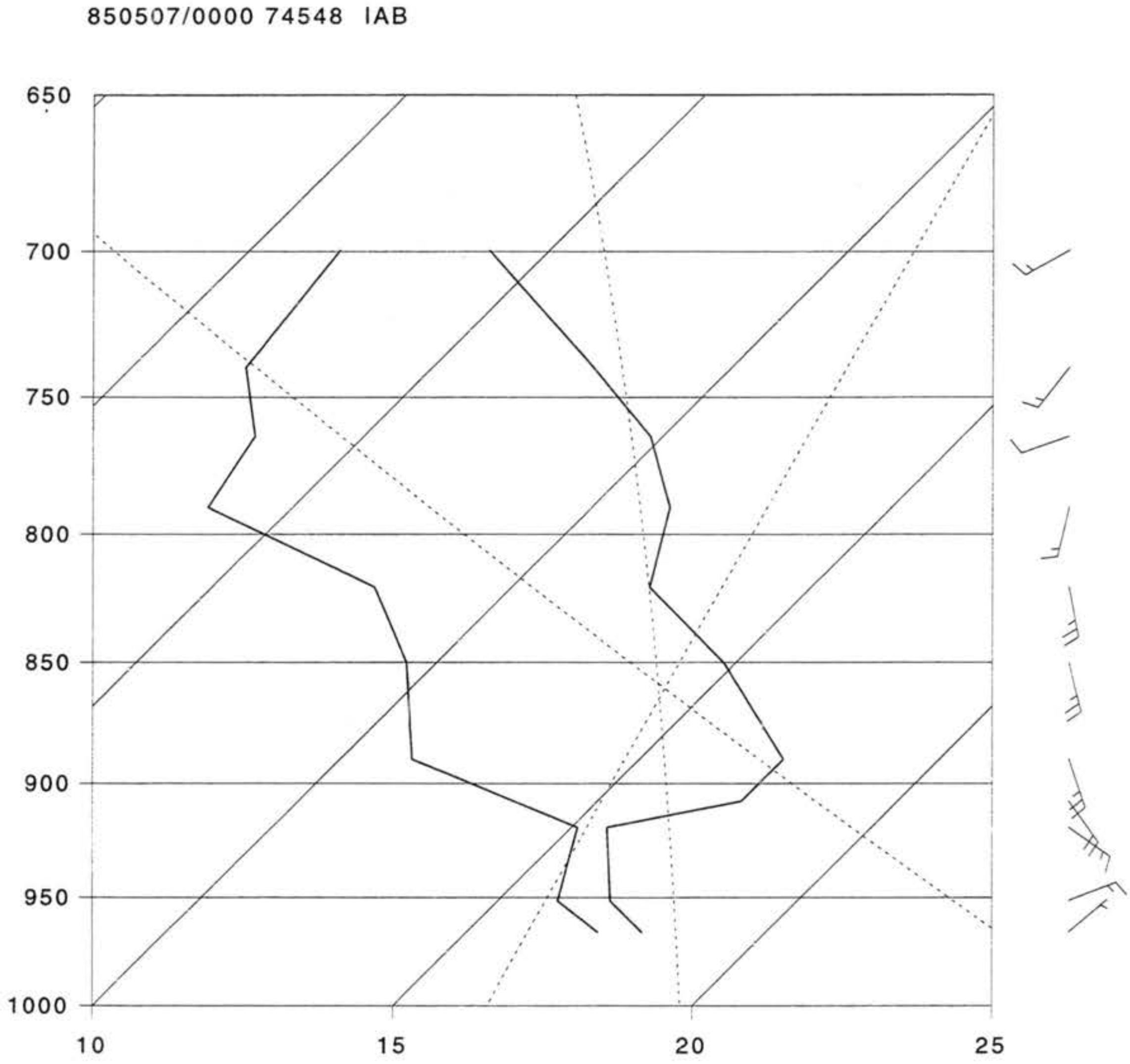

Figure 21. Sounding for IAB (Wichita, Kansas) at 0000 UTC on 7 May 1985. Dotted lines are representative θ, θ_e, and mixing ratios.

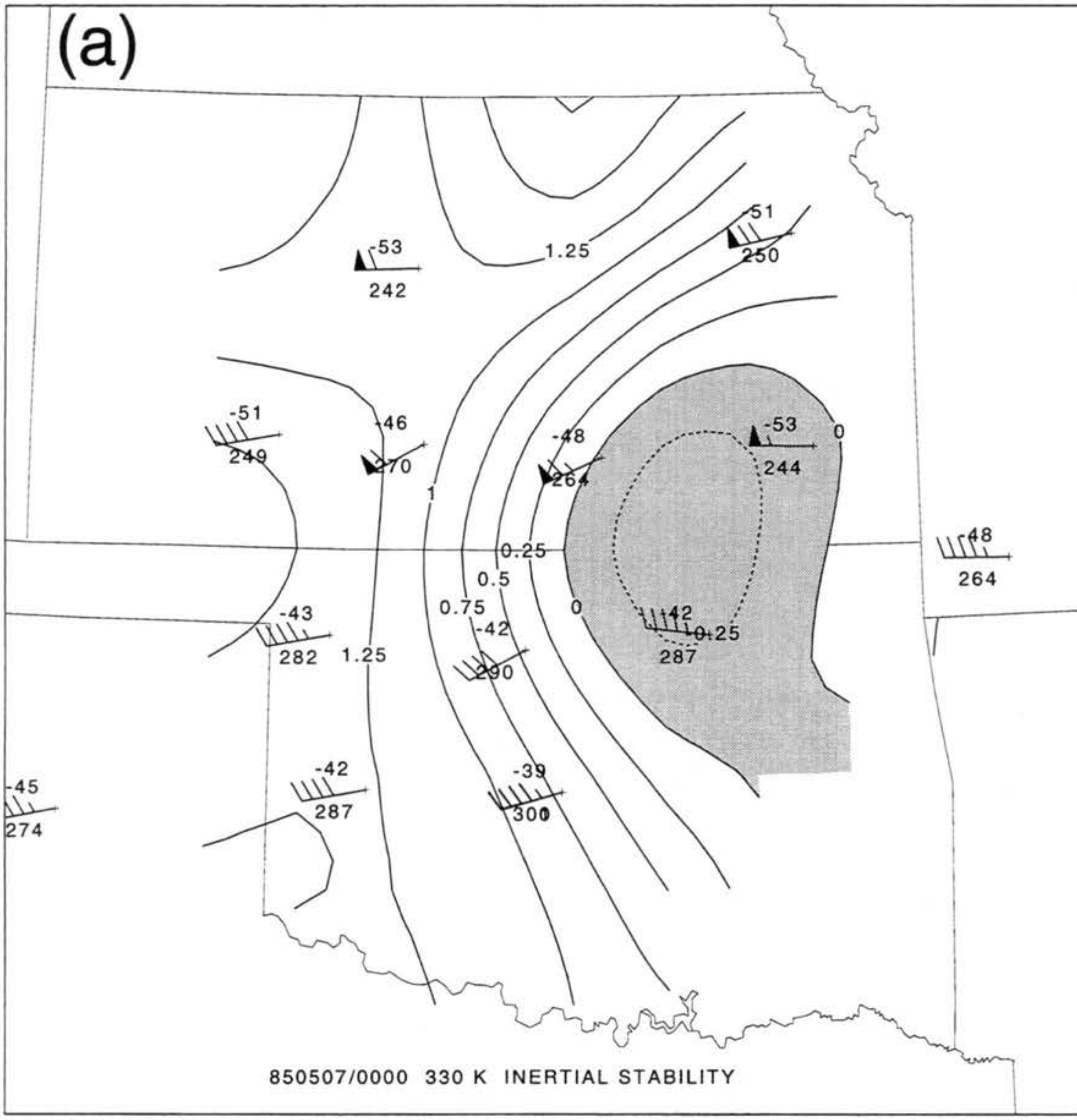

Figure 22. Plan view of the inertial stability parameter ($\alpha = \eta / f$) at a) 0000 and b) 0600 UTC on 7 May 1985 on the 330 K isentrope. Contour interval is 0.25. Positive values are solid; negative values are dashed and shaded. Plots of temperature and pressure are plotted to the left of the stations.

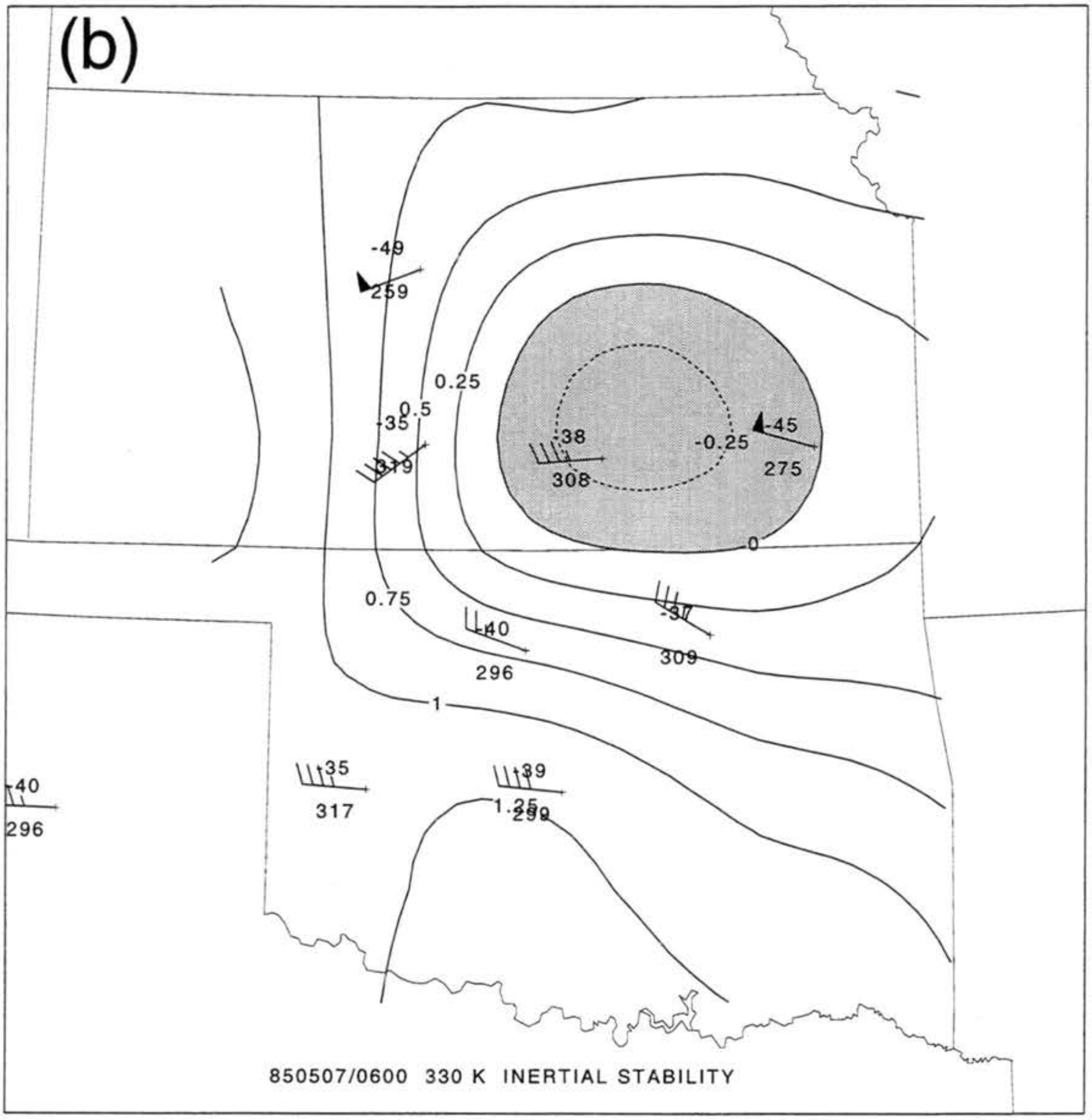

Figure 22. (Continued)

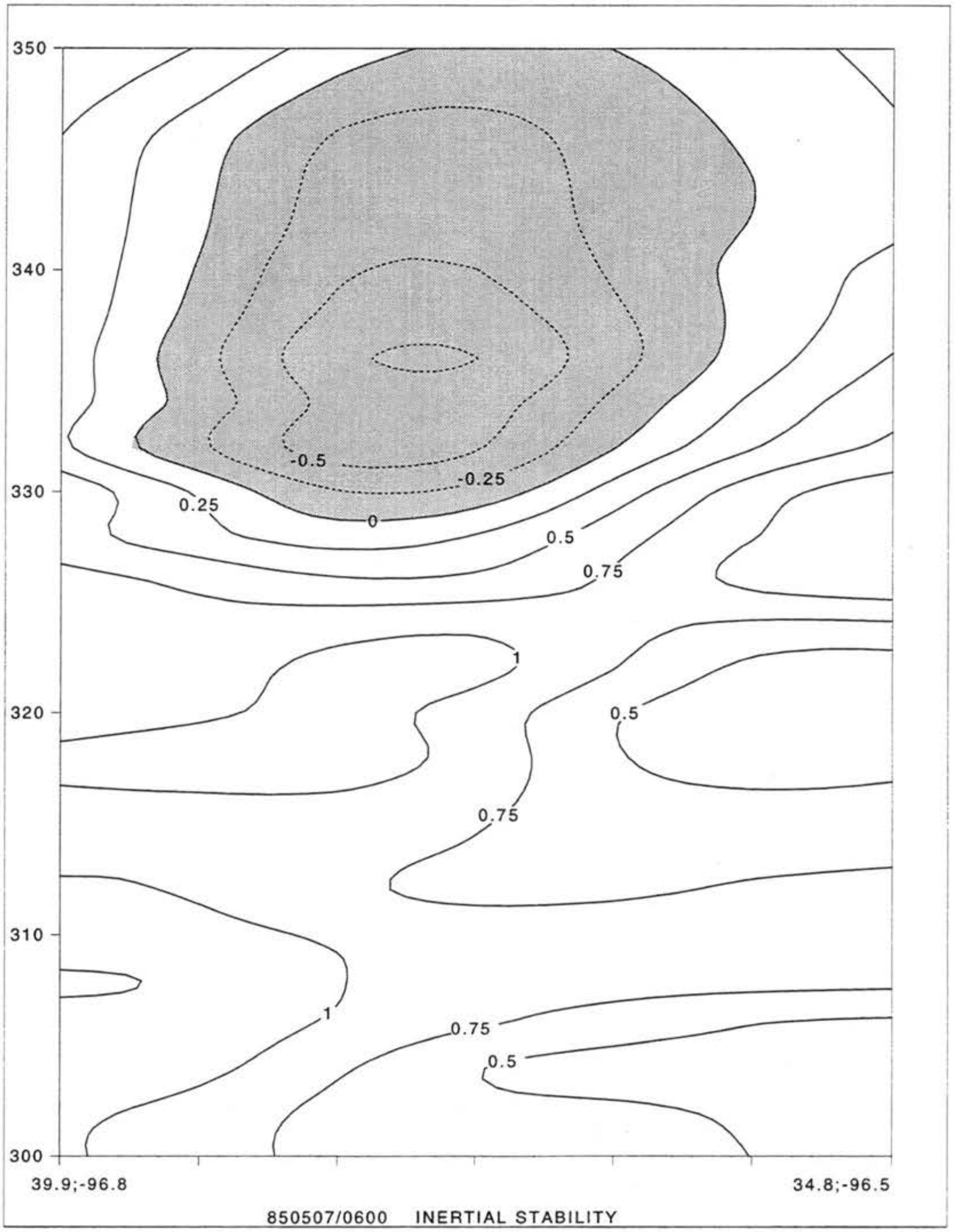

Figure 23. Vertical cross section through the PRE-STORM network depicting the inertial instability. Contour interval is 0.25. Positive values are solid; negative values are dashed and shaded.

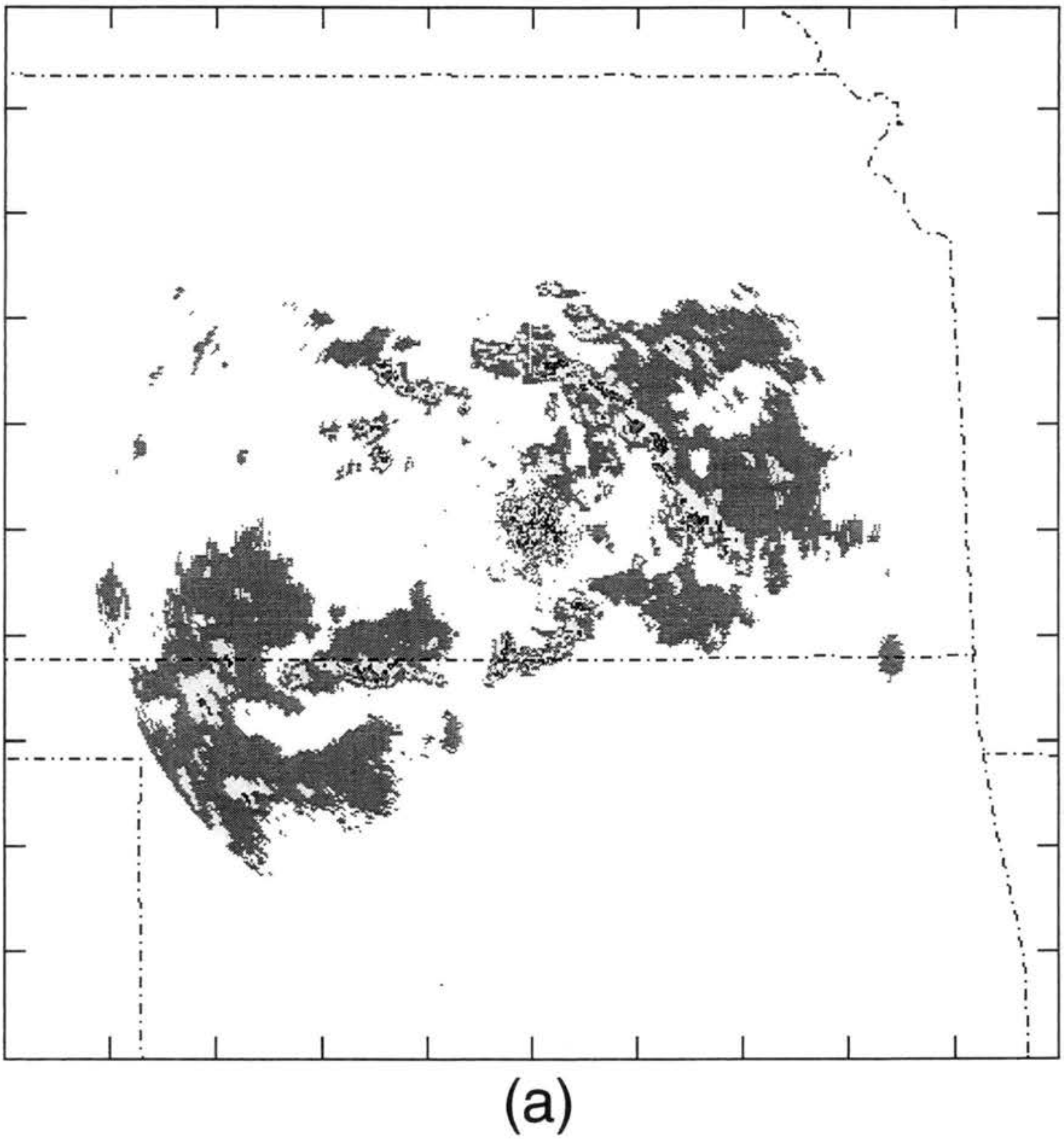

Figure 24. Radar imagery at a) 0700 and b) 1000 UTC on 7 May 1985. Radar reflectivities are shaded in repeating sequences of medium gray, light gray, and black, corresponding to thresholds of 18, 30, 41, 46, 50, and 55 dBz.

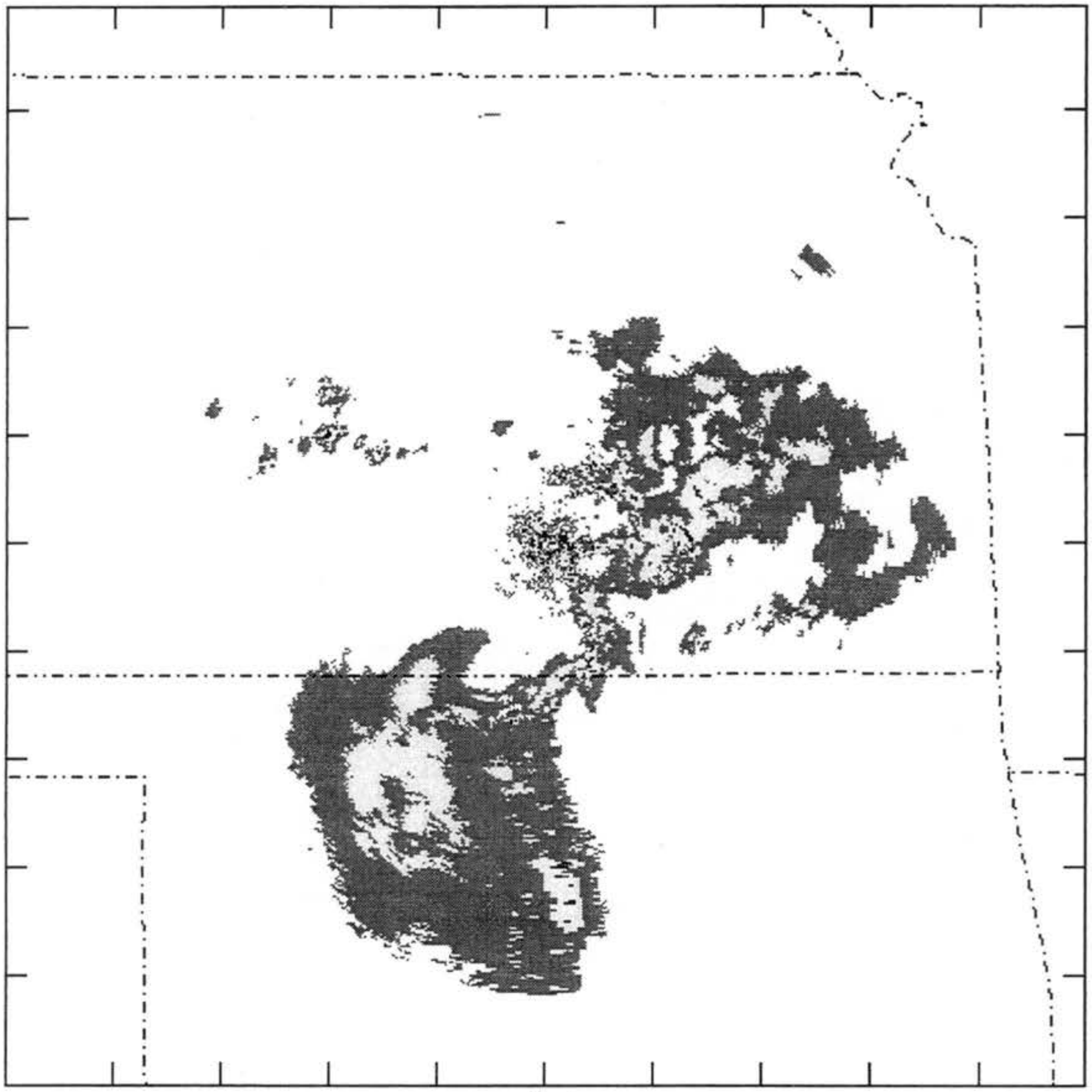

(b)

Figure 24. (Continued)

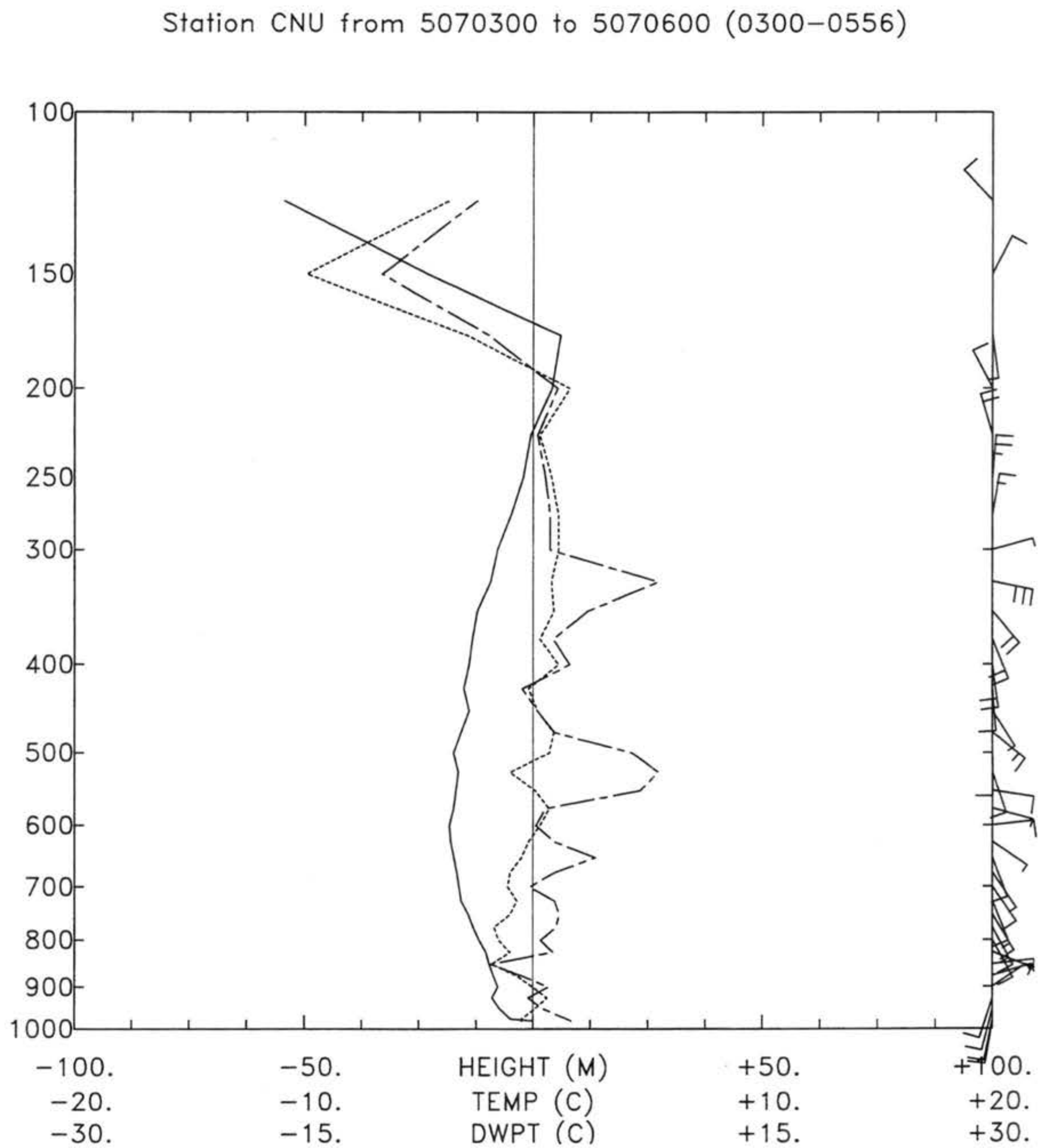

Figure 25. Vertical profile of 3-hour changes in the height (solid), temperature (dotted) and dewpoint (dashed) for Chanute, Kansas (CNU) for the period 0000–0300 UTC on 7 May 1985. Scale for each parameter is at the bottom. The vector change in the wind is plotted using the usual convention for wind speed.

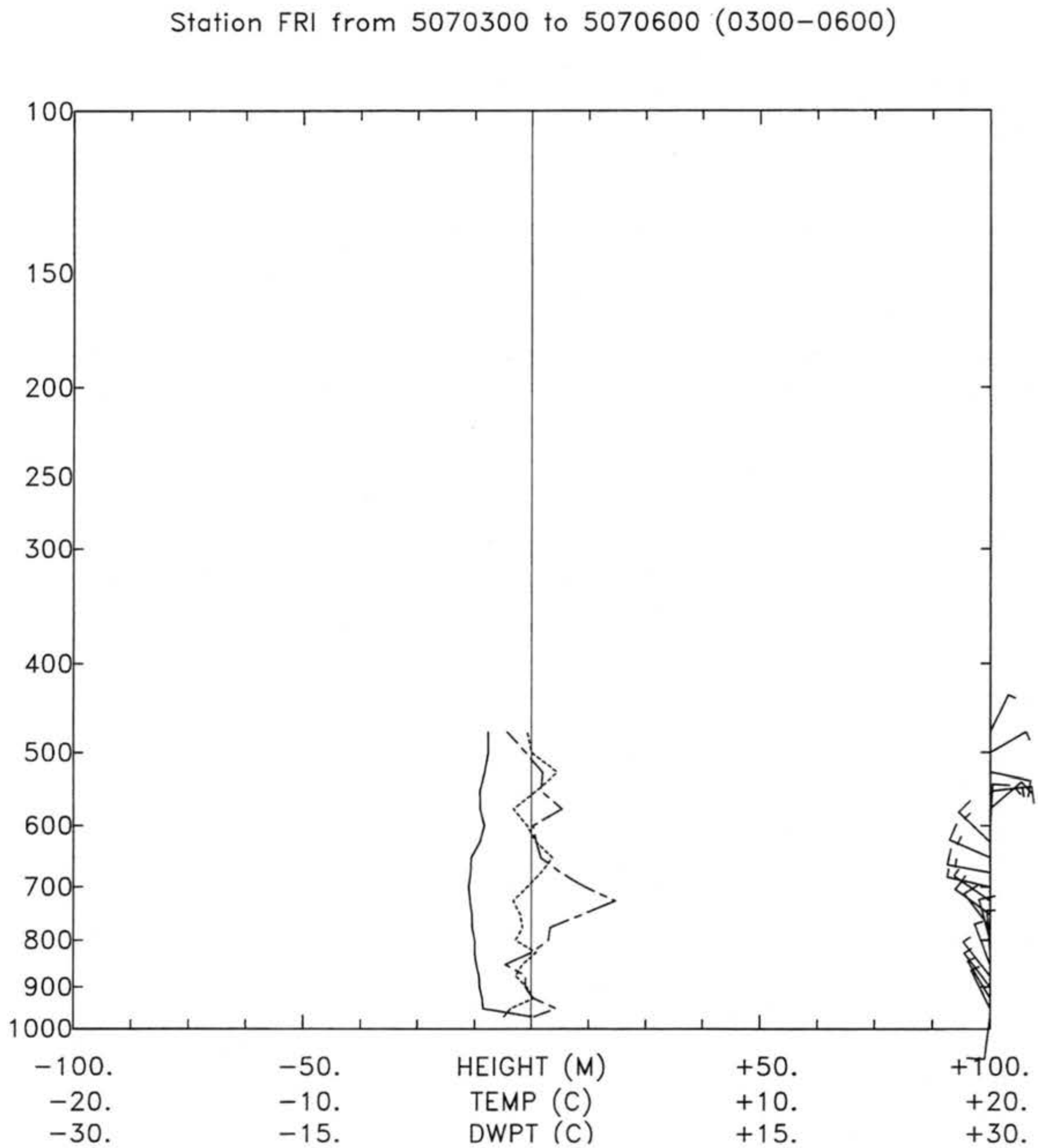

Figure 26. As in Fig. 25, except for Ft. Riley, Kansas (FRI).

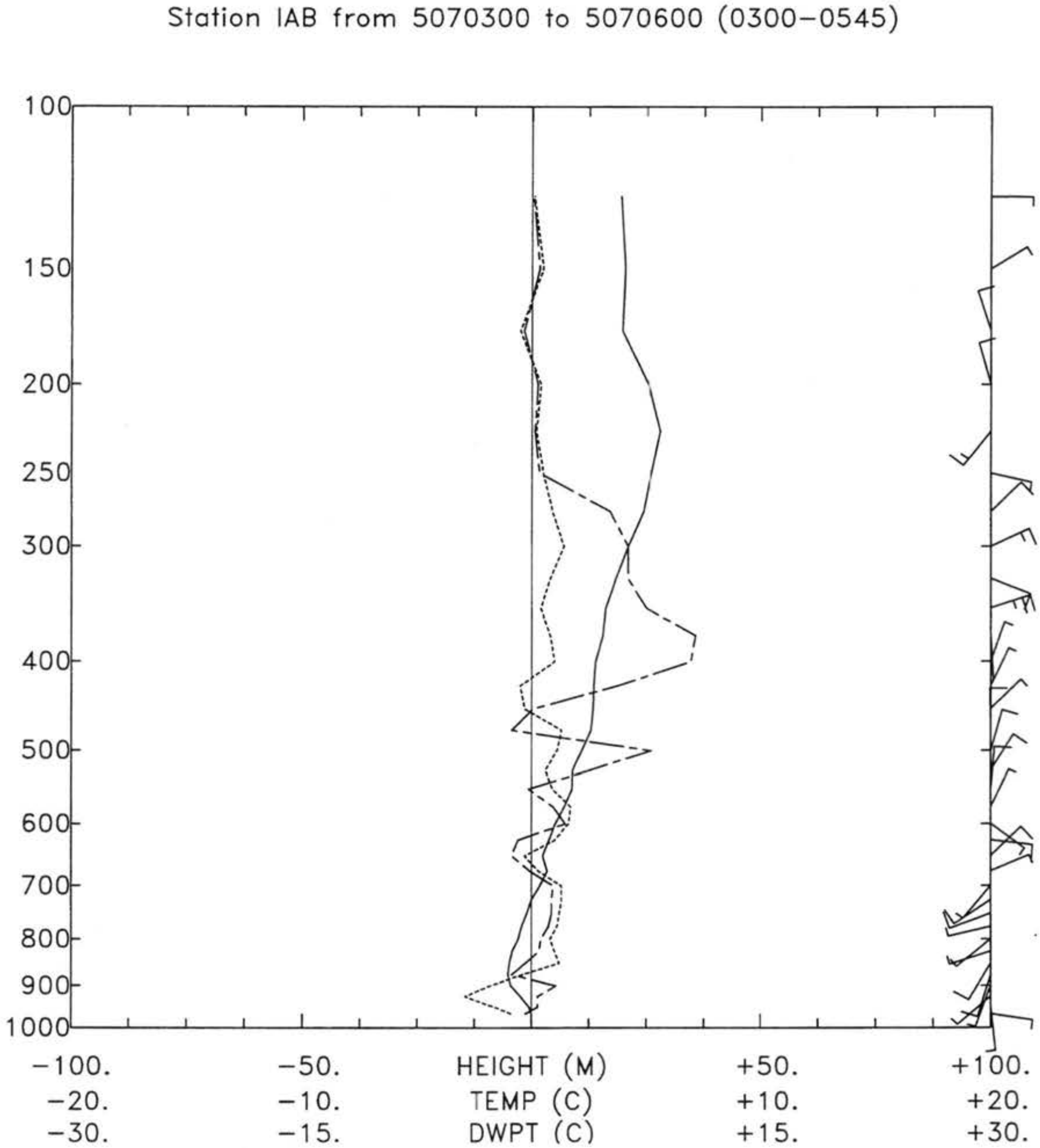

Figure 27. As in Fig. 25, except for Wichita, Kansas (IAB).

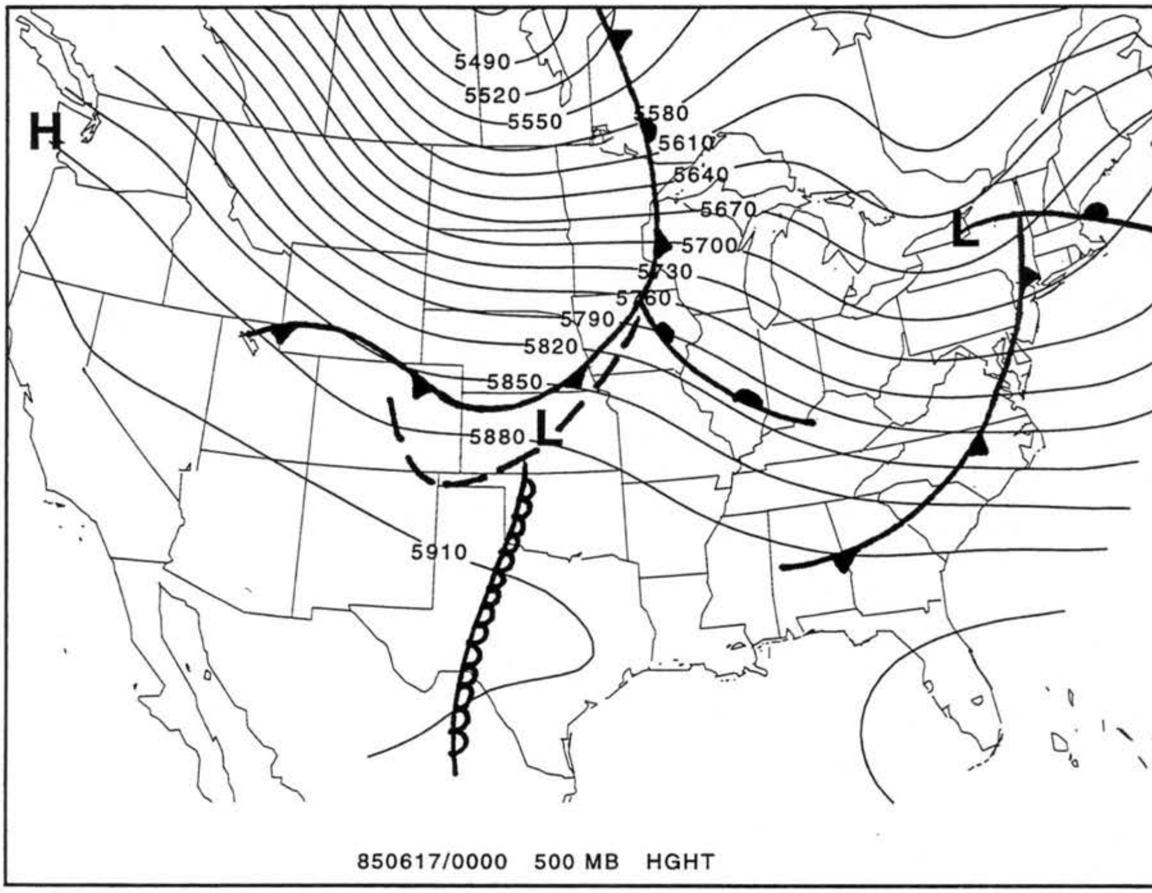

Figure 28. Composite chart for 0000 UTC on 17 June 1985 depicting conditions at 500 mb with surface fronts and pressure centers superimposed. 500-mb height contours every 30 m. High and low pressure centers marked with "H" and "L," respectively. Surface boundaries use standard convention for cold, warm and occluded fronts, and the dry line.

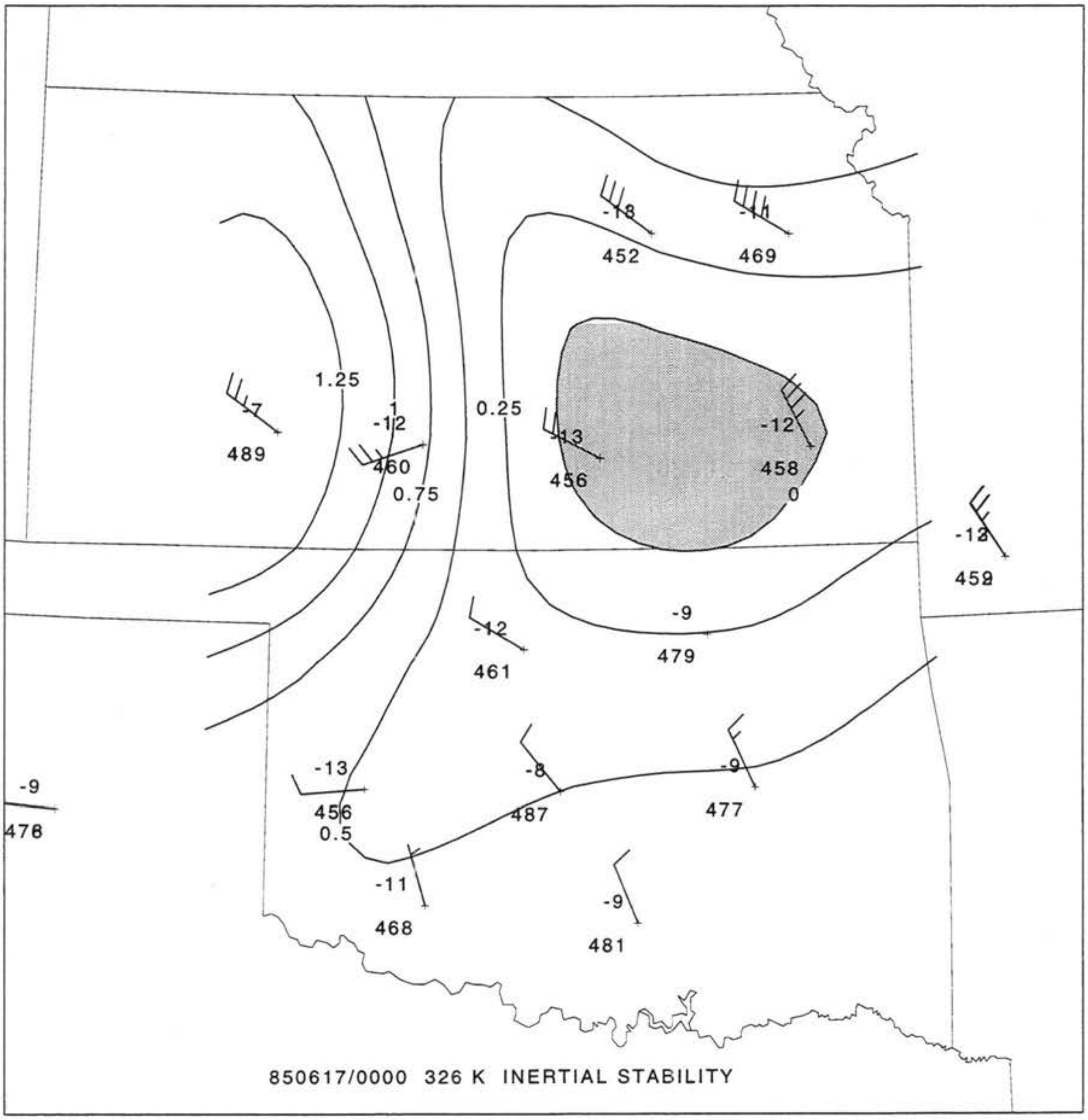

Figure 29. Plan view of the inertial instability parameter on the 326 K isentrope at 0000 UTC on 17 June 1985. Positive values are solid; negative values are dashed and shaded. Contour interval every 0.25.

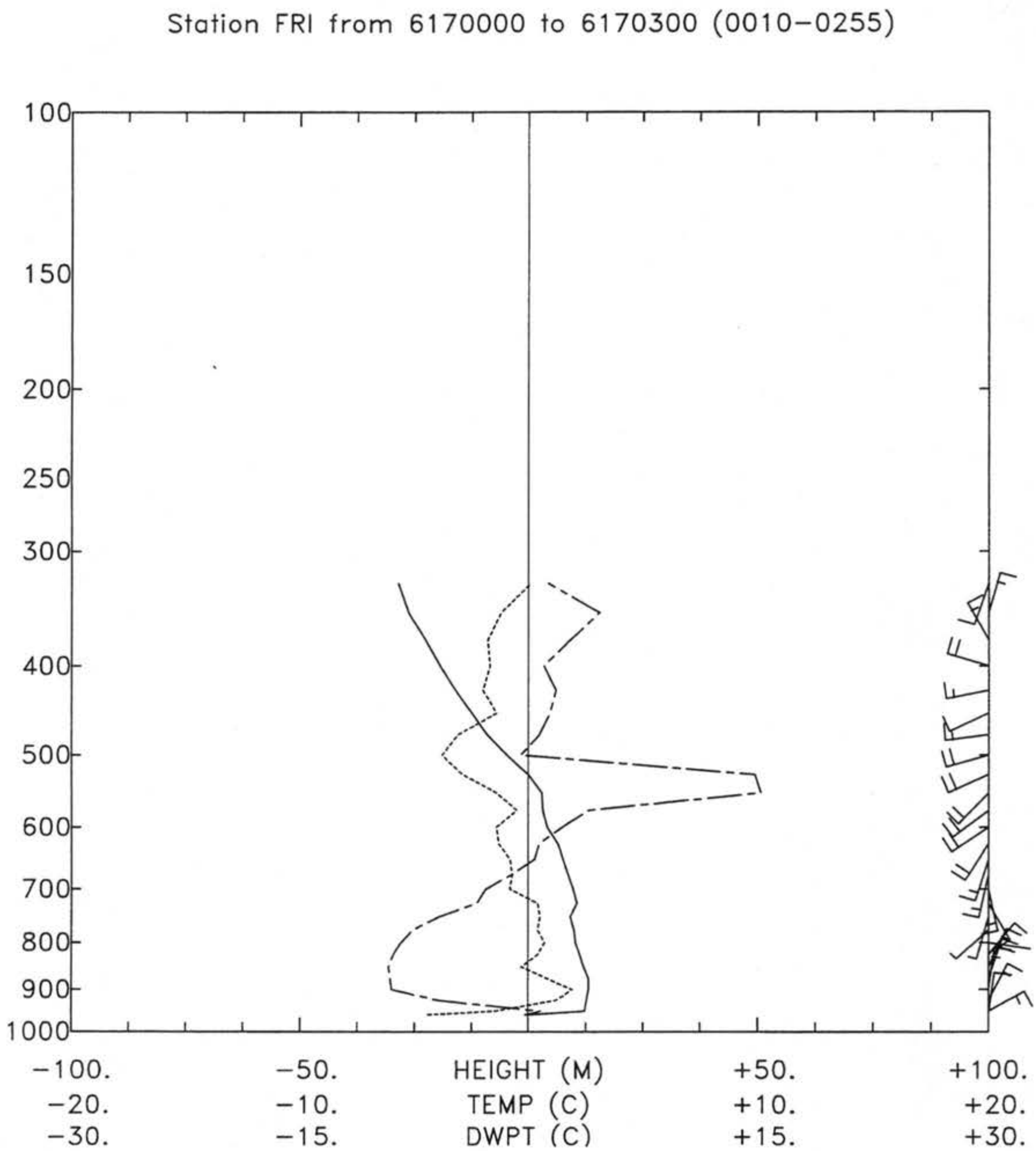

Figure 30. Vertical profile of 3-hour changes in the height (solid), temperature (dotted) and dewpoint (dashed) for Fort Riley, Kansas (FRI) for the period 0000–0300 UTC on 17 June 1985. Scale for each parameter is at the bottom. The vector change in the wind is plotted using the usual convention for wind speed.

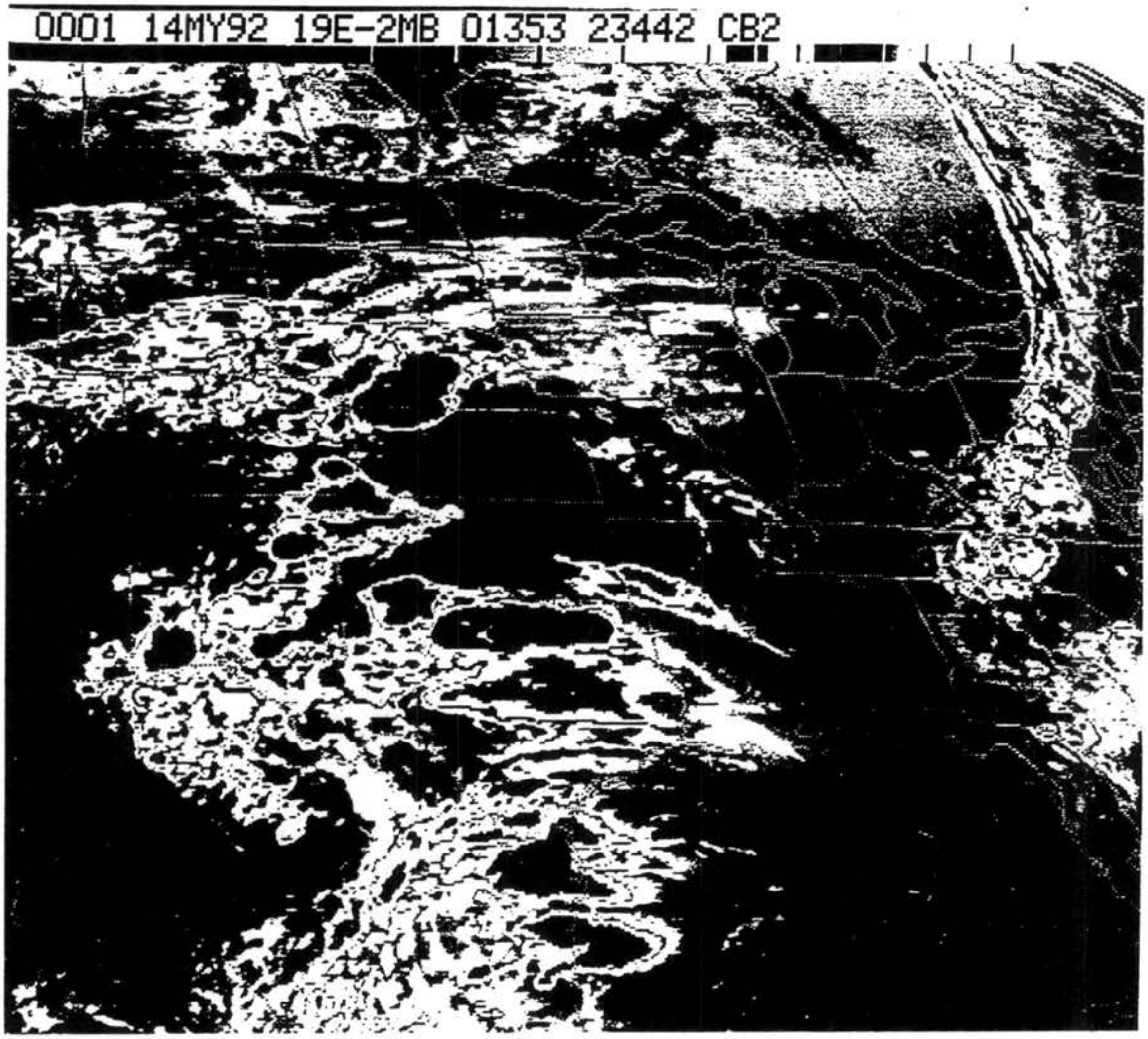

Figure 31. Satellite infrared image taken at 0000 UTC on 14 May 1992. The developing MCC can be seen in western Nebraska at this time. The infrared enhancement uses the standard MB curve.

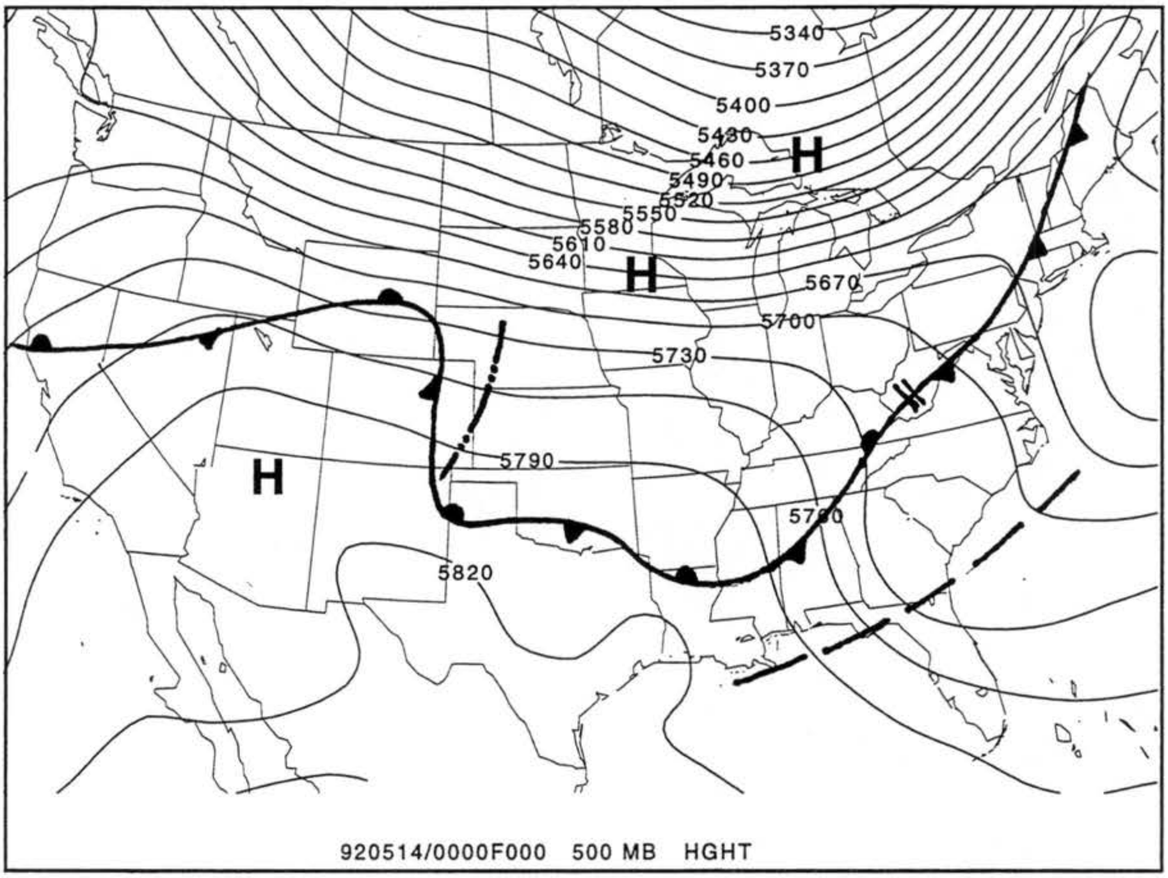

Figure 32. Composite chart for 0000 UTC on 14 May 1992 depicting conditions at 500 mb with surface fronts and pressure centers superimposed. 500-mb height contours every 30 m. High and low pressure centers marked with "H" and "L," respectively. Surface boundaries use standard convention for cold, warm and occluded fronts, and the dry line.

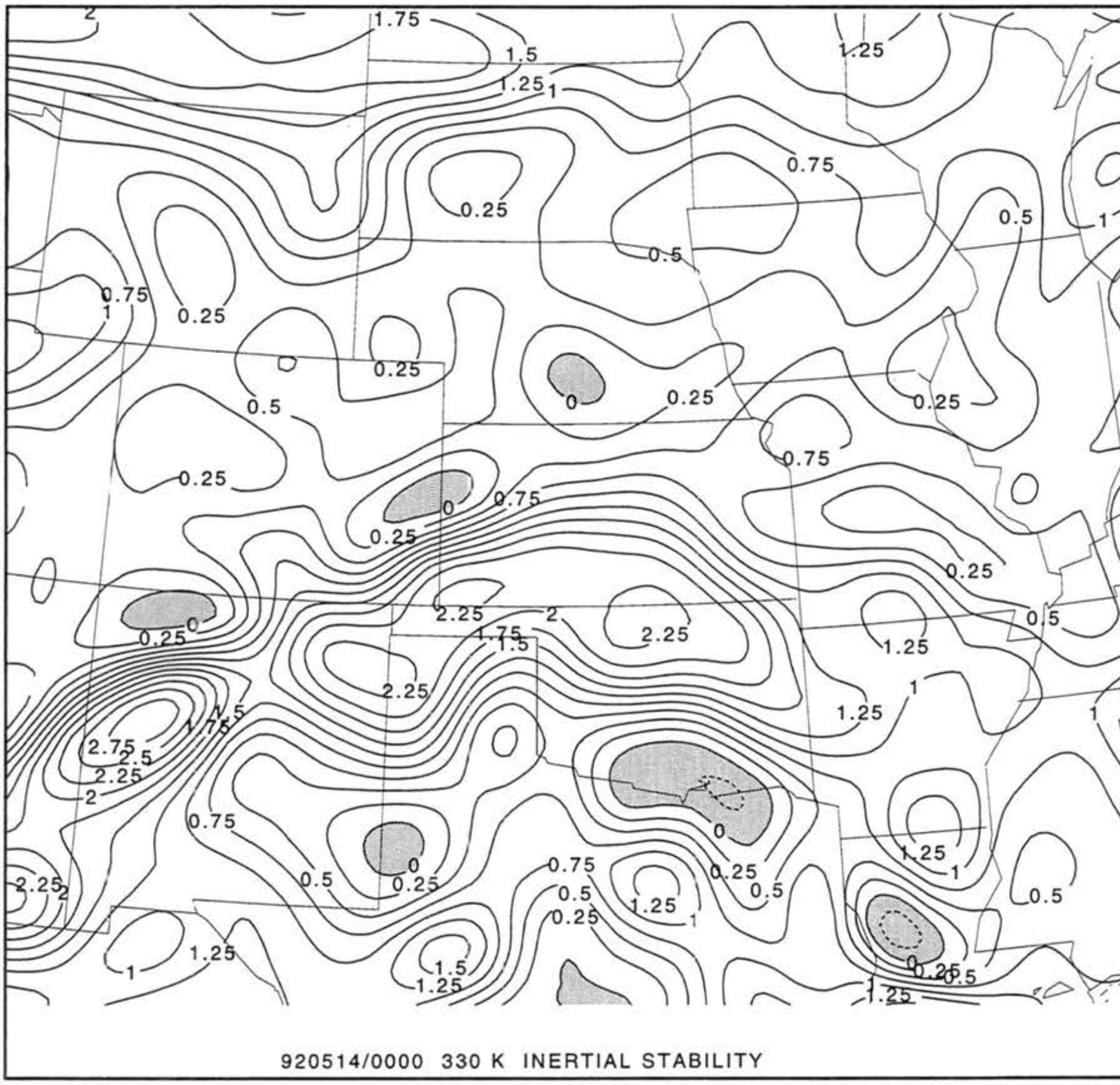

Figure 33. Plan view at 0000 UTC on 14 May 1992 showing the inertial stability parameter on the 330 K isentropic surface. Contour interval every 0.25. Positive values are solid; negative values are dashed and shaded.

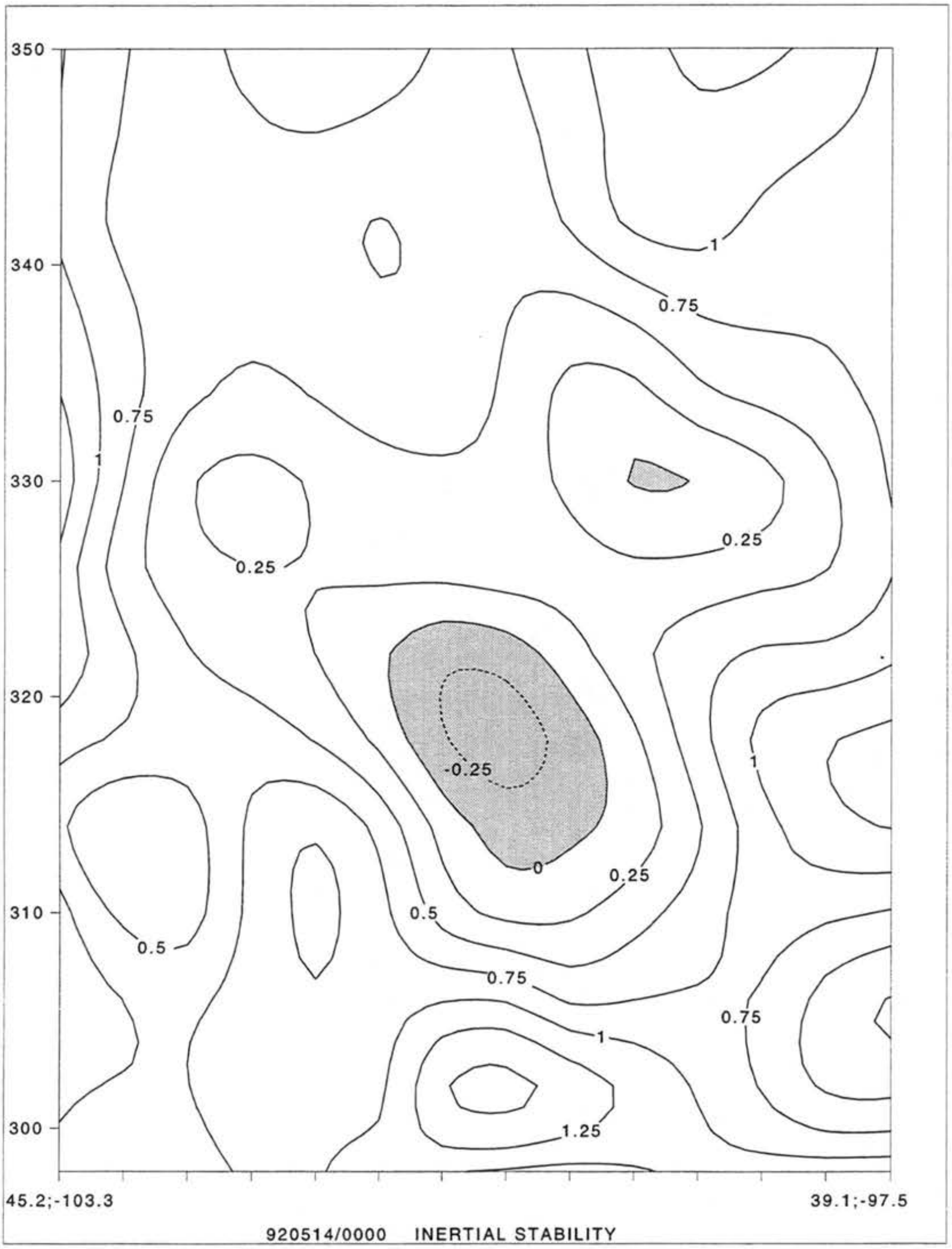

Figure 34. Vertical cross section showing the inertial stability. Cross section extends from northwest North Dakota to northeast Kansas. Contours every 0.25. Positive lines are solid; negative values are dashed shaded.

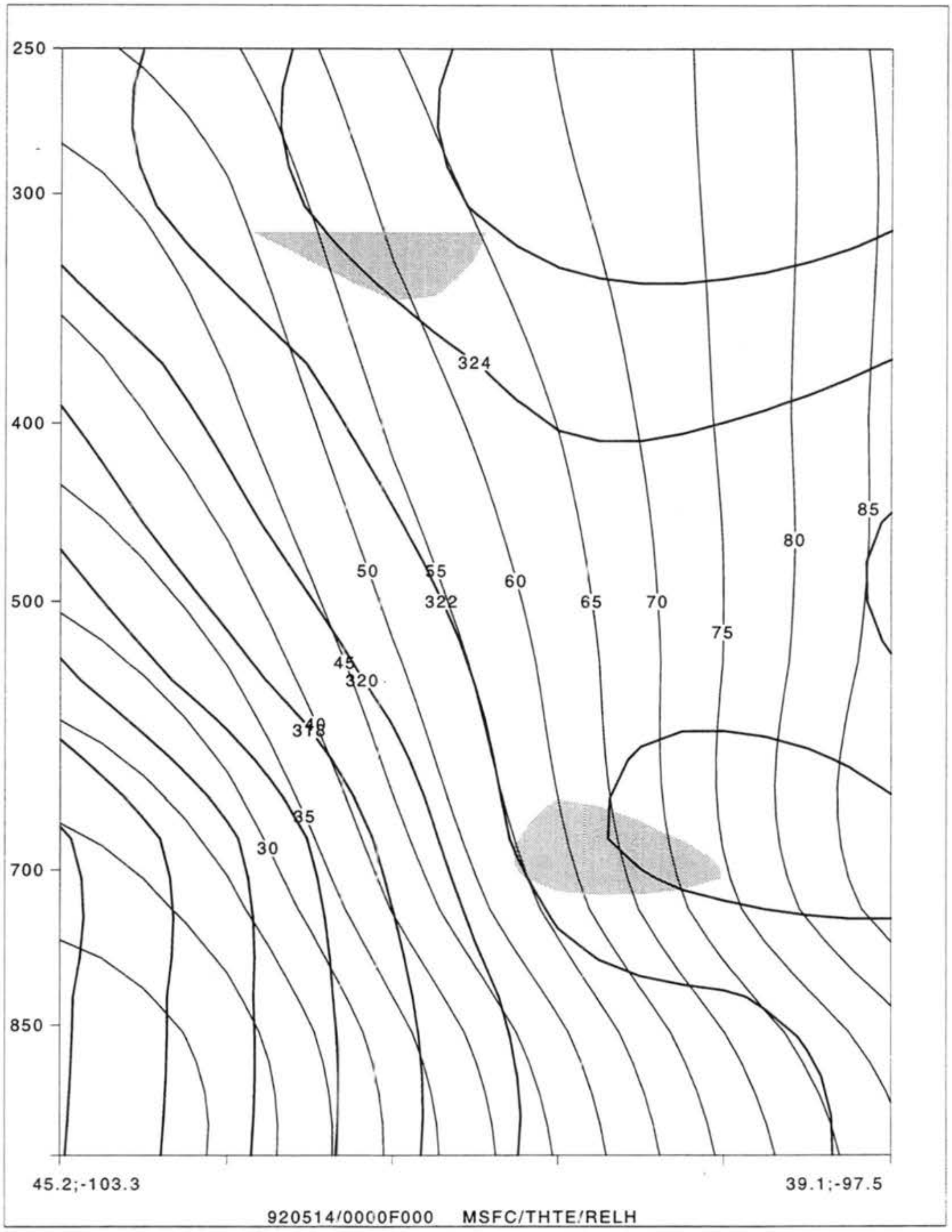

Figure 35. Vertical cross section showing momentum surfaces (contour interval 5 m s^{-1}) and equivalent potential temperature, θ_e (contour interval is 2 K). Cross section is the same as in Fig. 34.

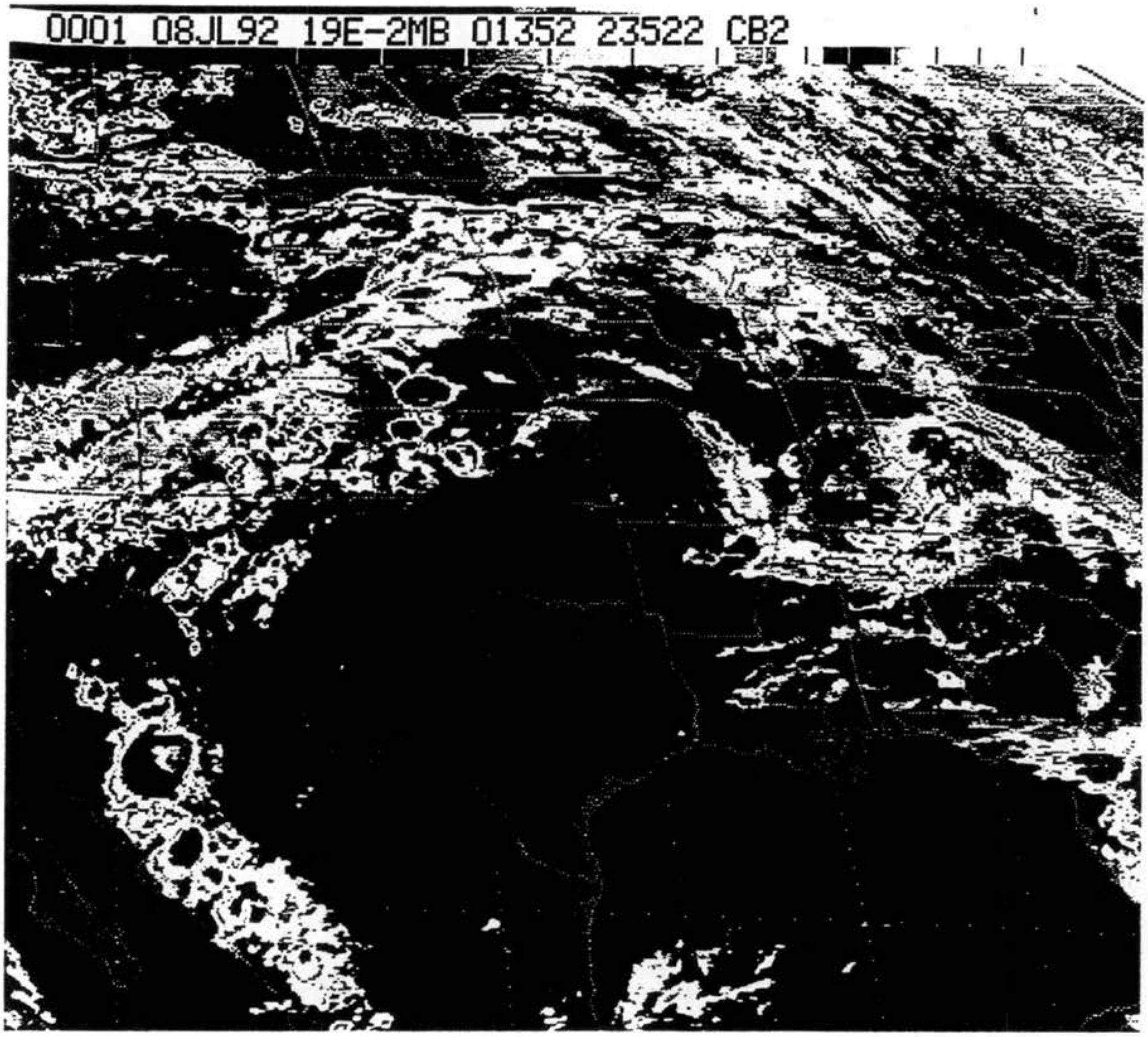

Figure 36. Satellite imagery for 7–8 July, 1992, at a) 0001 and b) 0601 UTC.

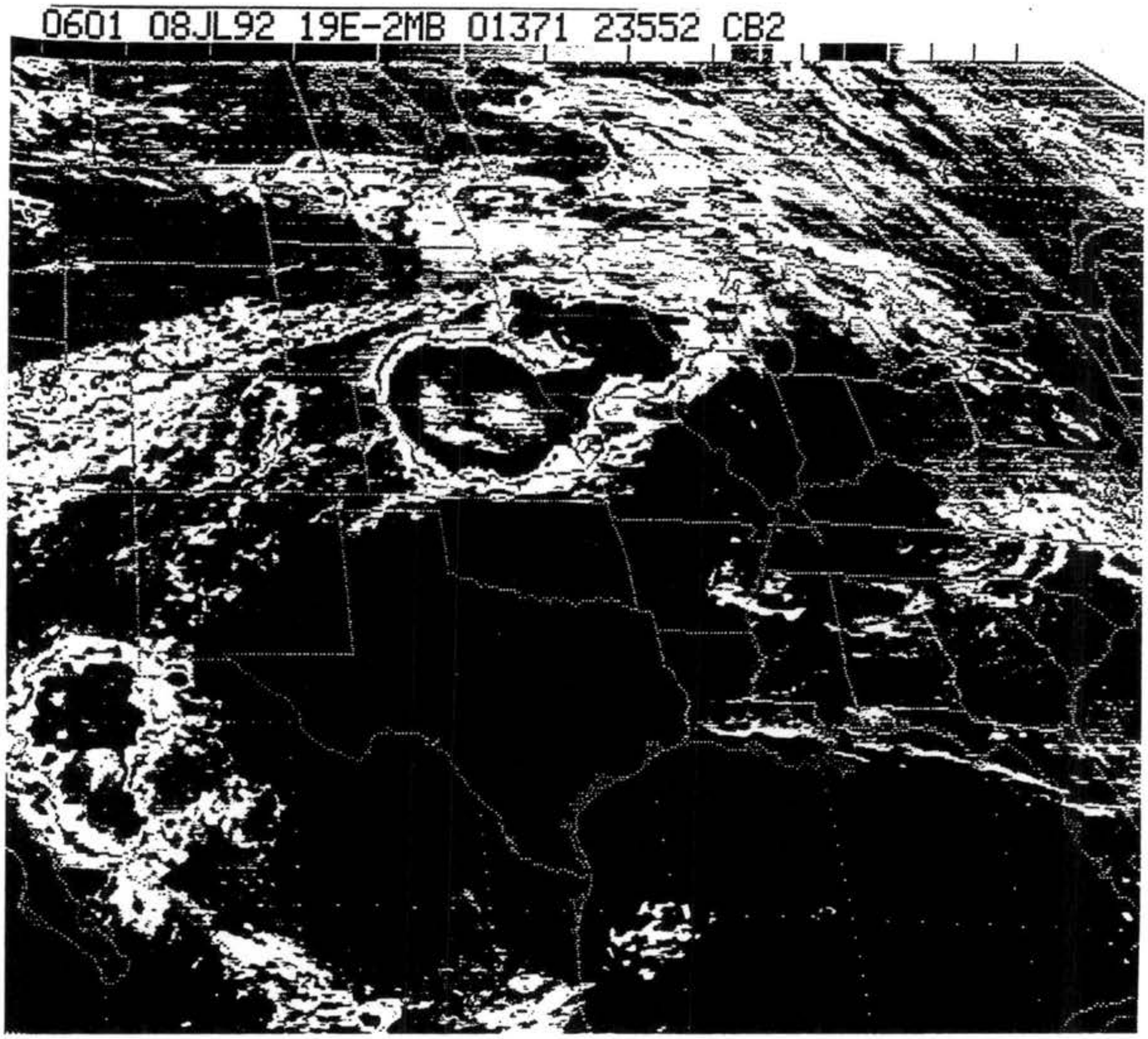

Figure 36. (Continued)

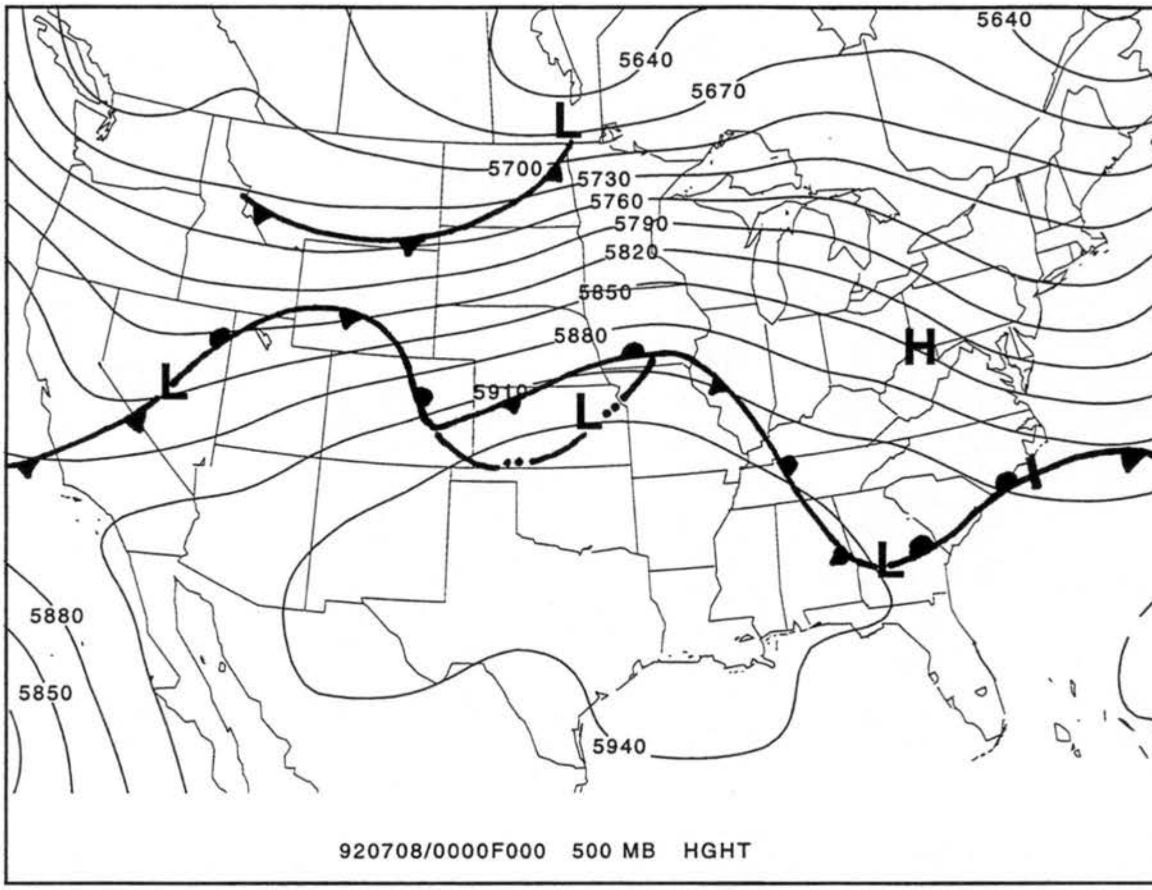

Figure 37. Composite chart for 0000 UTC on 8 July 1992 depicting conditions at 500 mb with surface fronts and pressure centers superimposed. 500-mb height contours every 30 m. High and low pressure centers marked with "H" and "L," respectively. Surface boundaries use standard convention for cold, warm and occluded fronts, and the dry line.

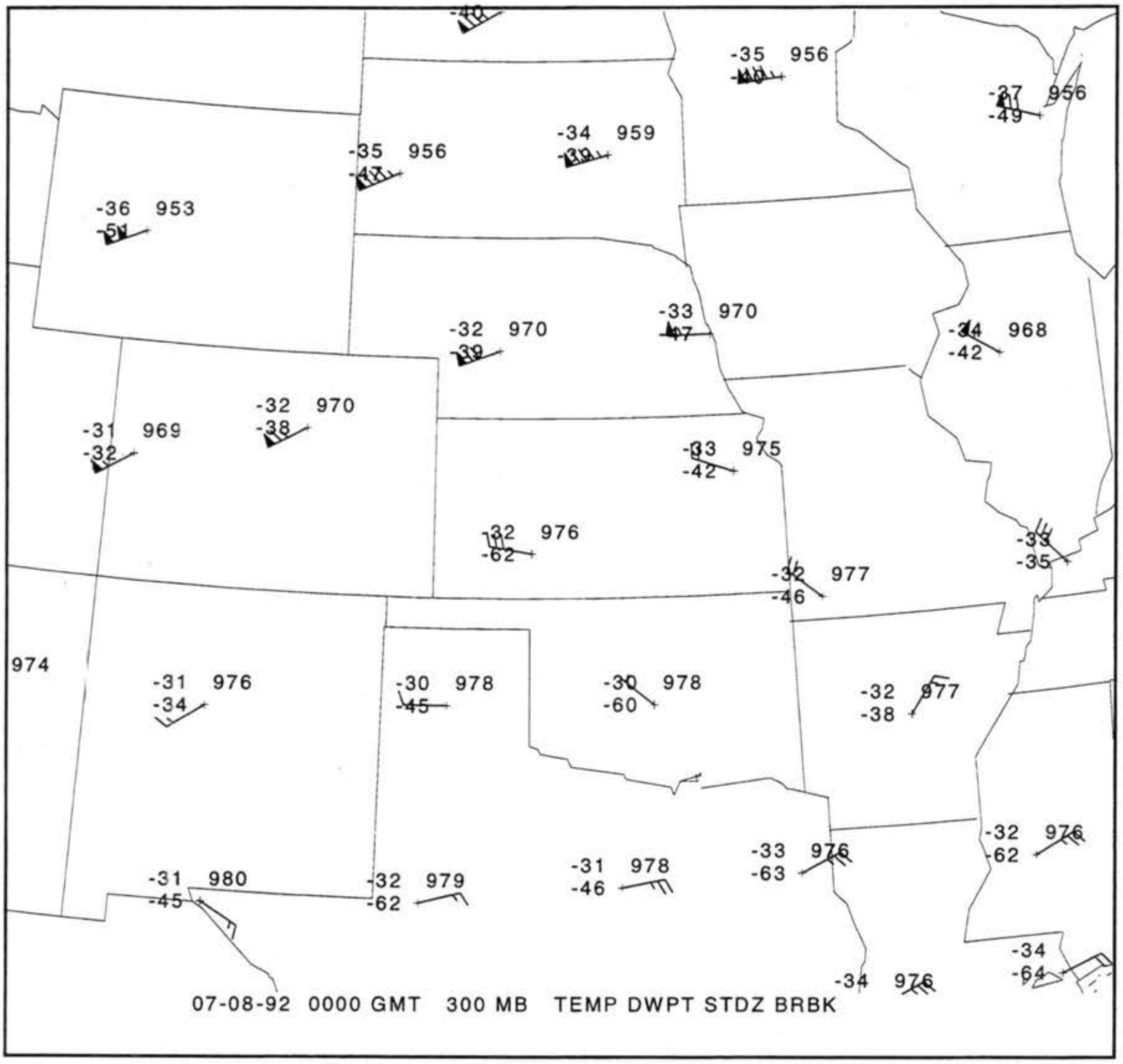

Figure 38. Plot of temperature, dewpoint, heights, and winds on the 300-mb pressure surface at 0000 UTC on 8 July 1992.

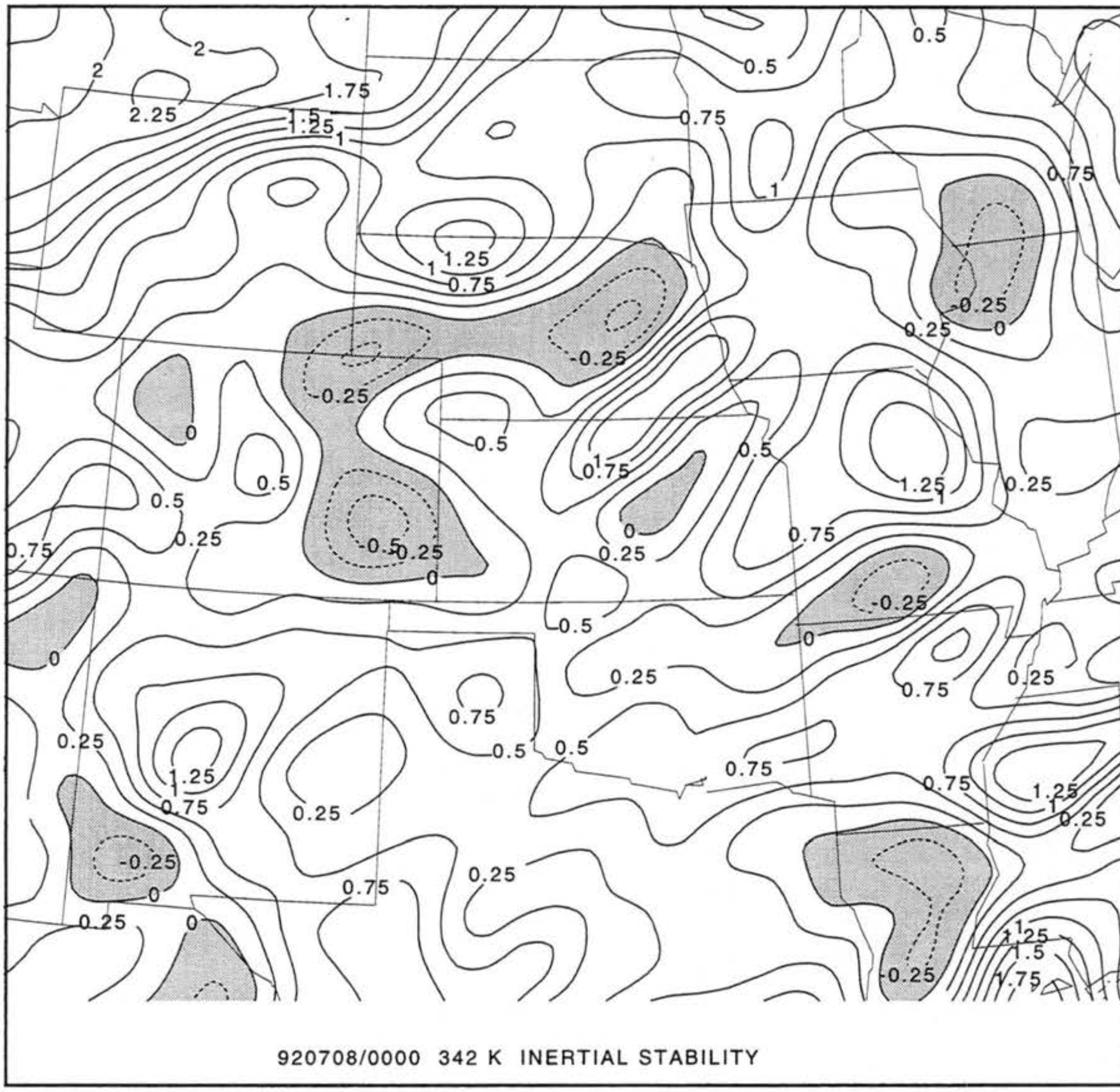

Figure 39. Inertial stability parameter on the 342 K isentropic surface at 0000 UTC on 8 July 1992. Contour interval is 0.25. Positive values solid; negative values dashed and are shaded.

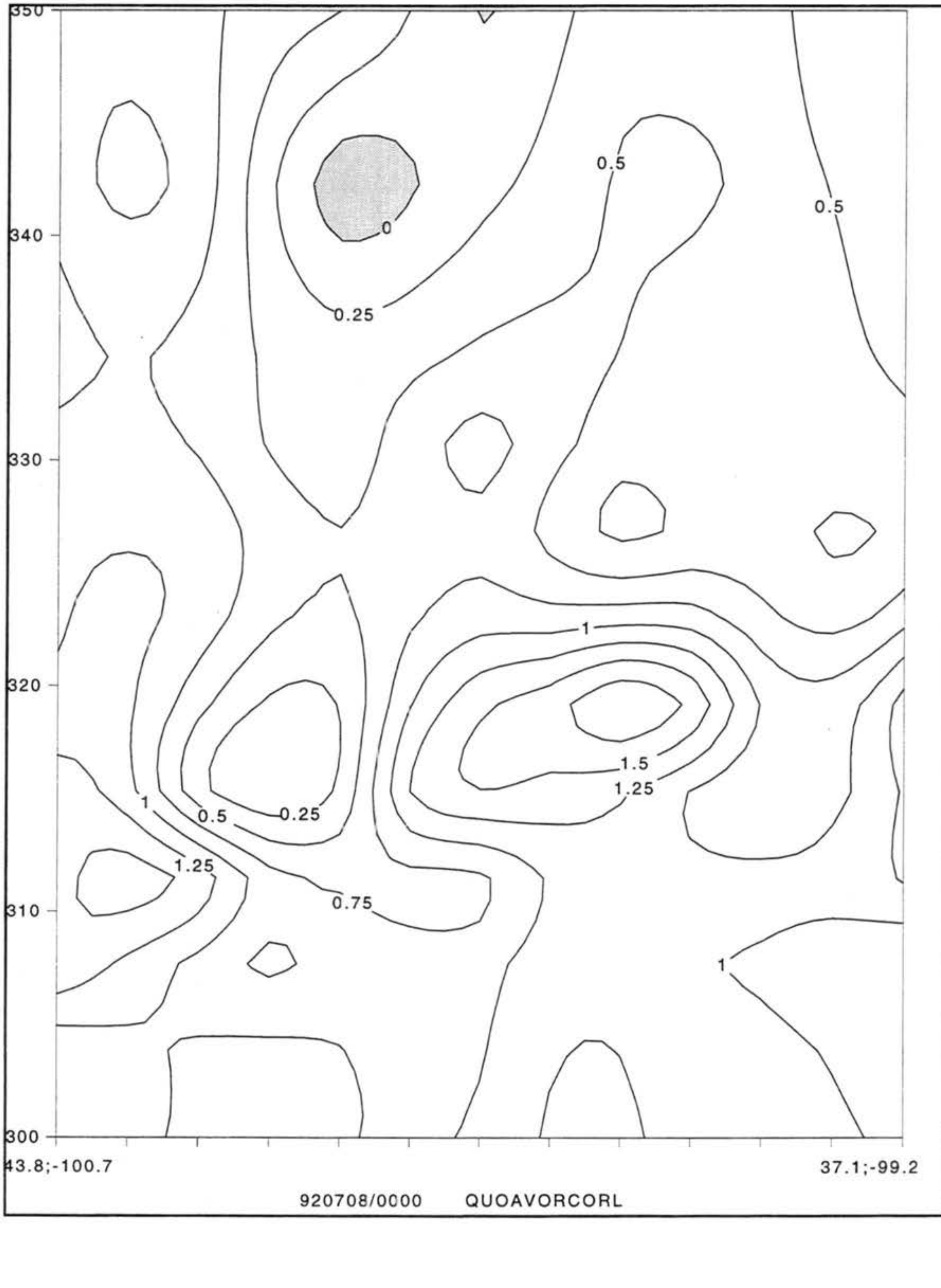

Figure 40. Cross section of the inertial stability parameter from northern Nebraska to southern Kansas. Contours every 0.25. Positive values are solid; negative values are dashed and shaded.

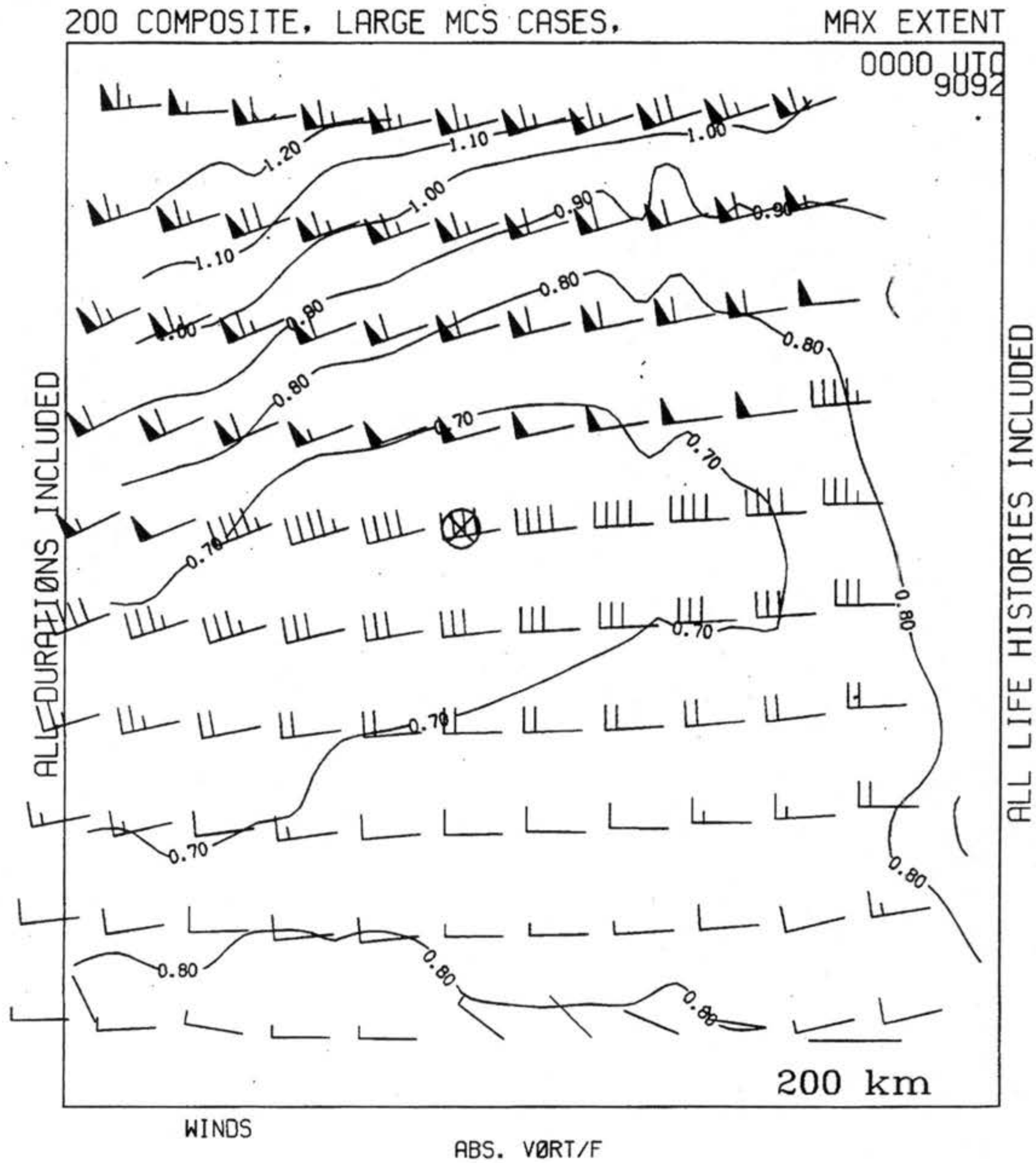

Figure 41. Composite of 38 events depicting the large scale environment associated with the development of large MCS at 200 mb. Contours represent inertial stability; contours every 0.10. Figure courtesy of John Augustine (NOAA/NSSL)

4. RAMS NUMERICAL MODEL

In this chapter, the results of a numerical modeling study are presented. The intent was to explore the importance of parameters such as Coriolis, strength of the jet and its associated anticyclonic shear, and heating on the evolution of mesoscale convective systems and the upper-level divergent outflow. A series of model simulations were run with variations of these parameters and their implications are discussed. The chapter starts with a description of the model, development of equations, and the initialization.

4.1. Model description

The model used in this study was the Regional Atmospheric Modeling System (RAMS) developed at Colorado State University. RAMS is a nonhydrostatic, primitive equation model and has been described extensively in the literature, most recently by Pielke et al. (1992). A general description of the model is given here and follows the discussion given by Bader (1987), but the reader is referred to the original papers for complete documentation of the model.

4.1.1. Theoretical development of model equations

RAMS is a modeling system combining features of a non-hydrostatic cloud model (Cotton et al., 1982; Tripoli and Cotton 1982; Tripoli and Cotton 1989a) and two hydrostatic mesoscale models (Pielke 1974; Mahrer and Pielke 1977; McNider and Pielke 1981; McCumber and Pielke 1981; Tremback et al.

1985). The resultant code is highly flexible and modular with many possible configurations.

The non-hydrostatic version of RAMS was used in which u, v, and w wind components, ice and liquid water equivalent potential temperature, dry air density, total water mixing ratio, and the mixing ratios of the various water variables are predicted. From these variables, pressure, potential temperature, temperature, vapor mixing ratio and cloud water mixing ratio are diagnosed.

One or more sets of nested and movable grids can be specified within a larger-scale grid.

The model equations are formulated to describe perturbations about a dry and hydrostatic base state. Finite-difference forms of the momentum equation, thermodynamic energy equation, and a combination of the ideal gas relation and continuity equation are used to predict velocity, potential temperature and normalized pressure. Absolute pressure and temperature are computed from diagnostic relationships involving the predicted quantities. Following the notation of Tripoli and Cotton (1982) and others, any variable A can be decomposed as

$$A = \overline{A} + A'' , \tag{9a}$$

where the overbar represents an ensemble-average value resolvable on the time and space scales of the model simulation, and the double prime denotes an unresolvable turbulent fluctuation about this average. The mean value can be further decomposed as

$$\overline{A} = A_0(z) + \overline{A'} , \tag{9b}$$

where $A_0(z)$ is the temporally and horizontally invariant base state and $\overline{A}'$ is the resolvable deviation from this state.

Potential temperature is used as the thermodynamic variable and is defined by Poisson's equation,

$$\theta = \frac{T}{\pi}, \tag{10}$$

in which θ is the potential temperature, T is the temperature, and π is the normalized pressure defined by

$$\pi = \left(\frac{p}{p_{00}}\right)^{R/c_p}. \tag{11}$$

Here, p is absolute pressure, the constant p_{00} is a reference pressure, usually taken to be 1000 mb, and R and c_p are the gas constant and constant pressure specific heat of dry air, respectively. Using (11), the ideal gas relation,

$$p = \rho R T, \tag{12a}$$

can be rewritten as

$$\pi = \left(\frac{R}{p_{00}}\rho\theta\right)^{R/c_v}, \tag{12b}$$

where ρ is the dry air density and c_v is the constant volume specific heat of dry air that is related to c_p and R by $c_p = c_v + R$. The base state is assumed to obey both (12b) and the hydrostatic relation and is therefore defined by

$$\pi_0 = \left(\frac{R}{p_{00}} \rho_0 \theta_0 \right)^{R/c_v}, \tag{13}$$

$$\frac{\partial \pi_0}{\partial z} = -\frac{g}{\left(c_p \theta_0\right)}, \tag{14}$$

where π_0, ρ_0, and θ_0 are the base state pressure, density and potential temperature, respectively.

The formulation of the elastic pressure equation is described in detail by Klemp and Wilhelmson (1978). Summarizing their development, the time derivative of (12b) is combined with the compressible continuity equation,

$$\frac{\partial \rho}{\partial t} + \frac{\partial}{\partial x_j}\left(\rho u_j\right) = 0, \tag{15}$$

then approximated to yield

$$\frac{\partial \overline{\pi}}{\partial t} + \frac{R\pi_0}{c_v \rho_0 \theta_0} \frac{\partial}{\partial x_j}\left(\rho_0 \theta_0 \overline{u}_j\right) = 0. \tag{16}$$

Justification for the approximation is made in the original paper, but basically they allow for mean mass adjustments to domain-averaged temperature changes that do not affect the dynamics in model simulations. The momentum equation is

$$\frac{\partial \overline{u}_i}{\partial t}+\frac{c_p\theta_0\partial\overline{\pi}'}{\partial x_i}=g\frac{\overline{\theta}'}{\theta_0}\delta_{i3}-\frac{1}{\rho_0}\frac{\partial}{\partial x_j}\left(\rho_0\overline{u}_i\overline{u}_j\right)+\frac{\overline{u}_i}{\rho_0}\frac{\partial}{\partial x_j}\left(\rho_0\overline{u}_j\right)-\frac{\partial}{\partial x_j}\overline{u_j''u_j''}, \tag{17}$$

where u_i is the ith component of the velocity vector, g is the gravitational acceleration and δ_{i3} is the Kronecker delta function. Completing the basic model equation set, the dry thermodynamic energy equation is described by

$$\frac{\partial\overline{\theta}}{\partial t}=\frac{1}{\rho_0}\frac{\partial}{\partial x_j}\left(\rho_0\overline{u}_j\overline{\theta}\right)+\frac{\overline{\theta}}{\rho_0}\frac{\partial}{\partial x_j}\left(\rho_0\overline{u}_j\right)-\frac{\partial}{\partial x_j}\left(\overline{\theta''u''}\right). \tag{18}$$

The terms in the pressure equation and the left-hand side of the momentum equation comprise the acoustically active or elastic terms capable of propagating sound waves. The terms on the right-hand side of (17) and the thermodynamic energy equations describe the nonacoustic processes, such as advection and diffusion, which are active on the longer gravity-wave time scale.

The turbulent flux terms are parameterized using an eddy viscosity closure scheme in which the mixing coefficients are determined from prognostic turbulent kinetic energy (TKE) equations formulated by Yamada (1983). This approach offers some of the advantages afforded by higher-order closure schemes (Mellor and Yamada 1982) without a great increase in computational expense. Unlike fully diagnostic closure schemes, the effects of inhomogeneous and nonstationary turbulence fields can be included.

The inclusion of uneven topography is accomplished using a terrain-following coordinate system developed by Gal-Chen and Sommerville (1975) and extended by Clark (1977). Known as a "sigma-z" system, it results from the transformation

$$x^* = x, \tag{19a}$$

$$y^* = y, \tag{19b}$$

$$z^* = \frac{z - z_s(x,y)}{H - z_s(x,y)} H, \tag{19c}$$

where quantities with an asterisk represent the transformed coordinates and those without an asterisk are Cartesian coordinates, z_s is the height of the surface and H is the height above the model reference level of the model domain top. Clark (1977) and Tripoli and Cotton (1982) describe the implementation of the coordinate transformation functions in more detail. Besides the terrain-following topography, a simple Cartesian vertical coordinate is available. The Cartesian coordinate was used in all the simulations described here.

4.1.2. Finite differences

The model equations were integrated on the Arakawa C grid (Arakawa and Lamb 1981), a staggered mesh described by Tripoli and Cotton (1982). This type of grid centers scalars in each grid box with velocity components defined normal to the sides. When used with standard fourth-order advection, this system is very effective at properly describing gravity wave propagation. A time-differencing scheme described by Klemp and Wilhelmson (1978) was used to integrate separately the acoustic and nonacoustic terms in the predictive equations. After the nonacoustic terms were integrated using a forward-backward time difference scheme, the acoustically active terms were integrated for a specified number of smaller Δt_s time steps using a semiimplicit scheme to complete the integration. An Asselin filter was then employed to prevent solution separation. The time steps for both the acoustic and nonacoustic tendency computations were chosen to avoid exceeding linear stability criteria. A more detailed description of the finite difference methods can be found in Tripoli and Cotton (1982) and Klemp and Wilhelmson (1978).

4.1.3. Model domain

All the simulations discussed here used a vertical domain of 40 grid points with 600 m resolution, giving an upper limit of ~23 km. The horizontal domain had 200 points with 5 km resolution, resulting in a cross section of 1000 km. The vertical domain was deep enough to capture the necessary wind and thermal structure required for the simulation and included the tropopause and a portion of the lower stratosphere; the horizontal domain was large enough to contain the jet, heating function, and a large area buffering these features from the lateral boundaries. The cross section was oriented east-west; this is the standard configuration for 2-D planes in RAMS. This configuration is the equivalent of a north-south cross section on an *f*-plane (constant Coriolis). Accordingly, the cross section can be viewed in either framework and will sometimes be referred to as a "north-south" cross section in the following discussions.

4.1.4. Boundary conditions

RAMS has four choices for the upper boundary condition, two of which are appropriate for non-hydrostatic simulations. The non-hydrostatic rigid wall on top was selected for the upper boundary condition. This option constrains the vertical velocity to be zero at the lid. This condition is simple, but has the disadvantage of causing strong reflection of upwardly propagating gravity waves. Consequently, a Rayleigh friction absorbing layer was used in the top six levels. The friction layer is designed to absorb gravity waves approaching the lid, sufficiently damping them before and after reflection so that they are effectively eliminated. Lateral boundaries use the Klemp-Wilhelmson condition in which the normal velocity component specified at the lateral boundary is effectively advected from the interior assuming a propagation speed (intended to be similar to a dominant gravity wave phase speed) specified in the input stream. In all simulations, the value was set to 20 m s^{-1}.

4.1.5. Initialization

The model was initialized using a typical midwestern springtime sounding (a slightly smoothed version of the sounding at 0000 UTC on 13 May 1985 at Oklahoma City, Oklahoma; see Fig. 42) prior to a large convective event. RAMS requires that 2-D simulations use a horizontally homogeneous initialization. To produce the necessary horizontal and vertical gradients in wind, additional code was added to the model to produce a jet core centered just below the tropopause (vertically) and near the center of the domain (horizontally). In RAMS, the Coriolis force does not act on base state winds in 2-D simulations because the horizontally homogeneous initialization does not have a balance of all forces. Since the Coriolis term was an important aspect of this simulation, it was necessary to create the jet as a perturbation on the base state winds. This was accomplished by starting the simulation and activating a forcing function for the wind. The function had the form

$$F_v = V_0 \, e^{-\alpha^2 (x - x_0)^2} e^{-\beta^2 (z - z_0)^2} , \tag{20}$$

where V_0 is the amplitude of the forced wind, and α and β are inverse half widths in the horizontal and vertical. This forcing function was allowed to perturb the base state for 72 h to allow slow increases in the wind and keep the wind and temperature responses in approximate thermal wind balance. After the initial 72 h spin-up period, the simulation was suspended. The results were saved in a history file and used as initial conditions for subsequent simulations.

The remaining part of the initialization concerns the heating. A forcing function was used that had the form

$$F_H = H_0 \, e^{-\alpha^2 (x-x_0)^2} e^{-\beta^2 (z-z_0)^2}, \tag{21}$$

where H_0 [°C h^{-1}] is the amplitude of the forced heating, and α and β are inverse half widths in the horizontal and vertical. The forcing function is similar to the function employed by Hertenstein and Schubert (1991) in their study of potential vorticity anomalies with squall lines. This forcing function was allowed to increase from zero to full strength over a period of one hour, approximating the actual heating taking place in convection over a meso-β-scale domain. The actual increase was non-linear and was of the form

$$F_{H*} = F_H \sin^2\left(\frac{\pi}{2}\delta t\right), \tag{22}$$

where F_{H*} is the "ramped" value for the heating function, t is the time in seconds and δ was set to the inverse of the spinup time; e.g., (3600 s)$^{-1}$ for a one-hour spinup. The values of α and β were chosen so that the heating had mesoscale dimensions in the horizontal and peaked at around 7 km in the vertical.

4.2. Discussion of model configuration

The RAMS numerical mesoscale model is capable of simulating many features of the atmosphere using both simple and complex formulations of relevant parameters. Although it would have been possible to perform the simulations discussed here using 3D grids, full microphysics, radiation, complex surface boundaries, and other features, the decision was made to proceed with the simplest configuration possible. All simulations were done in 2D, no moist convection was allowed, and both short- and long-wave radiation schemes were turned off. Although this configuration does not adequately simulate the real atmosphere, it has the benefit of isolating the effect of inertial instability on the develoment of enhanced divergence aloft and secondary circulations necessary for the upscale evolution of convection into mesoscale convective systems. Previous modeling results have shown the importance of diabatic effects from latent heat release, the dispersion of ice crystals from the primary convection into the stratiform region, the role of trapped gravity waves under a radiating and stabilizing anvil top, surface fluxes of moisture and temperature, and a myriad of other features. The work presented here is designed to isolate the fundamental role of inertial instability on the development of enhanced divergent flow and secondary circulations without the influence of these other processes.

4.3. Discussion of heating rates

It is useful at this point to discuss the heating rates applied in the simulations. Although these are dry simulations, it is convenient to express these heating rates in the form of rainfall rates to determine whether the values used here closely approximate what we might find in the atmosphere.

Following Yanai et al. (1973) and Wu (1993), the heat budget equation suitable for observational data or numerical models can be written as

$$\begin{aligned} Q_1 &\equiv \frac{\partial \bar{s}}{\partial t} + \mathbf{v}\cdot\nabla\bar{s} + \bar{\omega}\frac{\partial \bar{s}}{\partial p} \\ &= Q_R + L(\bar{c}-\bar{e}) - \nabla\cdot\overline{s'\mathbf{v}'} - \frac{\partial}{\partial p}\overline{s'\omega'} \end{aligned} \tag{23}$$

where the $\overline{(\ )}$ denotes resolvable components, that is, the running horizontal average, and a prime $(\ )'$ expresses unresolvable components, that is, the deviation from the horizontal average. $s = c_p T + gz$ is the dry static energy, c_p the specific heat of air at constant pressure, T the temperature, g the acceleration of gravity, $\mathbf{v}$ the horizontal velocity, ω the vertical p-velocity, Q_R the radiative heating rate, L the latent heat of condensation, and c and e are the rates of condensation and evaporation of cloud water per unit mass of air.

Integrating (23) from p_T (pressure at the cloud top or tropopause) to p_S (pressure at the surface), we obtain

$$\langle Q_1\rangle = \langle Q_R\rangle + LP + S - \left\langle \nabla\cdot\overline{s'\mathbf{v}'}\right\rangle \tag{24}$$

where

$$\langle(\ )\rangle \equiv \frac{1}{g}\int_{p_T}^{p_S}(\ )dp \tag{25}$$

P is the rate of precipitation, and S is the rate of sensible heat flux from the surface. If we assume for the purposes of this exercise that the sensible heat flux, the radiative heating rate, and the moisture flux term are negligible or zero, then (24) simplifies to

$$P = \langle Q_1 \rangle L^{-1} \tag{26}$$

or, using (25)

$$P = L^{-1}\left(\frac{1}{g}\int_{p_T}^{p_s}(Q_1)dp\right) \tag{27}$$

If we assume a cloud/heating depth of 600 mb, and let g = 9.8 m s^{-1} and L = 2.5X10^{6} J kg^{-1}, we obtain precipitation rates of 0.25, 0.74, and 1.23 cm h^{-1} for heating rates of 1, 3, and 5°C h^{-1}, respectively. These precipitation rates are small if we consider convective precipitation, but are typical values for an average mesoscale precipitation rate over large areas (Churchill and Houze 1984; Leary 1984; McAnelly and Cotton 1986, 1989; Johnson and Hamilton 1988)

4.4. Discussion of 2-D vs. 3-D

Another issue that needs to be addressed is the applicability of a 2-D simulation, as opposed to a full 3-D simulation. Note that while the simulations occur in the x–z (y–z) plane[7], the wind shear is in the *meridional* (*zonal*) direction, perpendicular to this plane such that the ambient meridional (zonal) wind is parallel to the axes of the circulations that develop. This is different from many two-dimensional simulations in which

[7]As discussed earlier, the domain of these simulations are oriented east-west, but can also be described as a north-south domain on an f-plane.

the wind blows in the plane of the simulations (e.g., Thorpe et al. 1982; Rotunno et al. 1988; Tripoli and Cotton 1989a; Fovell 1991). The geometry is set up this way so that the combined dynamical effects of baroclinic shear and Coriolis rotation can be studied. This geometry is essentially the same as that employed by Seman (1990, 1994) in his study of Conv-SI.

As shown by Raymond (1990), the wind can be decomposed into rotational and divergent components; i.e., an irrotational velocity potential, φ, and a non-divergent stream function, ψ. Then, the Cartesian coordinates of wind can be written as

$$\begin{aligned} u &= -\frac{\partial \psi}{\partial y} - \frac{\partial \phi}{\partial x} \\ v &= -\frac{\partial \psi}{\partial x} - \frac{\partial \phi}{\partial y} \end{aligned} \tag{28}$$

and the vorticity and divergence can be written as

$$\begin{aligned} \nabla^2 \psi &= \zeta_z \equiv \left(\partial v/\partial x - \partial u/\partial y\right) \\ \nabla^2 \phi &= -\delta \equiv -\left(\partial u/\partial x + \partial v/\partial y\right). \end{aligned} \tag{29}$$

If we restrict ourselves to working in an x–z domain, as in a 2-D simulation in RAMS, we can rewrite (29) as

$$\begin{aligned} \nabla^2 \psi &= \zeta_z \equiv \partial v/\partial x \\ \nabla^2 \phi &= -\delta \equiv -\partial u/\partial x. \end{aligned} \tag{30}$$

As can be clearly seen, the rotational component of the wind is completely described by the v-component, and the divergence is completely described by the u-component of the wind.

Because we are investigating the possibility that inertial instability can increase the cross-stream flow, and we are designing our experiment so that the jet flow is into the 2-D domain, the only component of divergence that should be affected by changes in the inertial stability is in the east-west direction; i.e., the cross-stream direction. Thus, the 2-D formulation greatly simplifies the problem while retaining the essential information for analysis and interpretation.

4.5. Preliminary experiments

Before discussing the results of the experiments described below it is useful to examine some preliminary simulations that were run to determine the optimal means of setting up the jet and heating functions.

Early attempts at simulating the jet simply initialized a full-strength jet in the domain. Because this initialization becomes part of the model's base state, no Coriolis force acts on these winds, leading to unrealistic results. A solution was to use the same function and impose it as a forcing function (acceleration) on the wind field, allowing it to perturb the base state wind field. Further testing revealed that reasonable winds resulted if the perturbation was allowed to act on the base state for a duration of about 72 h. Shorter time periods resulted in unreasonable "secondary" circulations to adjust the mass field. The longer spin-up times still had adjustment circulations present, but the amplitude was very small and was determined not to adversely affect the simulations.

The preliminary simulations were also used to fine tune the vertical placement of the jet so that it had a maximum value just below the tropopause. Comparisons with jet stream studies (e.g., Keyser and Shapiro 1986) indicate that this is the appropriate location for this feature. This placement permitted the best thermal adjustment of the isentropes near the jet during the spinup process.

Considerable effort was made to determine an appropriate strength for the jet and the resulting values of inertial instability. Not suprisingly, it was found that as long as the absolute vorticity, η, remained positive, the jet was stable with time. On the other hand, if the absolute vorticity was negative, an adjustment process began to operate in an attempt to reduce the instability. This adjustment process manifested itself as a vertically-stacked set of strong, horizontal accelerations having a spacing of $2\Delta z$ and vertical wavelengths of $4\Delta z$. This rapid adjustment of inertial instabilities on the smallest scales has been described by Stevens and Cielsielski (1986), who showed that the shallow modes should grow the fastest. A series of sensitivity experiments indicated that for large jet values (and large degrees of inertial instability with values of $\alpha = \eta_l' f \approx -0.6$) the adjustment process would occur even before the 72-h spinup process was complete. Moderate jets ($\alpha \approx -0.4$) resulted in an adjustment process occuring approximately four hours after the spinup process was complete. Weaker jets ($\alpha \approx -0.2$) did not start the adjustment process until after the six hour simulations were complete. The simulation jet strengths were selected so that $\alpha \geq -0.2$, resulting in environments that were "weakly inertially unstable" to "weakly inertially stable". It should be noted that the qualitative results of both the weakly stable and weakly unstable configurations were similar, and differed only in magnitude.

Another set of preliminary simulations varied the horizontal locations of both the jet core and the heating. Some variations included [–0.50*X*; +0.50*X*], [–0.25*X*; +0.25*X*], and [–0.25*X*; +0.0125*X*] for the horizontal location of the center of the jet and heating, respectively[8]. This simulation demonstrated that in order for the vertical motions and horizontal divergence to take advantage of the mesoscale instability associated with the jet, they must occur within or immediately adjacent to the region of the instability. This result was not an unexpected one, but was a necessary step in the further development of simulations. The remaining simulations used a jet placement at $-0.25X$ (-125.0 km) and a heating profile placement at $+0.125X$ ($+62.5$ km). Once the optimal separation was determined, additional simulations in which other parameters were varied were carried out.

It is also important to point out that the placement of the jet and heating profiles near the center of the domain allows a large region between these features and the lateral boundaries. This is useful for preventing any undesirable boundary effects from contaminating the simulation.

4.6. Modeling experiments

As discussed earlier, the RAMS model experiments were executed in a two-dimensional domain on an f-plane to simplify the understanding of the results. To provide a baseline for the comparison of results, a control experiment without a jet core was run. Next, the model was run with different jet strengths to test the sensitivity of the response to the strength of the inertial instability (as suggested earlier in Chapter 2, point (b)), and with different strength heating functions. Additional experiments were conducted to determine the role of (1) the Coriolis force by varying the latitude, and (2) varying degrees of convective instability.

---

[8]The RAMS model refers to the left and right hand edges of the domain as $-X$ and $+X$, respectively, and 0 is the center.

Certain parameters were fixed for all simulations and are shown in Table 1; variable parameters are listed in Table 2.

Table 1. Values for fixed parameters used in RAMS.

• Horizontal half width of the jet (α):	160000 m^{-1}
• Vertical half width of the jet (β):	4000 m^{-1}
• Horizontal half width of the heating (α):	40000 m^{-1}
• Vertical half width of the heating (β):	3000 m^{-1}
• Spinup time for the jet:	72 h
• Spinup time for the heating:	1 h
• Horizontal resolution:	200 points; 5 km
• Vertical resolution:	40 points; 600 m

Table 2. Characteristic values for the jet and heating profiles and variable latitudes used in the model simulations.

Simulation	Wind V_0 (m s^{-1})	Heating H_0 (°C h^{-1})	Latitude ϕ	Experiments/Comments
1a–c	0	1; 3; 5	40	Control experiments
1d–f	0	1; 3; 5	25	
2a–c	10	1; 3; 5	40	Moderate inertial stability
2d–f	10	1; 3; 5	25	
3a–c	20	1; 3; 5	40	Weak inertial stability
3d–f	20	1; 3; 5	25	
4a–c	30	1; 3; 5	40	Weak inertial instability
4d–f	30	1; 3; 5	25	
5 (WK)	30	1; 3; 5	40	Increased vertical stability
6 (WKV)	30	1; 3; 5	40	Vertical shear
7	30	1; 3; 5	40	Grid resolution

As can be immediately seen from Table 2, there are four wind speeds, three heating rates, and two latitudes being tested, giving a total of 24 simulations. An additional three experiments (5–7) were conducted as sensitivity tests.

4.7. Simulation 1

The first simulation imposes the heating function without any jet in the domain (Fig. 43). This simulation is the control experiment to which the other simulations will be compared. To ensure that the simulations are as similar as possible, this simulation was initialized in the same manner as the ones that do contain a [non-zero] jet. Specifically, the model is initialized with a base state of no winds anywhere in the domain. A forcing function to generate the jet is allowed to operate for 72 h of simulation time. The value of V_0 for the wind is set to zero in the control case. With this value, no jet develops, obviously, as the model steps forward in time. After 72 h, the simulation is suspended. The model is then restarted and progresses forward six hours with the heating function turned on. Simulations 1a–c use heating profiles of 1, 3, and 5°C h^{-1}, respectively.

4.7.1. Simulation 1a–c

Our attention will focus on the second of these three simulations, which has a heating rate of 3°C h^{-1}. Figure 44 shows the field of potential temperature, θ, after 72 hours. Because no forcing has been applied, the field has not been adjusted and remains horizontally homogeneous. Both the u- and v-components of the wind (hereafter referred to simply as u- and v-winds) are zero. After 1 h (total simulation time is now 73 h; all references to model simulation time will be relative to the restart time at 72 h), weak horizontal winds have developed in response to the vertical motions from the forced heating. The u-winds have maximum speeds of about ±1.25 m s^{-1}, and are diverging and symmetric with respect to the (vertical) axis of maximum heating. The v-winds have begun to respond also, have values less than 0.2 m s^{-1}, and are already showing signs of developing anticyclonic flow aloft.

After 2 h, the potential temperature field is just beginning to show the influence of the localized heating, although the changes are still small this early in the simulation. Figure 45 shows the vertical velocity, w. There are two areas of descent displaced laterally from the heating region. This descent is probably a result of the propagation of the lowest mode gravity wave away from the heat source. The u-winds have continued to increase in strength and have peak values of ±3.5 m s^{-1}. This increase in speed continues and after 3 h has peak values of ±5.0 m s^{-1} (Fig. 46). As before, the u-winds are divergent and symmetric about the vertical axis of the heating. Jumping ahead to the end of the simulation at 6 h, the u-winds (Fig. 47) have now attained speeds of close to ±6.0 m s^{-1}. The v-winds (Fig. 48) have peaked at ±6.0 m s^{-1} and are directed into the domain on the left side of the heating, and out of the domain on the other side, clearly indicating the development of a anticyclone above the heating. Figure 49 shows the total vorticity, $(\zeta + f)$, produced locally by the rotational component of the wind (the v-wind, in this case). Two areas of negative vorticity exist adjacent to the top of the updraft and are related to the generation of the v-winds that are displaced laterally from the updraft core; outside this region, the vorticity is strongly positive. This *in situ* generation of negative absolute vorticity has been discussed by Seman (1994), Raymond (1992) and others. The presence of this inertially unstable region can lead to mesoscale instabilities described by Seman (1991) and referred to as Convective-Symmetric Instability (Conv-SI). If the environment is baroclinic with strong vertical shear of the wind, then the atmosphere may be unstable to motions of saturated parcels along slantwise paths. Because there is no base state wind and no vertical shear in these simulations, this condition is not met. Nonetheless, it is important to recognize that the *in situ* development of the inertial instability, even in the absence of vertical wind shear and a baroclinic environment, can play an important role in the upscale evolution of MCSs.

The results discussed here are not unexpected; i.e., the development of an upper-level anticyclone, divergent flow aloft, and convergent flow in the lower and middle levels have been observed both in observational and modeling studies for many years. It is important, however, that this step be taken so that the remaining simulations have a benchmark for proper comparison.

The other two simulations (1a, 1c) use different heating rates. We should expect similar results to those in the first simulation, but because of the differences in heating, the strength of the responses will be different. Figure 50 shows the change in the strength of the u-winds as a function of time for each of the three heating rates. It is obvious that there is a stronger response for greater heating. As a consequence of stronger outflow and advection of the v-winds, the location of the rotational v-wind maximum is displaced farther from the heating core for stronger heating rates, resulting in the location of the vorticity pattern having similar displacements. This important result serves to emphasize how regions with stronger heating (and stronger outflow) can exert an influence over larger distances with increasing time, eventually attaining scales comparable to the Rossby radius of deformation.

4.7.2. Simulation 1d-f

Another set of three simulations was executed using no jet and the same values of heating (i.e., 1, 3, and 5°C h^{-1}). The difference in these simulations was the change in Coriolis. The original simulations used a latitude of 40° (f = 9.36X10^{-5}); the second set used a latitude of 25° (f= 6.16X10^{-5}). This reduces f to 66% of its original value. Consequently, the restoring force should be lessened in these simulations and divergence should be enhanced.

At the largest heating rate (5°C h^{-1}), and after 6 h, the divergent u-wind (not shown) is stronger at the lower latitude than the equivalent high latitude experiment (1c). The winds are ±9.3 m s^{-1}, compared to ±8.4 m s^{-1} at the higher latitude. This is a clear indication of how Coriolis acts to control the rate of cross-stream divergence. Also, the rotational v-wind was smaller by a factor of two for the low latitude case. Thus, at low latitudes, with a comparatively weaker restoring force, more of the wind is in the divergent component than the rotational component compared to the higher latitude case. There is less tendency, in the same amount of time, for the low latitude case to spin up an anticyclone, and greater tendency to have divergent flow. Since the inertial period is inversely proportional to f, it should take longer for geostrophic balance to occur. Certainly, it does not occur within the short time of these simulations at low latitudes.

The location of the vorticity maximum (Fig. 51) is essentially the same as the higher latitude experiments however, suggesting that the preferred location for the development of the anticyclonic, rotational v-winds is more strongly affected by the strength the heating function than to the strength of the Coriolis force.

4.7.3. Discussion

The control experiments discussed in the preceding sections were executed to provide a baseline against which to compare the remaining simulations. Differences between the control simulations and the experiments will likely be the result of the imposed jet on the environment.

It was shown in the previous sections that the warm plume that is the result of the forced heating function will result in the development of a divergent anticyclone above the level of maximum heating. The strength of the outflow (as shown by the u-winds) increases with increased heating or decreased Coriolis force. Further, the rotational component of the wind (i.e., the v-wind), also increases with increased heating. An important result is that the distance at which the maximum v-wind develops is related to the strength of the heating so that stronger heating forces the maximum farther away. Outside the region of maximum v, the vorticity is cyclonic; inside this region it is anticyclonic. The anticyclonic vorticity region may have values less than zero if the v-winds are strong enough, resulting in inertial instability. This anticyclonic vorticity region expands outwards with larger heating rates along with the maximum v winds and can dynamically destabilize larger domains.

4.8. Simulation 4

The next set of experiments has a jet imposed on the base state winds. The jet forcing uses (20) to accelerate the winds over a 72-h period. After 72 h, the simulation is suspended, then restarted with the heating function (21) turned on. After 72 h, the u- and v-winds are both nonzero. Figure 52 shows the u-wind; Fig. 53 shows the v-wind. Owing to the continuous acceleration of the v-winds over the 72-h period, there has been a small response in the u-winds, although the speeds are less than ± 0.5 m s^{-1} in all regions. Values are negative along the left- and right-hand edges at mid-levels, and positive throughout most of the remaining domain. As we shall see, the response generated by the heating is considerably larger than the initial background speeds so that we need not be concerned with them.

The core of the jet is in excess of 18 m s^{-1}. This appears to be a weak "jet," but it must be remembered that this wind is superimposed upon any background wind that may exist. Thus, the winds can be thought of as being 18 m s^{-1} greater than the ambient winds. The forcing function (20) uses a value of 30 m s^{-1} for V_0 but the realized value is only 18 m s^{-1}. A portion of the wind has been deflected into the u-component by Coriolis acceleration, and a portion of it has been lost to diffusion and dissipation terms in the model. This is not considered a flaw in the simulation; the Coriolis portion is a real effect, and the diffusion is a necessity in numerical modeling.

Figure 54 depicts the thermal field. After 72 h of gentle acceleration of the wind, the isentropes have maintained thermal wind balance and become slightly distended near the jet. Figure 55 shows how the formation of the jet has created a vorticity dipole, with large positive values in the left half, and smaller positive and slightly negative values in the right half. This initial setup corresponds to a weakly inertially unstable environment. (Simulations 2 and 3 use a weaker jet and result in weakly stable environments.)

4.8.1. Simulation 4a

The first experiment with this imposed jet uses a small heating value of 1°C h^{-1}. The heating is turned on at 72 h and ramps up from zero to full strength in one hour. At the end of two hours, the u-wind (Fig. 56) has begun to show a divergent pattern about the axis of maximum heating. Because of the existence of a weak u-wind prior to the heating, the resulting flow is asymmetric, with a slightly larger region exceeding 1.0 m s^{-1} on the right. After 3 h, the strength of the two regimes have increased to 1.5 m s^{-1} and are more symmetric in appearance (Fig. 57). This is a consequence of the strength of the outflow becoming stronger than the background winds.

After 4 h, there are significant differences noted in the diverging u-winds (Fig. 58). The leftward-moving (easterly) winds are now exceeding –2.0 m s^{-1}, while the rightward moving (westerly) winds are only in excess of 1.5 m s^{-1}. By this time, the vorticity field (Fig. 59) has begun to develop some interesting characteristics. A vertically-oriented notch has developed in the vorticity field; leftward of this feature, the locally increased gradient and magnitude of the v-winds has resulted in the vorticity becoming less positive, while on the other side, the vorticity is slightly more positive than it was previously. Recall from the control experiment that after a few hours an anticyclone had begun to develop near the top of the heating. This anticyclone is present here, too, although it is masked by the larger strength jet. Consequently, the addition of these winds has resulted in a distortion of the vorticity field.

By 6 h, the easterly u-winds are exceeding –2.5 m s^{-1}, whereas the westerly regime is only in excess of 2.0 m s^{-1} (Fig. 60). If we examine the contours outlining the ±0.5 m s^{-1} speeds, it is clear that the total area is significantly larger for the region of negative u-winds that are being influenced by the jet. The remaining contour levels exhibit the same characteristics, but the differences are less obvious. Thus, we have strong evidence that in the presence of jet-induced inertial instability, the outflow wind speeds will be greater than in a region that is inertially stable.

4.8.2. Simulation 4b

The next experiment increases the heating to 3°C h^{-1}. The evolution of this experiment is similar to the previous experiment so it is not necessary to describe all the intermediate results. Instead, we will focus on the ending period after 6 h and compare and contrast some features.

The divergent u-wind (Fig. 61) has experienced greater accelerations owing to the increased strength of the heating function and the associated updraft. At this time, the easterly winds are more than –8.0 m s^{-1}, whereas the westerly winds are weaker and are only slightly greater than +6.0 m s^{-1}. The addition of the rotational winds onto the ambient jet has perturbed the flow significantly (Fig. 62). Instead of a nearly circular jet with only slight variations in the gradient, there is now a strengthening of the gradient and magnitude in the region between the heating and the jet core. The vorticity field (Fig. 63) clearly shows the consequences of this evolution. Starting with a vorticity couplet with values only slightly less than zero initially (see Fig. 55), we now have a region that is strongly negative, and consequently, inertially unstable. This inertially unstable region is the result of local vorticity generation superimposed on a larger-scale background that was near neutral in stability prior to the addition of the heating.

4.8.3. Simulation 4e

We now turn to another experiment using the same jet forcing and the same heating (V_0=30 m s^{-1}; H_0=3°C h^{-1}) but with a weaker Coriolis acceleration. After 72 h of acceleration, the u-winds are similar to those in experiment 4. The jet has a maximum of 20 m s^{-1}, slightly greater than the equivalent experiment at a higher latitude. The vorticity couplet has a slightly weaker positive branch and the negative region has greater magnitudes than the previous experiment, resulting in a larger region of inertial instability.

After 1 h, the divergent *u*-winds (Fig. 64) are asymmetric because of the pre-existing westerly current. Maximum easterly outflow is around -0.5 m s^{-1}; maximum westerly outflow is greater than $+1.5$ m s^{-1}.

By 3 h, the easterly outflow (Fig. 65) has speeds in excess of -5.0 m s^{-1} and the westerly current is greater than $+5.5$ m s^{-1}. After 4 h, the easterly outflow has continued to increase and exceeds the westerly outflow by approximately 0.5 m s^{-1}. This trend continues until 6 h when the easterly current has attained speeds of -9.0 m s^{-1} whereas the westerly current is considerably weaker with speeds of only $+6.5$ m s^{-1} (Fig. 66). As before, the development of the rotational component has modified the larger-scale jet so that the gradient and magnitude of winds is considerably stronger over a portion of the wind field. The vorticity has become large and negative in this region, leading to large values of inertial instability.

4.8.4. Discussion

The simulations in this class of experiments have been markedly different from the results of the control group. In the latter group, the results of the outflow were symmetric about the axis of the maximum heating. The vorticity pattern developed as a result of the evolution of an anticyclone above the level of maximum heating. With time, the vorticity developed a symmetric pattern of inertial instability adjacent to the region of maximum heating, with a region of moderate inertial stability laterally displaced from the unstable region.

In the presence of a horizontally-sheared wind due to a jet, the evolution is different. An anticyclone develops aloft above the level of maximum heating and this local vorticity pattern is superimposed on the larger-scale vorticity. The presence of the jet produces a dipole of vorticity with a region of moderate-to-strong absolute vorticity displaced to the left (west) of the horizontal wind speed maximum, and a region of small positive and slightly negative values to the right (east) of the maximum. As the locally generated vorticity modifies the larger-scale vorticity, the region of inertial instability grows in magnitude and size. This increased instability permits greater cross-stream accelerations of the easterly outflow, which can advect the v-winds associated with the jet from lower to higher speeds, resulting in a strengthened gradient and stronger winds in the jet core. These features all work together in a positive feedback process, continually increasing the gradient and magnitude of the jet, resulting in additional instability, causing greater accelerations of the easterly outflow. Thus, we have shown that the presence of a heat source in a region that is inertially unstable can lead to a positive feedback process, as pointed out by Eliassen (1951) and discussed earlier in Chapter 2.

It was also shown that the response generated for a given jet and heating strength was greater at lower latitudes. This is simply the result of the fact that at these latitudes the Coriolis force is weaker, hence the restoring force is also weaker. There is less tendency to restore the outflow to its original position and it is allowed to expand farther and at greater speeds.

4.9. Discussion of other simulations

As shown in Table 2, many experiments were conducted using various jet speeds, heating strengths, and latitudes. Instead of discussing each of these individually, the following figures serve to illustrate how the variations of the strength of the jet and latitude can affect the simulation.

Figures 67a–c depict the strength of the divergent, u-component of the wind for each of the three heating profiles (1, 3, and 5°C h^{-1}) at 40° latitude for each of the four jets strengths (0, 10, 20, and 30 m s^{-1}). In Fig. 67a, it is clear that by approximately 3 h, there are differences in the strength of the outflow. By the end of the simulation at 6 h, the differences are greatest, although the slope of the curves suggest that rates of change are decreasing. At this time, the strength of the outflow associated with the strongest jet is ~47% greater than that associated with the no-jet, control experiment. Figure 67b shows the same as the previous figure, except for a heating rate of 3°C h^{-1}. As before, differences are obvious at about 3 h and greatest at 6 h; the differences between the no-jet, control experiment and the strongest jet are almost ~47%. Finally, Fig. 67c compares the results obtained with the maximum heating rate of 5°C h^{-1}. The differences between the maximum and minimum are about 37%, or about 3 m s^{-1}.

Figure 68 is similar to Fig. 67b except it is for the 25° latitude case. The differences in the strength of the outflow associated with the different jet speeds take slightly longer to manifest themselves (about 3.5 h) than the higher latitude case. The percentage differences between the no-jet and strongest jet outflow for the 1, 3, and 5°C h^{-1} heating rates are 33%, 38%, and 38%, respectively. The absolute strength of the outflow is increased in the low-latitude cases relative to the high latitude. Percentage increases range from 12% (no jet) to 9% (strongest jet); these increases are a direct consequence of the reduced restoring force present at the lower latitude.

These results show that given similar heating and wind profiles, more upper-level divergence and outflow are present with reduced Coriolis. This suggests that the effect of this inertial instability is enhanced at the lower latitudes. Further, it suggests that there may be a latitudinal limit to the inertial instability process. As Coriolis increases, it may present a restoring force that cannot be overcome with the strengths of typical convective season jet streams. Observations have suggested that mesoscale convective systems are more likely to occur in low and middle latitudes than in higher latitudes. Of course, the lack of high latitude systems may simply be due to a lack of sufficient low-level moisture being advected northward to provide the fuel for the system; nonetheless, the results presented here suggest that this may be another factor that must be considered.

Figure 69 shows the speeds of the upper-level outflow winds that have a westerly component; i.e., the winds diverging from the right side of the heating function. For brevity, only one heating configuration (i.e., 3°C h^{-1}) is shown. As can be seen, there is little difference between the no-jet control experiments and the strong jets. The results for the remaining heating profiles and latitudes show similar results. This provides ample evidence that the divergent outflow has a strong, dynamic response in the region where the inertial stability is weakest or unstable and that the response is not uniform over the full domain of the simulations.

It should be expected that with increased divergence aloft, as shown by the increase in the outflow of the u-winds, that the vertical velocity should be affected. Figures 70 and 71 show how the vertical velocity in the core of the heated region responds to the variations in jet stream strength. All the simulations are similar during the first few hours; differences begin to appear after about 2.5 hours, approximately the same amount of time required for the divergence profiles to show differences. The jet simulation vertical velocities, w, exceed the no-jet control simulations by 8–17% for the low latitude cases, and from 13–18% for the high latitude cases; variations in percentage change are a result of the three different heating rates. The smaller increases at the low latitude may be a consequence of the fact that they are already taking advantage of a weaker restoring force compared to the northern latitude. This result suggests that an increase in heating rates can overcome the resistance from Coriolis at higher latitudes. While this result should not be surprising (intuitively it makes sense), it is an important consequence. In other words, a positive feedback process producing inertial instability can be created through a decrease in the restoring force because of pre-existing weak inertial stability or through increased heating.

4.10. Sensitivity tests

As a check on the model results, sensitivity tests were run and the results compared with previous results. These simulations were used to check how variations in convective instability, vertical shear, and grid point resolution might affect the results. These simulations are discussed in the following sections.

4.10.1. Vertical stability

It is instructive to compare the results obtained from using a vertical sounding with a different degree of convective stability than that used in the previous simulations. The original thermodynamic data are an actual sounding that has been slightly smoothed for input into the model. The model input thermodynamic data were modified by using a highly idealized sounding. This particular sounding has been used by other modelers (e.g., Weisman and Klemp 1982, 1984; Rotunno et al. 1988; Straka and Liu 1993; Skamarock et al. 1994) for simulating supercells, mesoscale convective systems, bow echoes, and other convection. For purposes of discussion, the original sounding will be referred to as OKC, and the second sounding as WK. The two soundings are similar, but the differences are important (see Fig. 42). The WK sounding has a slightly more stable lapse rate at all levels, but especially in the upper troposphere; the WK sounding is also more moist at all levels. Both soundings define the tropopause at or near 200 mb. We shall see that the minor changes in stability can have important impacts on the model results.

The model simulations using the WK sounding were initialized in the same manner as the OKC simulations and were allowed to run for 72 h, then suspended. For comparison purposes, only one jet speed and one heating rate were used (V_0=30 m s^{-1} and H_0=3°C h^{-1}, corresponding to experiment 4b). At t=0 h (i.e., after 72 h of spinup), there are no differences noted in either the u-winds or v-winds. The thermal structure, however, is different and is shown in Fig. 72a. Compare this with the thermal structure for experiment 4, shown in Fig. 72b. The major distinction is the nearly constant vertical gradient of θ in the WK simulation; the OKC simulation shows vertical variations, especially in the layer from 7–10 km. After 1 h, differences are already apparent in the diverging u-winds (not shown). The maximum winds in the WK simulation are approximately 50% of the value of the original simulations. The vertical velocity, w (not shown), is ~33% less than the original. By t=3 h, the differences are quite large. The u-winds have speeds of –2.5 and +2.0 m s^{-1} in the WK simulation (Fig. 73a), compared to values of –5.5 and +5.0 m s^{-1} in the OKC simulation (Fig. 73b). Figures 74a–b show that the heating function has had a smaller impact on the thermal field owing to the greater stability. Finally, after 6 h, the differences in the u-winds are greatest. The WK simulation has u-winds of –3.0 and +1.5 m s^{-1}, compared to the OKC simulation that has speeds of –8.0 and +6.0 m s^{-1} (Fig. 75a–b). Not only are the speeds in the WK simulation less than the original OKC simulation, but the westerly winds expanding out on the right side of the heating profile away from the jet have decreased from their peak value, which occurred at t=3 h. This is quite different from the previous simulations in which the winds increased or remained quasi-steady with time.

Figure 76 shows the time rate of change in the easterly and westerly components of the outflow for both the WK and OKC simulations. The differences are quite clear; the OKC wind speeds exceed the WK wind speeds right from the start. As noted above, the WK westerly winds peak at t=3 h, then decrease slightly with time while the OKC winds do not show this characteristic until after 5 h. If we look back at the sounding profile shown in Fig. 42, we see that the largest differences in lapse rate occur between ~350 and 200 mb. This is the same region in which the divergence is occurring and is above the level of maximum heating. It should now be obvious that the simulations are very sensitive to the *vertical* stability (and we have already shown that variations in the *horizontal* stability can affect the results). It is noteworthy that as the vertical stability increases, the asymmetry between the easterly and westerly outflow becomes more pronounced (see Fig. 75). Because of the greater vertical stability, the updrafts are weaker for a given heating rate; the weaker updrafts subsequently produce weaker divergent outflows and the inertial instability can play a larger role on these weaker flows. A possible explanation for this behavior is that the diverging air must descend within the model domain and the enhanced vertical stability inhibits the descending motion. In the region of the jet and inertial instability, this inhibiting factor is partially offset because the thermal wind balance between the jet and the isentropes has resulted in sloped θ surfaces. These sloped surfaces provide a mechanism for adiabatic descent of the parcels. This sloped descent defines the return branch of the Conv-SI solenoid described earlier and depicted in Figure 3. Further, the presence of a descent region permits additional air parcels to continue to diverge from the updraft and into this region to replenish the parcels evacuated through the downdrafts. In the stable region, the inhibition of downdrafts results in a mass surplus and, consequently, a reduction in the divergence of parcels into this region.

4.10.2. Vertical shear

Another sensitivity test was conducted to evaluate the influence of vertical shear of the v-component of the wind. For this simulation, the WK sounding was used again, but the base state included v-winds that increase with height. The initial state of the v-winds and the jet are shown in Fig. 77. The winds increase with height up to the level of the jet core, then decrease with additional height. This is a typical configuration for a vertically-sheared environment with winds increasing up to the jet level and the tropopause. The jet core was imposed as a perturbation on the base state as before; the jet forcing function was allowed to gently accelerate the winds for 72 h. At that point the simulation was suspended, then restarted with the heating function turned on. It should be noted that there is a physical inconsistency present in these simulations. Because the base state winds are independent of the base state thermal structure, they are not in thermal wind balance. To support vertical shear like that depicted here, there should be gently sloping isentropes; however, the isentropes would remain nearly horizontal and would likely have little influence on the simulations shown here. This decoupling of the pressure and wind fields is typical of 2-D model simulations and should not be considered a negative factor here.

In many ways, this simulation (hereafter referred to as WKV) is similar to the previous simulation (WK), that is, the maximum easterly flow and updrafts are less than similar experiments using the OKC sounding (i.e., experiment 4b). The differences are most apparent after 6 hours. The u-wind

(Fig. 78) shows remarkable asymmetry with values of –4.0 and +1.0 m s^{-1}. The WK simulation had values of –3.0 and +1.5 m s^{-1} and simulation 4b had values of –8.0 and +6.0 m s^{-1}. As before, we see that the greater stability in the vertical reduces the magnitude of the divergent outflow. Also, the asymmetry present in WK is also apparent in WKV. What is interesting is the increase in magnitude of the easterly current and the decrease in the westerly current.

Figure 79 shows the structure of the v-wind after 6 hours. Especially prominent is the advection of low-level, low-momentum air to upper levels. The effect of this advective process is to increase the horizontal gradient of the wind and the horizontal shear on both sides of the updraft. The superposition of this vorticity on the background vorticity results in the pattern shown in Figure 80. The vertical advection of low-momentum air has resulted in the development of a strong inertially-unstable region adjacent to a strong inertially-stable region. The unstable region supports and enhances cross-stream accelerations while the stable region quickly damps out these motions. The result of these two processes is to create the highly asymmetric pattern revealed in Fig. 78. This pattern is similar to that described by Seman (1990, 1994), Raymond and Jiang (1990), and Raymond (1992) in their discussion of the *in situ* development of inertial instabilities.

Finally, this simulation is the most interesting because it has both horizontal and vertical shear of the v-wind and more closely approximates the real atmosphere and environments associated with the development of mesoscale convective systems.

4.10.3. Model resolution

The results discussed above need to be tested to ensure that they are occurring for the proper physical reasons and are not simply related to the numerics and resolution of the simulation. To this end, the model was re-run using the same parameters as Simulation 4, except that the model resolution was changed. Two simulations were run with horizontal domains of 100 grid points (10 km grid spacing), and with 50 grid points (20 km grid spacing). The simulations were started with no base state winds. The jet winds were allowed to increase as before over a period of 72 h, at which time the simulation was suspended. The heating was turned on and the simulation resumed for an additional 6 h.

In both simulations, the results are essentially identical with the results of Simulation 4b. The only difference was a minor one and resulted in the coarser grids having slightly smoother contours. The strength of the secondary circulations, divergent outflow, and the updraft/downdrafts remained essentially the same, although the peak values were slightly smaller with the coarser resolutions. The conclusion that can be drawn from this is that the responses that are taking place in the model simulations are large enough in scale that they can be properly simulated even with the coarse resolution. Stated differently, the responses are mesoscale in size, and are not a function of the model resolution and numerics. This is a positive result because it reaffirms the hypothesis that the responses to the inertial instability are on the mesoscale.

4.10.4. Discussion

In this section, the model was used to test the response of the atmosphere when the vertical stability is increased, and when a vertically-sheared base state wind is present.

The results indicated that as the vertical stability increases, the divergent outflow is inhibited because there is a resistance to the descending parcels. In the jet region where the isentropes are sloped, descending parcels encounter less resistance and the overall response to the parcels moving through the inertial instability is greater than the response of parcels moving through the inertially stable region with quasi-horizontal isentropes.

The presence of a vertically-sheared base state results in the advection of low momentum air aloft where it acts to increase the horizontal shear and, coupled with the background vorticity, leads to strong inertially unstable and stable regions adjacent to the updraft region. These regions act to enhance and resist, respectively, the cross-stream accelerations and result in highly asymmetric outflow patterns that resemble what is often observed in MCSs.

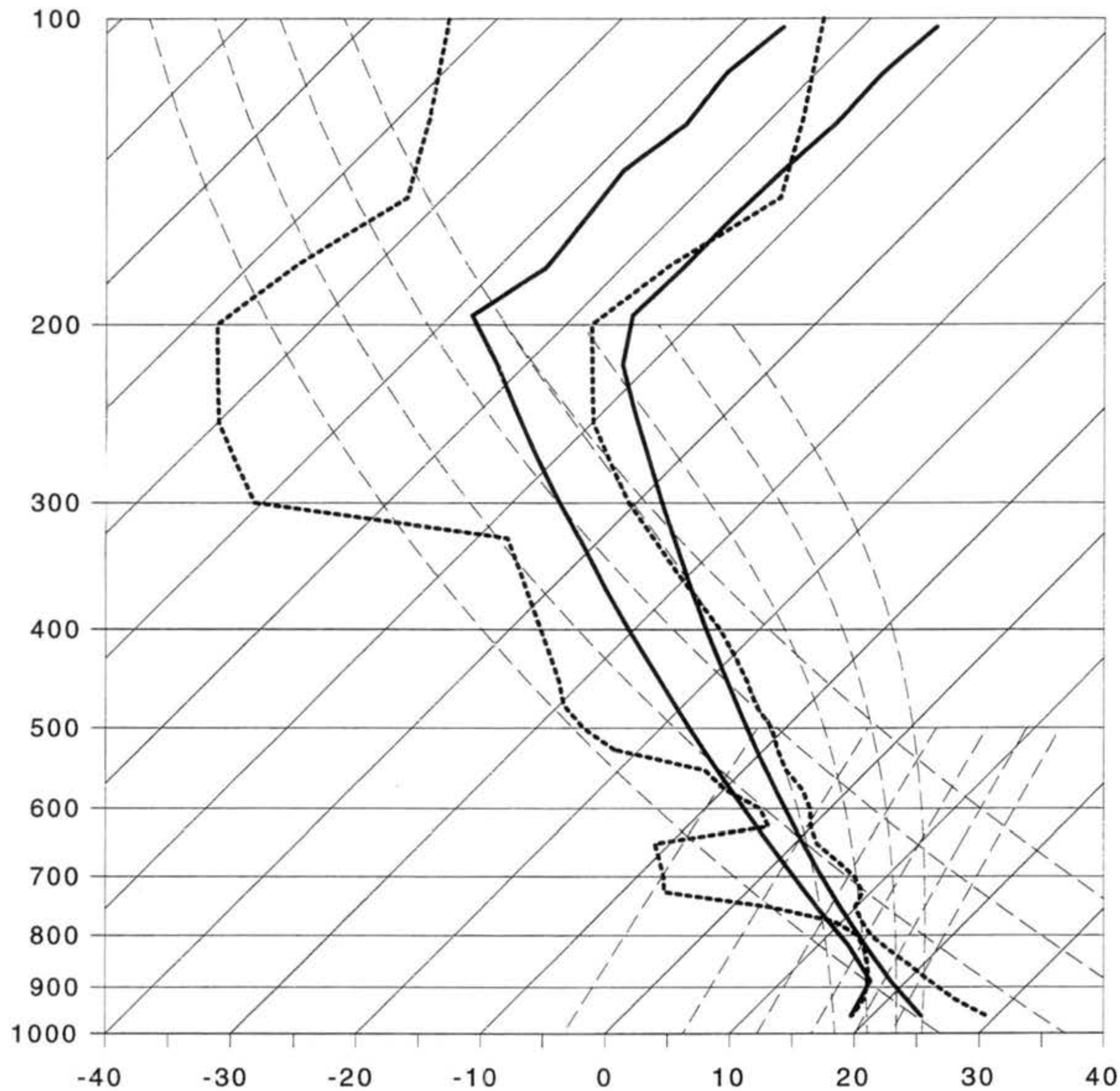

Figure 42. Skew *T*–ln *P* diagram of the two soundings used in the model simulations. The short dashed lines are a slightly smoothed version of the temperature and moisture profiles from the Oklahoma City, Oklahoma (OKC) sounding taken at 0000 UTC on 13 May 1985. sounding. The solid lines are the temperature and moisture profiles from the Weisman-Klemp (WK) model sounding.

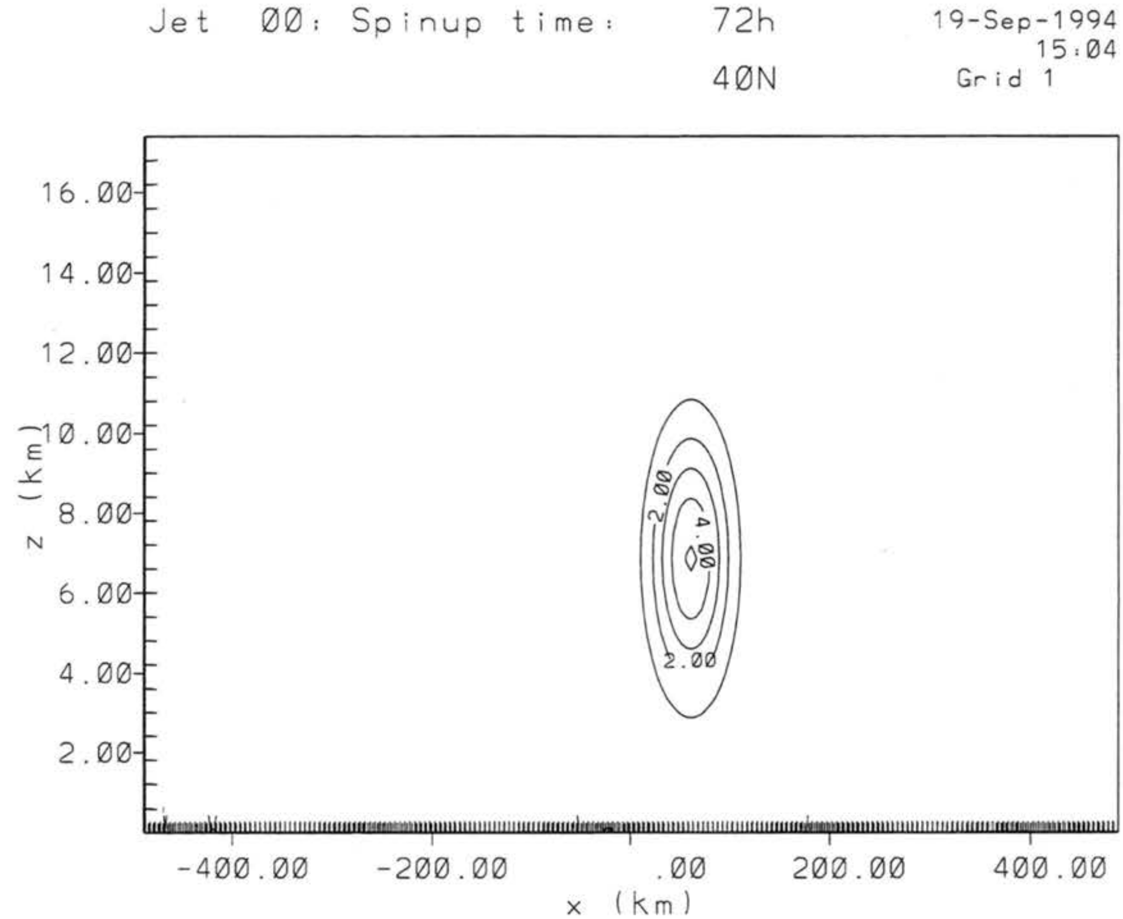

Figure 43. Vertical cross section of the heating function profile. Heating rate is 5°C h^{-1}. Contours interval 1°C.

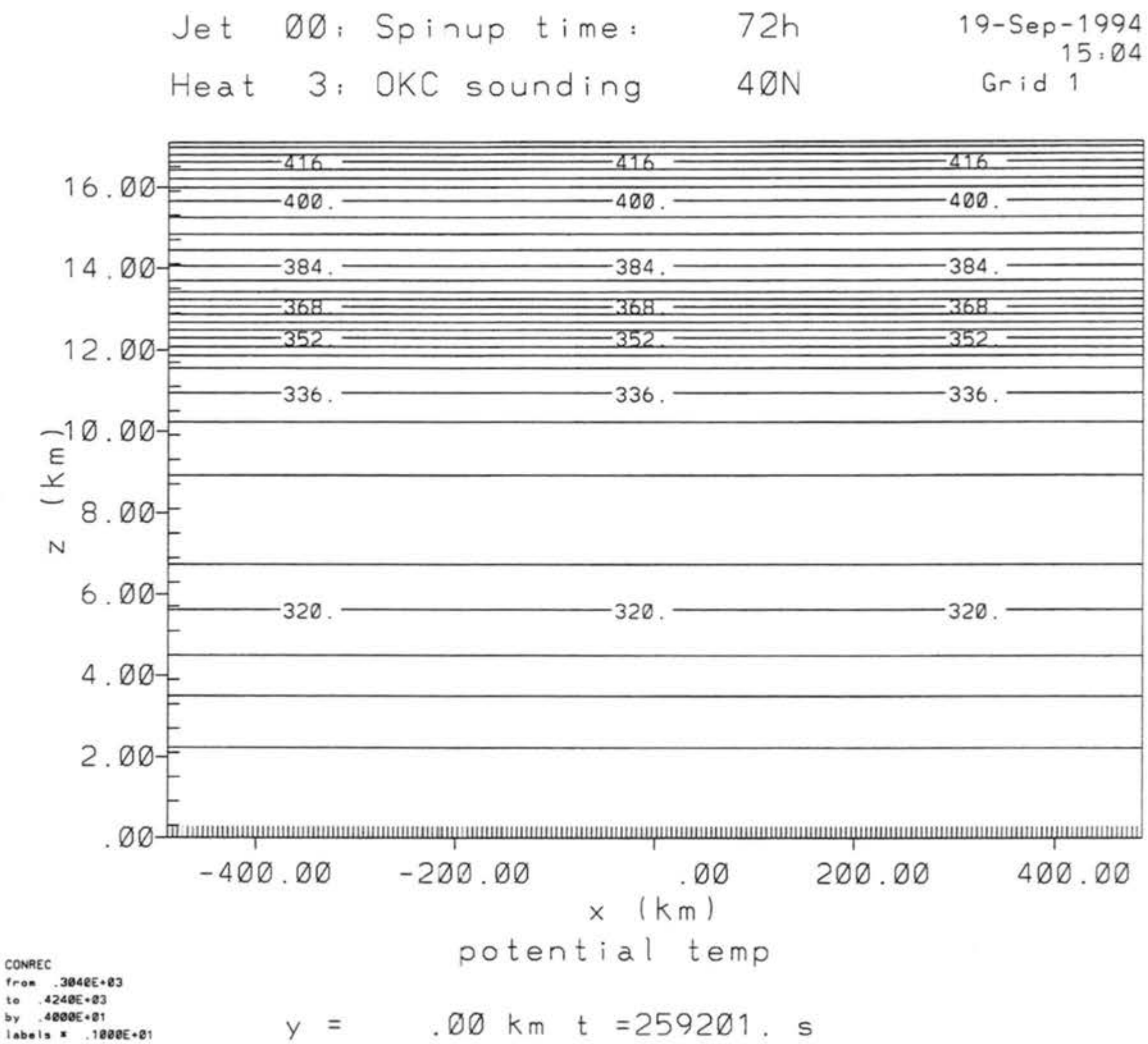

Figure 44. Vertical cross section of the potential temperature field, θ, at t=0 h for experiment 1. Contours every 4 K.

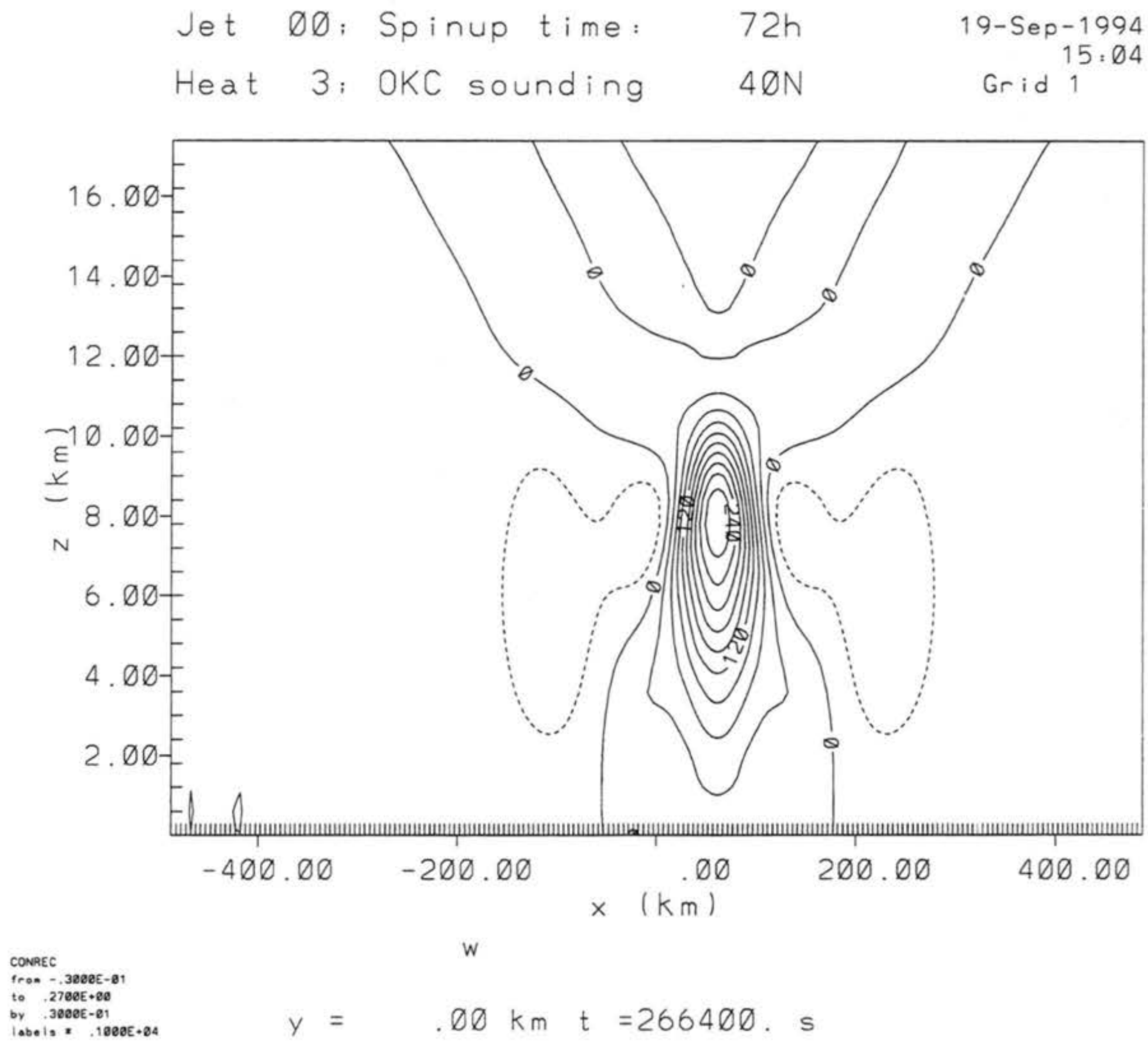

Figure 45. Vertical cross section of the vertical velocity field, w, at t=2 h for experiment 1b. Contours every 0.03 m s^{-1}; negative values (downward motion) are dashed.

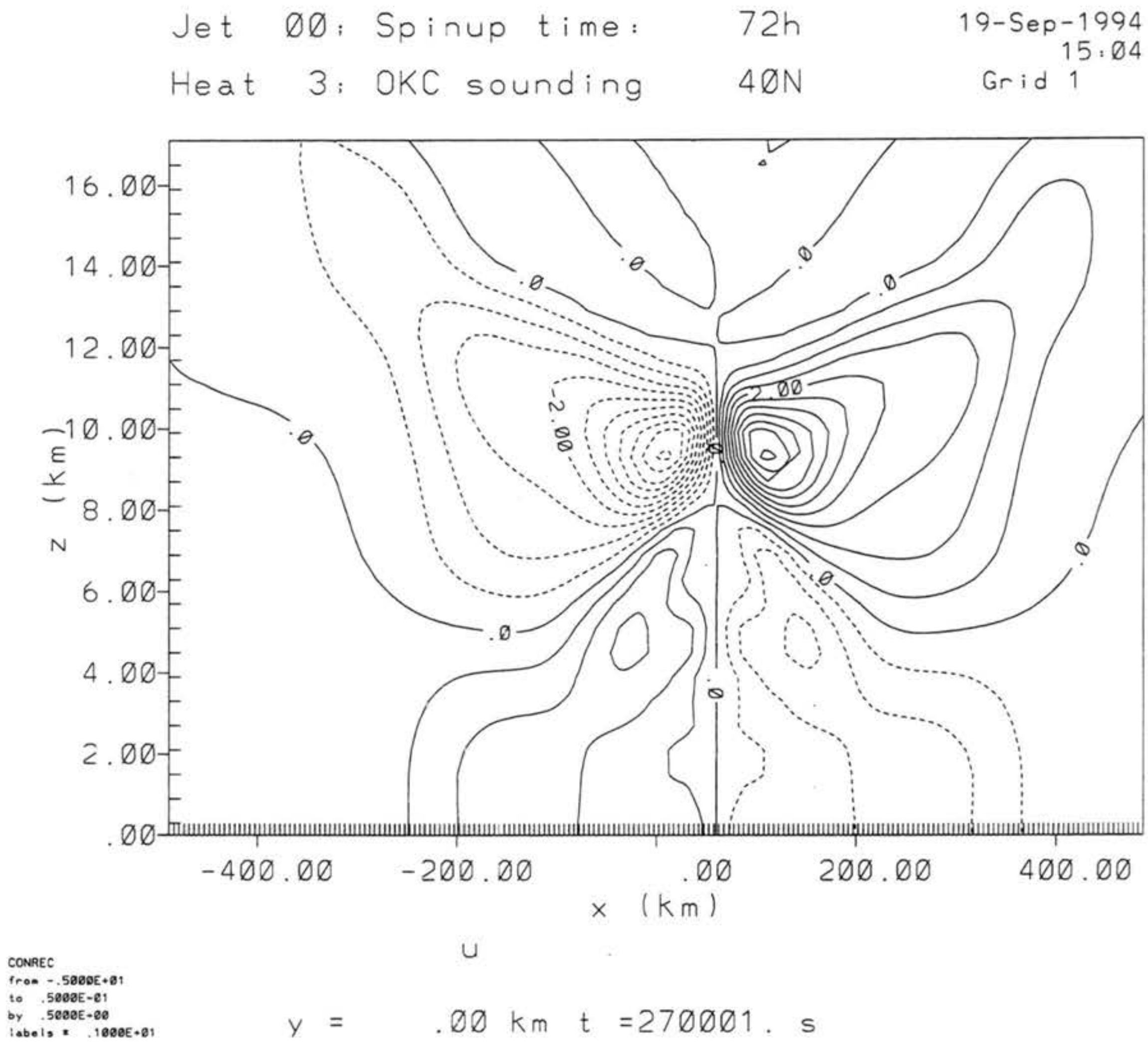

Figure 46. Vertical cross section of the *u*-component of the wind at t=3 h for experiment 1b. Contours every 0.5 m s^{-1}; negative values are dashed.

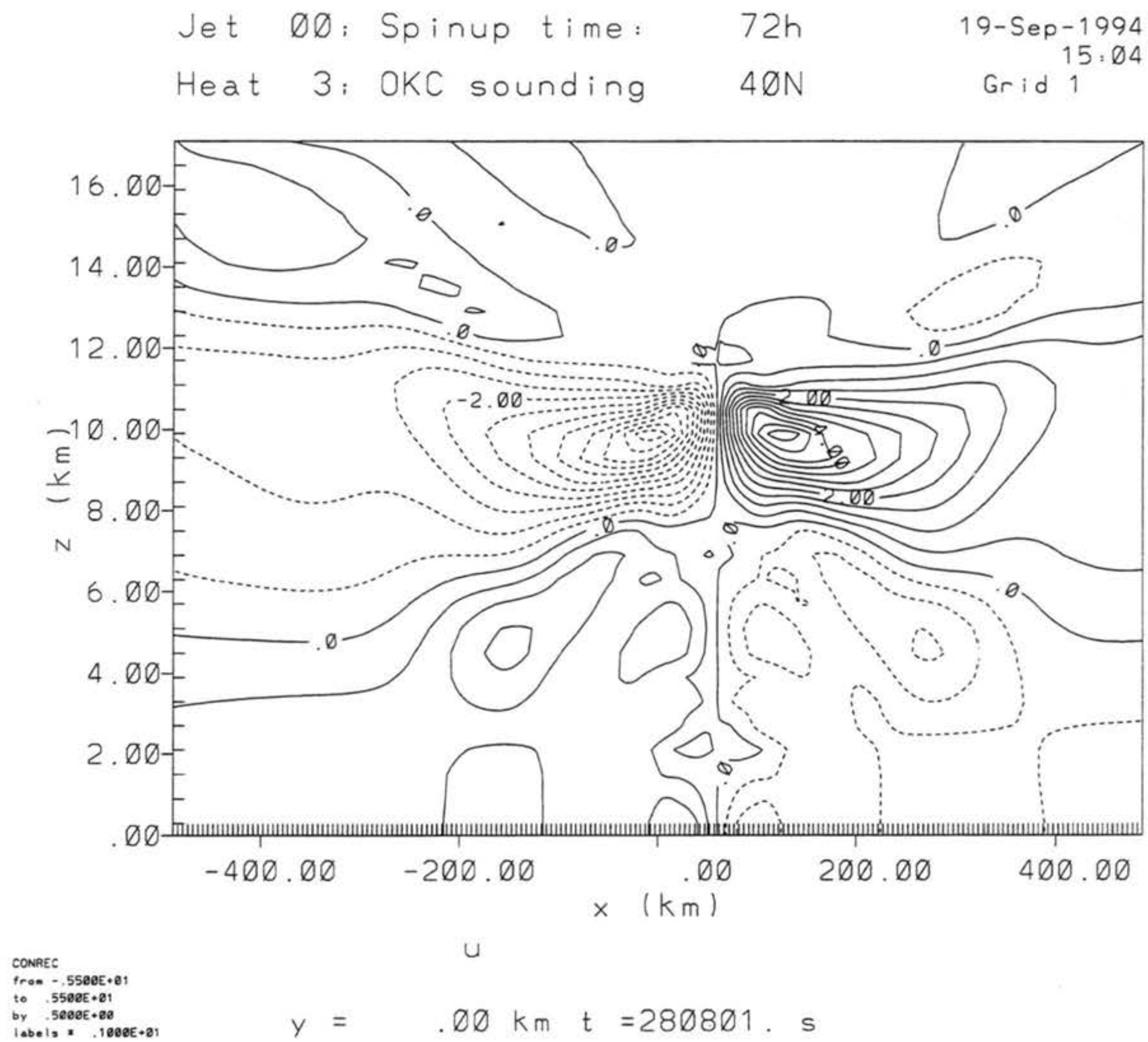

Figure 47. As in Fig. 46, except for t=6 h.

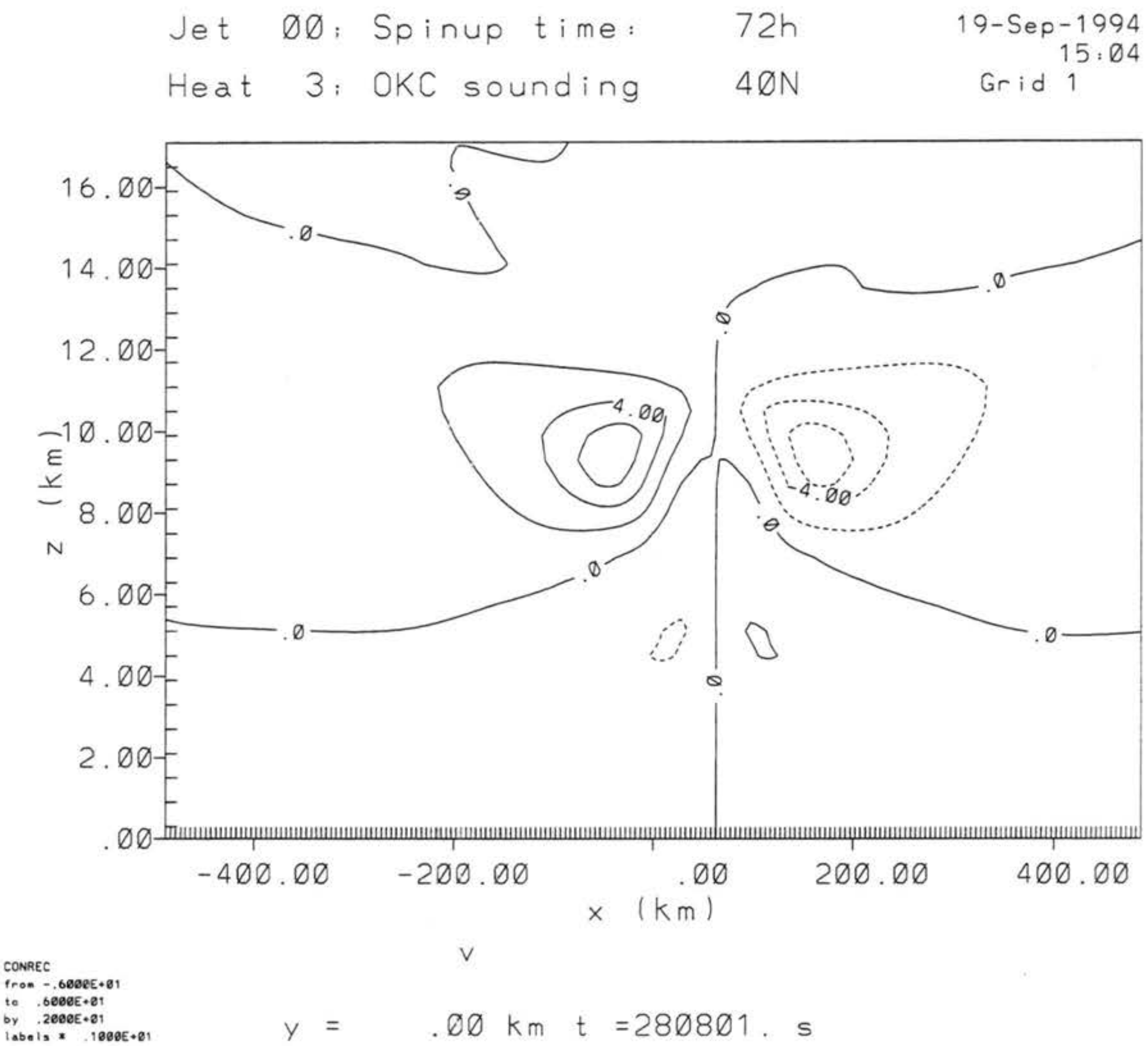

Figure 48. Vertical cross section of the v component of the wind at t=6 h for experiment 1b. Contours every 2.0 m s^{-1}; negative values are dashed.

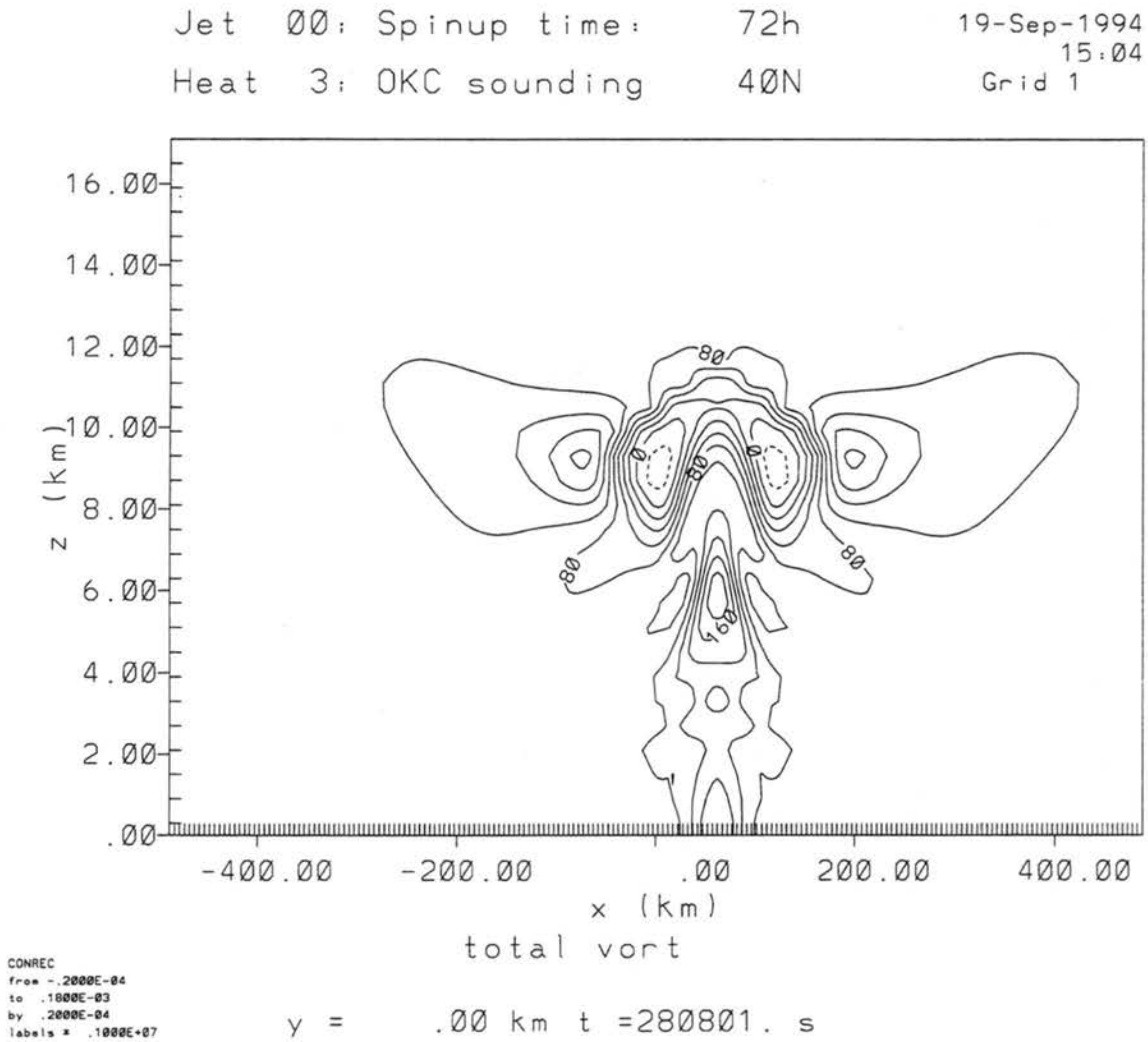

Figure 49. Vertical cross section of the absolute vorticity, $(\zeta + f)$, at t=6 h for experiment 1b. Contours every 2.0×10^{-5} s^{-1}; negative values are dashed.

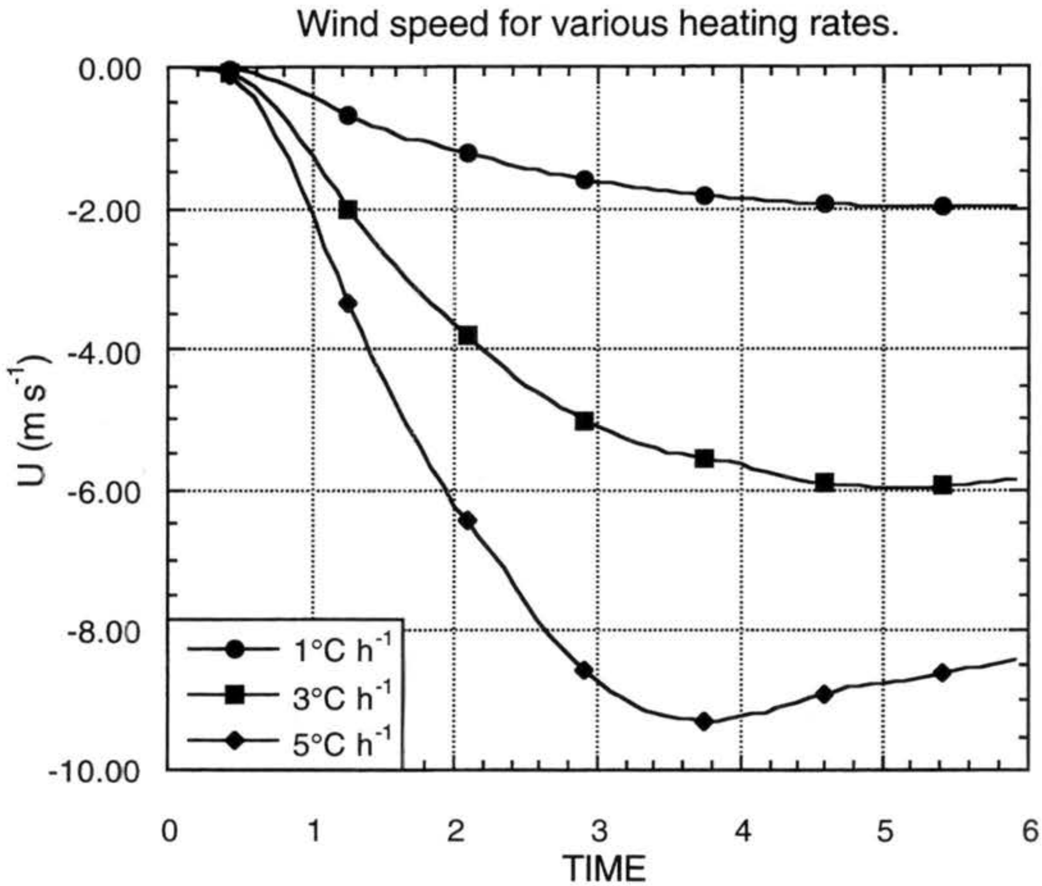

Figure 50. Time rate of change of the divergent *u*-component of the wind for the three heating rates (1, 3, and 5°C h^{-1}) for the no-jet control case.

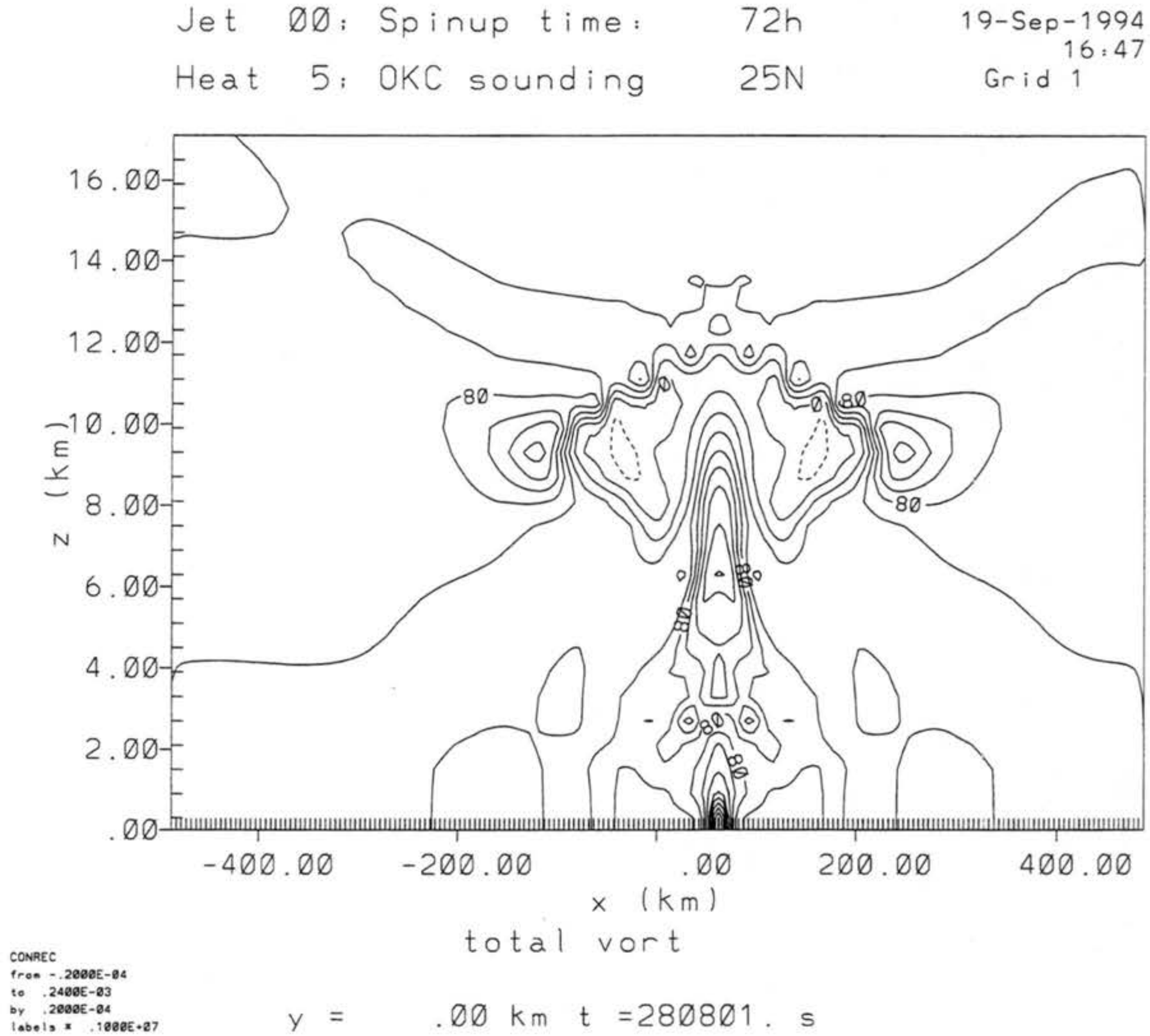

Figure 51. As in Fig. 49, except for t=6 h and for simulation 1f.

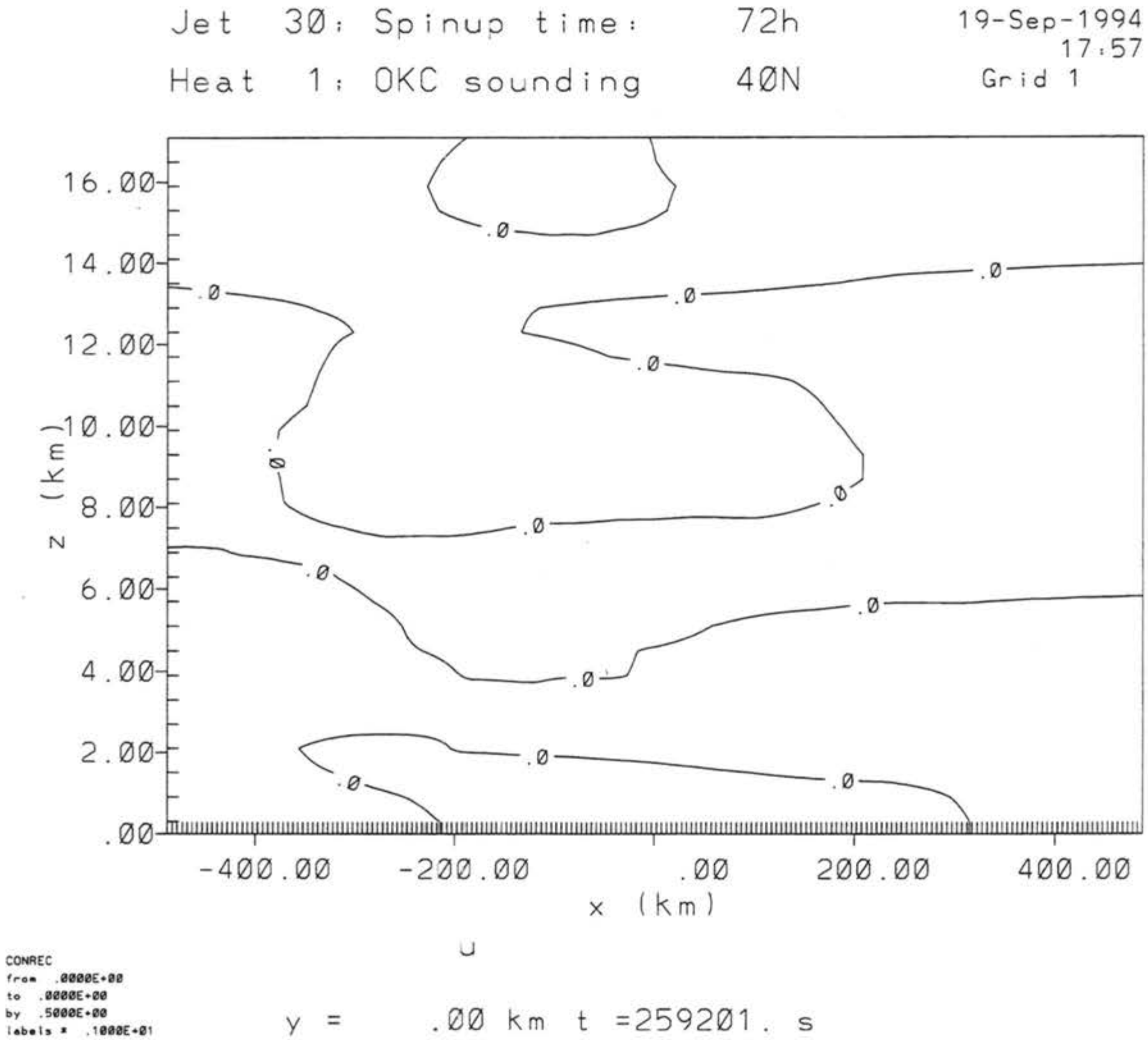

Figure 52. As in Fig. 46, except for t=0 h and for experiment 4.

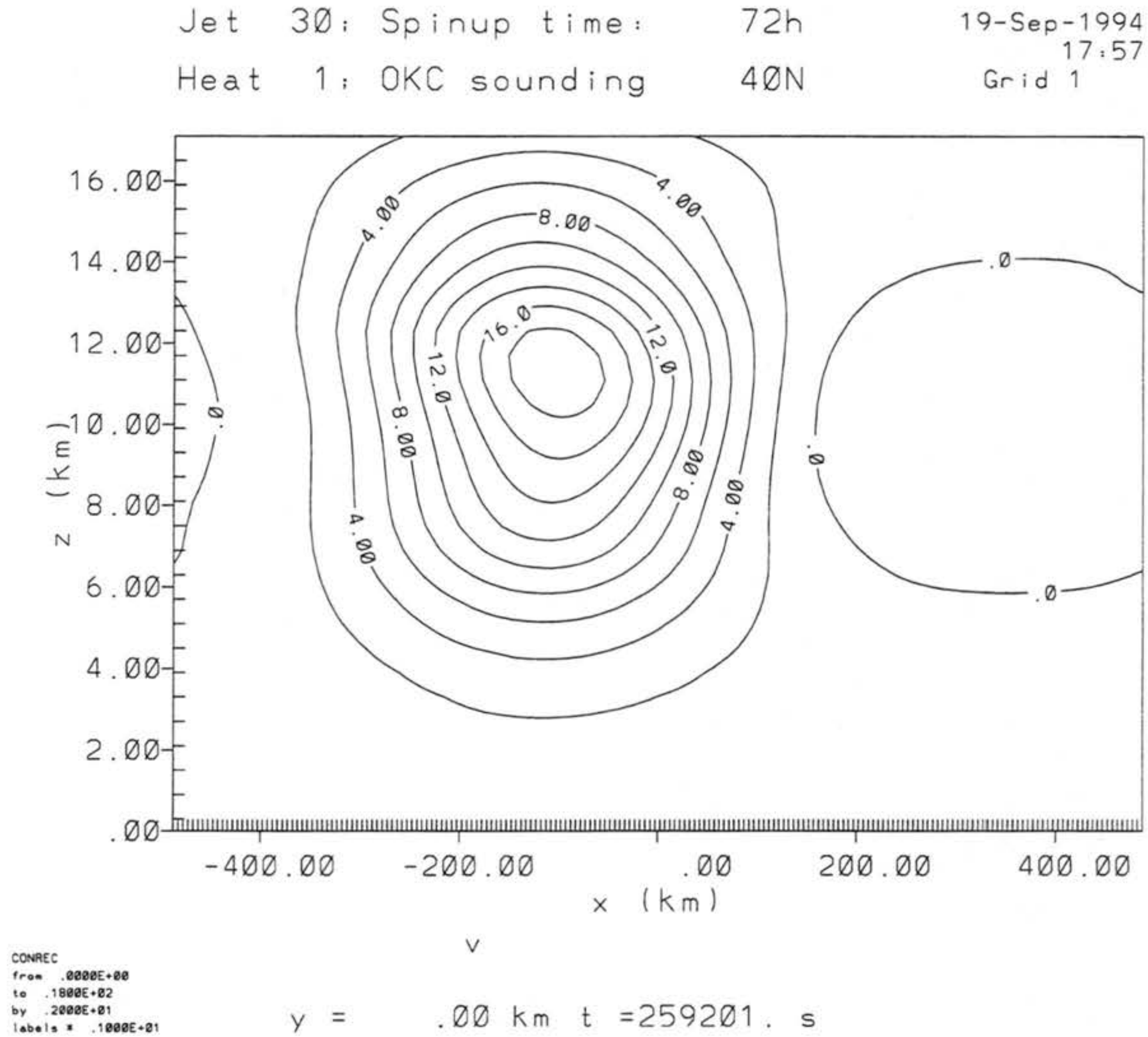

Figure 53. As in Fig. 48, except for t=0 h and for experiment 4.

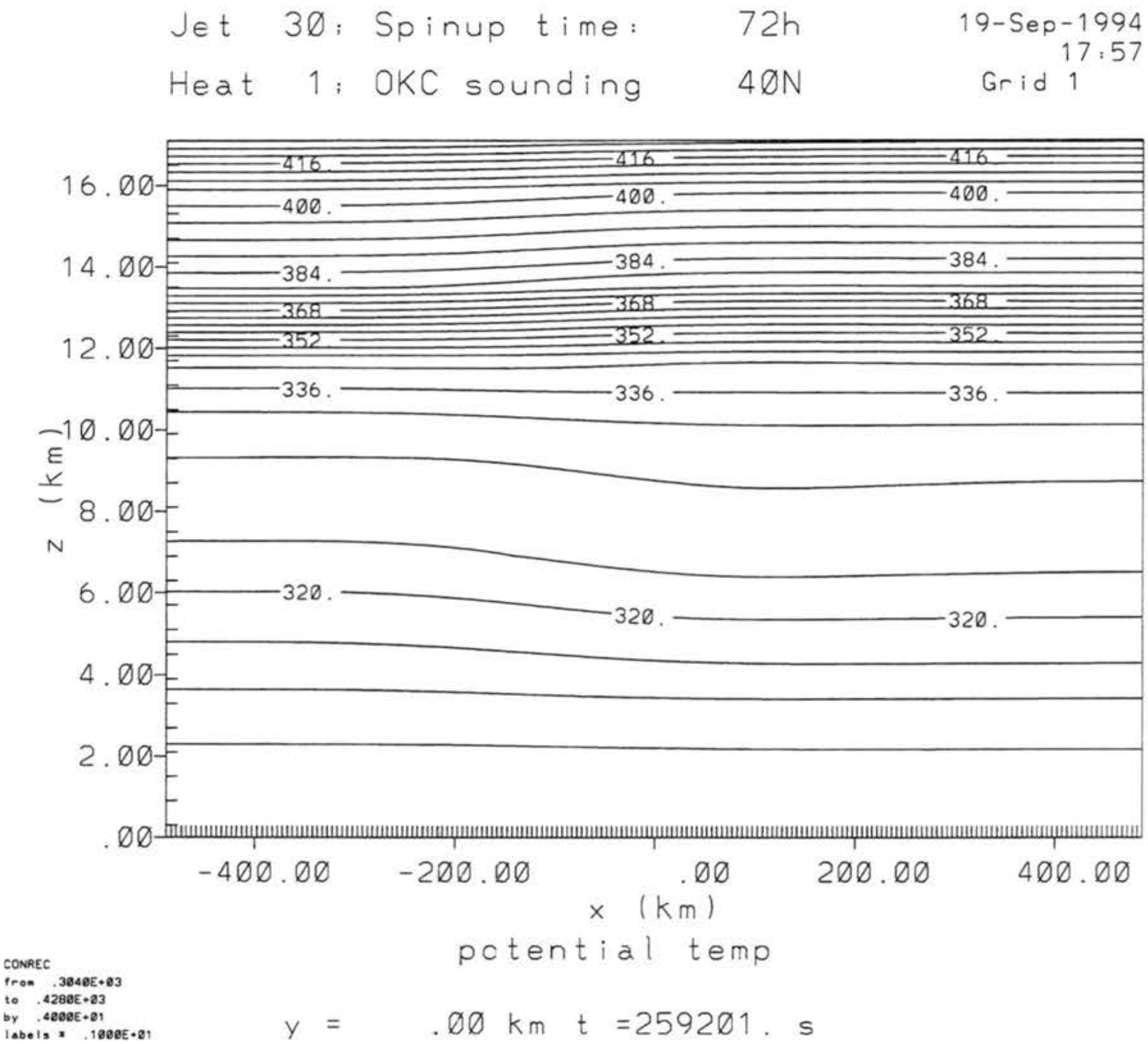

Figure 54. As in Fig. 44, except for t=0 h and for experiment 4.

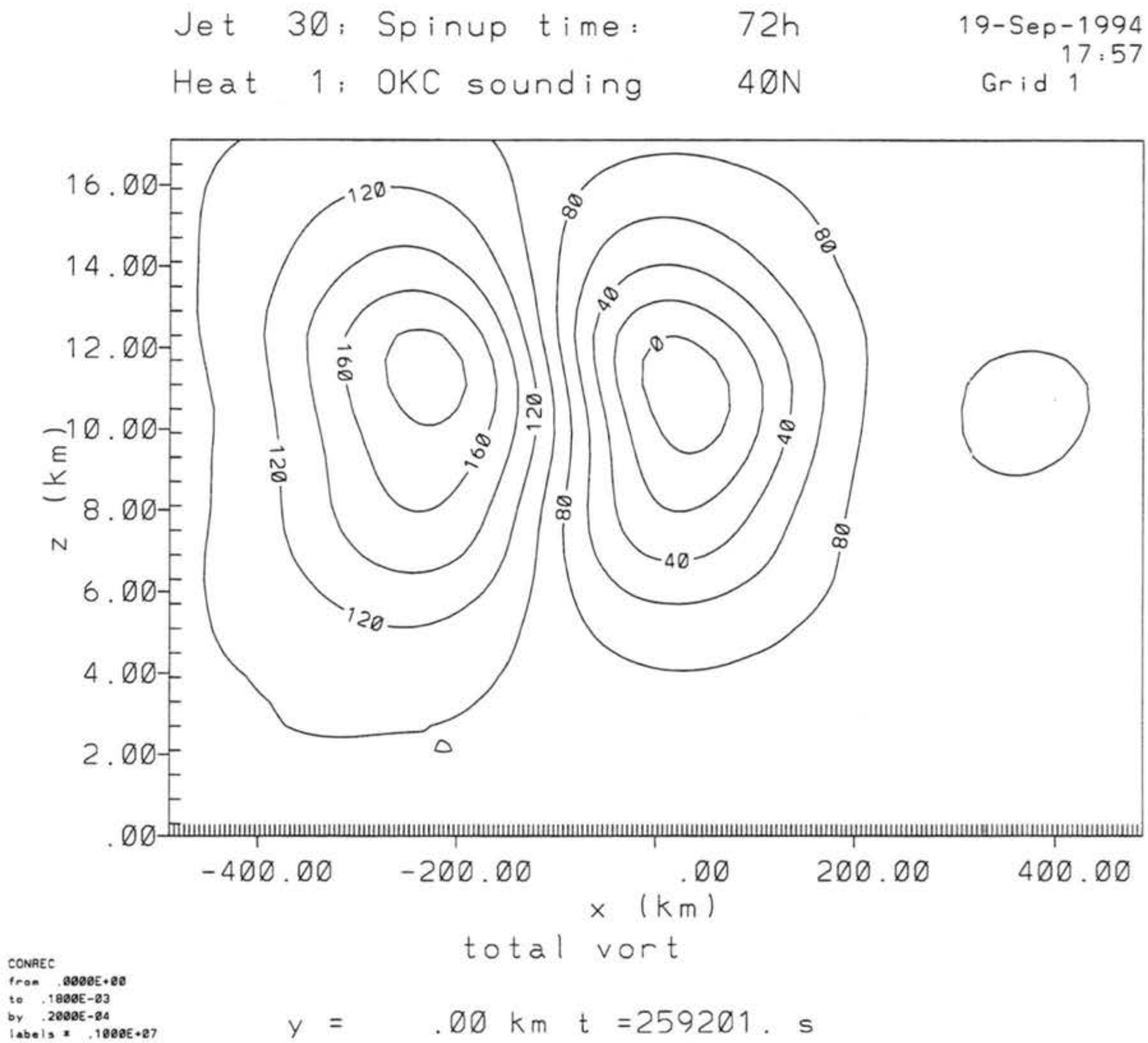

Figure 55. As in Fig. 49, except for t=0 h and for experiment 4.

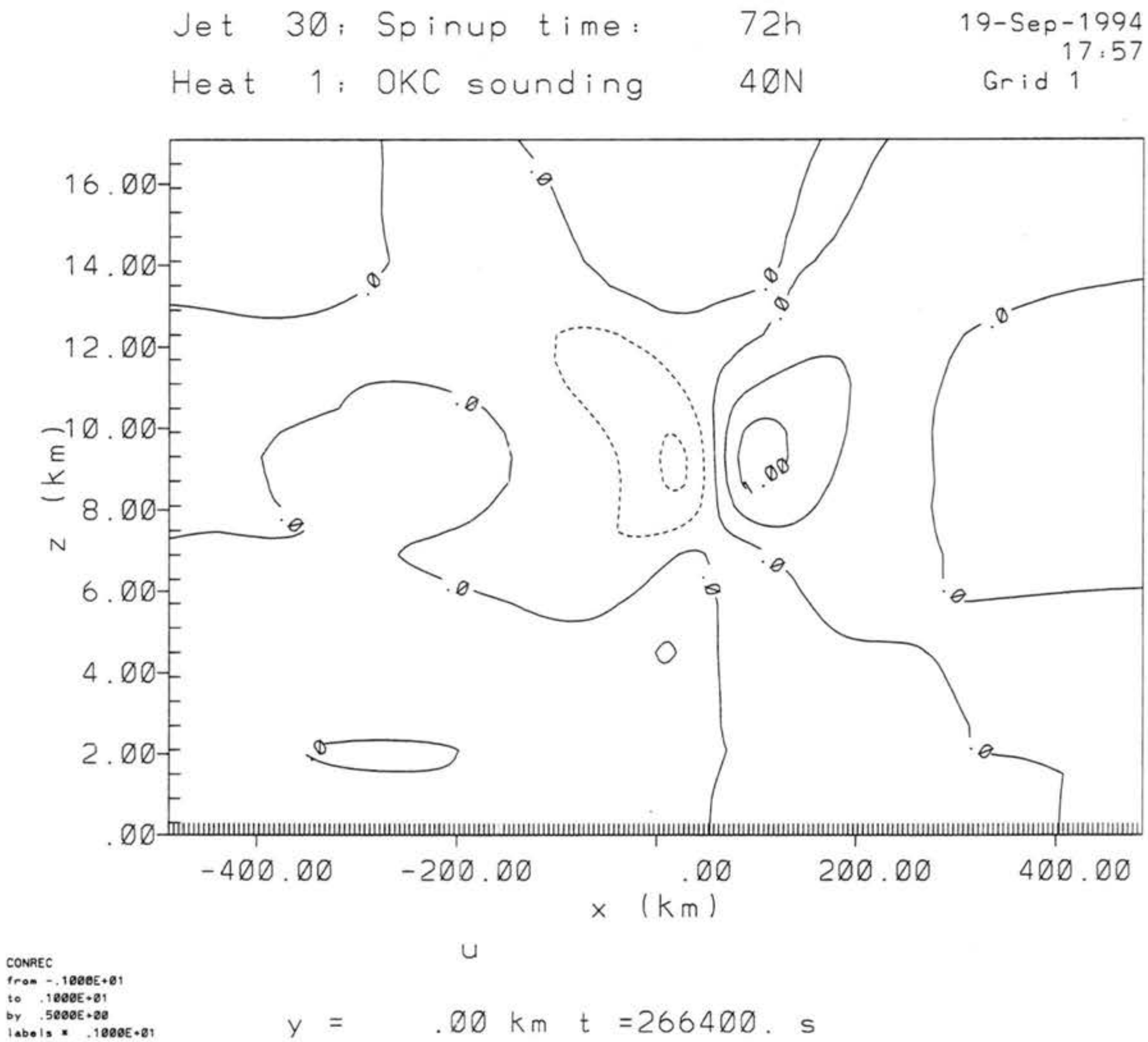

Figure 56. As in Fig. 46, except for t=2 h and for experiment 4a.

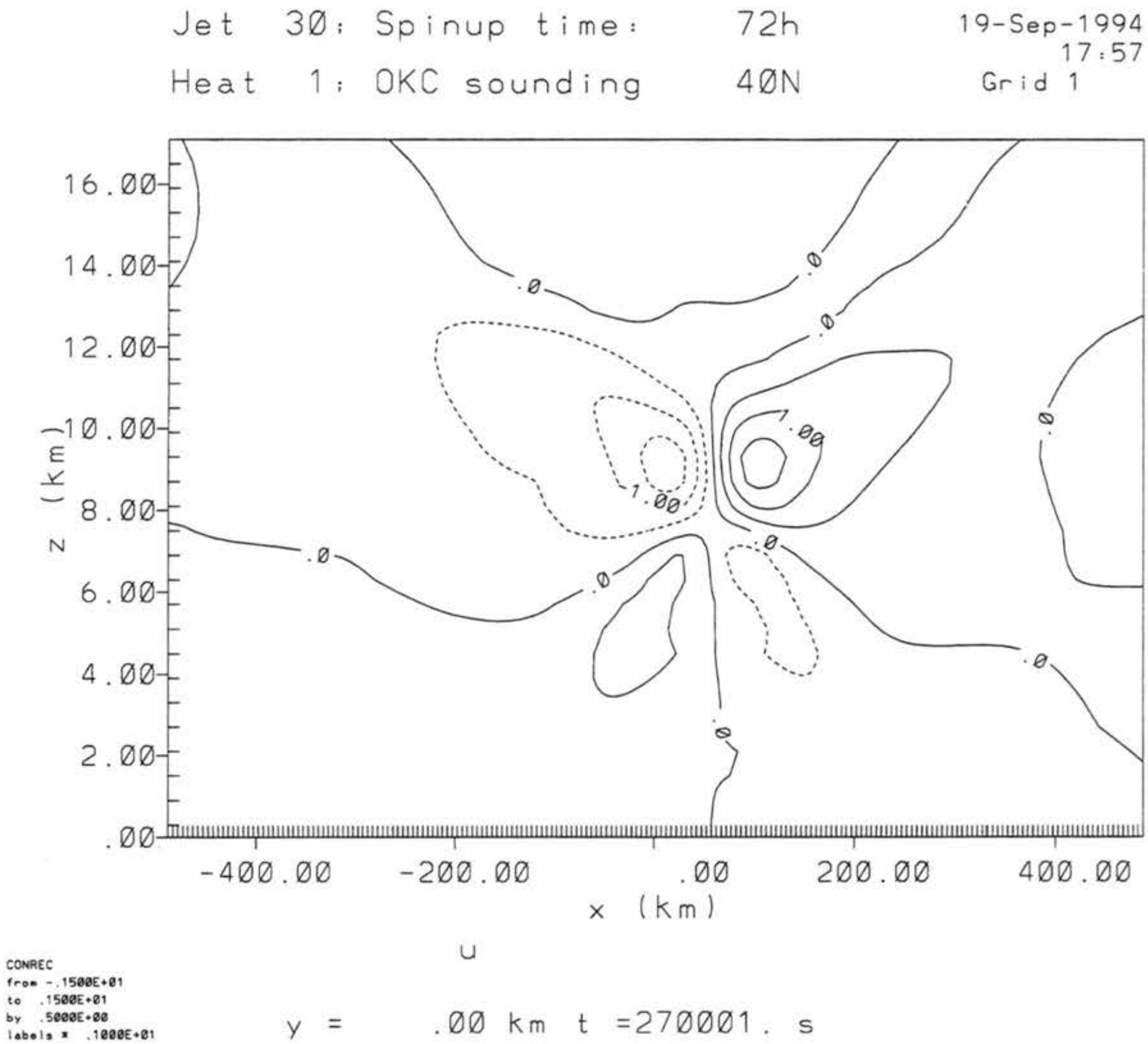

Figure 57. As in Fig. 46, except for t=3 h and for experiment 4a.

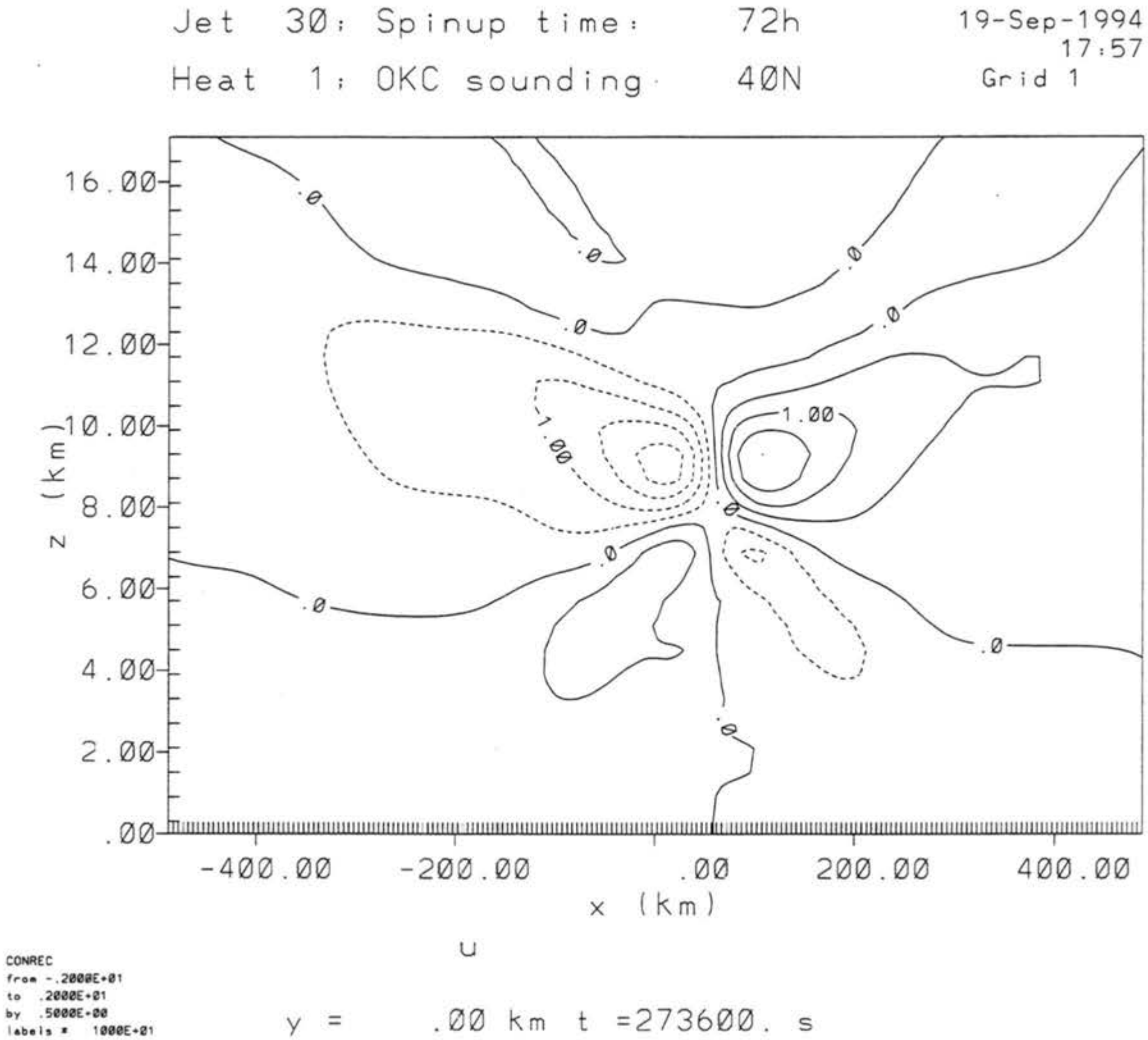

Figure 58. As in Fig. 46, except for t=4 h and for experiment 4a.

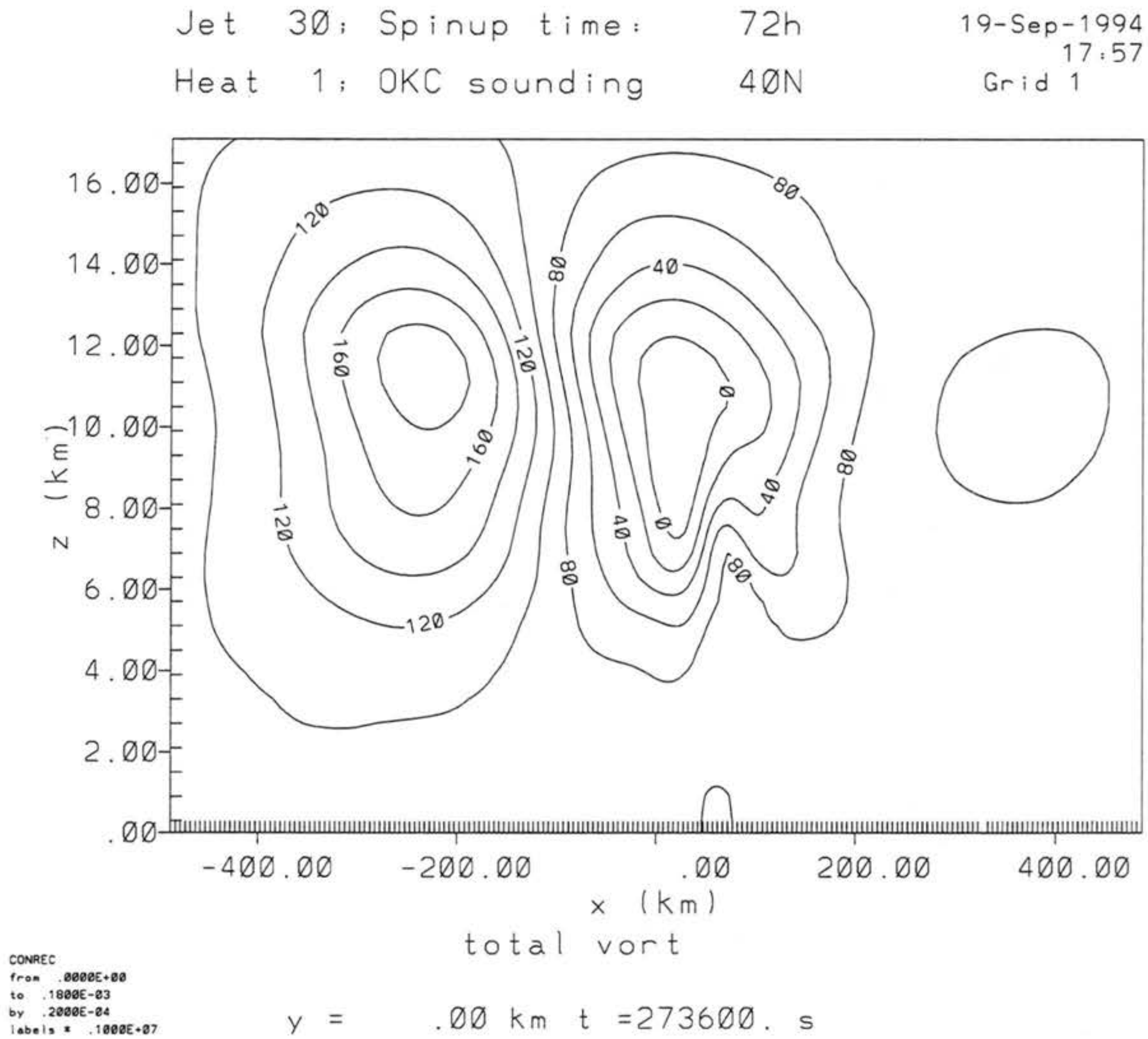

Figure 59. As in Fig. 49, except for t=4 h and for experiment 4a.

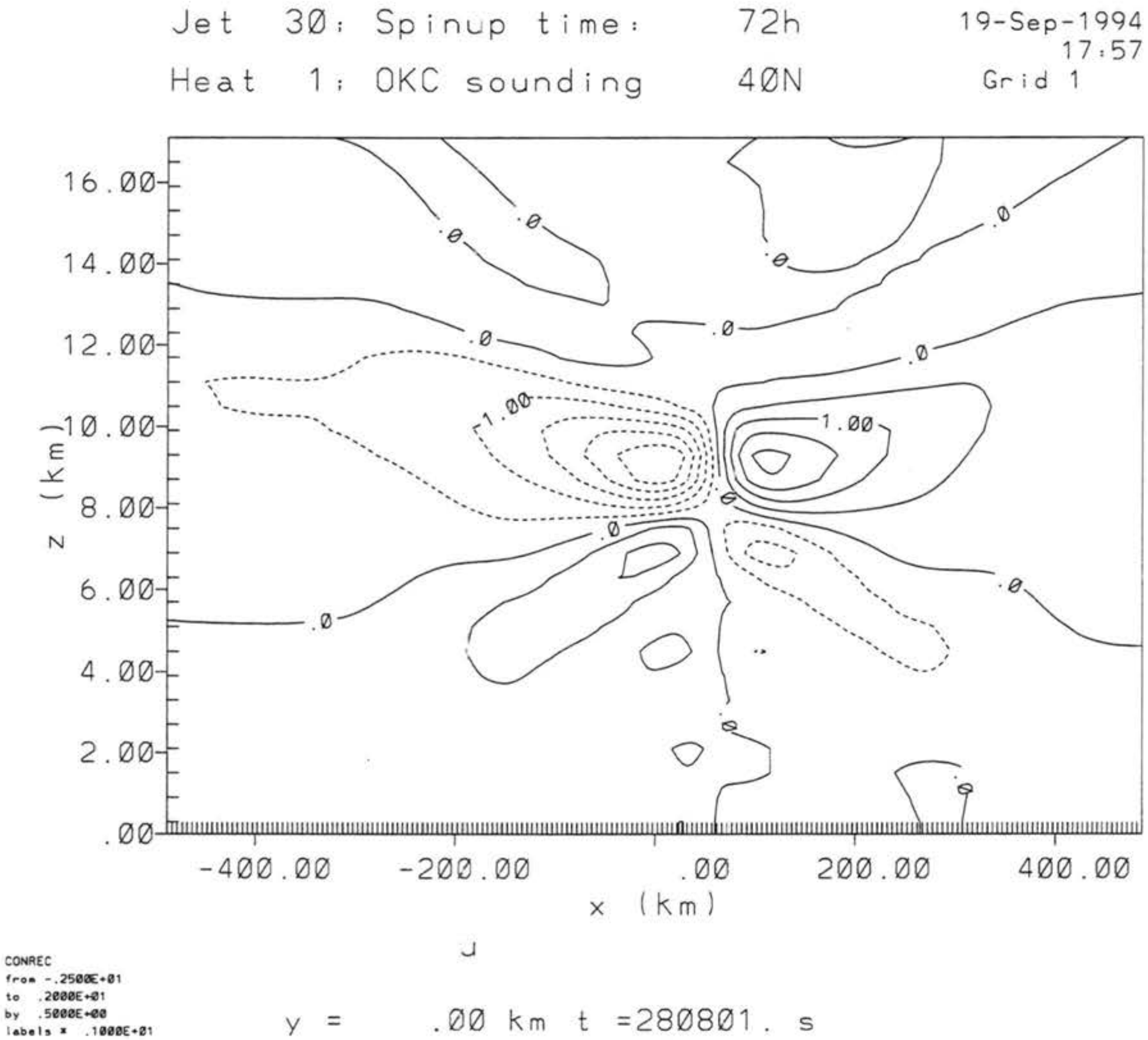

Figure 60. As in Fig. 46, except for t=6 h and for experiment 4a.

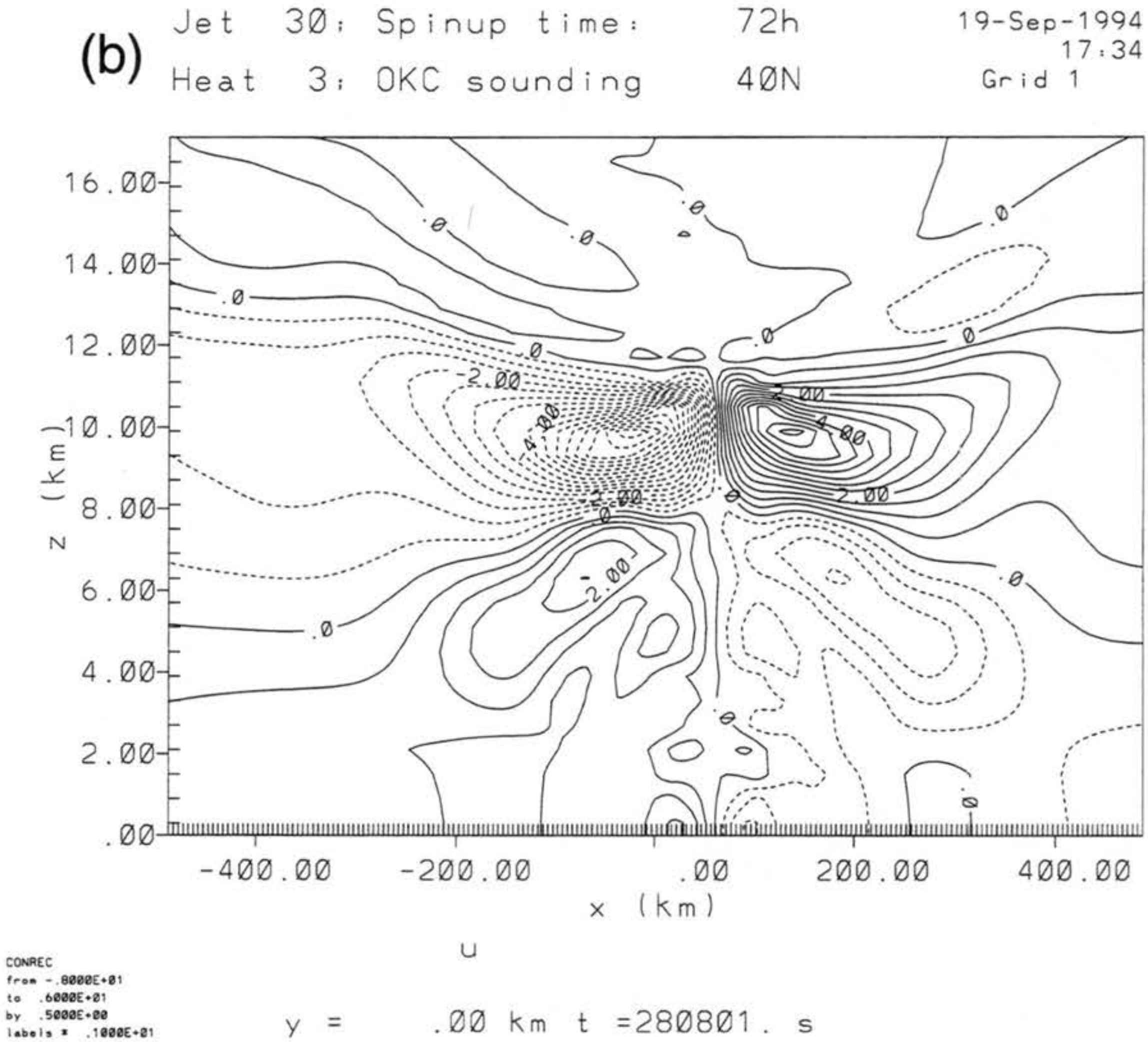

Figure 61. As in Fig. 46, except for t=6 h and for experiment 4b.

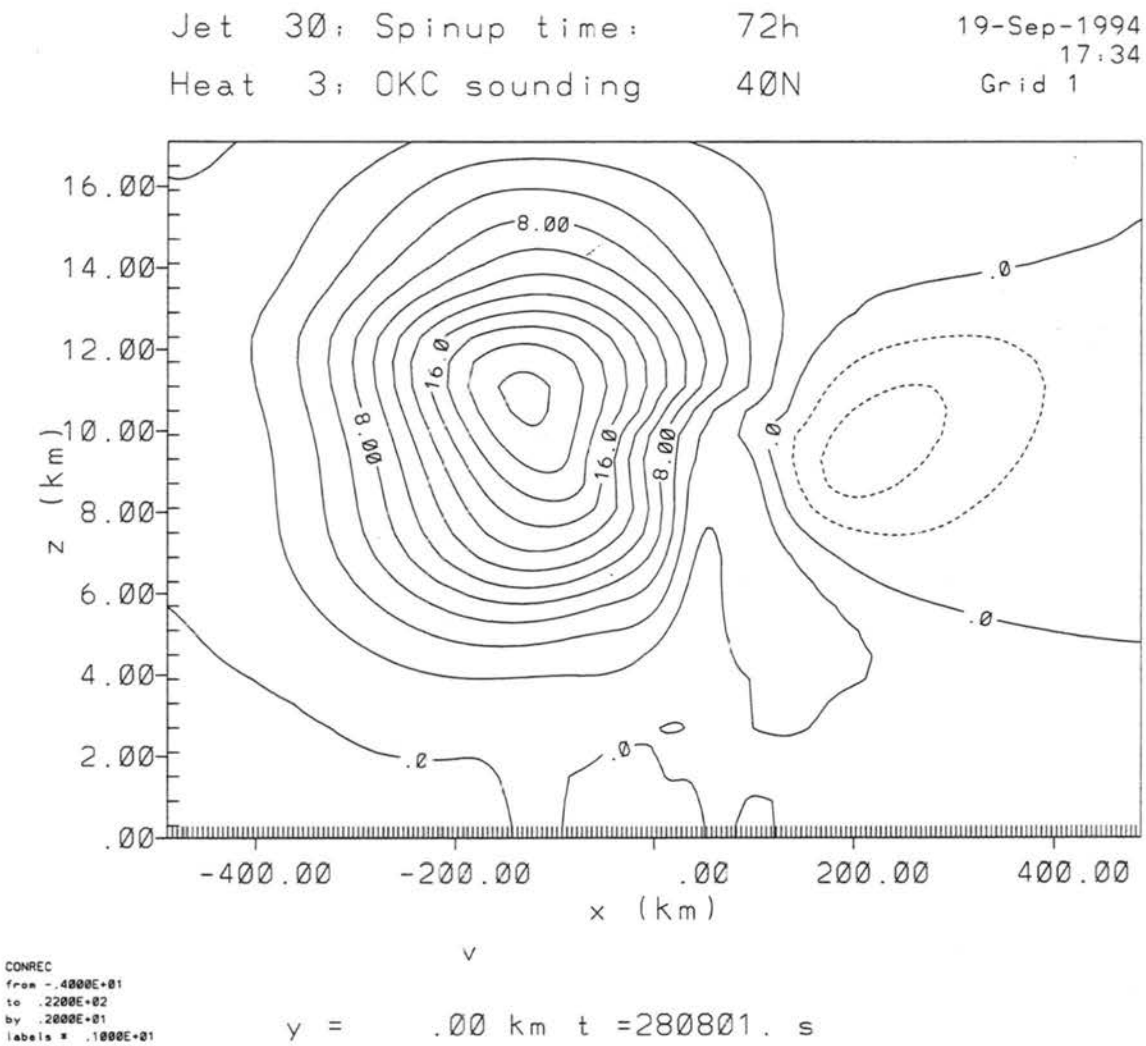

Figure 62. As in Fig. 48, except for t=6 h and for experiment 4b.

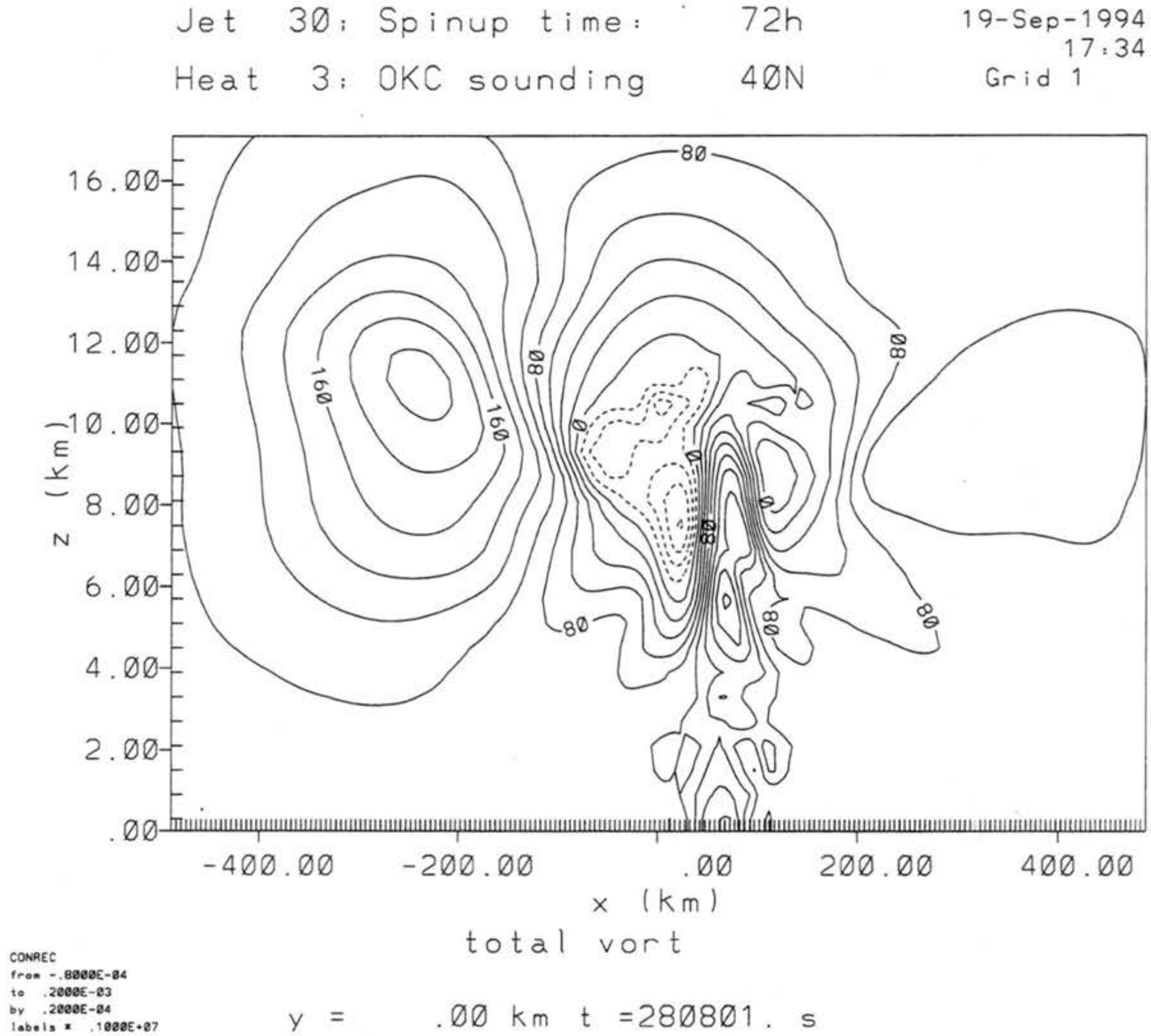

Figure 63. As in Fig. 49, except for t=6 h and for experiment 4b.

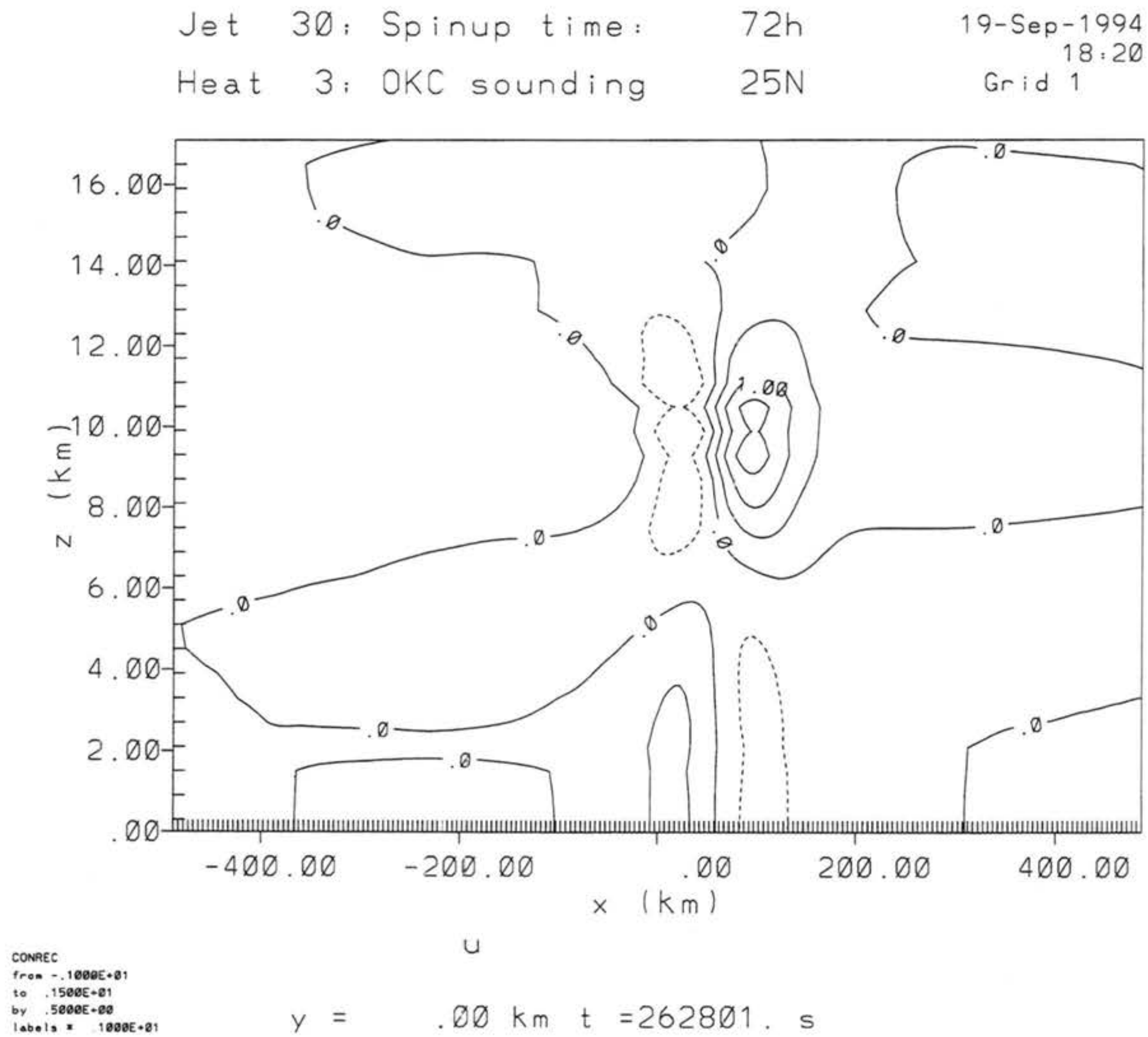

Figure 64. As in Fig. 46, except for t=1 h and for experiment 4e.

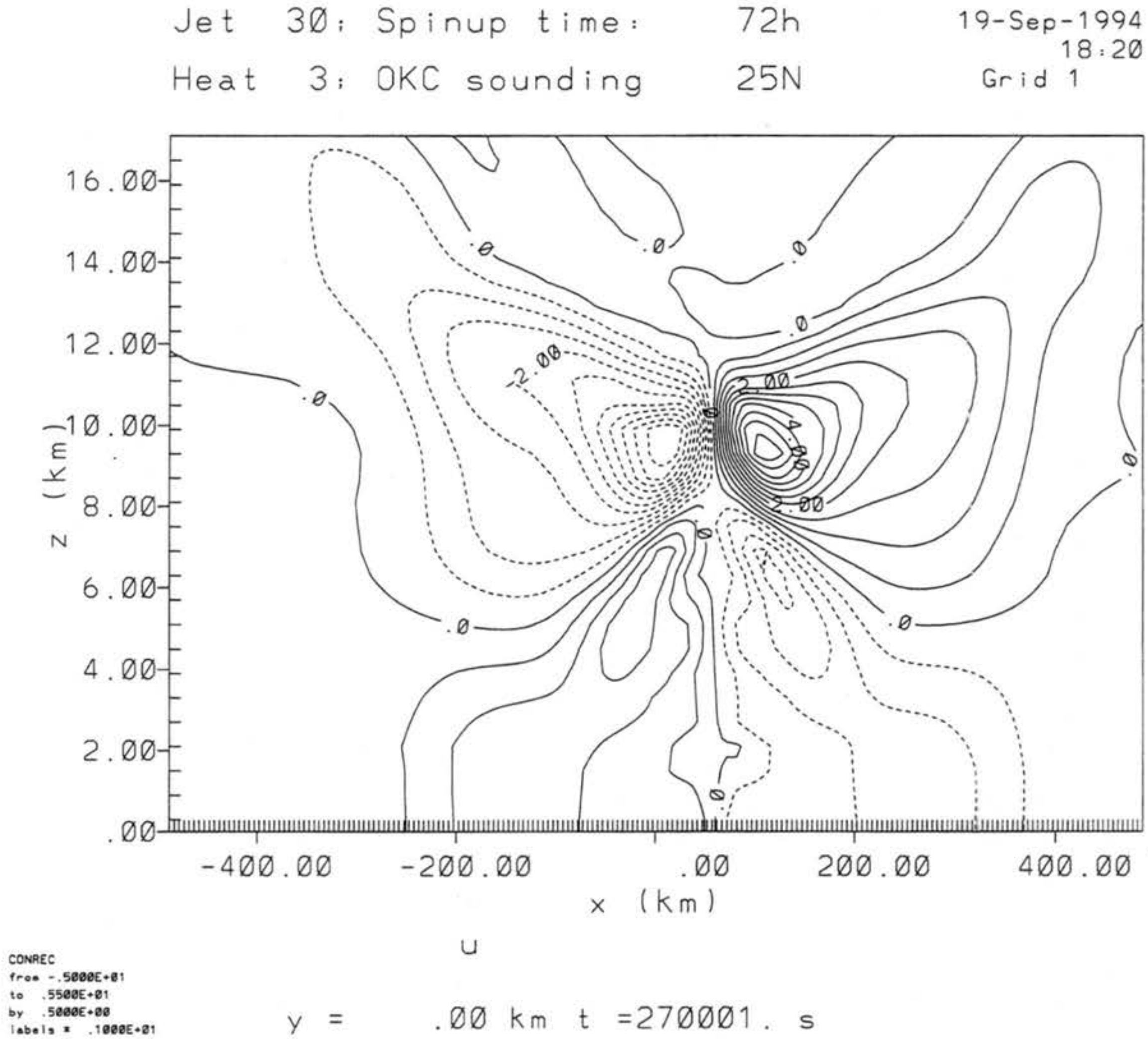

Figure 65. As in Fig. 46, except for t=3 h and for experiment 4e.

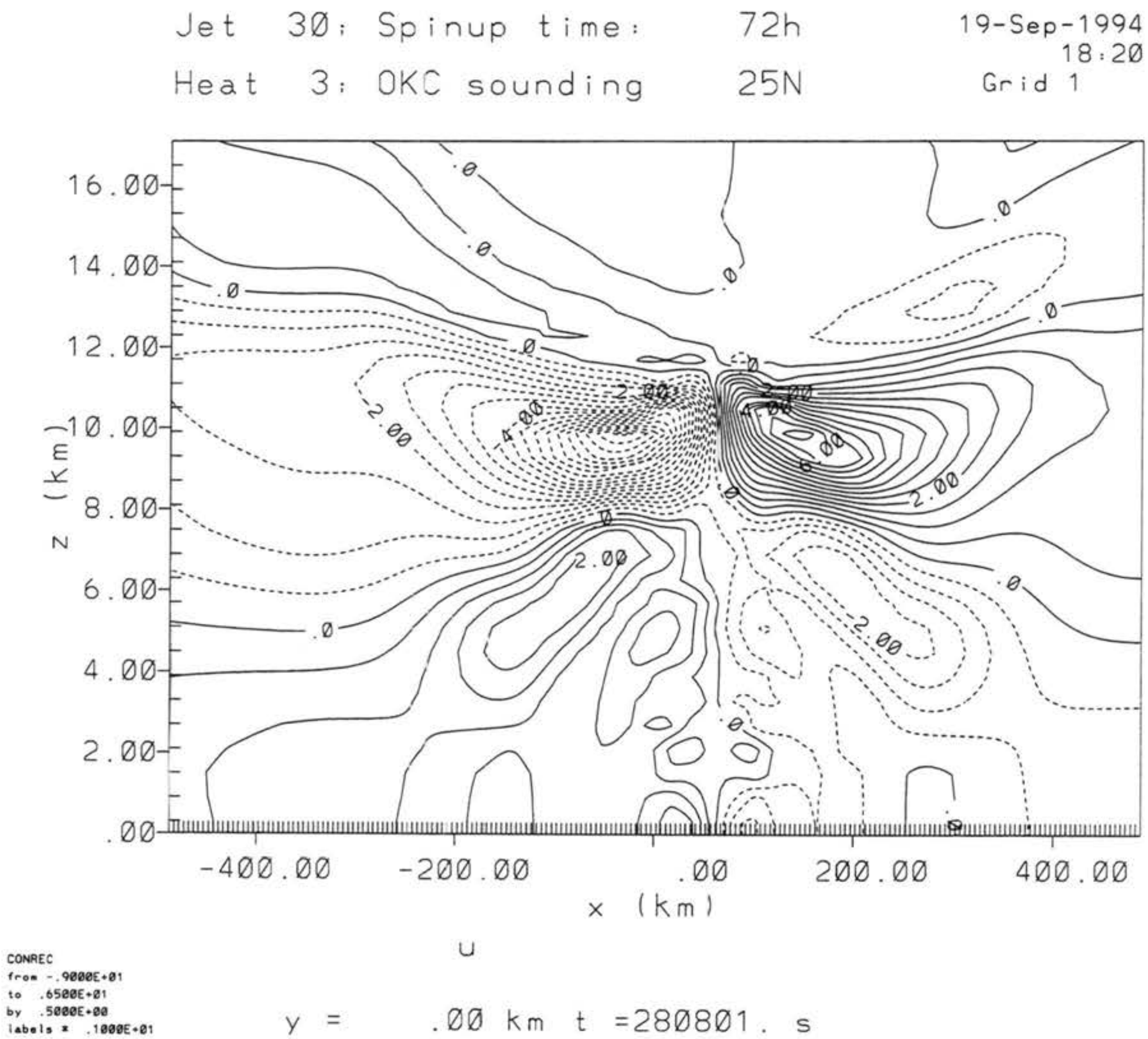

Figure 66. As in Fig. 46, except for t=6 h and for experiment 4e.

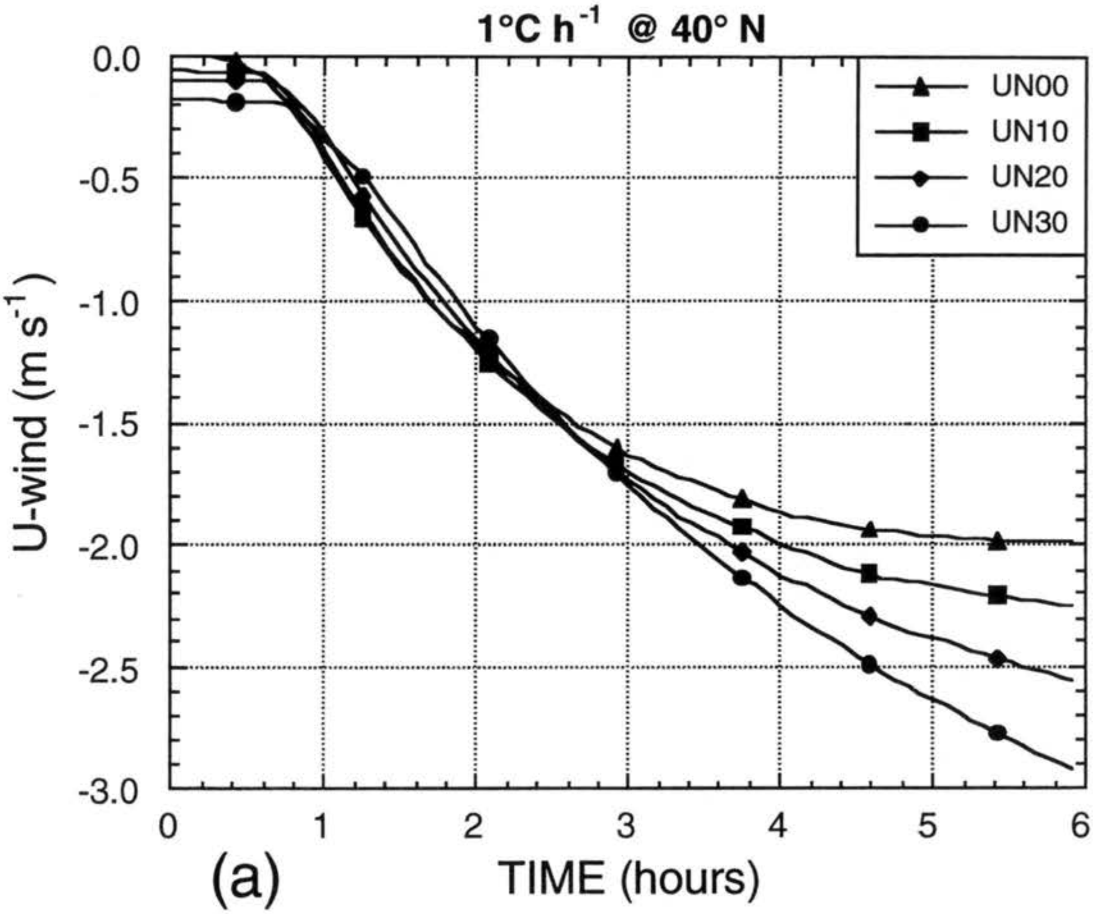

Figure 67. Time profile showing the rate of change of the *u*-component of the wind for the four wind strengths (0, 10, 20, and 30 m s^{-1}) for a heating rate of a) 1°C h^{-1}, b) 3°C h^{-1}, and c) 5°C h^{-1}.

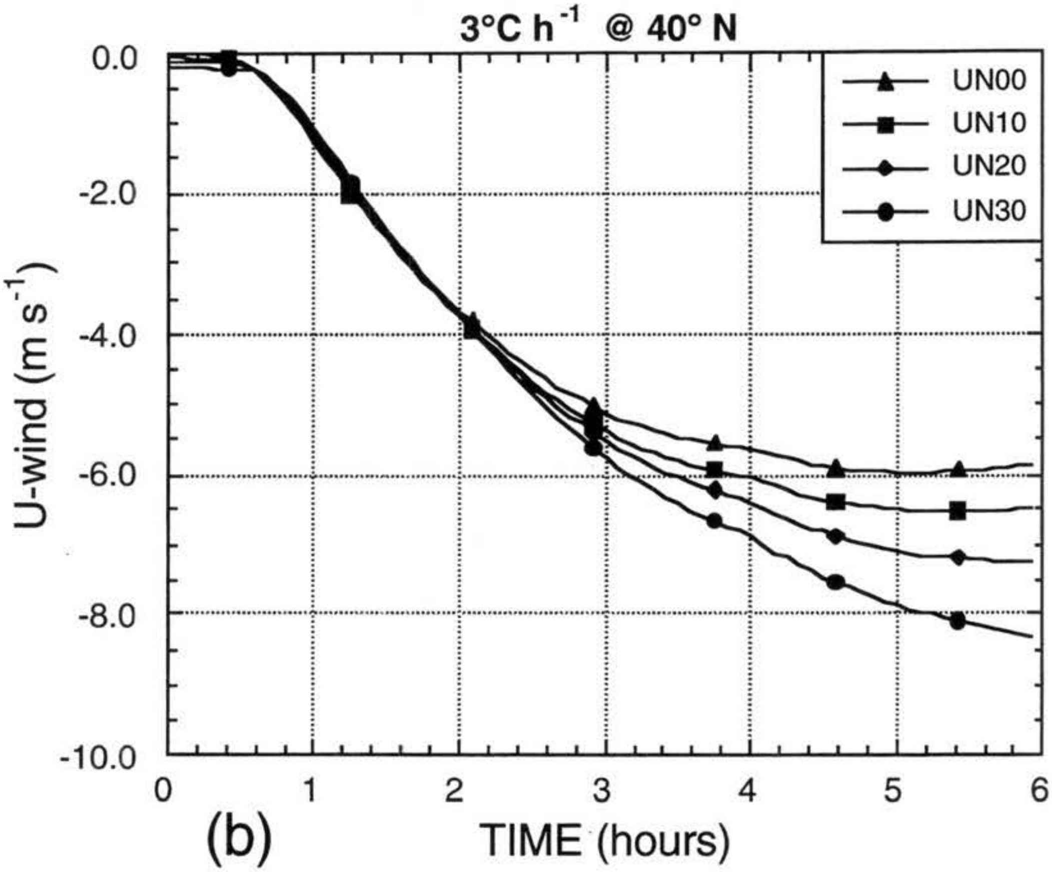

Figure 67. (Continued)

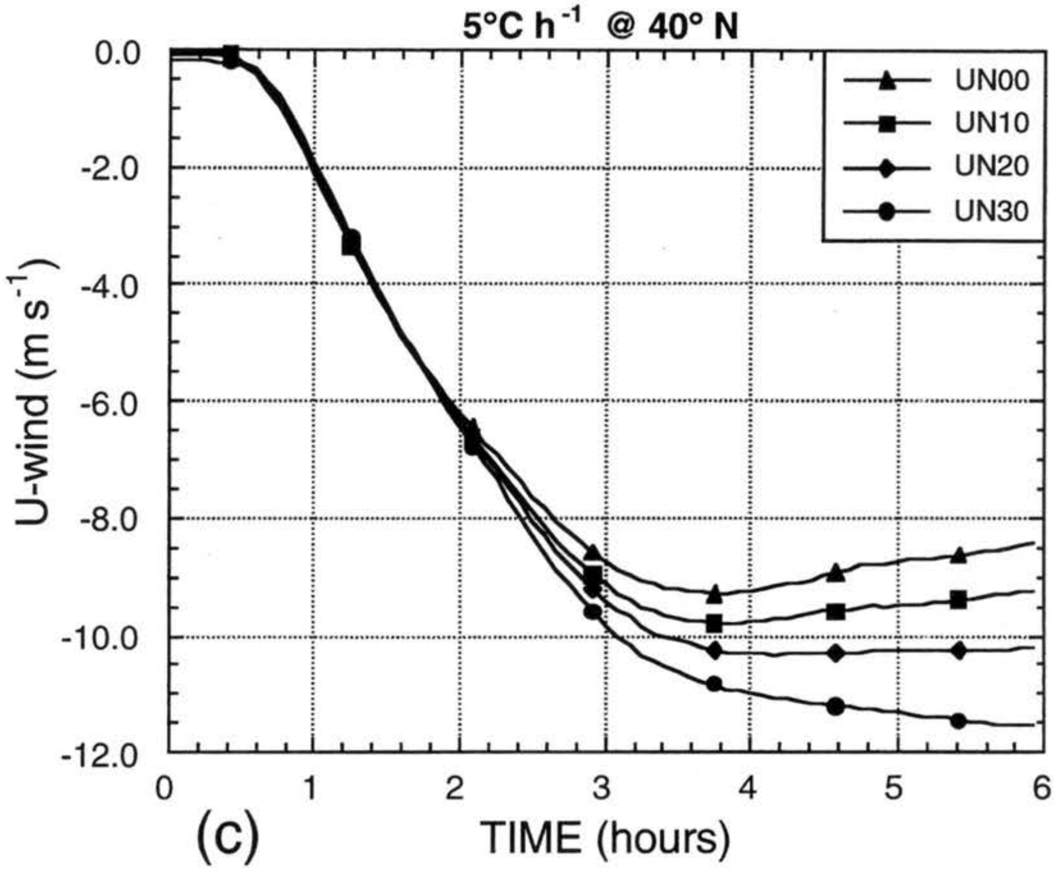

Figure 67. (Continued)

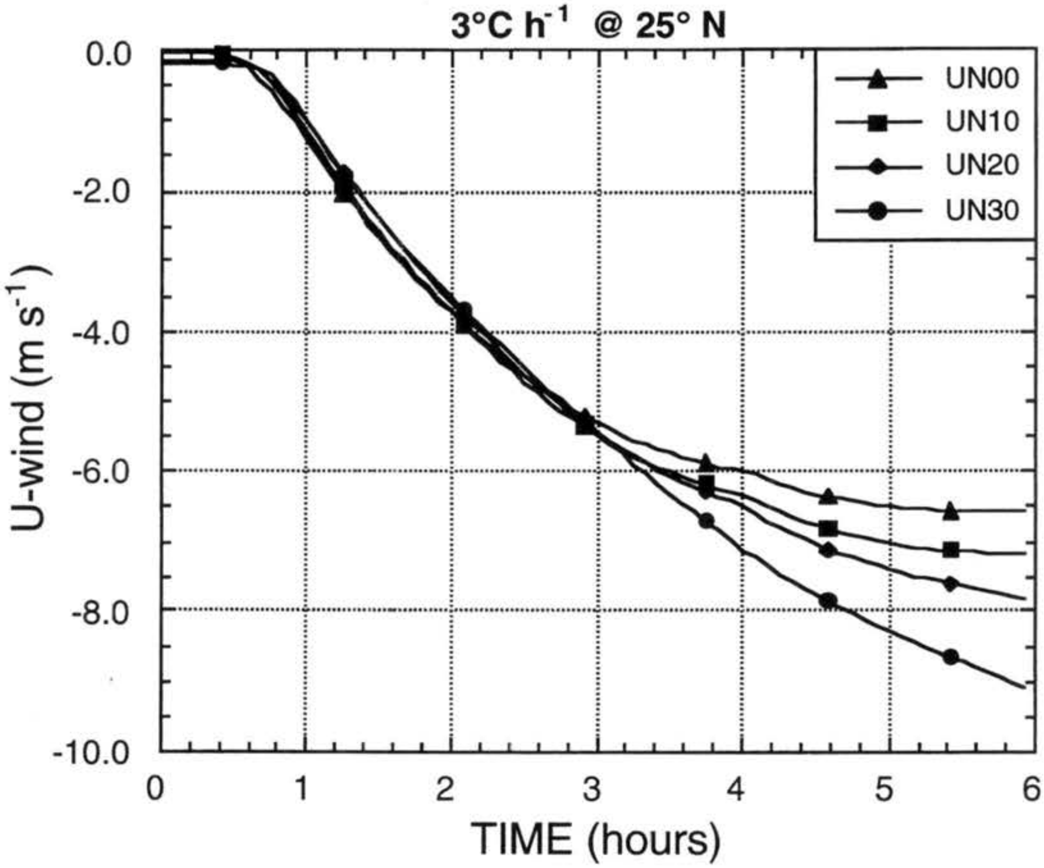

Figure 68. As in Fig. 67a, except for a latitude of 25° and heating rate of 3°C h^{-1}.

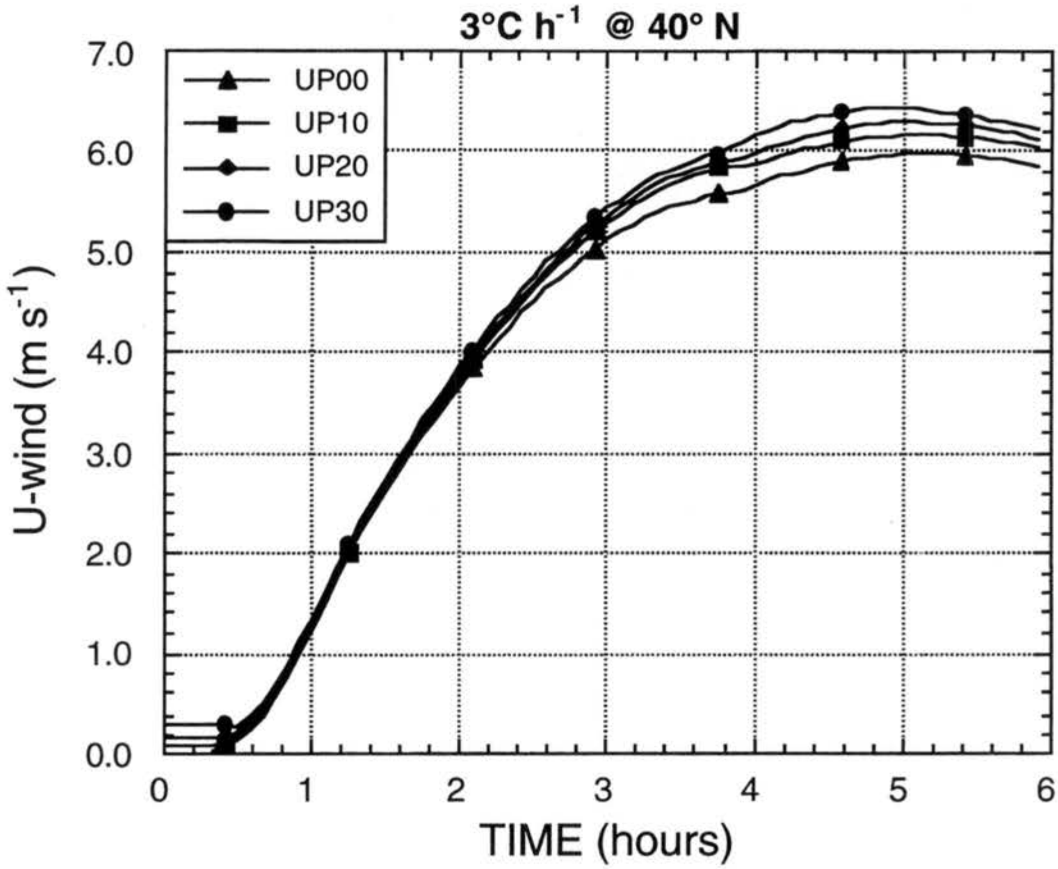

Figure 69. As in Fig. 67a, except for 3°C h^{-1} and only the winds with a westerly component are shown.

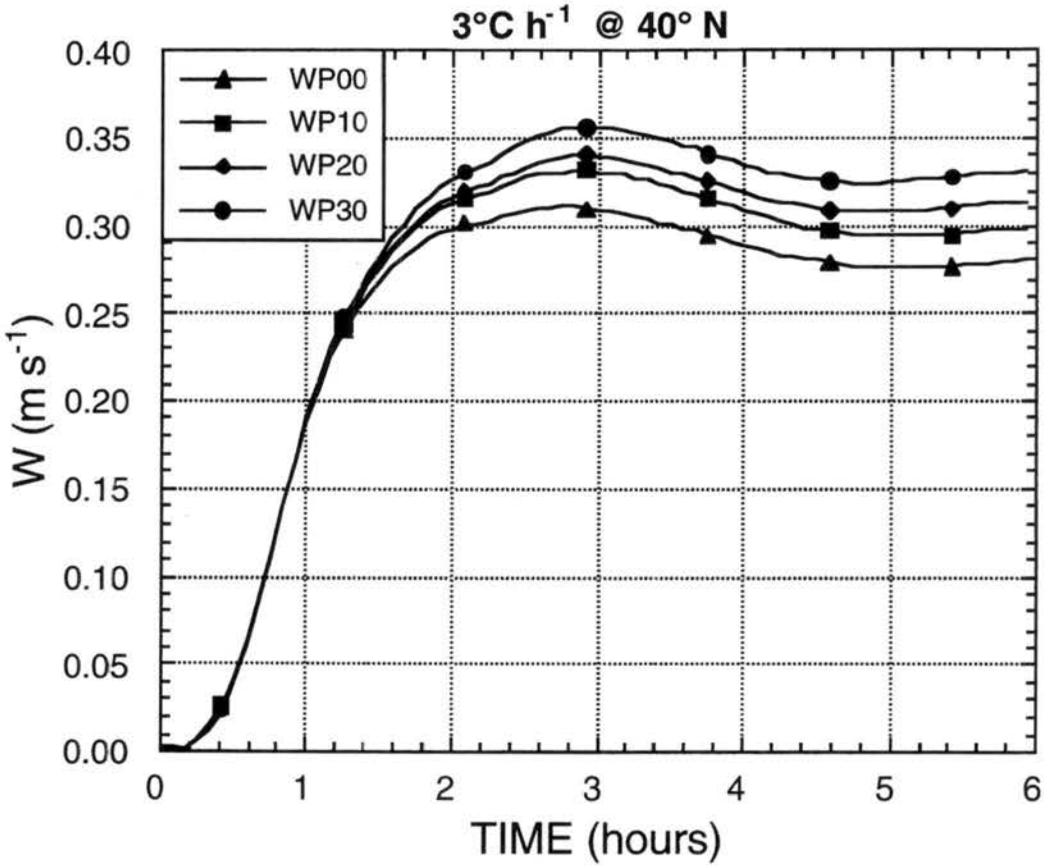

Figure 70. Time profiles showing the rate of change of the vertical velocities associated with different strengths of the jet (0, 10, 20, and 30 m s^{-1}). Heating rate is 3°C h^{-1}; latitude is 40°.

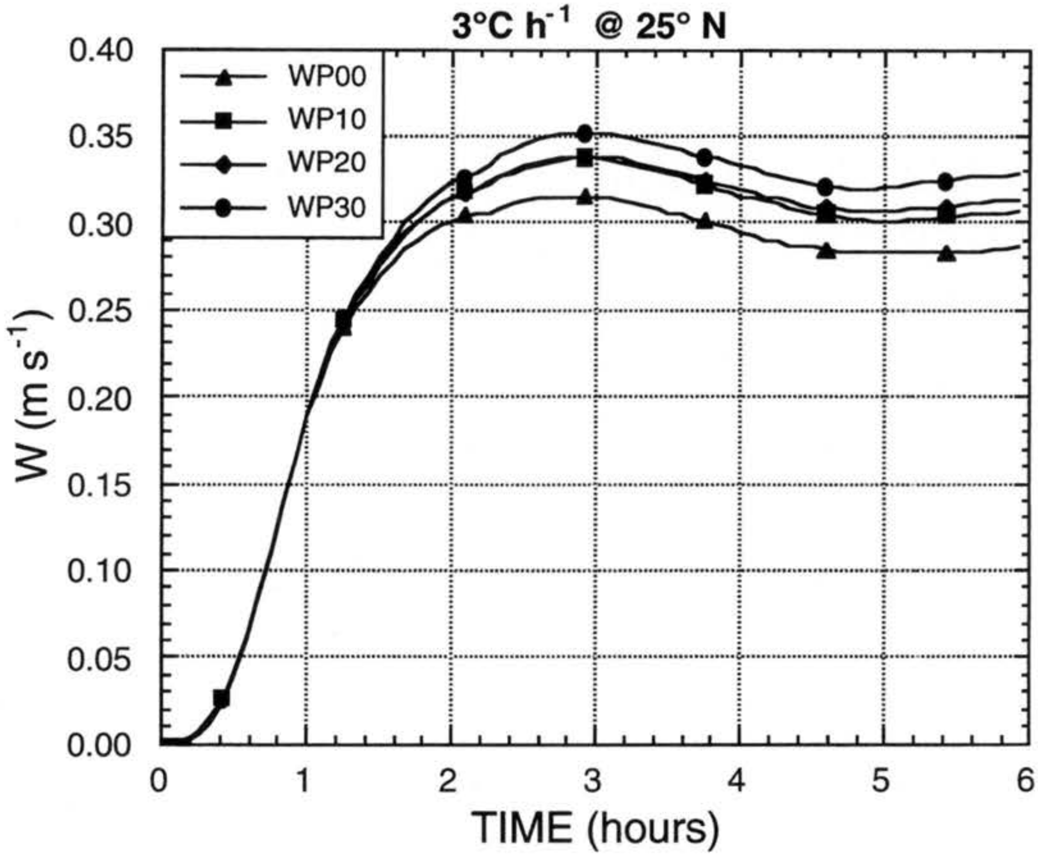

Figure 71. Time profiles showing the rate of change of the vertical velocities associated with different strengths of the jet (0, 10, 20, and 30 m s^{-1}). Heating rate is 3°C h^{-1}; latitude is 25°.

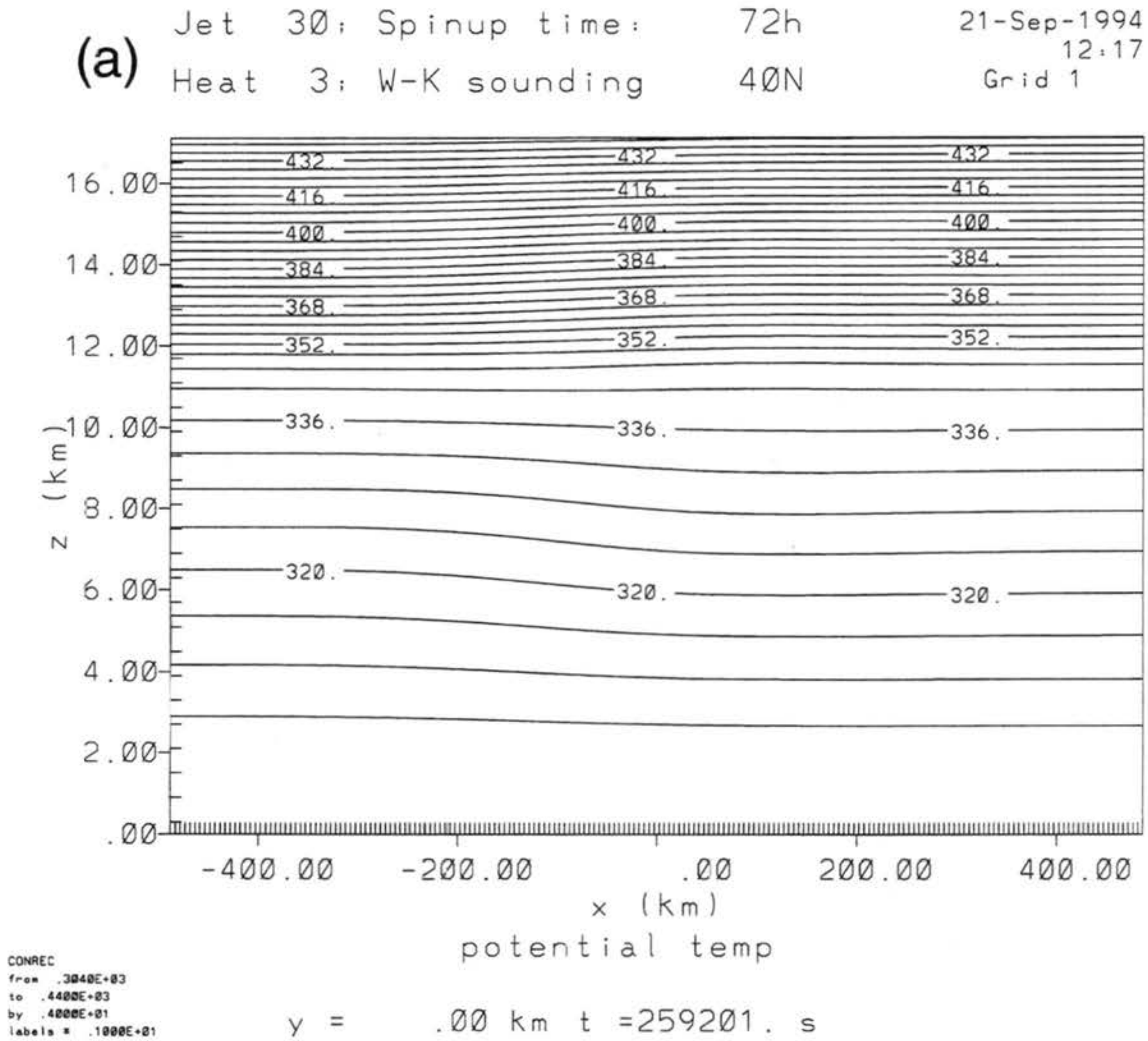

Figure 72a. As in Fig. 44, except for t=0 h and for experiment 5.

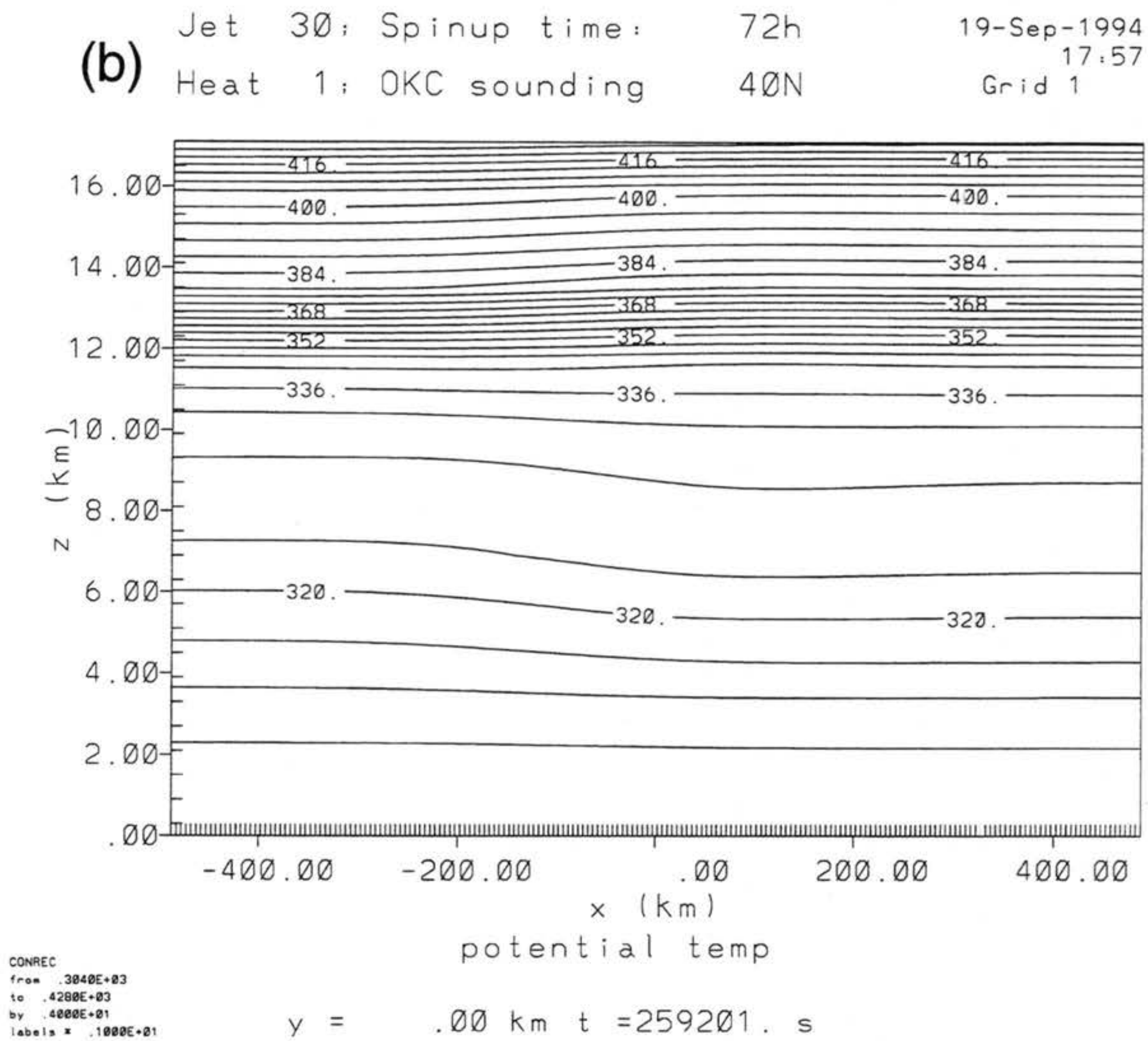

Figure 72b. As in Fig. 44, except for t=0 h and for experiment 4b.

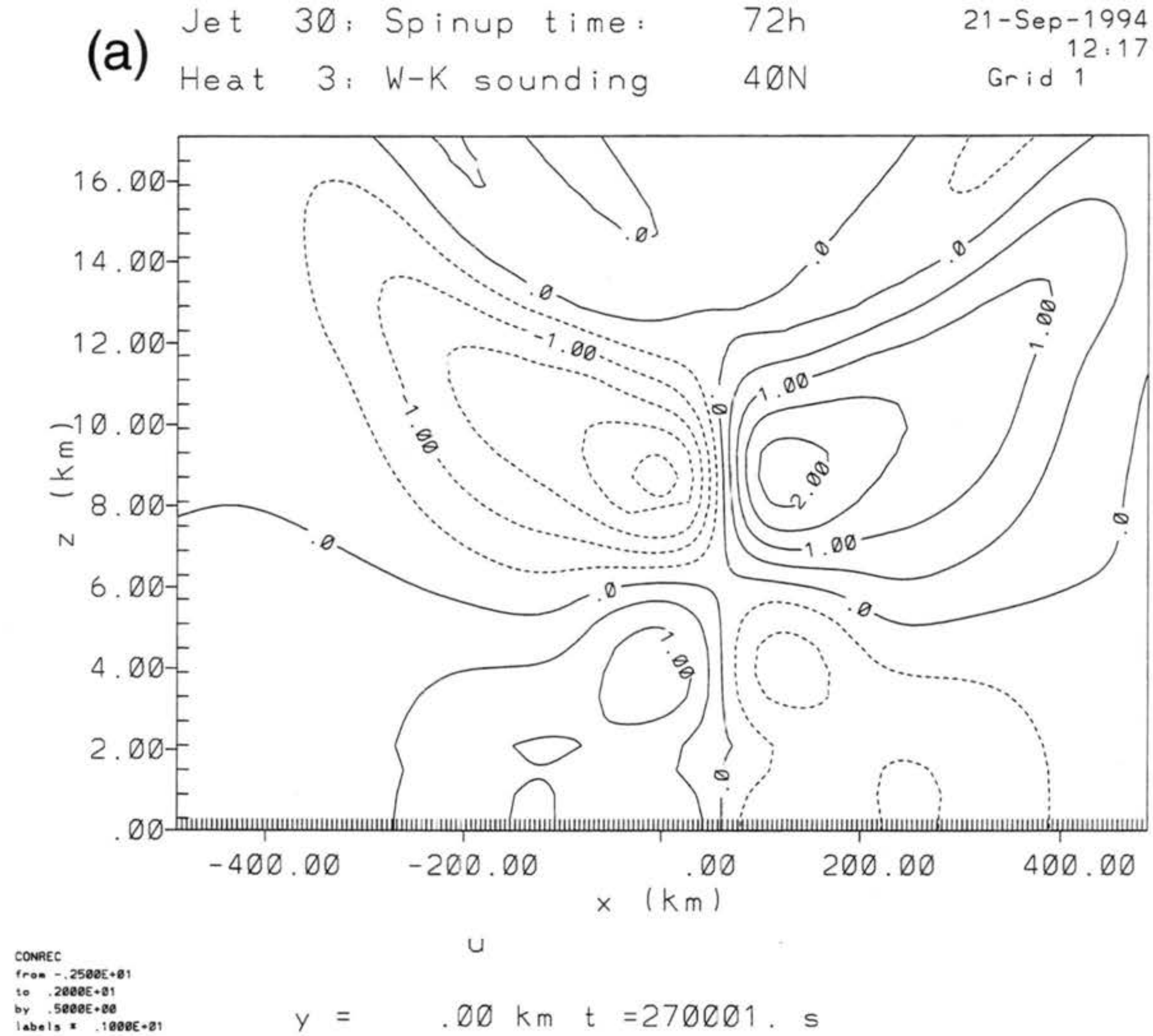

Figure 73a. As in Fig 46, except for t=3 h and for experiment 5.

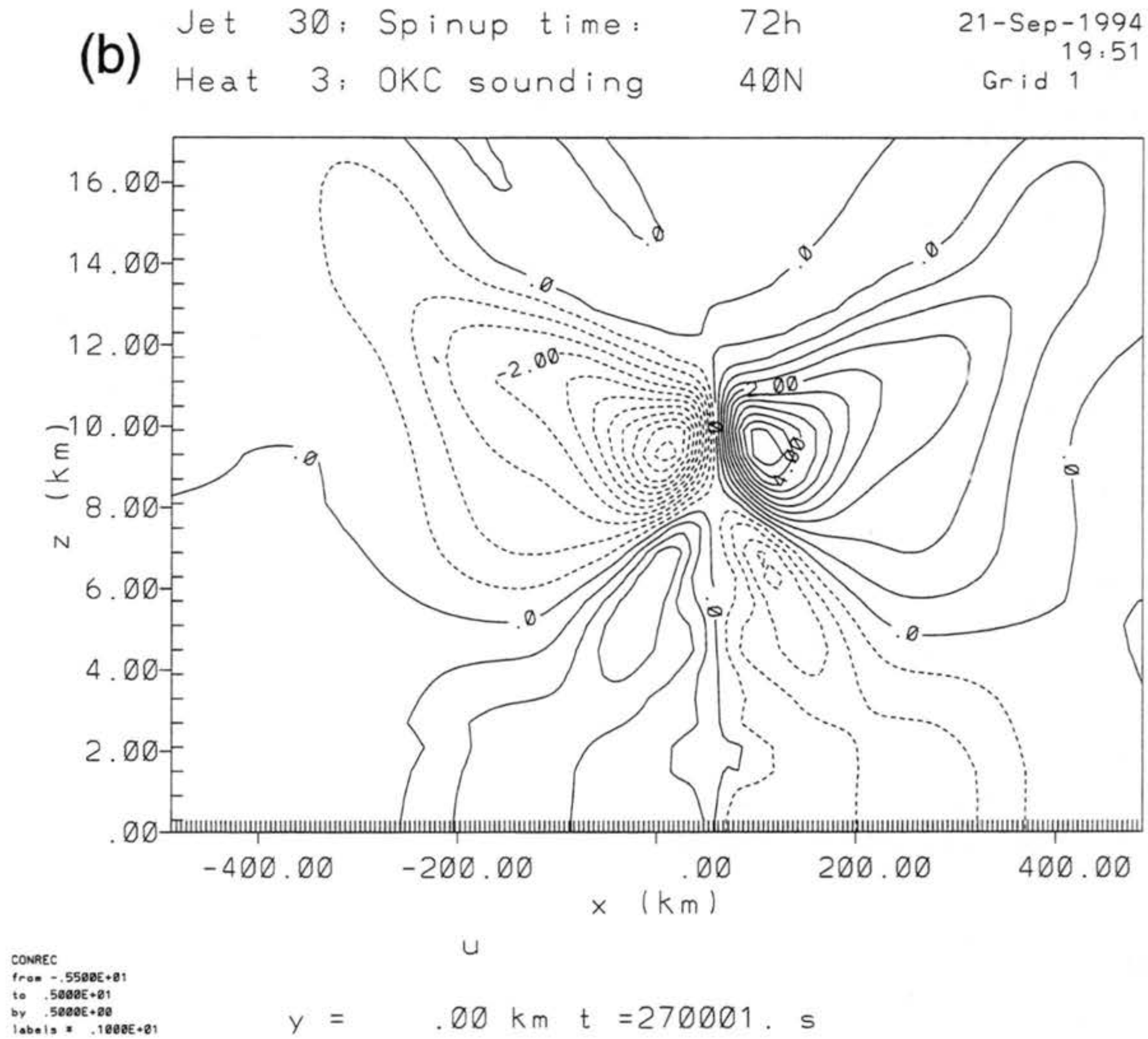

Figure 73b. As in Fig. 46, except for t=3 h and for experiment 4b.

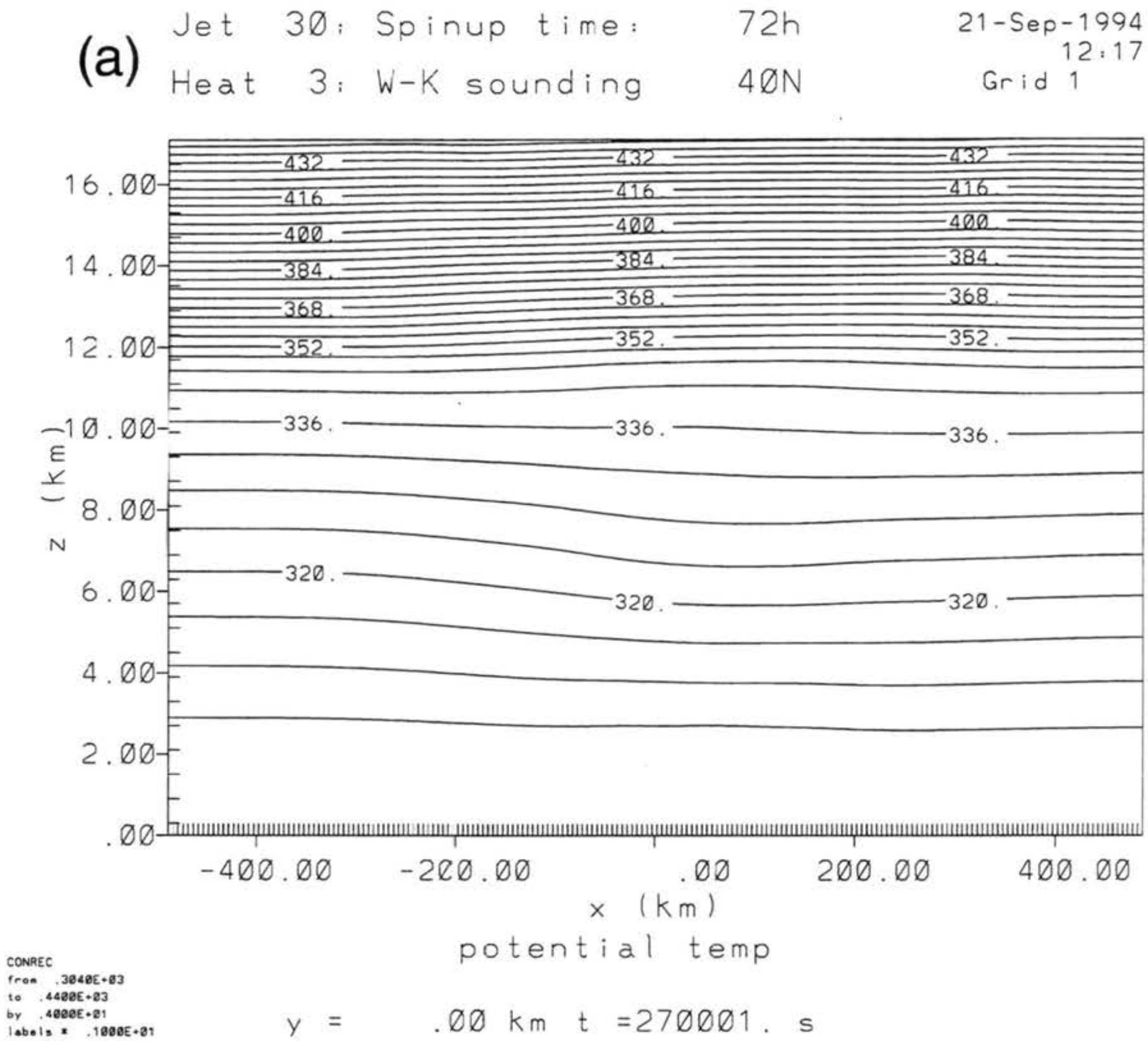

Figure 74a. As in Fig. 44, except for t=3 h and for experiment 5.

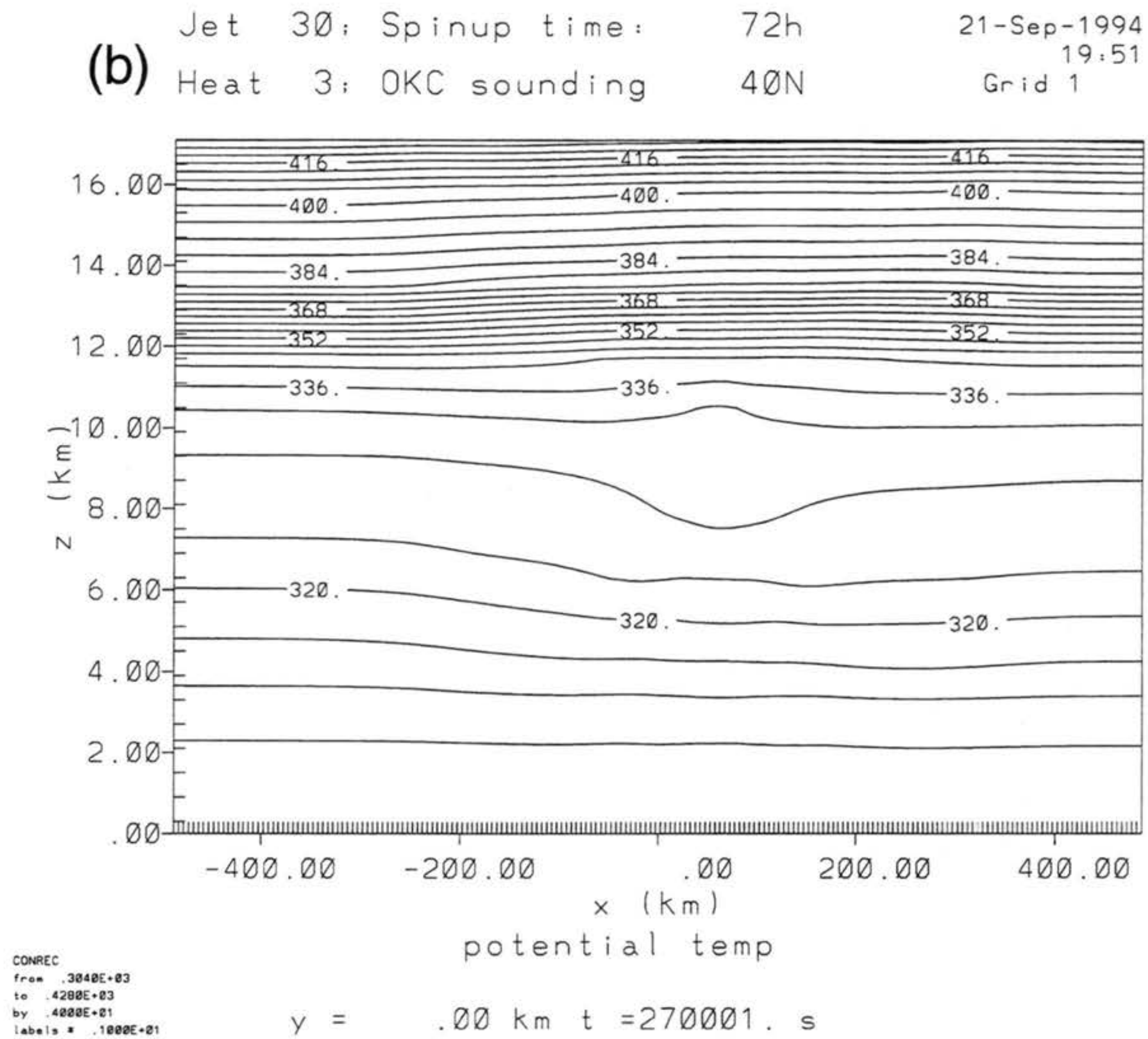

Figure 74b. As in Fig. 44, except for *t*=3 h and for experiment 4b.

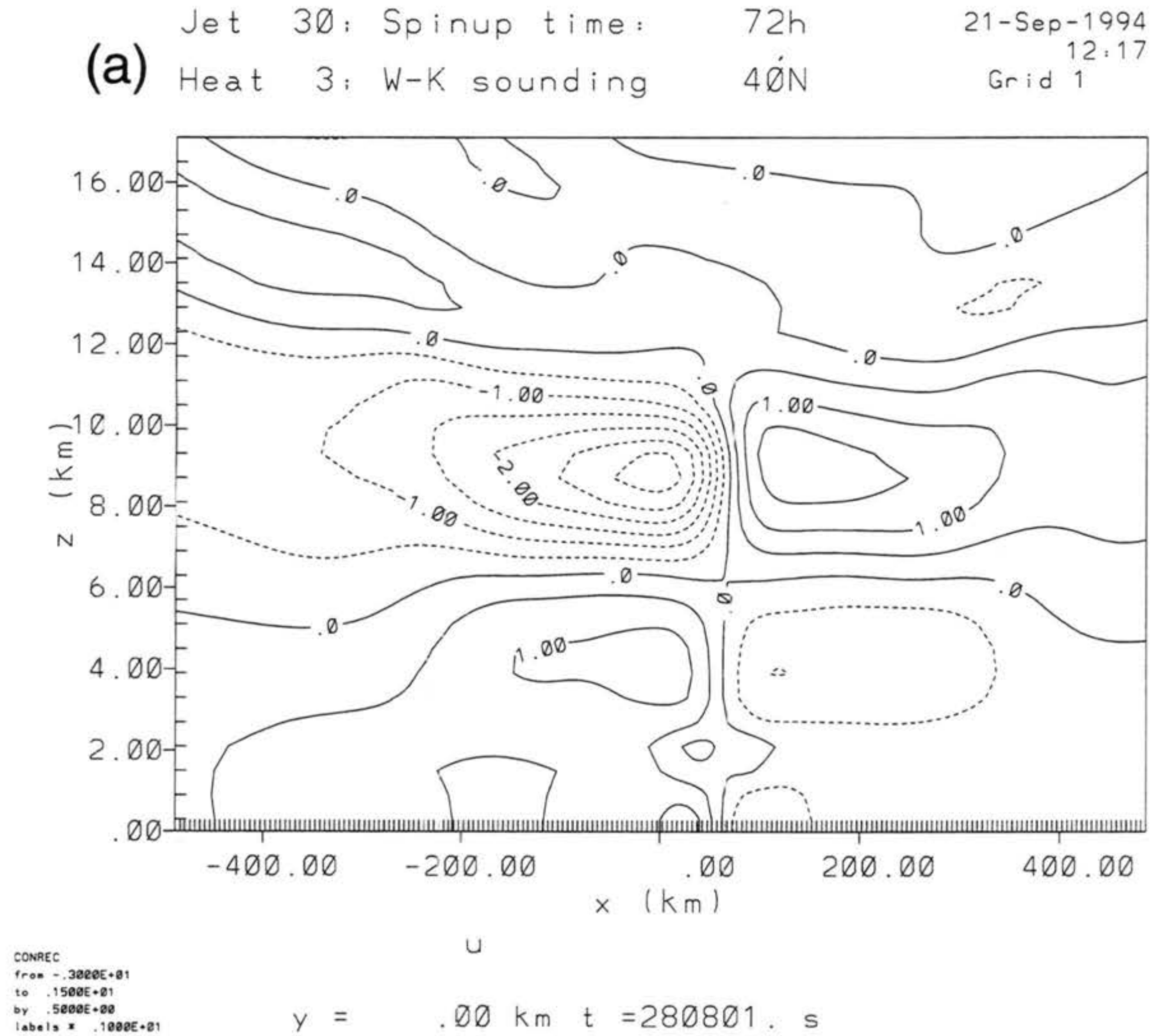

Figure 75a. As in Fig. 46, except for t=6 h and for experiment 5.

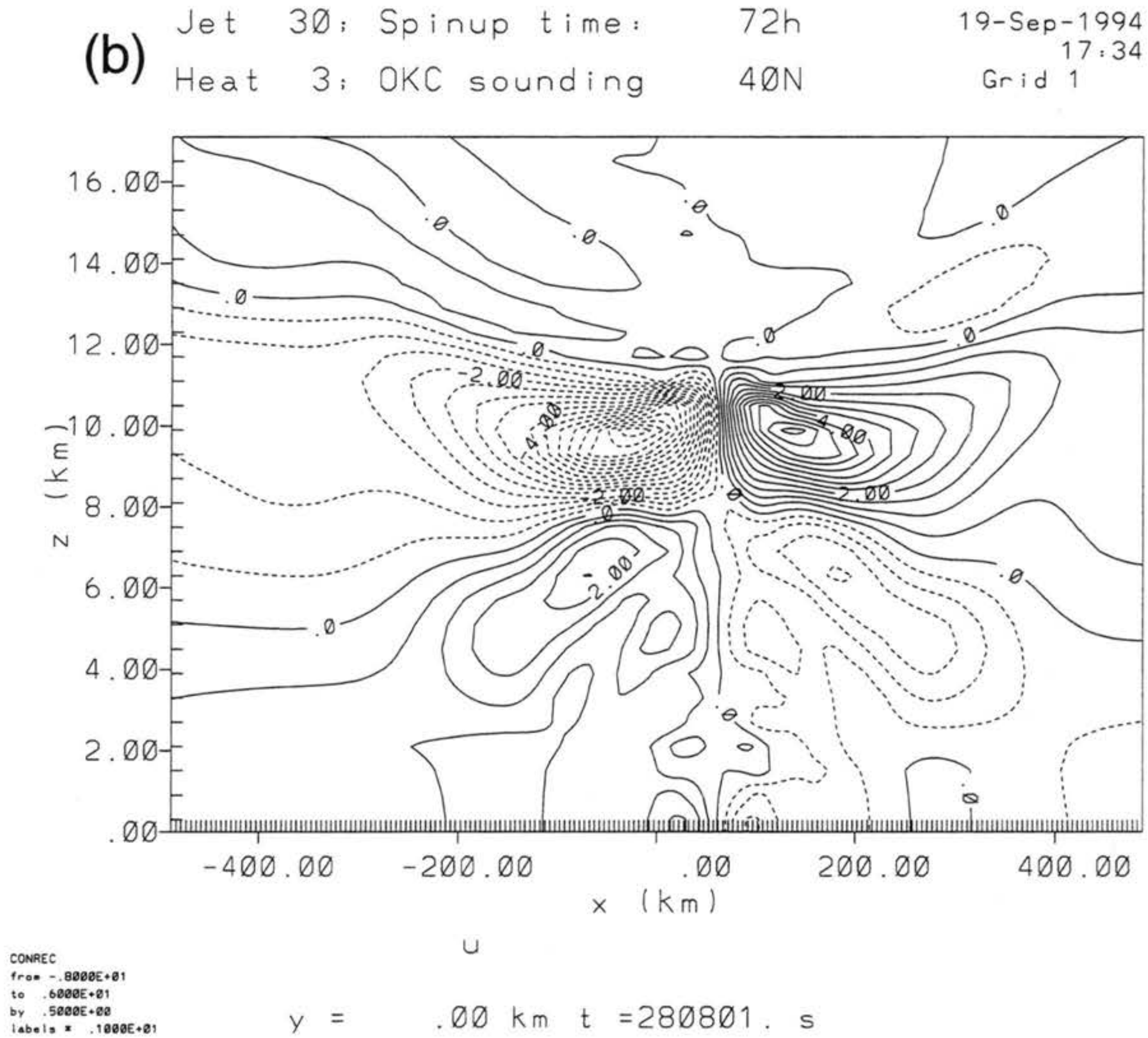

Figure 75b. As in Fig. 46, except for t=6 h and for experiment 4b.

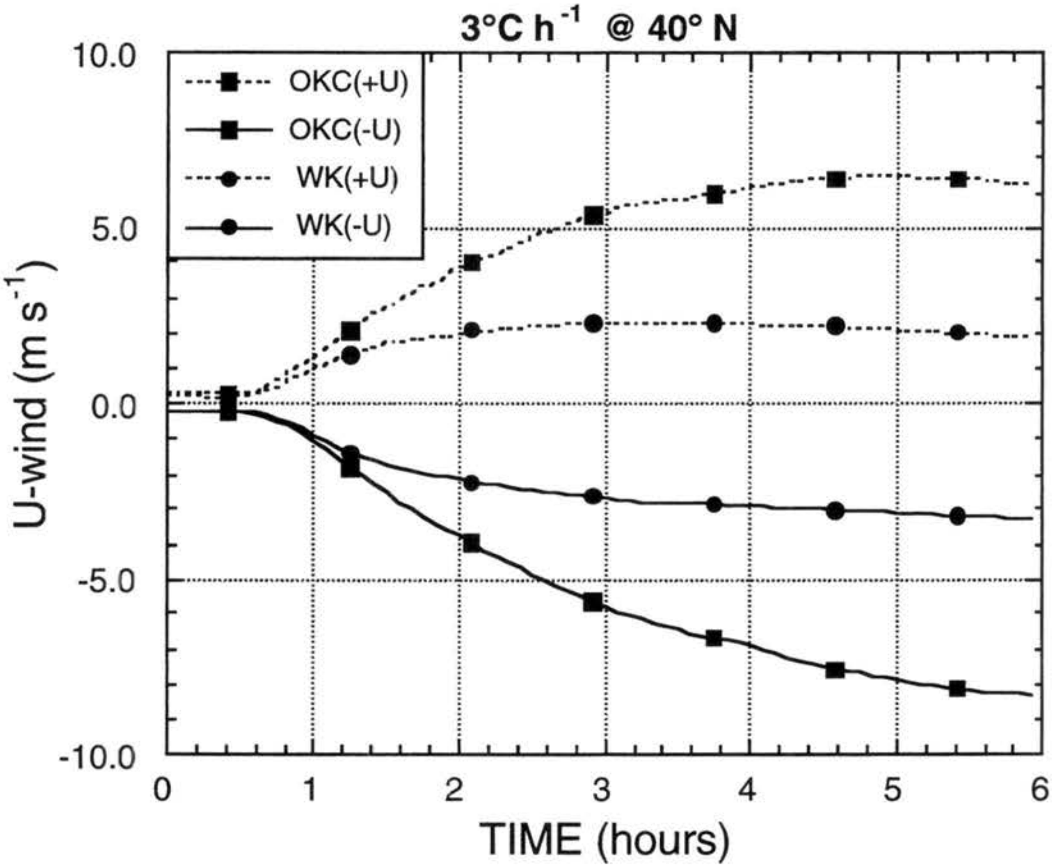

Figure 76. As in Fig. 67, except comparing the results of the OKC sounding and the WK sounding. The solid lines refer to the easterly outflow; the dashed lines refer to the westerly flow.

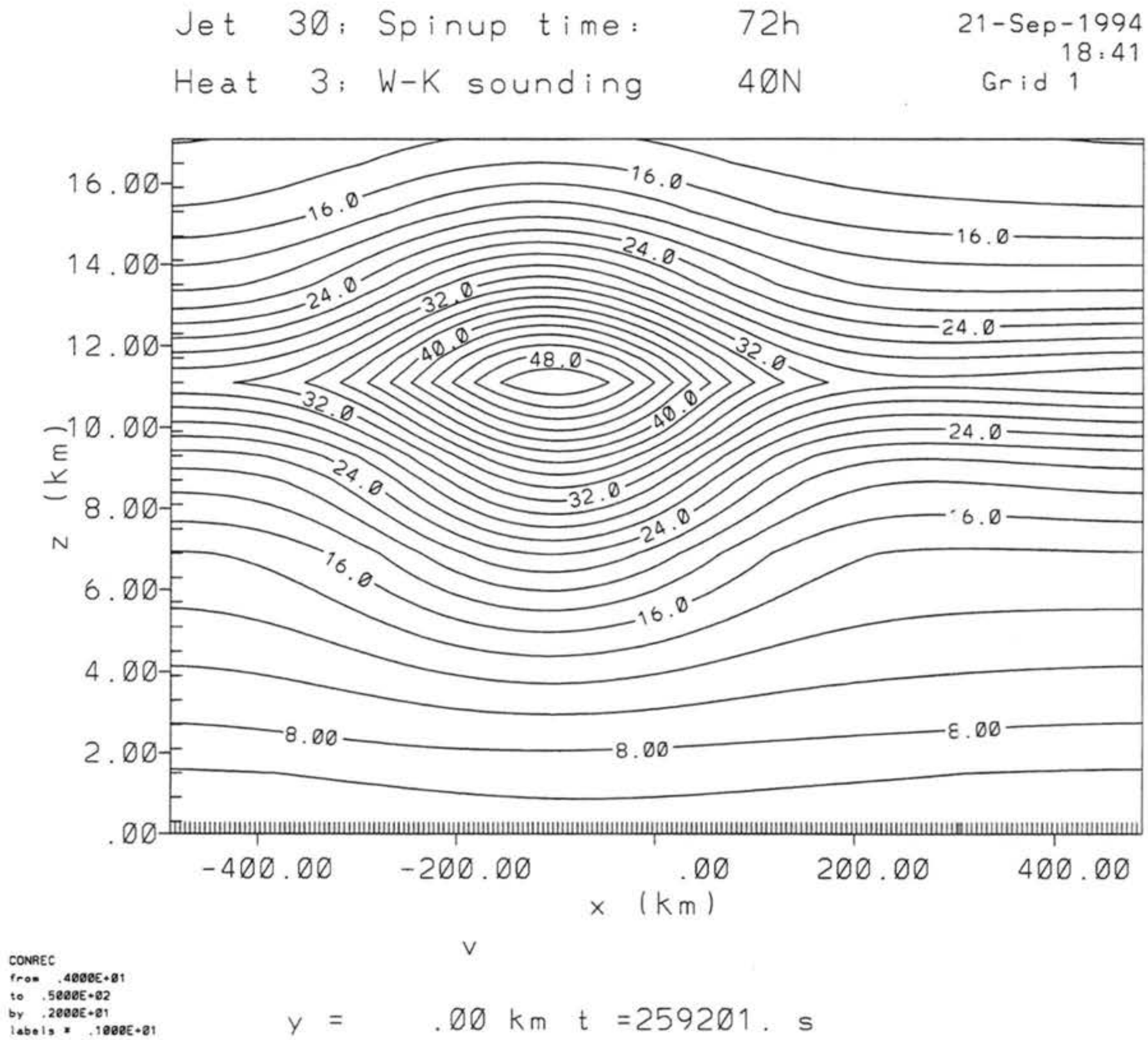

Figure 77. As in Fig. 48, except for t=0 h and for experiment 6 (WKV).

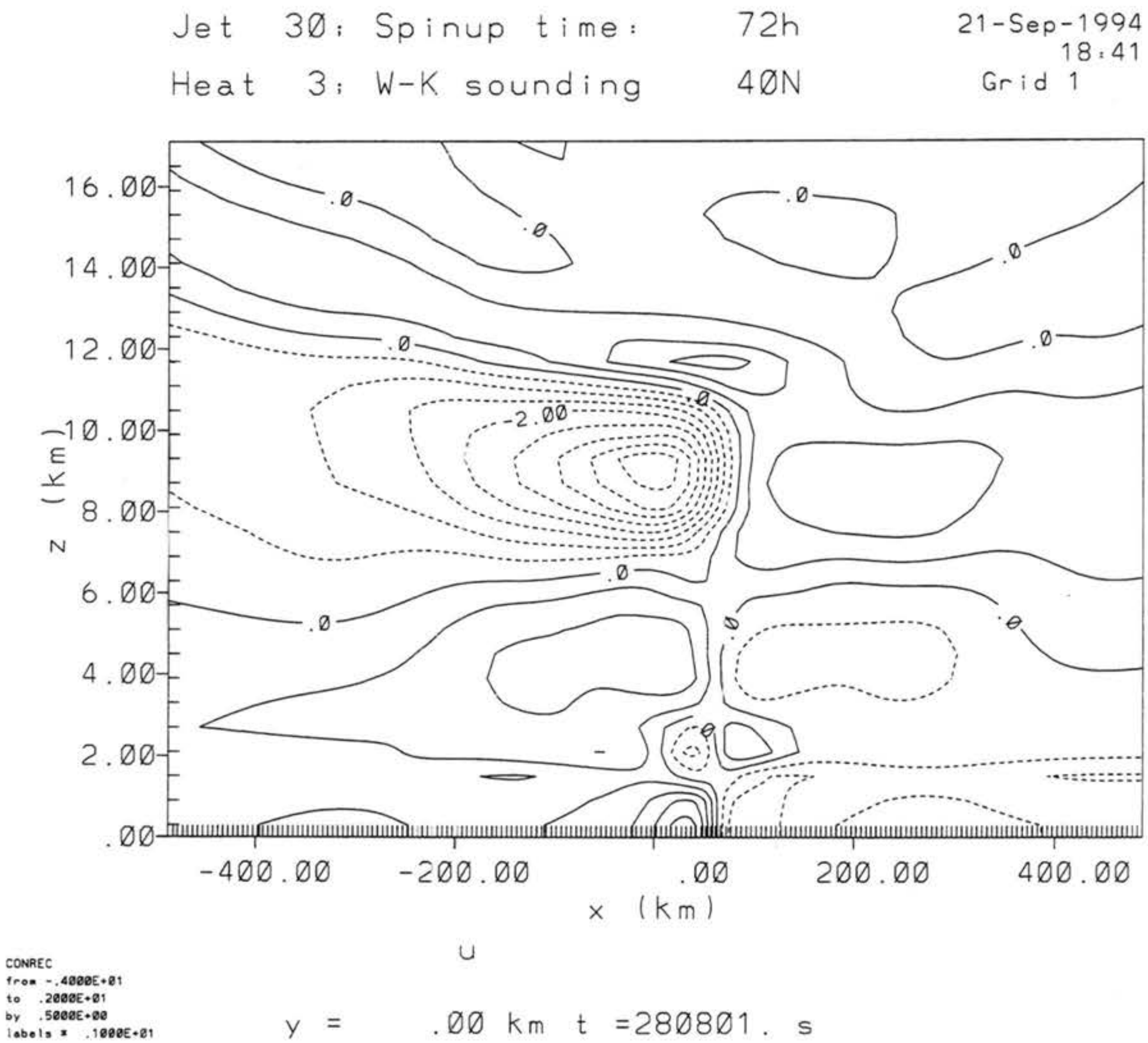

Figure 78. As in Fig. 46, except for t=6 h and for experiment 6 (WKV).

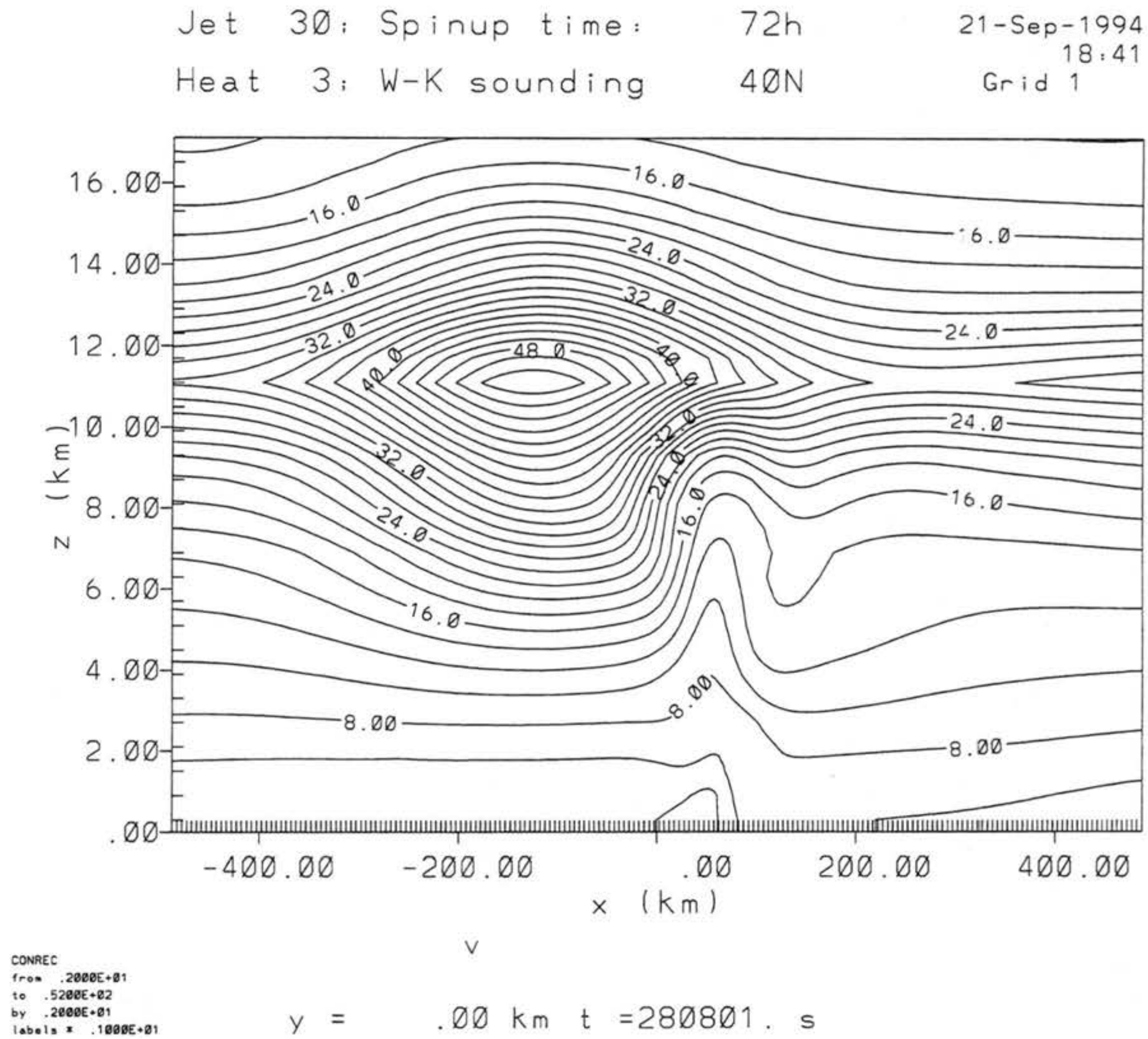

Figure 79. As in Fig. 48, except for t=6 h and for experiment 6 (WKV).

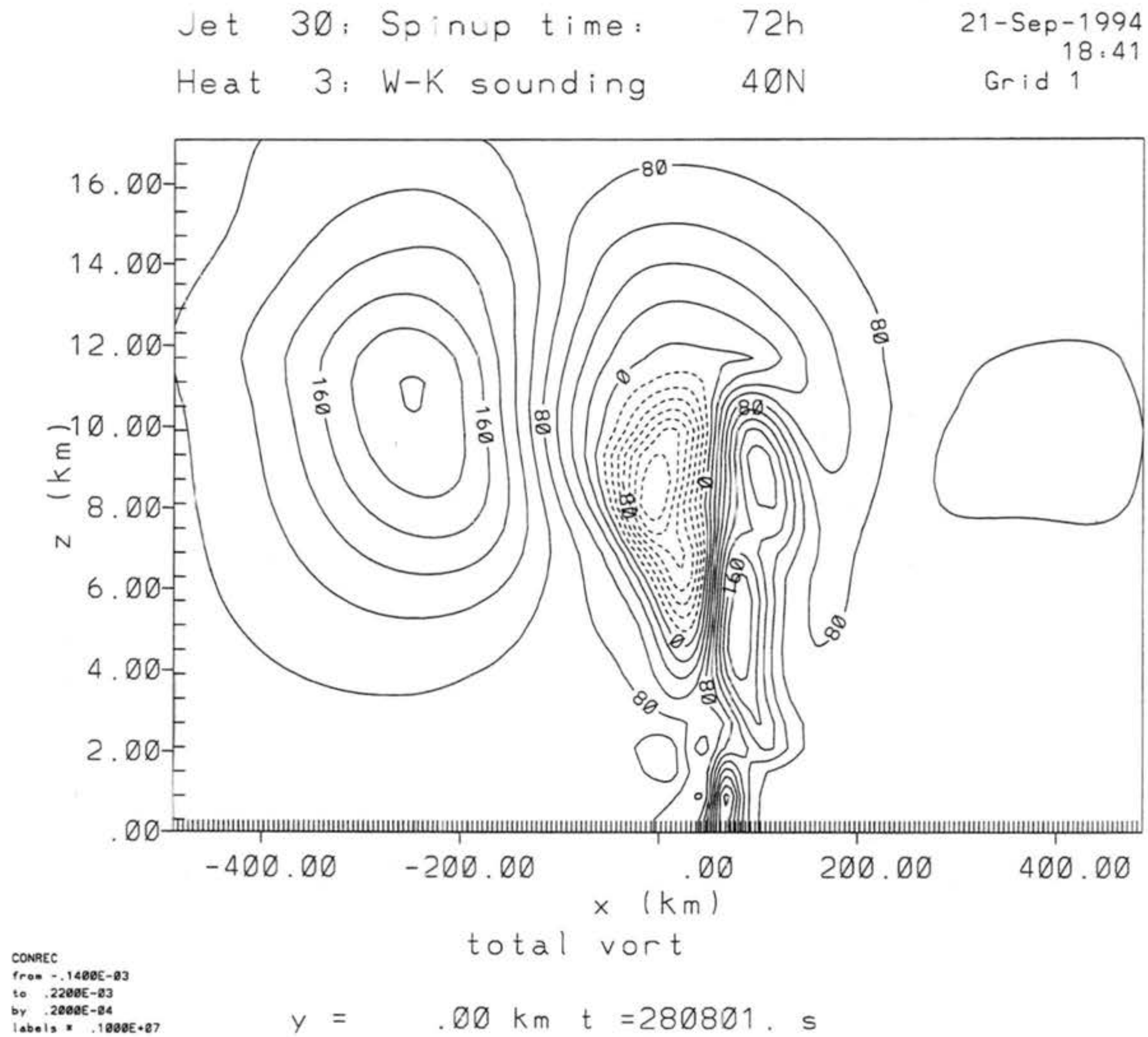

Figure 80. As in Fig. 49, except for t=6 h and for experiment 6 (WKV).

5. SUMMARY AND CONCLUSIONS

The genesis and development of isolated convective cells and meso-β-scale clusters into meso-α-scale mesoscale convective systems (MCSs) and mesoscale convective complexes (MCCs) occur in repeatable subsynoptic environments. Features that are common to many convective system environments include the presence of a mesoscale jet streak and/or a strong subsynoptic-scale ridge. Both of these environments can lead to mesoscale regions of either weak isentropic inertial stability (defined as $\alpha = \eta / f$), or even inertial instability. In the inertially unstable environments, there is no longer a balance between the pressure gradient force, the Coriolis force, and the centripetal force. Parcels accelerated along the pressure gradient are no longer balanced, will not be restored to their initial positions, and may continue to accelerate away from their initial position. In cases of weak inertial stability, the rapid divergence of mass at the cloud top can force a parcel down the pressure gradient; the parcel will attempt to move back to its original position but may take considerable time to do so compared to a displaced parcel in a moderately stable region. If air parcels evacuated from the top of convection can be forced to move both downstream along the shear vector and cross stream through the inertially unstable region, the cloud-top divergence will be enhanced. Additionally, if the divergence at cloud top is rapid enough, a high pressure anomaly and its downward-directed pressure gradient force may not have time to build above the updraft. This pressure gradient acts to decelerate the updrafts. In the absence of this adverse pressure anomaly, updraft strength is maintained for longer durations. The culmination of these effects is to maintain stronger convection for longer periods of time, and to spread warm, saturated updraft air over larger horizontal areas more quickly, eventually reaching horizontal scales approaching the Rossby radius of deformation.

The Rossby radius of deformation can be written as $\lambda_R = c_g / f$, and $c_g \propto NH_k$, where N is the Brunt-Väisällä frequency, and H_k is the scale depth of the k^{th} mode. Since the Brunt-Väisällä frequency is reduced in a saturated, cloudy atmosphere (Fraser et al. 1973; Lalas and Einaudi 1974; Durran and Klemp 1982), the process of rapid horizontal spreading of warm, saturated air aloft can quickly change the Rossby radius of deformation (Tripoli and Cotton 1989b) and bring the convective system into a near-balanced stated. Once this balance is attained, the mesoscale convective system can last for hours, or even days.

The presence of isentropic inertial instabilities requires that the potential vorticity is also less than zero. It has been shown (Haynes and McIntyre 1987) that negative PV anomalies must be created by diabatic or frictional processes. This study has not attempted to ascertain the genesis of the PV anomalies, but an examination of satellite imagery and rawinsonde data suggest that the upper-level anomalies are most probably associated with convection that occurred over the Rocky Mountains. The high altitude of the mountains becomes an effective source for injecting heat and moisture to high levels that is advected east of the mountains.

5.1. Summary of case studies

The high spatial and temporal resolution rawinsonde data from the PRE-STORM field program was carefully analyzed to determine the environmental characteristics associated with mesoscale inertial instabilities. The resolution of these data provided an unprecedented look at these features and showed that:

- Inertially unstable and weakly stable regions are often present when the environment is examined with high spatial and temporal resolution data. The unstable environments are more ubiquitous than commonly assumed and, more importantly, can play an important role in the upscale development of convection.
- The standard NWS rawinsonde spacing and frequency can not adequately sample these regions. The presence of inertially unstable regions sampled by the lower resolution data will typically appear as regions of low stability, but rarely ever unstable.

In regions having a relatively homogeneous environment in the lower troposphere, convection may form in multiple locations during the course of the afternoon and early evening. Convective clusters that are located near or within regions of upper tropospheric inertial instability will often continue to grow upscale during the evening/night while the other convective clusters usually dissipate with the loss of solar heating of the ground and the development of a low-level nocturnal inversion.

In addition to documenting the presence of inertially unstable regions, the rawinsonde data were also used to examine rapid changes in the environment. Temporal changes were computed for temperature, pressure, moisture, and winds using soundings taken 3 h apart . Analyses of these fields on isentropic surfaces revealed:

- Strong divergence and cross-stream accelerations occurred at upper tropospheric levels where inertial instabilities were present. Parcels typically accelerated down the pressure gradient and through the unstable region before turning to align with the shear vector. The accelerations were not uniform over the domain, but were focused in the regions of the instability.

- Accelerations were in the opposite direction in the lower and middle tropospheric levels and were indicative of mass inflow towards the convection.

Analyses of the local changes in temperature, moisture, and winds at an individual rawinsonde site were equally revealing. Rawinsonde data collected in the inertially unstable regions characteristically showed:

- Warming and moistening of the environment at upper tropospheric levels. The isallobaric winds in this warm, moist layer were directed away from the convection.
- Warming and drying below the moist outflow with the isallobaric winds directed back towards the convection. The warming and drying are direct consequences of the adiabatic descent of the flow and, coupled with the outbound flow at upper levels, defines the solenoidal circulation described by Conv-SI theory.

To increase the number of case studies evaluated in this work, mesoscale convective events that occurred during the warm season in 1992 were selected and analyzed using the MAPS model data. The data ingest process for MAPS uses hourly surface reports, vertical wind data from wind profilers, automated aircraft reports (ACARS), and other sources of data to provide the optimal analysis of mesoscale and synoptic-scale features. Output from the model is on isentropic surfaces ranging from 4–8K in the vertical, and 60 km spacing in the horizontal. Using the MAPS analyses, many MCC and MCS environments were analyzed and documented. The results indicate that:

- Mesoscale regions of inertial instability are ubiquitous over the domain of the MAPS analysis, and developing MCCs were often colocated with the diagnosed regions of instability. Values of the inertial stability parameter, $\alpha = \eta / f$, were similar to those diagnosed with the PRE-STORM data.
- These same regions of inertial instability were typically depicted as regions of weak stability in the synoptic-scale numerical models, such as the NGM.

The MAPS analysis and forecast model is in current use at the National Meteorological Center (designated the Rapid Update Cycle, or RUC) and is updated every 3 h. Forecasters can use the high-resolution products available from this model to aid in their diagnosis of mesoscale inertial instabilities and the possibilities of convection growing upscale into mesoscale convective systems.

5.2. Summary of model studies

To complement the analysis of the case studies, the Regional Atmospheric Modeling System (RAMS) was used to simulate inertially unstable and weakly stable environments. A two-dimensional simulation with a jet directed into the plane of the domain was used to explore its effects on nearby convection, represented in the model by an explicit heating function. Note that while the simulations occured in the x-z plane, the wind shear was in the y-direction, perpendicular to this plane such that the ambient meridional wind was parellel to the axes of the circulations that developed. The geometry was set up this way so that the combined dynamical effects of shear and Coriolis rotations could be studied. Various jet strengths (0, 10, 20, and 30 m s^{-1}) were combined with different heating rates (1, 3, and

5°C h^{-1}) and variations in the Coriolis parameter (ϕ=25 and 40°) to ascertain the effects of varying degrees of inertial [in]stability, convective growth rates, and latitude. The first set of experiments was designed as a control experiment with no jet imposed. All three heating rates and both latitudes were tested. The results of the control experiments showed that:

- Outflow at the top of the updraft is symmetric and divergent. The speed of the outflow is determined primarily by the strength of the heating rate, and secondarily by the resistance imposed by the Coriolis parameter.
- An upper-level anticyclone develops over the top of the convection and can generate regions of *in situ* inertial instability.

To understand the full implications of the importance of the Coriolis parameter, all of the jet and heating experiments were run for two latitudes. The results of the simulations indicate that:

- The reduction of the Coriolis force at lower latitudes results in stronger degrees of inertial instability for a given jet strength. This is important since jets are generally weaker in the tropics.
- The response of the outflow generated by the convection to the instability is stronger for a given heating rate.
- These results suggest that there may be a latitudinal limit to this process; that is, at high latitudes, the strength of the Coriolis force is strong enough so that inertial instabilities cannot be achieved by the horizontal shear typical in mid-latitude jet streaks.

This latitudinal limit may be a factor in explaining why mesoscale convective systems are not common at high latitudes. Of course, the lack of deep moisture and a low-level jet to transport it poleward may also be important. Nonetheless, it is one more factor that must be considered.

In addition to the control experiment with no jet, three additional jet speeds were tested. The strongest jet resulted in the development of an weakly inertially unstable region prior to the convection. The remaining two jets produced areas that were moderately and weakly inertially stable. The results of the differing jet strengths simulations show that:

- The presence of inertial instabilities and weak stabilities can have a pronounced effect on the rate of divergence from convective updrafts and the ensuing outflow in the upper troposphere. The strength of the outflow associated with the strongest jet was ~47% greater than that associated with the no-jet control experiment.
- The experiments all showed nearly symmetric outflow during the initial periods of the simulations.
- With the progression of time, the strength of the outflow branch in the presence of the weaker stability continued to increase with time; the branch in the stable environment did not grow as quickly in some simulations, and actually decreased in others.
- The stronger jets generated a greater degree of asymmetry of the outflow, clearly showing that the response grows with decreasing inertial stability.

As noted above, in some simulations, one branch of the divergent outflow actually decreased in strength with time. The explanation for this phenomenon is related to the increase of inertial stability in this region with time. The increase of inertial stability is a consequence of the horizontal advection of higher momentum air associated with the jet into regions of weaker winds and locally increasing the relative vorticity and inertial stability.

Additional experiments were conducted with varying heating rates. It was found that:

- The stronger heating rates produced greater amounts of vertically-advected mass that needed to be transported away from the source. Consequently, the divergent outflow was stronger from the outset in these cases. This stronger outflow also resulted in the rotational winds associated with the anticyclone to be located farther from the updraft core and the *in situ* development of inertial instability to be similarly displaced.
- The presence of the pre-existing inertial instability produced stronger asymmetries in the diverging flows associated with the larger heating rates than for the weaker rates.

An additional set of experiments was conducted to test the sensitivity of the simulations to the degree of convective instability. The original data used to initialize RAMS was a slightly smoothed sounding from Oklahoma City, Oklahoma (OKC sounding). This sounding sampled the environment immediately prior to an outbreak of convection that grew upscale into an MCC in the presence of inertial instability. One of the characteristics of this sounding was the presence of elevated mixed layers resulting in deep layers with a dry adiabatic lapse rate. The comparison simulations used a sounding (WK sounding) that had no elevated mixed layers, although the deep layer instability was similar to the original. The results were interesting because they indicated that:

- The degree of asymmetry and the strength of the outflow were controlled in part by the environmental lapse rate in the layers where the mass was diverging.

The differences in outflow speeds and the resulting asymmetry in the divergent outflow can be explained by the fact that:

- In the simulations using the OKC sounding, subsiding air encountered less reisistance to descent in the deep adiabatic layers than did the parcels in the simulations using the WK sounding.
- This increased resistance for descending parcels in the WK simulations resulted in slower descent rates which, in turn, limited the amount of air that could diverge from the top of the heated region and, ultimately, decreased the strength of the updrafts and increased the asymmetry of the outflow.

The presence of both convective and symmetric (or isentropic inertial) instability has been termed both "Convective-Symmetric Instability (Conv-SI; Emanuel 1980; Seman 1991) and "nonhydrostatic, nonlinear CSI (Seman 1994), and represents unbalanced dynamics associated with convective momentum transport and Coriolis rotation. The instability starts with momentum transport in the deep convection which creates negative isentropic absolute vorticity and the potential for symmetric instability in the upper levels of the system. Coriolis rotation allows the symmetric instability to be realized. Finally, a mesoscale outflow jet grows as the symmetric instability is released which in turn ventilates the upper levels of the systems and assists in the development of more convection. This mesoscale jet develops inertial instability that can feed back into the larger environment instability. A positive feedback mechanism exists on mesoscale time scales because the deep convection transports more low-level momentum to the upper levels, replenishing the supply of symmetrically-unstable flow aloft. As noted in the Introduction, and shown in the results presented here, the presence of weak inertial stability or instability prior to the convection enhances the likelihood of this process occurring. Thus, if the environment is already tending toward a state of inertial instability, very little additional momentum transport may be required to tip the scales from stability to instability. Conversely, in an environment that is inertially very stable, the Conv-SI process may never develop the required instabilities.

5.3. Discussion of conceptual model

In Chapter 2, we presented a conceptual model (Figs. 2–4) of the processes involved in the upscale growth of convection into mesoscale systems in the presence of inertial instabilities. It is useful to compare the conceptual model with the previously discussed observational and modeling results.

The presentation of observational data from both the PRE-STORM cases and MAPS model data have indicated that many MCSs form in the presence of weak inertial [in]stability. It should be clear, however, that the presence of inertial instability is neither a necessary nor sufficient conditon for the upscale growth of convection into mesoscale convective systems. It is simply another factor that needs to be considered in the total process of MCS evolution.

The spatial and temporal resolution of the sounding data from the PRE-STORM field program was of sufficient quality to investigate the enhanced expansion of outflow material through the inertially unstable regions and the generation of a solenoidal circulation, and that the evolution was similar to that depicted in Fig. 4. There was a perceptible tendency for greater acceleration of the divergent winds through the unstable region than through the stable region. The development of a secondary circulation consisting of a drying and warming return flow from the upper troposphere to the middle and lower troposphere in the vicinity of the convection was also discernible.

The inferences made from the observational data were supplemented with the results from a simple set of numerical model simulations. These simulations similarly demonstrated that the presence of weak inertial [in]instability can have an important impact on the development of secondary circulations. The model-simulated secondary circulations that developed were similar to those observed in the case study data and further support the conceptual model presented in Fig. 4.

5.4. Future Research

The results of this study show that convection can be enhanced in the presence of upper-tropospheric inertial instabilities. The work presented here should be considered a starting point for future research into this interesting topic.

The use of model simulations can be greatly enhanced with high quality data collected from research experiments. It is suggested that the U.S. Weather Research Program should endeavor to provide a high concentration of rawinsonde launch sites and wind profiler Dopper radars in the field to provide the scale of coverage required to analyze these mesoscale instabilities. The data collected during PRE-STORM provided an unprecedented look at these features, but because these were not expected and were not part of the original program and scientific goals, the collection of data was not optimized for this purpose. Given this new information, future deployments should take into consideration the collection of data that can provide further insight into the spatial and temporal characteristics of this phenomena.

As computer hardware becomes progressively faster and less expensive, it becomes easier to run more sophisticated models with more features. Modeling studies should attempt to expand this simple two-dimensional study into a full three-dimensional analysis. The 3-D simulations could be constructed so that they look at the more complex situation in the strongly curved, anticyclonic flow present in a subsynoptic-scale ridge. The curved flow in 3-D presents a problem with balances between the pressure gradient force, Coriolis forces, and centripetal accelerations.

Finally, because the effects of melting hydrometeors can affect the development of convection and mesoscale convective systems, simulations using explicit convection with full microphsyics could be attempted. Comparisons of simulations with and without ice could provide evidence of the importance of the melting layer to the develoment of these circulations.

6. REFERENCES

Arakawa, A. and V.R. Lamb, 1981: A potential enstrophy and energy conserving scheme for the shallow water equations. *Mon. Wea. Rev.*, **109**, 18–36.

Augustine, J.A. and K.W. Howard, 1988: Mesoscale convective complexes over the United States during 1985. *Mon. Wea. Rev.*, **116**, 685–701.

———— and F. Caracena, 1994: Lower-tropospheric precursors to nocturnal MCS development over the central United States. *Wea. Forecasting*, **9**, 116–135.

Bader, D, 1987: Mesoscale boundary layer evolution over complex terrain. Part I: Numerical simulation of the diurnal field. *J. Atmos. Sci.*, **44**, 2823–2838.

Barnes, S.L., 1964: A technique for maximizing details in numerical weather map analysis. *J. Appl. Meteor.*, **3**, 396–409.

————, 1985: Omega diagnostics as a supplement to LFM/MOS guidance in weakly forced convective situations. *Mon. Wea. Rev.*, **113**, 2122–2141.

Bartels, D.L. and R.A. Maddox, 1991: Midlevel cyclonic vortices generated by mesoscale convective complexes. *Mon. Wea. Rev.*, **119**, 104–118.

Benjamin, S.G., K.A. Brewster, R.L. Brummer, B.F. Jewett, T.W. Schlatter, T.L. Smith, and P.A. Stamus, 1991: An isentropic three-hourly data assimilation system using ACARS aircraft observations. *Mon. Wea. Rev.*, **119**, 888–906.

————, R. Bleck, G. Grell, Z.-T. Pan, T.L. Smith, J.M. Brown. J.E. Ramer. P.A. Miller, and K. Brundage, 1993: Aviation forecasts from the hybrid-b version of MAPS — effects of a new vertical coordinate and improved model physics. *Preprints, 5th Conf. on Aviation Weather Systems*, American Meteorological Society, Boston, Mass., J5–J9.

Bennetts, D.A. and B.J. Hoskins, 1979: Conditional symmetric instability—a possible explanation for frontal rainbands. *Quart. J. Roy. Meteor. Soc.*, **105**, 945–962.

Blanchard, D.O., 1990: Mesoscale convective patterns of the southern High Plains. *Bull. Amer. Meteor.* Soc., **71**, 994–1005.

Brandes, E.A., 1990: Evolution and structure of the 6–7 May 1985 mesoscale convective system and associated vortex. *Mon. Wea. Rev.*, **118**, 109–127.

Brown, J.M., 1979: Mesoscale unsaturated downdrafts driven by rainfall evaporation: A numerical study. *J. Atmos. Sci.*, **36**, 313–338.

Caracena, F., 1987: Analytic approximation of discrete field samples with weighted sums and gridless computation of derivatives. *J. Atmos. Sci.*, **44**, 3753–3768.

Charney. J.G. and A. Eliassen, 1964: On the growth of the hurricane depression. *J. Atmos. Sci.*, **21**, 68–75.

Churchill, D.D. and R.A. Houze, Jr., 1984: Development and structure of winter monsoon cloud clusters on 10 December 1978. *J. Atmos. Sci.*, **41**, 933–960.

Clark, T.L., 1977: A small-scale dynamic model using a terrain following coordinate transformation. *J. Comput. Phys.*, **24**, 186–215.

Cotton, W.R., M.A. Stephens, T. Nehrkorn, and G.J. Tripoli, 1982: The Colorado State University three-dimensional cloud/mesoscale model - 1982. Part II: An ice parameterization. *J. Rech. Atmos.*, **16**, 295–320.

————, R.L. George, P.J. Wetzel, and R.L. McAnelly, 1983: A long-lived mesoscale convective complex. Part I: The mountain-generated components. *Mon. Wea. Rev.*, **111**, 1893–1918.

————, M. Lin, R.L. McAnelly, and C.J. Tremback, 1989: A composite model of mesoscale convective complexes. *Mon. Wea. Rev.*, **117**, 765–783.

Cram, J.M., R.A. Pielke, and W.R. Cotton, 1992: Numerical simulations and analysis of a prefrontal squall line. Part II: Propagation of the squall line as an internal gravity wave. *J. Atmos. Sci.*, **49**, 189–208.

Cunning, J. B., 1986: The Oklahoma-Kansas preliminary regional experiment for STORM-Central. *Bull. Amer. Meteor. Soc.*, **67**, 1478–1486.

Doswell, C.A. III, 1987: The distinction between large-scale and mesoscale contributions to severe convection: A case study example. *Wea. Forecasting*, **2**, 3–16.

Durran, D.R. and J.B. Klemp, 1982: The effects of moisture on trapped mountain lee waves. *J. Atmos. Sci.*, **39**, 2490–2506.

Eliassen, A., 1951: Slow thermally or frictionally controlled meridional circulation in a circular vortex. *Astrophys. Norv.*, **5**, 19–60.

Emanuel, K.A., 1979: Inertial instability and mesoscale convective systems. Part I: Linear theory of inertial instability in rotating viscous fluids. *J. Atmos. Sci.*, **36**, 2425–2449.

———, 1980: Forced and free mesoscale motions in the atmosphere. *Collection of lecture notes on dynamics of mesometeorological disturbances, CIMMS Symposium*. University of Oklahoma/NOAA, Norman, Okla., pp 189–259.

———, 1982: Inertial instability and mesoscale convective systems. Part II. Symmetric CISK in a baroclinic flow. *J. Atmos. Sci.*, **39**, 1080–1097.

———, 1983: The Lagrangian parcel dynamics of moist symmetric instability. *J. Atmos. Sci.*, **40**, 2368–2376.

———, 1992: Slantwise circulations in middle latitude cyclones. *Preprints, 5th Conference on Mesoscale Processes*. American Meteorological Society, Boston, Mass., 233–234.

Fortune, M.A., W.R. Cotton, and R.L. McAnelly, 1992: Frontal-wave-like evolution in some mesoscale convective complexes. *Mon. Wea. Rev.*, **120**, 1279–1300.

Fovell, R.G., 1991: Influence of the Coriolis force on a two-dimensional model storm. *Mon. Wea. Rev.*, **119**, 603–630.

Fraser, A.B., R. Easter, and P.V. Hobbs, 1973: A theoretical study of the flow of air and fallout of solid precipitation over mountainous terrain: Part I. Air flow model. *J. Atmos. Sci.*, **30**, 801–812.

Fritsch, J.M, and R.A. Maddox, 1981: Convectively driven mesoscale weather systems aloft. Part II: Numerical simulations. *J. Appl. Meteor.*, **20**, 20–26.

———, R.J., Kane and C.R. Chelius, 1986: The contribution of mesoscale convective weather systems to the warm-season precipitation in the United States. *J. Clim. and Appl. Meteor.*, **25**, 1333–1345.

Gal-Chen, T., and R.J. Sommerville, 1975: On the use of coordinate transformations for the solution of the Navier-Stokes equations. *J. Comput. Phys.*, **17**, 209–228.

Greene, D.R., J.D. Nelson, R.E. Saffle, D.W. Holmes, M.D. Hudlow, and P.R. Ahnert, 1983: RADAP II: An interim radar data processor. *Preprints,* *21st Conference on Radar Meteorology*, American Meteorological Society, Boston, Mass., 404–408.

Haynes, P.H. and M.E. McIntyre, 1987: On the evolution of vorticity and potential vorticity in the presence of diabatic heating and frictional or other forces. *J. Atmos. Sci.*, **44**, 828–841.

Hertenstein, R.F.A and W.H. Schubert, 1991: Potential vorticity anomalies associated with squall lines. *Mon. Wea. Rev.*, **119**, 1663–1672.

Holliday, C.R. and A.H. Thompson, 1979: Climatological characteristics of rapidly intensifying typhoons. *Mon. Wea. Rev.*, **107**, 1022–1034.

Holton, J.R., 1992: An introduction to dynamic meteorology: 3rd Edition. Academic Press, San Diego, California.

Hoskins, B.J., 1974: The role of potential vorticity in symmetric stability and instability. *Quart. J. Roy. Meteor. Soc.*, **100**, 480–482.

———— , I. Draghici, and H Davies, 1978: A new look at the ω-equation. *Quart. J. Roy. Met. Soc.*, **104**, 31–38.

———— , and M.A. Pedder, 1980: The diagnosis of middle latitude synoptic development. *Quart. J. Roy. Meteor. Soc.*, **106**, 707–719.

Houze, R.A., B.F. Smull, and P. Dodge, 1990: Mesoscale organization of springtime rainstorms in Oklahoma. *Mon. Wea. Rev.*, **118**, 613–645.

Jascourt, S.D., S.S. Lindstrom, C.J. Seman, and D.D. Houghton, 1988: An observation of banded convective development in the presence of weak symmetric stability. *Mon. Wea. Rev.*, **116**, 175–191.

Johnson, R.H.and J.J. Toth, 1986: Preliminary data quality analysis for May–June 1985 Oklahoma-Kansas PRE-STORM PAM II mesonetwork. *Dept. of Atmospheric Science Paper No. 407*, Colorado State University, Ft. Collins, CO., 41 pp.

———— , and P.J. Hamilton, 1988: The relationship of surface pressure features to the precipitation and airflow structures of an intense midlatitude squall line. *Mon. Wea. Rev.*, **116**, 1444–1472.

Kane, R.J., C.R. Chelius, and J.M. Fritsch, 1987: Precipitation characteristics of mesoscale convective weather systems. *J. Climate Appl. Meteor.*, **26**, 1345–1357.

Keyser, D. and M.A. Shapiro, 1986: A review of the structure and dynamics of upper level frontal zones. *Mon. Wea. Rev.*, **114**, 452–499.

Klemp, J.B., and R.B. Wilhelmson, 1978: The simulation of three-dimensional convective storm dynamics. *J. Atmos. Sci.*, **35**, 1070–1096.

Koch, S.E., M. DesJardins, and P.J. Kocin, 1983: An interactive Barnes objective map analysis scheme for use with satellite and conventional data. *J. Clim. and Appl. Meteor.*, **22**, 1487–1503.

Lalas, D.P. and F. Einaudi, 1974: On the correct use of the wet adiabatic lapse rate in stability criteria of a saturated atmosphere. *J. Appl. Meteor.*, **13**, 318–324.

Leary, C.A., 1984: Precipitation structure of the cloud clusters in a tropical easterly wave. *Mon. Wea. Rev.*, **112**, 313–325.

Maddox, R.A., 1980: Mesoscale convective complexes. *Bull. Amer. Meteor. Soc.*, **61**, 1374–1387.

———— , 1983: Large–scale meteorological conditions associated with mid-latitude convective complexes. *Mon. Wea. Rev.*, **111**, 1475–1493.

Mahrer, Y. and R.A. Pielke, 1977: A numerical study of the airflow over irregular terrain. *Beitr. Phys. Atmos.*, **50**, 98–113.

McAnelly, R.L. and W.R. Cotton, 1986: Meso-β-scale characteristics of an episode of meso-α-scale convective complexes. *Mon. Wea. Rev.*, **114**, 1740–1770.

———— and ———— , 1989. The precipitation life cycle of mesoscale convective complexes over the central United States. *Mon. Wea. Rev.*, **117**, 784–808.

———— and ———— , 1992: Early growth of mesoscale convective complexes: A meso-β-scale cycle of convective precipitation? *Mon. Wea. Rev.*, **120**, 1851–1877.

McCumber, M and R.A. Pielke, 1981: Simulation of the effects of surface fluxes of heat and moisture in a mesoscale numerical model. Part I: Soil model. *J. Geophys. Res.*, **86**, 9929–9938.

McNider, R.T. and R.A. Pielke, 1981: Diurnal boundary-layer development over sloping terrain. *J. Atmos. Sci.*, **38**, 2198–2212.

McIntyre, M.E., 1970: Diffusive destabilization of the baroclinic circular vortex. *Geophys. Fluid Dyn.*, **1**, 19–57.

Meitín, J.G., 1988: The Oklahoma-Kansas Preliminary Regional Experiment for STORM-Central (O-K PRE-STORM). Volume III: Aircraft Mission Summary. *NOAA Tech. Memo ERL ESG-30*, 109 pp.

Mellor, G.L. and T. Yamada, 1982: Development of a turbulence closure model for geophysical fluid problems. *Rev. Geophys. Space Phys.*, **20**, 851–875

Menard, R.D. and J.M. Fritsch, 1989: A mesoscale convective complex-generated inertially stable warm core vortex. *Mon. Wea. Rev.*, **117**, 1237–1261.

Nachamkin, J.E., R.L. McAnelly, and W.R. Cotton, 1994: An observational analysis of a developing mesoscale convective complex. *Mon. Wea. Rev.*, **122**, 1168–1188.

Ooyama, K., 1964: A dynamical model for the study of tropical cyclone development. *Geofis. Int.*, **4**, 187–198.

——— 1969: Numerical simulation of the life cycle of tropical cyclones. *J. Atmos. Sci.*, **26**, 3–40.

Pielke, R.A., 1974: A three-dimensional numerical model of the sea breezes over south Florida. *Mon. Wea. Rev.*, **102**, 115–134.

——— , W.R. Cotton, R.L. Walko, C.J. Tremback, W.A. Lyons, L.D. Grasso, M.E. Nicholls, M.D. Moran, D.A. Wesley, T.J. Lee, and J.H. Copeland, 1992: A comprehensive meteorological modeling system–RAMS. *Meteorol. Atmos. Phys.*, **49**, 69–91.

Rasmussen, E.N., and S.A. Rutledge, 1993: Evolution of quasi-two-dimensional squall lines. Part I: Kinematic and reflectivity structure. *J. Atmos. Sci.*, **50**, 2584–2606.

Raymond, D.J., 1987: A forced gravity wave model of self-organizing convection. *J. Atmos. Sci.*, **44**, 3528–3543.

——— , 1992: On the formation of jets and vortices in mesoscale convective systems. *Preprints, 5th Conference on Mesoscale Processes.* American Meteorological Society, Boston, Mass., 333–336.

——— , and H. Jiang, 1990: A theory for long-lived mesoscale convective systems. *J. Atmos. Sci.*, **47**, 3067–3077.

Rotunno, R., J.B. Klemp, and M.L. Weisman, 1988: A theory for strong long-lived squall lines. *J. Atmos. Sci.*, **45**, 463–485.

Rutledge, S.A., R.A. Houze, M.I. Biggerstaff and T. Matejka, 1988: The Oklahoma-Kansas mesoscale convective system of 10–11 June 1985: Precipitation structure and single-Doppler radar analysis. *Mon. Wea. Rev.*, **116**, 1409–1430.

Schaeffer, J.T., 1986: The Dryline. In, "Mesoscale meteorology and forecasting" (P. Ray, ed.). American Meteorological Society, Boston, Mass.

Schmidt, J.M. and W.R. Cotton, 1990: Interactions between upper and lower tropospheric gravity waves on squall line structure and maintenance. *J. Atmos. Sci.*, **47**, 1205–1222.

Seman, C.J., 1990: Numerical simulation of deep moist convection in a baroclinic atmosphere. *Preprints, 4th Conference on Mesoscale Processes*, American Meteorological Society, Boston, Mass., 104–105.

———, 1991: Numerical study of nonlinear convective-symmetric instability in a rotating baroclinic atmosphere. Ph.D. Thesis, University of Wisconsin-Madison, 185 pp.

———, 1994: A numerical study of nonlinear nonhydrostatic conditional symmetric instability in a convectively unstable atmosphere. *J. Atmos. Sci.*, **51**, 1352–1371.

Schubert, W.H. and J.J. Hack, 1982: Inertial stability and tropical cyclone development. *J. Atmos. Sci.*, **39**, 1687–1697.

———, ———, P.L. Silva Dias, and S.R. Fulton, 1980: Geostrophic adjustment in an axisymmetric vortex. *J. Atmos. Sci.*, **37**, 1464–1484.

Shea, D.J. and W.M. Gray, 1973: The hurricane's inner core region. I: Symmetric and asymmetric structure. *J. Atmos. Sci.*, **38**, 2021–2030.

Skamarock, W.C., M.L. Weisman, and J.B. Klemp, 1994: Three-dimensional evolution of simulated long-lived squall lines. *J. Atmos. Sci.*, **51**,2563–2584.

Smull, B.F. and R.A. Houze, 1985: A midlatitude squall line with a trailing region of stratiform rain: Radar and satellite observations. *Mon. Wea. Rev.*, **113**, 117–133.

———, and ———, 1987: Rear inflow in squall lines with trailing stratiform precipitation. *Mon. Wea. Rev.*, **115**, 2869–2889.

Stevens, D.E. and P.E. Cielsielski, 1986: Inertial instability of horizontally sheared flow away from the equator. *J. Atmos. Sci.*, **43**, 2845–2856.

Straka, J. and Y. Liu 1993: The influence of ice-phase microphysics on convective storm structure and evolution. *Preprints, 17th Conference on Severe Local Storms,* American Meteorological Society, Boston, Mass., 178–183

Thorpe, A.J., M.J. Miller, and M.W. Moncrieff, 1982: Two-dimensional convection in non-constant shear: A model of mid-latitude squall lines. *Quart. J. Roy. Meteor. Soc.*, **108**, 739–762.

Tremback, C.J., G.J. Tripoli, and W.R. Cotton, 1985: A regional scale atmospheric numerical model including explicit moist physics and a hydrostatic time-split scheme. *Preprints, 7th Conference on Numerical Weather Prediction*, American Meteorological Society, Boston, Mass., 355–358.

Tripoli, G.J. and W.R. Cotton, 1982: The Colorado State University three-dimensional cloud/mesoscale model–1981. Part I: General theoretical framework and sensitivity experiments. *J. Rech. Atmos.*, **16**, 185–210.

——— and ——— , 1989a: Numerical study of an observed orogenic mesoscale convective system. Part 1: Simulated genesis and comparison with observations. *Mon. Wea. Rev.*, **117** 272–358.

——— and ——— , 1989b: Numerical study of an observed orogenic mesoscale convective system. Part 2: Analysis of governing dynamics. *Mon. Wea. Rev.*, **117**, 305–328.

Verlinde, J., and W.R. Cotton, 1990: Mesoscale vortex-couplet observed in the trailing anvil of a multicellular convective complex. *Mon. Wea. Rev.*, **118**, 993–1010.

Waton, A.I., J.G. Meitín, and J.B. Cunning, 1988: Evolution of the kinematic structure and precipitation characteristics of a mesoscale convective system on 20 May 1979. *Mon. Wea. Rev.*, **116**, 1555–1567.

Weisman, M.L. and J.B. Klemp, 1982: The dependence of numerically simulated convective storms on vertical shear and buoyancy. *Mon. Wea. Rev.*, **110**, 504–520.

——— and ——— , 1984: The structure and classification of numerically simulated convective storms in directionally varying wind shears. *Mon. Wea. Rev.*, **112**, 2479–2498.

Wetzel, P.J., W.R. Cotton, and R.L. McAnelly, 1983: A long-lived mesoscale convective complex. Part II: Evolution and structure of the mature complex. *Mon. Wea. Rev.*, **111**, 1919–1937.

Wu, X., 1993: Effects of cumulus ensemble and mesoscale stratiform clouds in midlatitude convective systems. *J. Atmos. Sci.*, **50**, 2496–2518.

Xu, Q., 1986: Conditional symmetric instability and mesoscale rainbands. *Quart. J. Roy. Met. Soc.*, **112**, 315–334.

Yamada, T., 1983: Simulations of nocturnal drainage flows by a q^2-l turbulence closure model. *J. Atmos. Sci.*, **40**, 91–106.

Yanai, M.S., S. Esbensen, and J.-H. Chu, 1973: Determination of bulk properties of tropical cloud clusters from large-scale heat and moisture budgets. *J. Atmos. Sci.*, **30**, 611–627.

Zhang, D.-L. and J. M. Fritsch, 1988: Numerical investigation of a convectively generated, inertially stable, extratropical warm-core mesovortex over land. Part I: Structure and evolution. *Mon. Wea. Rev.*, **116**, 2660–2687.

——— and H.-R. Cho, 1992: The development of negative moist potential vorticity in the stratiform region of a simulated squall line. *Mon. Wea. Rev.*, **120**, 1322–1341.

7. APPENDIX

7.1. Description of Eliassen's basic model

The system under consideration in Eliassen (1951) is a compressible fluid performing a circular vortex motion in a gravity field. The speed of rotation, the thermodynamical state of the fluid particles, and the gravity potential are assumed to be constant along each circular streamline so that the vortex is symmetric with respect to its axis. It was then sufficient for Eliassen to consider the conditions in one meridional plane. The vortex motion remains stationary while no friction is operating, and no heat is added to or withdrawn from the fluid particles. Such a stationary circular vortex is characterized by a balance between the force of gravity, the pressure gradient, and the centrifugal force. Eliassen did not use this simplistic formulation, but instead assumed heat sources, sinks, and frictional forces, distributed symmetrically with respect to the axis of the vortex, are present. These additions lead to a change with time of the entropy of the fluid particles and the frictional forces will generally have a torque with respect to the axis, and thus cause a change with time of the angular momentum of the particles. As a result, the balance of the vortex will be disturbed, and meridional motions, superimposed on the vortex motion, will occur. It is the study of these meridional motions that forms the core of the work in Eliassen. To simplify the problem, Eliassen assumed the sources of heat and angular momentum to be weak, and to change so slowly with time that resonance phenomena could not occur. The resulting meridional currents can then be considered to be so slow that the accelerations due to these currents are small compared to the centripetal accelerations. Doing so allows the vortex to be very close to a state of balance at all times. By assuming it to be in balance at all time, it can be determined what meridional motions are required to maintain this balance.

7.2. Determination of initial state

Eliassen's Eqs. 2-27, a set of relationships between the geopotential (Φ) and streamfunctions (ψ), form a system of linear, first-order differential equations in the two space coordinates, and time drops out as an independent variable. In the quasi-static theory, the determination of the meridional motion is therefore not an initial value problem; the meridional motion depends only on the instantaneous sources of heat and angular momentum and the instantaneous structure of the vortex.

7.3. Description of angular momentum changes

Eliassen described a cause and effect relationship between the meridional motions present in the vortex and the angular momentum. He stated that since the sources of angular momentum in the free atmosphere presumably are comparatively weak, one should expect that meridional circulations would cause a weakening of the gradient of angular momentum [in the meridional plane]. It is not unreasonable to assume the weak gradient of angular momentum equatorward of the jet maximum is caused by meridional currents, which in this strongly baroclinic region must have a pronounced tendency to follow the sloping isentropic lines, thus carrying angular momentum from low levels into the upper troposphere. The weakening of the gradient of angular momentum in a region where meridional circulations are occurring must be accompanied by a strengthening of the gradient in the adjacent regions. Since the inertial stability is proportional to the gradient of angular momentum, meridional circulations will tend to reduce the inertial stability in the region where these circulations occur, and to increase the inertial stability in adjacent regions. Therefore, a meridional circulation will support itself by reducing the stability within this region, and will suppress meridional circulations in the adjacent regions by increasing the stability of these regions.